SAR imaging of an asteroid's regolith : simulation and data processing

Oriane Gassot

THÈSE

Pour obtenir le grade de

DOCTEUR DE L'UNIVERSITE GRENOBLE ALPES

Spécialité : **Astrophysique et Milieux Dilués**

Arrêté ministériel : 25 mai 2016

Présentée par

Oriane GASSOT

Thèse dirigée par **Alain HERIQUE,** Maitre de Conférences, Université Grenoble Alpes

préparée au sein de **l'Institut de Planétologie et d'Astrophysique de Grenoble**
dans **l'École Doctorale Physique**

Imagerie SAR du régolithe d'un astéroïde : Simulation et traitement des données.

SAR imaging of an asteroid's regolith : Simulation and data processing.

Thèse soutenue publiquement le **11 juin 2020**
devant le jury composé de :

Monsieur Stéphane GARAMBOIS
Professeur des Universités, Université Grenoble Alpes - France, Président.

Monsieur Sampsa PURSIAINEN
Professeur associé, Université de Tampere – Finlande, Rapporteur.

Madame Amélie LITMAN
Maître de conférence, HDR, Université Aix-Marseille - France, Rapporteur.

Monsieur Daniel HESTROFFER
Astronome, Observatoire de Paris – France, Examinateur.

Monsieur Dirk PLETTEMEIER
Professeur, Université Technique de Dresde – Allemagne, Examinateur.

Monsieur Wlodek KOFMAN
Directeur de recherche émérite, Université Grenoble Alpes - France, Examinateur.

Abstract

In recent years, surface-penetrating radars were part of several space missions dedicated to study the bodies of the solar system. These radars, associated with repeat-pass observations and processing, can lead to 3D radar tomography, which results in 3D imagery of the sub-surface of planetary bodies. This technique can be used to better understand and model the formation processes and post-accretion evolution of asteroids. However, even though spaceborne SAR is a classical technique used for the detection and reconstruction of planetary structures, the small body geometry of observation reconsiders the hypotheses usually formulated for Earth observation. Furthermore, in order to achieve the metric-resolution necessary to study kilometric-sized asteroids with sufficient precision, the radar has to be ultra-wideband in range and in Doppler, which also question the SAR synthesis models established for narrow band signals. As the radar geometry of study and configuration drives the instrument performance, and thus the mission science return, simulation of the radar signal and the SAR synthesis needs to be developed while taking into account the specificity of the small body geometry.

Thus, this work aims at assessing the performances of the ultra-wideband radar HFR (High Frequency radar), which is dedicated to the study of small bodies with frequencies ranging from 300 to 800 MHz, by performing a first complete simulation/processing/analysis chain of the radar signal.

First, I studied the surface of a kilometric-sized asteroid to create a realistic asteroid digital terrain model (DTM). The asteroid Itokawa, observed by the mission Hayabusa (JAXA) was found out to be made of rough surfaces (the Highlands) and smooth surfaces (the Lowlands). Using the roughness parameters obtained from Hayabusa instruments, I developed terrain models representative of Highlands, Lowlands, and a model composed of mixed roughness. Then, I reviewed the state of the art in surface scattering models in order to simulate the signal backscattered from previously obtained DTM. Several scattering models exist; each of them being adapted to a specific domain of validity with a computation cost. The Kirchhoff Approximation (KA) was selected as a surface scattering model and applied to the small body geometry of the main asteroid of the Didymos binary system. The KA was proven efficient to model the signal backscattered by the asteroid surface with HFR. Using a multipass orbitography, the level of the left/right ambiguity, an undesirable artefact on spherical bodies was reduced to an acceptable level.

However, in order to model the signal scattered by the subsurface of the asteroid, volume scattering models need to be investigated as well. The Born approximation (BA) was selected and applied to model the field scattered by one inclusion embedded under the asteroid surface. The Born approximation successfully retrieve the embedded inclusion and is consistent with point target results, but with a poor resolution in the vertical direction, as expected from a single-pass SAR geometry.

Thus, to improve the resolution of HFR in the elevation direction, I conducted a tomography study performed from the Born approximation results. Among all available tomography methods, I chose the compressive sensing (CS) method based on its high resolution and its low computation times capabilities as well as the possibility to easily compensate the delay induced by the medium's permittivity . CS was found out to improve the resolution in elevation by a factor of almost four, to obtain a resolution in the elevation direction of less than one meter, and to improve the localisation of the target when taking into account the permittivity $\epsilon \neq 1.0$ of the subsurface.

Finally, the overall performances of UWB scattering were investigated: several standard SAR hypotheses are reconsidered because of the UWB characteristics of the radar signal, and the consequences on the resolution were investigated. In the end, even if the classical SAR hypotheses are not respected, our ongoing work seems to indicate that observing a surface with a UWB has no major consequences on the radar resolution.

Abstract

Les radars pénétrant sont des instruments embarqués à bord de multiples missions spatiales depuis plusieurs années. En mettant à profit des observations obtenues depuis différentes orbites séparées spatialement, ils peuvent mener à l'utilisation de techniques de tomographie radar en 3D afin d'imager la structure interne de corps planétaires, notamment des astéroïdes, et améliorer les modèles de formations et d'évolution des astéroïdes.
Cependant, même si les radars à synthèse d'ouverture (SAR) spatiaux sont classiques afin de détecter et reconstruire des structures planétaires, pour une telle étude effectuée à quelques kilomètres d'un astéroïde, la taille, la vitesse de rotation et au final la géométrie d'observation elle-même remets en question les hypothèses habituellement formulées pour l'observation de la Terre. De plus, afin d'atteindre la résolution métrique nécessaire afin d'observer des astéroïdes kilométriques, le radar doit être à très large bande (UWB) en range et en doppler, ce qui remets également en cause les modèles de synthèse SAR. Puisque les performances du radar, et donc le retour scientifique de la mission, dépendent de la géométrie d'observation et de la configuration du radar, des simulations du signal radar et de la synthèse SAR dans la géométrie d'un petit corps doivent être mis en place.
Le but de ce manuscrit est d'étudier les performances du radar à très large bande (UWB) HFR, développé afin d'étudier les petits corps avec des fréquences allant de 300 à 800 MHz, en établissant une première boucle complete de simulation/analyse/traitement du signal radar.
Dans un premier temps, j'ai étudié une surface standard d'un astéroïde de taille kilométrique afin de créer un modèle de terrain numérique (DTM) réaliste. L'astéroïde Itokawa, étudié par la mission Hayabusa (JAXA) est composée de surfaces très rugueuses (les Highlands), et de surfaces plus planes (les Lowlands). A partir des paramètres de rugosités obtenus par les instruments d'Hayabusa, j'ai pu simuler des DTM des Lowlands, des Highlands et d'une zone composée d'un mélange entre des surfaces de Highlands et de Lowlands. J'ai ensuite fait un état de l'art des modèles de diffusion de surface, afin de simuler le signal réfléchi par les DTM crées. Plusieurs modèles de diffusion existent, chacun d'entre eux étant adapté à un domaine spécifique de rugosité. Parmi eux, l'approximation de Kirchhoff (KA) a été sélectionnée et appliquée à l'étude de l'astéroïde principal de l'astéroïde binaire Didymos. KA s'est révélée efficace pour modéliser le signal réfléchi par la surface d'un astéroïde : les zones rugueuses sont correctement localisées, et distinguées des zones plus planes. En utilisant des orbites multipass, la puissance de l'ambiguïté nord/sud, attendue sur des corps sphériques, a été réduite.
Cependant, afin de modéliser le signal diffusé par la sous-surface de l'astéroïde, des modèles de diffusion volumiques ont également été étudiés. L'approximation de Born (BA) a été choisie et appliquée pour modéliser le champ réfléchi par une inclusion enfouie dans la sous-surface d'un l'astéroïde. L'approximation de Born a réussi à situer correctement l'inclusion et est consistante avec les résultats d'une cible ponctuelle. Cependant, la résolution atteinte dans la direction verticale est mauvaise, ce qui est attendu d'une géométrie single pass. Ensuite, afin d'améliorer la résolution de HFR dans la direction d'élévation, un algorithme de tomographie a été appliqué depuis les résultats de l'approximation de Born. Parmi différents algorithmes, la méthode compressive sensing (CS) a été choisie, en se basant sur ses capacités de haute résolution, son temps de calcul faible et son adaptabilité à compenser le retard induit par la propagation de l'onde dans un milieu quand la permittivity $\epsilon \neq 1.0$. CS a permis d'obtenir une résolution en élévation inférieure au mètre, en la divisant par 4 et permet d'améliorer la localisation de la cible en prenant en compte la permittivité du milieu.
Enfin, les performances de diffusion en UWB ont été étudiées : plusieurs hypothèses SAR sont remises en questions à cause des caractéristiques UWB du radar, et les conséquences sur les performances du radar, notamment la résolution, sont analysées. Même si les hypothèses classiques de la synthèse SAR ne sont plus respectées, les conséquences de la résolution sont assez limitées.

Acknowledgments

First of all, I would like to express my gratitude to the members of the jury, the referees Sampsa Pursiainen and Amélie Litman, the president Stéphane Garambois, as well as Dirk Plettemeier and Daniel Hestroffer for accepting to spend time and energy evaluating my work and correcting my mistakes. I would like to thank as well Christopher Buck for his advice during these three years and for welcoming us at ESA. Special thanks go to for Wlodek Kofman as well for his guidance. I wish we could have celebrated together.

Naturally, I would like to thank my advisor Alain Hérique. I think I have not learnt as much in three years since my childhood, even if your drawings may be a little messy sometimes. Thank you for encouraging me to have some breaks and for your support when I was unwell. Thank you Yves for your constant help during these three years and for the cookies you always bring back when you go on holidays.

I am also grateful for the work environment I had at IPAG, thank you to the radar and planeto teams, to the kindness of the GAD and the administrative team who always took time to correct my paper works and to check if I was feeling fine. Thanks go to the Ph.D. students, post-docs, and interns who went with me at IPAG, made my days brighter and offered me the worst gifts you could ever think for a Ph.D. defense. I wish I would have taken the time to be closer to all of you.

I have a special thought for the Covid-19, which made the end of this Ph.D. even more dynamic than it was supposed to be.

Thank you to my friends from Cherbourg and Toulouse, with whom nothing changed despite the distance. The few times I saw you during these years were a breath of fresh air, even though I will never admit it in front of you.

A special mention to my parents, who gave me the taste of science and always encouraged me with everything. To my sisters, who never recovered from the idea that I would study signal processing. To my grandparents, who were so happy with the idea that I was starting a Ph.D.

And, obviously, thank you Florent.

Acronyms

SAR : Synthetic Aperture Radar

UWB : Ultra-Wide Band

SPRATS : Simulation and Processing RAdar ToolS

SEPO : Surface Echo PO

RMS : Root Mean Square

DTM : Digital Terrain Model

SPM : Small Perturbation Method

KA : Kirchhoff Approximation

SSA : Small-Slope Approximation

WCA : Weighted Curvature Approximation

BA : Born Approximation

CS : Compressive Sensing

Contents

List of Figures

List of Tables

Part I

Introduction

Contents

Chapter 1

Asteroids in the solar system

1.1 Formation and evolution of asteroids in the solar system

1.1.1 Formation of asteroids in the early solar system

The solar system formed about 4.6 billion years ago from a giant molecular cloud, a dense and cold agglomeration of dust and gas, called the pre-solar nebula. Because of its own gravity, the pre-solar nebula ended up collapsing : most of the cloud's mass formed the Sun at its center, while the rest flattened into a protoplanetary disk from which the solar system bodies formed (Moltenbrey, 2016). The different zones of the protoplanetary disk then differentiated in distinct ways depending on their temperatures : for regions farther from the sun, beyond a boundary called the frost-line (illustrated in figure 1.1), the temperature was low enough for molecules to remain in a icy form. However, the region closest to the Sun, ranging up to about 4 AU, was too warm for these molecules to remain solid and they evaporated. Heavier molecules, which have a higher melting point such as metals or rocky silicates remained, and made this area dominated by rocky bodies.

It is thought that the particles of the protoplanetary disk formed the solar system planets with an accretion process. First, they agglomerated by collision to form millimeter-sized objects. Then, through further contacts, the grains gathered to form several hundred meters large objects, which in turn collided to form larger bodies, called planetesimals, of about 10 kilometers in size. Additional collisions and reaccretion of these bodies led to the formation of the telluric planets.

1.1.2 Perturbation of asteroids due to the planets' migration

With the accretion, the protoplanetary disk ended up dissipating. The solar system then consisted of the Sun, the planets, and a large amount of smaller bodies. These asteroids mostly lied on the outer

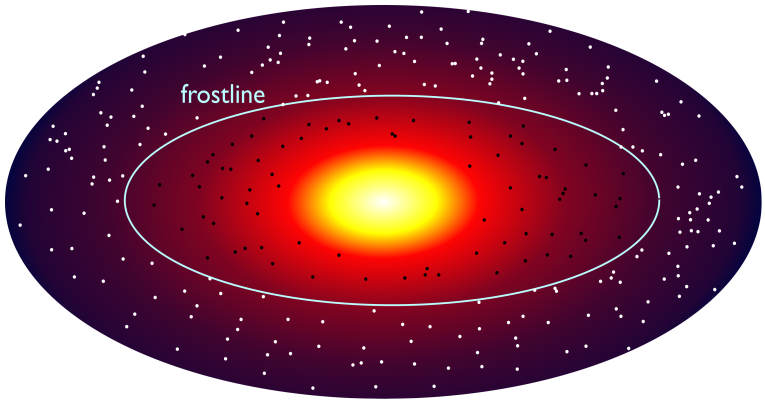

Figure 1.1: Different zones of differentiation in the solar system. Rocky bodies are pictured in black and icy bodies in white. Adapted from 2005 Pearson Education Inc, published as Addison Wesley.

edge of the inner solar system, between 2 and 4 AU, at a gap where no planet had formed because of Jupiter's influence. Indeed, the giant planet's gravity perturbed the orbits of some of the asteroids in its neighborhood and increased their velocities. Some of the asteroids were thus ejected into the inner or outer solar system and even out of the solar system. As a result of their increased velocities, the remaining asteroids produced heavier collisions and were shattered in the process, preventing the formation of any large bodies.
The asteroid belt was further perturbed because of the planetary migration, described by the Grand Tack model (Walsh et al., 2012). A large disk of icy bodies is supposed to have existed in the proto-Kuiper belt, an area ranging from about 15-20 AU. The icy bodies in the inner part of the proto-Kuiper belt occasionally suffered from the gravitational influence of the outermost gas giant at the time, Neptune or Uranus, and were scattered in the inner solar system. This, in turn, slightly pushed the giant planet in the outer part of the solar system. The cumulative effect of all the interactions ended up shifting the planets orbit significantly. Meanwhile, a similar process occurred with Jupiter, where the giant planet's orbit was moved closer to the sun because of its confrontation with the small asteroids in the inner solar system.
After about 500 to 600 million years of slow but constant migration, where Jupiter moved closer to the Sun and the other gas giants farther from it, Jupiter and Saturn ended up orbiting with a 1:2 mean motion resonance. This resonance influenced the asteroid belt by destabilizing even more the asteroids' orbits and increased their velocities, encouraging further collisions.
During these millions of years of planetary migration, small asteroids collided, were shattered into smaller fragments, which reaccreted to form new asteroids. This process may have formed asteroids with a rubble pile structure, bodies constituted by several smaller shattered pieces held together by gravity. Moreover, after the formation of a rocky asteroid, numerous smaller impacts began striking and weakening the asteroid surface layer. Each impact produced a small layer of regolith, a fine layer of dust and broken rocks, which is found on almost all small asteroids (Delbo et al., 2015). The numerous impacts ended up producing a more or less deep regolith on the asteroid surface.

The evolution of asteroids since their formation explains how such a large variety of asteroids can be found in various areas of the solar system: asteroids exist in different sizes, from more than tens of kilometers to a few meters. They also have various compositions and structures depending on their formation process, their collisional history, or the amount of space weathering they endured. As remains of the protoplanetary disk, small, kilometric sized asteroids, which are the focus of our study, are thought to be primitive, which means that they have endured few alterations since their formation. Thus, knowledge of their state and comprehension of primitive asteroid formation processes can lead to a better insight into the formation of the solar system.
A first understanding of the asteroids can be carried out by classifying them according to two information : their location in the solar system, and their spectral type.

1.2 Classification of asteroids

1.2.1 Families of asteroids

During the 19th century, several large rocky bodies such as Ceres, Palla, Juno or Vesta, were discovered in the region between Mars and Jupiter and were classified as minor planets. However, it became quickly obvious that so many planets could not exist at a similar distance from the Sun. Considering the fact that these bodies were much smaller than the existing planets, they were declassified as large asteroids and were the first asteroids observed.
Nowadays, we know about 800 000 asteroids in the solar system, but there might be millions of them since only the largest ones can be detected. Most of them have an irregular shape since the mass of the smaller ones is not large enough for them to be spherical.

Depending on their location, we can consider several types of asteroids:

- Near Earth Asteroids (NEA), whose orbits go close to the Earth's: their perihelia is closer

than 1.3 AU from the Sun. Some Near Earth Asteroids are potential dangerous asteroids for the Earth. Thus a large number of programs are dedicated to study and count them (*NASA NEO Program*, 2020), such as LINEAR: Lincoln Near Earth Asteroid Research (USA Air Force, NASA, MIT), the Catalina Sky Survey (NASA), Pan-STARRS: Panoramic Survey Telescope And Rapid Response System (Hawaii university, MIT, Maui High Performance Computing Center and Science Applications International Corporation), NEAT: Near Earth Asteroids Tracker (NASA, JPL) and LONEOS: Lowell Observatory Near-Earth-Object Search (NASA and Lowell Observatory).
Near Earth asteroids can be further divided into :

  - Atens, which orbit crosses the Earth's orbit. They have a semi-major axis of less than one Astronomical Unit (AU), the average distance between Earth and the Sun.
  - Apollos, which cross the Earth's orbit with a period longer than a year. Their orbits are wider than the Earth's.
  - Amors, whose orbits approach but do not cross Earth orbit.
  - Atira, whose orbits are entirely within the orbit of the Earth.

- Main Belt Asteroids, that are located between the orbits of Mars and Jupiter, as pictured in figure 1.2, with the exception of the dwarf planet Ceres. They include the majority of all known asteroids.

According to their formation mechanism and their location, asteroids have different chemical compositions. Few asteroids were closely observed, and even less were sampled and had their composition analyzed in a laboratory. However, with the advance of spectral analysis techniques, the chemical compositions of asteroids and the processes of their surface can be investigated and they can thus be divided into different classes: this process is called taxonomic classification.

1.2.2 Taxonomic classification

The taxonomy was introduced with the will to better understand and classify asteroids. At first, the taxonomy was based on the color of the asteroids, their albedo, and their spectral class by performing infra-red spectroscopy (Moltenbrey, 2016). In this way, asteroids were divided into three distinct

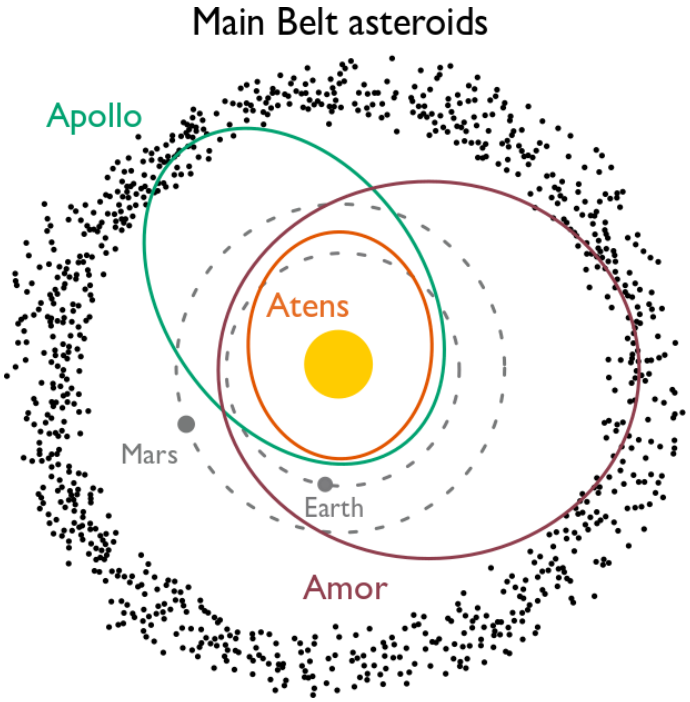

Figure 1.2: Main belt asteroids.

types. However, with the discovery and study of more asteroids, this classification was expanded several times, once in 1984, with the description of 14 types, and another in 2002, to finally comprise in 24 types. This update is called the SMASS classification (Small Main-Belt Asteroid Spectroscopic Survey) (Bus & Binzel, 2002) and contains 3 main types (C, S, and M) and many secondary types. Different surveys were carried out and resulted in different taxonomic systems, such as the Tholen (Tholen, 1989) or Bus-DeMeo (DeMeo et al., 2009) classification, but all classifications agree on the main types:

- C-type asteroids, whose spectrum has characteristics similar to carbonaceous meteorites found on Earth: they are dark objects, with a low albedo.
- Dark-albedo asteroids, which have a D-type spectrum, with a lower albedo than C-types, and a featureless reddish spectrum. They are thought to have formed in the Kuiper belt.
- Rocky, silicate-rich asteroids, which have a S-type spectrum. They have higher albedo, consistent with iron and magnesium silicates. They are common in the main belt, but almost not represented in the regions outside of it.
- M-type asteroids, mostly metallic.

The asteroids taxonomic classification is established most of the time from Earth-based observation. However, as the knowledge of an asteroid spectrum does not mean knowledge of the asteroid state, and as performances of Earth measurements are more limited than in-situ measurements, several space missions were launched to closely observe asteroids, and gather more precise data.

1.3 Rendez-vous missions to small asteroids

1.3.1 NEAR Shoemaker

NEAR (Near Earth Asteroid Rendezvous) Shoemaker (Prockter et al., 2002) is the first mission of the NASA Discovery program, a series of low-cost planetary space missions.

NEAR Shoemaker overall objectives were to rendezvous with the near-Earth asteroid 433 Eros (Figure 1.3), a 33 km large S-class asteroid. The spacecraft was designed to achieve orbit around Eros and conduct the first scientific investigation of an NEA. The mission had three science objectives :

1. Characterize the asteroid physical and geophysical properties.
2. Clarify the relationship between comets, asteroids, and meteorites.
3. Improve the understanding of the formation and early evolution of solar system planets.

NEAR Shoemaker arrived around the orbit of Eros on the 14th of February 2000, performed several flybys and landed on the asteroid on February 2001 with a touchdown, where it remained until March 2001.
NEAR Shoemaker boarded several instruments to achieve these science objectives, such as MSI, a multi-spectral imager which imaged the asteroid 'ssurface, a radio science experiment which determined several physical parameters of Eros, such as its mass and gravity field, and a magnetometer (MAG) to measure the asteroid magnetic field. Near-Infrared (NIS), X-ray (XRS) and gamma-ray (GRS) spectrometers mapped the surface composition of the asteroid and a laser range finder (NLR) was used for navigation purposes and estimation of the surface topography. NEAR Shoemaker was thus able to produce a precise study of Eros as a solid, monolithic, undifferentiated body, provided about 160.000 images of Eros's craters, boulders, and debris and gave a detailed map of the surface of the asteroid. Chemical data obtained from the spacecraft's spectrometers helped linking the origin of meteorites found on Earth to asteroids similar to Eros.

1.3.2 Hayabusa1

The Hayabusa spacecraft (JAXA, 2016) was developed by the Japanese Space Agency (JAXA) and was launched on May the 9th, 2003 to study the asteroid (25143) Itokawa, a 600 meters long and 300 meters large S-type NEA. Hayabusa was designed as a technology demonstrator with four main technologies:

- Ion engines used in interplanetary cruise.
- Autonomous guidance obtained with optical instruments.
- Sample collection under a low-gravity environment.
- Direct reentry from interplanetary trajectory for a sample return.

However, Hayabusa was designed to produce maximum science products. Therefore, it has two science objectives:

1. Clarify the chemical, mineralogical and physical properties of the returned samples.
2. Understand the samples' relationship with the spectral type of the asteroid, obtained with remote sensing techniques.

All instruments on Hayabusa are dedicated to serving these science objectives. Hayabusa's principle payload was the sampling mechanism, but the spacecraft also embarked an imaging camera AMICA (Asteroid Multiband Imaging Camera), a Near-Infrared spectrometer (NIRS), an X-ray spectrometer (XRS) and a LIDAR to study the topology and composition of the asteroid's surface. AMICA and the LIDAR were used for navigation purposes mainly but also estimated the surface topology. NIRS and XRS provided data on elemental abundances and mineralogy of the surface.
As Hayabusa was developed as an engineering test mission, it confirmed the capabilities of ion engine for space exploration missions and was the first mission to succeed in bringing samples from an asteroid's regolith back on Earth, despite the failure of the sampling mechanism. Hayabusa revealed Itokawa as a rubble pile, with rough and smooth terrains, as well as the presence of boulders, while the

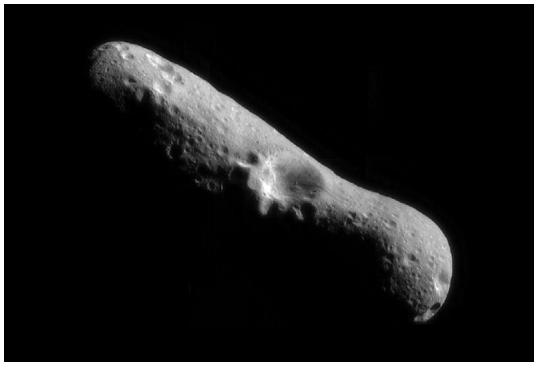

Figure 1.3: Picture of Eros obtained by NEAR Shoemaker (NASA). Image Credit: JPL

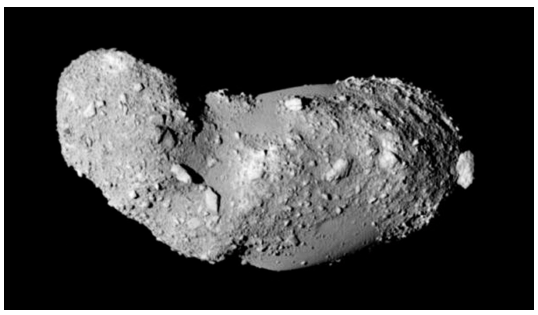

Figure 1.4: Picture of Itokawa obtained by Hayabusa (JAXA). Image Credit: JAXA

sampled particles revealed the link between S-type asteroids, which are the most common Near Earth Asteroid and ordinary chondrites, the most frequency recovered meteorites on Earth (Nakamura et al., 2011).

1.3.3 Hayabusa2

The Hayabusa2 spacecraft (Watanabe et al., 2017) was launched in 2014 as the successor of Hayabusa. It aims at observing the 900-meter large C-type Near-Earth Asteroid (162173) Ryugu, retrieving samples from the surface and bringing them back on Earth. Hayabusa2's science objectives were :

1. Characterizing the distribution of materials (such as hydrated silicated or organic matter) on the surface of Ryugu, in order to understand the mixing and transport of such materials in the early solar system.

2. Characterizing mineral/water/organic reactions on the parent bodies of asteroids. This is done by searching for a variety of organic materials and minerals representing aqueous alteration, both in the returned samples and with the remote sensing operations.

3. Characterizing thermal alteration and space weathering since the formation of the asteroid to understand the material evolution in the early solar system

4. Characterizing impact-related properties of Ryugu and reconstruct its collisional history to understand the dynamical processes that planetesimals endured during the early solar system.

Even though Hayabusa1 managed to bring back samples since the sampling mechanism failed, the surface sampling is Hayabusa2's most challenging operation. In order to select the sampling site, retrieve a scientifically interesting sample and understand its context, Hayabusa2 conducted measurements on the global, local and micro scale of the asteroid, by remote sensing from the orbiter and in situ measurements. Once the samples are brought on Earth, further measurements will be conducted on the returned samples. To follow these scientific objectives, Hayabusa 2 carries several instruments on an orbiter and a lander (Watanabe et al., 2017) :

- The orbiter boards an optical navigation camera (ONC), in order to create shape models of the asteroid, conduct multi-band surface mappings that can estimate the presence of hydrated silicate minerals, and for navigation purposes. The Near Infrared Spectrometer (NIRS3) boards the spacecraft with the objective to observe the surface's reflectivity, to map the surface distribution of hydrated silicates and to estimate space weathering altering the surface of the asteroid. The Thermal Infrared Imager (TIR) was built in order to image the thermal emission of the asteroid's

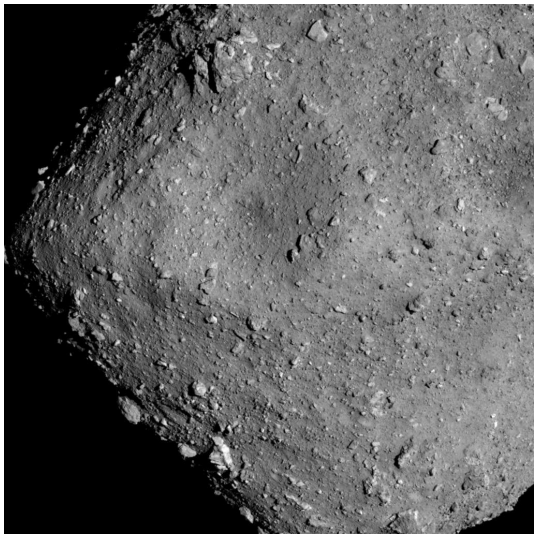

Figure 1.5: Picture of Ryugu obtained by Hayabusa2 (JAXA). Image Credit: JAXA

surface, estimate the surface temperature distribution, and derive the distribution of the thermal inertia. The LiDAR is used for navigation purpose but also to derive Ryugu's topography, shape, gravity, surface roughness, and albedo.

- The lander MASCOT has four instruments : a multiband camera (MasCam), a thermal radiometer (Mara), and magnetometer (MasMag) that measured the landing site spectrum directly on the surface, serving as a reference for both orbital observations and analysis of the return sample.

1.3.4 OSIRIS-REx

OSIRIS-REx (Lauretta et al., 2017) was launched in November 2018 to rendezvous the asteroid Bennu and map its physical, geological, and chemical properties. A landing site on the surface was then selected, where the spacecraft aims at collecting at least 60 grams of asteroid's regolith, which will be brought back on Earth. OSIRIS-REx has five science objectives :

1. Return pristine carbonaceous regolith from Bennu.
   OSIRIS-REx is a sample return mission. The returned samples will be analyzed to understand the role of asteroids in the origin of life on Earth, and their role as the building blocks of larger planetesimals.

2. Map Bennu global properties.
   The first operations of OSIRIS-Rex once arriving in the vicinity of the asteroid were to conduct global analysis of Bennu, which serves as context from additional local observations. The measurements will be used to understand the global properties, chemistry, and mineralogy of primitive carbonaceous asteroids, to characterize their geologic and dynamic history and to provide context for the returned samples.

3. Document the sampling site.
   To assess both the possibility of landing and the scientific interest of landing sites, local, higher resolution measurements on smaller surfaces were needed. These measurements allow understanding the sample's origin, its location in this asteroid, and its history.

4. Measure the YORP effects and constrain the asteroid's properties that contribute to this effect.
   Understanding and measuring the YORP effect, which alters the asteroid rotation rate (Bottke Jr et al., 2006), can improve the precision of the asteroids' orbit predictions, which can be used for potentially hazardous asteroids.

5. Improve asteroid astronomy.
   As many small body observations are carried out on Earth, the OSIRIS-REx mission is thus an opportunity to compare the Earth-based observation with in situ measurements. They can be used to assess the validity of the Earth-based measurements.

To achieve these science objectives, OSIRIS-REx boards a sampling mechanism, called SARA (Sampling Acquisition and Return Assembly), 3 cameras (OCAMS: OSIRIS-REx CAMera Suite) used for navigation purposes to set the shape model, measure the spin rate, image the sampling site, and record the sampling operation. A LiDAR, the OSIRIS-REx Laser Altimeter (OLA) is used for navigation purposes and to establish the asteroid topography. A Near-Infrared Spectrometer (OVIRS) is used to compute the asteroid's spectrum for global mapping operations, to identify volatile and organic-rich areas of the asteroid, and thus guide the selection of the sampling site. A Thermal emission spectrometer called OTES measures the thermal radiations emitted from the asteroid. REXIS (Regolith X-ray Imaging spectrometer) measures solar X-ray fluorescence from Bennu to map the distribution of elements across its surface, such as Oxigen, Iron, and Magnesium. The Radio Science Experiment measures the Doppler delay, ranging and Delta-DOR (Delta Differential One-way ranging) to provide estimations of the gravity field, the mass, and YORP effects of the asteroid.

As Hayabusa2, OSIRIS-REx is still an ongoing mission. Bennu was found out to be a small asteroid with the classic diamond shape, as Ryugu. The asteroid is also covered with boulders, much more

than what was expected and than Itokawa.

The scientific knowledge on asteroids is on constant evolution, thanks to regular missions sent to observe and analyze new targets. These missions helped to gain data on asteroids that would not have been obtained without in-situ measurements. However, as each mission is a trade-off between cost and science return, some data are still lacking to get a complete overview of asteroids.

1.4 Missing knowledge about asteroids

1.4.1 Structure

Despite this consequent number of missions to study asteroids, so far, the inner structure of an asteroid has never been directly measured. Yet, knowledge of asteroids' structure is crucial for our understanding of the formation of the solar system (Herique et al., 2018)

As some asteroids have been collided and reacretting for millions of years, two main types of structures could be existing, as presented in figure 1.7 :

- Monolithic asteroids, which are composed of one fragment that constitutes the core of the asteroid, and smaller particles that would agglomerate on the surface and form what we call the asteroid's regolith.
- Rubble pile, that would be an agglomerate of smaller fragments held together by gravity, covered by regolith.

However, no optical remote sensing instrument can differentiate between a monolithic and a rubble pile structure, or estimate the bodies' porosity. All information on the asteroid's subsurface come from inferences from measurements on the bulk density or images of the surface, and thus several scientific returns are based on hypotheses. This is why asteroids have properties than cannot yet be

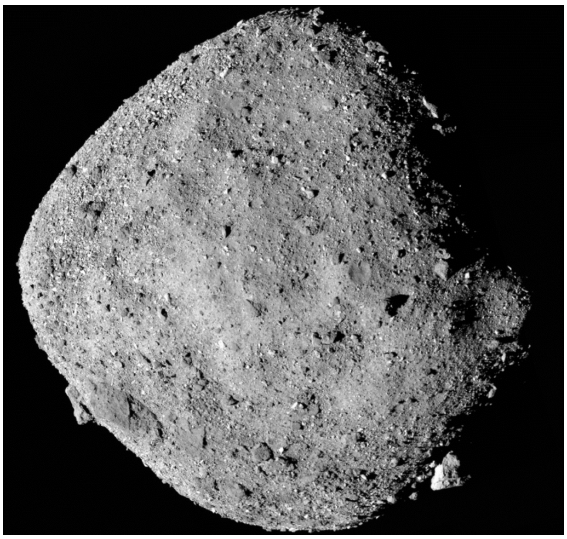

Figure 1.6: Picture of Bennu obtained by OSIRIS-REx (NASA). Image Credit: JPL

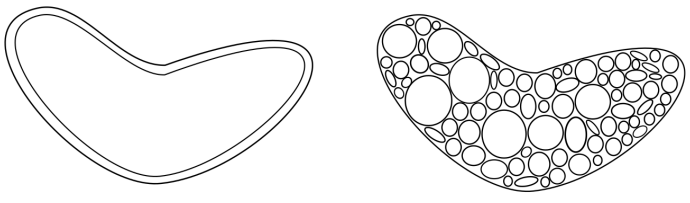

Figure 1.7: Two different possible asteroids structures: monolithic structure (left) and rubble pile (right).

fully understood: namely, the asteroid 101955 Bennu, the target of the OSIRIS-Rex mission, has a bulk density of about than 1.5g cm $^{-3}$ (Chesley et al., 2014), which could be explained by a low density of the internal structure of the asteroid. The asteroid Itokawa, the target of the mission Hayabusa1 has a bulk density of about 1.9g cm $^{-3}$ (Abe et al., 2006), which is lower than the density measured from its meteorite analogs, between 3 and 4 g.cm $^{-3}$. These measurements seem to indicate a rubble pile structure, which would be common for medium-sizes asteroids (Whiteley et al., 2002). Moreover, the asteroid Bennu was interpreted as a shattered monolithic block (Cheng et al., 2009), or a sand pile (Asphaug, 2009). Only a geophysical sounding investigation could discriminate between possible asteroid structures.

Understanding the asteroids' inner structure could be used to achieve several objectives:

- Refine solar system formation models
  Understanding the internal structure of asteroids is crucial for our understanding and modeling of the evolution of an asteroid, from its formation in the primitive solar nebula to its present state. Indeed, the inner structure of an asteroid illustrates its history relative to impacts by other small bodies. Small bodies' collisions were crucial events during the evolution of the solar system, as explained by the Nice model, and our models of the collisional evolution of small body populations are dependent on the assumptions made on their internal structure. Thus, uncertainties in these properties can result in major differences in our understanding of planetary accretion and collisional history.

- Understand binary asteroids formation processes
  Binary asteroid systems are an unexpected structure that are quite largely found in near-Earth asteroid populations (15%, Margot et al. 2002).Two different scenarios were developed to explain the formation of binary asteroids.
  The most realistic formation scenario for small binary systems in the near-Earth asteroid population and in the inner main belt is the acceleration of the rotation speed of a rubble pile due to the YORP effect. This effect explains how thermal torques are generated by the heating of the object through the absorption of sunlight, and the reradiation of this energy as heat (Rubincam, 2000). The generated torques increase the rotation velocity beyond the spin frequency at which the centrifugal force causes a loss of particles, which can then reaccrete into small satellite (Walsh et al., 2008). This scenario also explains the top shape observed on several small bodies such as Bennu (Barnouin et al., 2019), 1999KW4 (Soumbatov-Gur, 2018), or Ryugu (Michel et al., 2018).
  The second scenario is that the YORP effect may also cause fission of the primary body (Jacobson & Scheeres, 2011), and create a small satellite. In this case, the mass loss is due to a single, catastrophic event and the reaccretion of the lost mass is supposed to have given the top shape. Both of these scenarios require an aggregate structure to start with, but the structure of the resulting primary and its moon are quite different. Direct information on the internal structure is needed in order to better constrain the mechanism that forms binaries and discriminate between their formation models for binaries.

1.4.2 Regolith

During their observation, asteroids were found to be covered by a layer of soil, dust, broken rocks, and other fine materials which are called regolith, which is omnipresent on asteroid surfaces, but differ from one small body to another. The regolith can consists of fine grains such as on Eros (Cheng et al., 2001), or gravels and pebbles such as on Itokawa (Barnouin-Jha et al., 2008). As only surface measurements were carried out on asteroids, the depth and structure of the regolith lack direct measurements and our knowledge relies only on inferences from surface or global measurements. Knowledge of the structure of the regolith could be beneficial for several reasons (Herique et al., 2018):

- Understand the regolith formation and evolution
  The regolith properties depend on the asteroid formation process (Murdoch et al., 2015) : hav-

ing direct measurements of the regolith properties, such as size distribution of particles, or its depth and stratigraphy, will allow to better constraint the regolith formation processes, and discriminate between thermal fragmentation (Delbo et al., 2014) and accumulation from ejecta originating from impact cratering (Richardson, 2011). This data can be used to improve models of the solar system formation, and in the case of a sample return mission, better understand the vertical context of a returned sample.

- Predict the interaction between asteroids' surface and spacecrafts.
  Asteroid surface processes such as mass migration, size segregation or landslides depend on the material properties. By combining observations of the surface, observations of the subsurface and numerical modeling, these properties can be constrained, and used to predict with more accuracy the surface processes on small bodies, and thus the interaction of future spacecraft with their surfaces. In the case of space missions aimed at deflecting an asteroid, the regolith structure and depth can have a major influence on the efficiency of the various deflection techniques. All techniques relying on anchoring or similar surface interaction need some knowledge of the regolith properties.

- Overcome the possible non-representability of the surface.
  The grains of regolith have been exposed to solar radiation for millions of years and have been altered by space weathering, which flattens their spectral signature (Lantz et al., 2013). This makes difficult to compare asteroid spectra with meteorite spectra since the surface spectrum is not comparable to the subsurface composition. Moreover, because of grain segregation and the fact that a fraction of exogenous materials could also be present on the surface, remote sensing observations of the surface only could introduce a bias in the observation (Herique et al., 2018). Thus, in order to grasp a complete view of the asteroid, subsurface probing are necessary.

1.5 Summary

Despite their numerous numbers, asteroids have been relatively ignored since the beginning of the 1990's, notably because of the lack of technology to perform a complete study. However, since their role in the solar system formation, and their potential hazardous nature has been assessed, attention has turned to the study of these bodies and a number of space missions have been dedicated to the in-situ study of asteroids. However, the internal structure of asteroids has never been measured, and is only known by inferences from surface and global measurements.
Yet, the knowledge of the asteroid's structure as well as its regolith's state, could help understanding asteroids' formation processes, which have a large influence on possible deflection techniques that could be used for planetary defense, or sampling site selection for sample return missions. It could also set a reference for the study of meteorites, and on a larger scale, help refining the solar system models.
The most mature instrument that could peer into the subsurface of asteroids on board a spacecraft is the radar, which uses electromagnetic waves to probe an asteroid's surface and its interior. Radars have been developed for a little less than a century for remote sensing purposes and for few decades to probe into the subsurface of planetary bodies.

Chapter 2

Radar

2.1 History

Radio systems began to be developed following the results of Maxwell about the laws of electromagnetics and Hertz's work on electromagnetic waves at the end of the 19th century. In the early 20th century, a ship detection device was built by the German inventor Christan Hülsmeyer, which is thought to be the first radar developed (van Loon, 2005) and in 1922, A.H Taylor, L.C Young and L.A Hyland applied for a patent in radio science (Susskind, 1985).

The development of these systems, which use short pulses of radio energy to detect targets, was accelerated during the second world war: by 1945, Britain, Germany, the United States, the USSR, and Japan had a wide diversity of radars. After the war, development on the instrument carried on, and evolution of computers into more and more efficient engines expanded their use to the wide range of application it has nowadays.

2.2 Radar principles

The principle of radar measurement can be understood by looking at nature: for example, bats use echolocation to locate themselves by sending acoustic waves and process their reflection to move and to hunt. Radar (RAdio Detection And Ranging) techniques proceed in a similar way by using radio frequency signals to detect a target position and velocity (Curlander & McDonough, 1991):

- The distance to the target is estimated using the speed of light in the medium of propagation and the round trip time from the radar to the target.
- The target's velocity is estimated with the frequency shift between the received signal and the emitted signal, due to the Doppler effect.

A radar system is formed by a transmitter that emits a radio-frequency (RF) signal, and one or more receivers to register the reflection from the target. From this, we can distinguish two different kinds of radars:

- Monostatic radars, which use the same antenna for the transmission and the reception.
- Bistatic radars, which use different antennas for the transmission and the reception.

The radar is called a pulsed radar when it emits electromagnetic pulses at a frequency called the PRF (pulse repetition frequency), and thus at a time interval called the PRI, that is the inverse of the PRF. After transmitting, the radar listens to the scattered echoes during its echo window time, and stores the received signals on board, as shown in figure 2.1. If a target is located at a distance x_1 on a one-dimensional surface, the radar will receive the echo at a time $t_1 = \frac{2x_1}{c}$ as depicted in figure 2.2. The transmitted signal shape is called the waveform and depends mainly on the signal's frequencies.

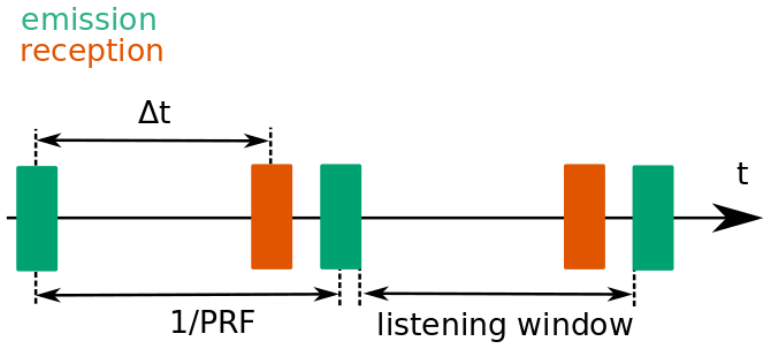

Figure 2.1: Illustration of the radar time windows.

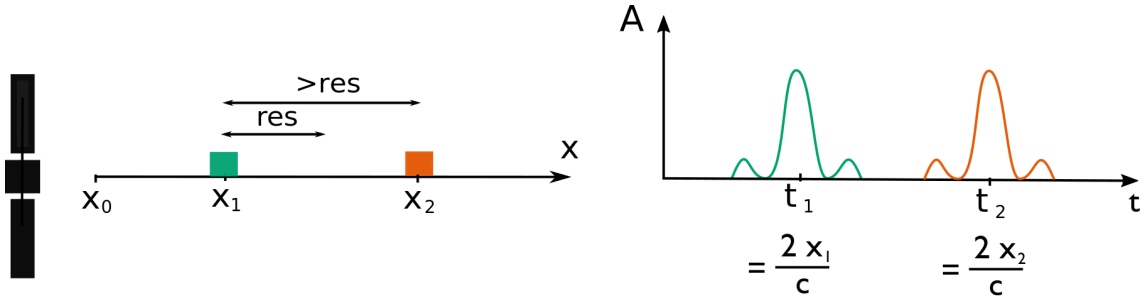

Figure 2.2: Illustration of the radar operation. Left represents a one dimensional surface and right represents the corresponding registered signal.

The received signals give information about the target's radar cross section (RCS) (Curlander & McDonough, 1991), which is the target equivalent area that would intercept the transmitted signal in the far field, and scatters it isotropically. The RCS is the measurement of the surface reflectivity, the amount of energy scattered by a surface: a larger RCS indicates that an object is more easily detected: for example, a stealth aircraft will have a low RCS thanks to its surface, specifically designed not to reflect the signal to the source. However, passenger airliners will have a high RCS, bare metal, or rounded surfaces made to backscatter the signal so that they can be easily detected by the radar.

Instead of the RCS, the normalized radar cross-section or backscatter coefficient, σ_0, may be used, which is the average radar cross-section of a set of objects per unit area:

$$\sigma_0 = \frac{RCS}{A_i} \tag{2.1}$$

with A_i the area of the object.

Even if radars were developed for military purposes, they are now used in many backgrounds, like in meteorology (Fabry, 2015), civil aviation with aircraft surveillance (Shrader, 1973), road safety with speed control, in medicine (Panzer et al., 2013), or in imaging landscapes with synthetic aperture radars (SAR) (Moreira et al., 2013).

2.3 Synthetic Aperture Radars

One of the interesting use of radar systems is their imagery capability. Synthetic Aperture Radars (SARs) are forward-moving radars, used for the reconstruction of two or three-dimensional objects or landscapes. This imaging system is independent of daylight, cloud coverage and weather conditions (Moreira et al., 2013), which explains why it is so widely used.

2.3.1 History

Until the 1950s, imaging radars were called SLAR (Side-Looking Airborne Radar) and were located on a forward-moving platform. With λ the wavelength of the radar, d_a the antenna width and r_0 the range distance, the azimuth resolution of a SLAR system could be expressed as :

$$\delta_a = \frac{\lambda}{d_a} \cdot r_0 \tag{2.2}$$

In this way, the azimuth resolution worsens as the range distance increased. This led to low or unusable resolution, notably for spaceborne systems: a SLAR with parameters similar to the TerraSAR-X radar (Werninghaus, 2004), operating at a range distance of 500 km, with an antenna size of 3 meters will have an azimuth resolution of 50 km, according to equation 2.2. This low azimuth resolution has been the main drawback of the SLAR systems.

In 1951, Carl Wiley overcame this limitation by conceiving a coherent side-looking radar (Wiley, 1985), which led to an improvement of the azimuth resolution. Indeed, for forward-moving radars, we can consider that each target stays illuminated by the radar for a length called the synthetic aperture. Thus, using the new information about the Doppler delay of each target during the whole synthetic aperture, the radar resolution in the azimuth resolution can be improved to :

$$\delta_a = \frac{d_a}{2} \tag{2.3}$$

Thus, a short-length antenna yields a high azimuth resolution. This is quite clear when considering that a radar with a shorter antenna has a larger beam-width, sees any point on the ground for a longer time, and can acquire information about this point for a longer time during the trajectory. Thus, with a SAR, the resolution becomes independent of the range distance. Thus, the SAR azimuth resolution of the TerraSAR-X radar becomes 1.5m, more than 30.000 times more accurate than the resolution using a SLAR system.

The developments of SAR systems continued in the 1950s and 1960s, mainly led by military research for reconnaissance purposes and target detection. The 1970s and 1980s saw the emergence of several civilian systems, developed for recovering geophysical and biophysical parameters from the Earth's surface, such as SeaSat (NASA), launched in 1978 (W. H. Johnson J. W.and Lee et al., 1979) as the first civilian SAR satellite designed for remote sensing of the Earth"'s oceans. We can also quote ERS-1/2 (ESA, 2003), which followed in 1991 and 1995, designed to provide environmental monitoring on the Earth, or JERS (JAXA, 2003), which was launched in 1992 to gather data on global landmasses like agricultural lands or forest. Radarsat-1 (ASC, 2014) (ASC) was launched in 1995 to monitor Earth resources and climate change, and Envisat (ESA) (ESA, 2001) was launched in 2002 to monitor environmental changes.

In the last 20 years, considerable progress has been achieved with the development of additional techniques used to improve the quality of the retrieved SAR image. We can quote polarimetry, the study of the state of polarization of the backscattered wave which can be used to gain information of the imaged surface (Migliaccio et al., 2007), interferometry, implemented to derive the surface topography (Gens & Van Gerenden, 1996), or differential interferometry which has been used to measure the Earth surface displacement (Moreira et al., 2013). Polarimetry SAR Interferometry (PolInSAR) (Tebaldini, 2009) and SAR tomography (Zhu et al., 2010) were then used to solve the problem associated with layover effect in urban areas. The development of these techniques improved the information capabilities of SAR images.

2.3.2 Description of the SAR principle

SARs are radars dedicated to the imaging of natural or anthropic surfaces: they are based on a pulsed radar on a platform with a forward movement: the flight direction is denoted as azimuth and the

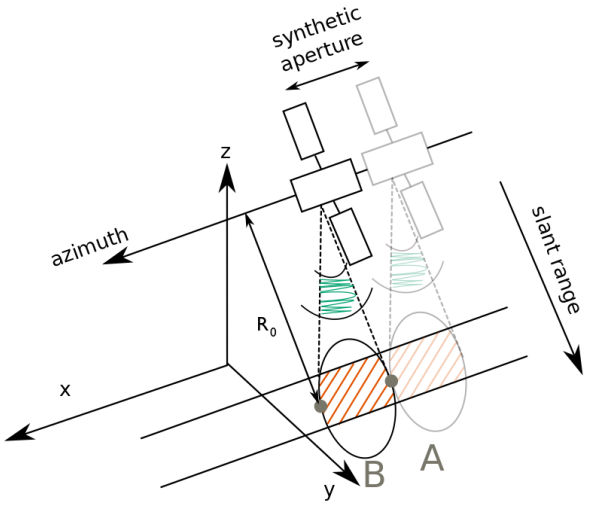

Figure 2.3: SAR geometry

line-of-sight as slant range direction as depicted in figure 2.3 (Moreira et al., 2013). Electromagnetic waves are transmitted and received after being backscattered from the ground. The amplitude and the phase of the received signal from the imaged surface depends on the physical (geometry, roughness) and electrical (permittivity) properties of the surface. For a SAR, these emissions and receptions happen at different positions in the platform movement: then a coherent combination of the received signal allows the construction of a virtual, or synthetic, aperture which is much longer than the actual antenna length.

The SAR basic principles can be understood using a simplified model. Surfaces are modeled as a repartition of isotropic and non-dispersive point scatterers, which means that they have the same response depending on the illuminating frequency and angle of incidence. Each target, or what we also call "point scatterer", will scatter the energy in different directions. Thus, the surface can be modeled as a sum of diracs associated with each point's reflectivity γ_i:

$$h(r) = \sum_{i=1}^{N} \gamma_i \cdot \delta(r - r_i) \tag{2.4}$$

With r_i indicating the position of a scatterer.
The SAR emitted signal x(t) will then be scattered by each point composing the surface. Thus, the scattered signal y(t) can be written as :

$$y(t) = \sum_{i=1}^{N} \gamma_i \cdot x(t - 2 \cdot t_i) \tag{2.5}$$

Where $t_i = r_i/c$, and the factor 2 comes from the round trip of the wave.

To recover h(r), one can use the Fourier transform and equation 2.5 can be written:

$$Y(f) = X(f) \times H(f) \tag{2.6}$$

With Y(f) the Fourier transform of the received signal, X(f) the Fourier transform of x(t) and H(f) the Fourier transform of h(r). From equation 2.6, H(f) can easily be obtained:

$$\begin{aligned} H(f) &= \frac{Y(f)}{X(f)} \\ &= \frac{\sum_{i=1}^{n} \gamma_i X(f) \exp(-2\pi j f \frac{2r_i}{c})}{X(f)} \\ &= \sum_{i=1}^{n} \gamma_i \exp(-2\pi j f \frac{2r_i}{c}) \end{aligned} \tag{2.7}$$

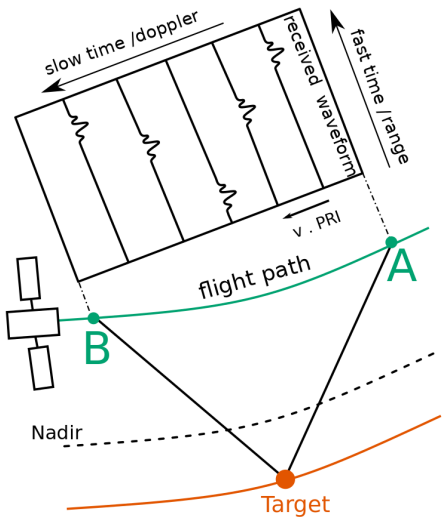

Figure 2.4: Recording of the SAR signal. Adapted from Cumming and Wong (2005)

And then the 2-dimensional SAR image can be built with an inverse Fourier transform.

However, in practice, the emitted spectrum has a limited band of frequencies centered around a central frequency and not an infinite range of frequencies: as the Fourier transform of the square window of frequencies is a cardinal sine, the image can be written:

$$h(r) = \sum_{i=1}^{N} \gamma_i \operatorname{sinc}[\pi \Delta k (r - r_i)] \tag{2.8}$$

Where $k = \frac{2f}{c}$ is the wavenumber, $\operatorname{sinc}[\pi \Delta k (r - r_i)]$ is called the point target response, and is spread on a certain distance compared to the exact dirac model of the image.

The resulting image is thus the 2D reflectivity map of the imaged area and targets with a high backscattered signal power will be identified as bright spots on the radar image.
As a SAR follows a forward movement, the geometry is more complex than with motionless radars, and needs to be defined.

2.3.3 SAR geometry

Figure 2.4 depicts the two dimensions of a SAR system. The first dimension is called cross-range since it is the direction of the slant range, projected on the direction normal to the trajectory. For simplicity, we will call the cross-range direction, the range direction. A range line contains the signal echoes of one pulse, registered and sampled in memory. The radar acquires a range line whenever it travels a distance $v \times PRI$. The repetition of the range lines forms a second dimension, which is called the azimuth or Doppler direction.
Time and distance are closely related in radar systems, only to a factor c_0, the speed of light. The time scale in the range direction is called fast time, and slow time in the azimuth direction. This denotation makes sense when considering the time interval length: the time interval between one signal emission and one signal reception is much smaller than the time interval between the beginning and the end of the SAR synthesis.
Using the signal scattered from the surface under study, the SAR synthesis will be performed to obtain the 2-dimensional range/azimuth SAR image.

2.3.4 SAR synthesis

Understanding the raw SAR data, the received spectrum, is not immediate, as raw SAR data do not give any useful information on the scene. It requires some signal processing before being analyzed,

which are called the SAR processing steps. The traditional SAR processing algorithm can be seen as two separate matched filters operated along the range and azimuth dimensions.

- Range Compression :
  As a first step, the transmitted signals are compressed to a short pulse. Each range line is convolved with the transmitted signal, as a matching filter operation, and the operation is done in the frequency domain. The result gives a range-compressed image, which reveals information about the relative distance between the radar and any point on the ground.

- Azimuth Compression :
  The same operation is done in the azimuth direction: the signal is convolved with a reference function, which is the response expected from a point target on the ground.

After the 2D SAR processing, a target is located on a surface with a delay in the range direction, and one delay in the azimuth direction, which indicate the target position in both dimensions:

- All targets having the same range delay from the radar's position form a sphere, whose center is the radar position, and whose radius equal to the range distance around the radar position, as depicted in figure 2.5. These spheres are called the iso-range spheres.

- If the doppler frequency is $\delta f = \pm\frac{2v}{\lambda}$, then points having the same Doppler delay will be cones, whose center is the radar position, and with axes along the line of flight of the radar, as depicted in figure 2.5. These cones are called the iso-doppler cones.

The target is then located at the intersection of each iso-range spheres and iso-doppler cones of the trajectory. When studying a surface with only one trajectory, this intersection is a circle for each position of the trajectory. Thus all targets located on this circle will be having the same range and doppler delays, will be imaged with the same power, and the true position of the target is said to be ambiguous.

After the SAR processing, the resulting SAR image can be displayed with intensity values which are an indication of the reflectivity of the corresponding point on the ground. However, SAR images are geometrically distorted representations. The reason for this is that the radar only measures the projection of a three-dimensional scene on the radar coordinates range and azimuth. This causes various effects such as shadowing for areas hidden from the radar illumination, as well as layover manifested by a relief displacement when the surface is too sloped, or foreshortening when the slope of the terrain tends to be normal to the slant-range direction, and the top and the base of the relief are imaged simultaneously, as depicted on figure 2.6.

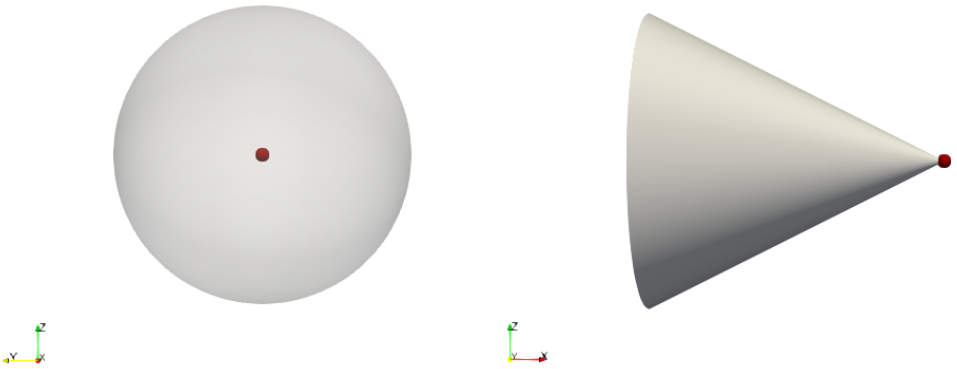

Figure 2.5: Spherical iso-range delay (left) and conic iso-doppler delay (right), obtained from the radar position (in red).

2.3.5 Sampling requirements

An issue in SAR imaging is the choice of the sampling of the signal. In range, the sampling rate of the signal must be larger than the transmitted signal bandwidth, according to Shannon's sampling theorem (Shannon, 1949). The sampling requirement is the same in azimuth. The sampling rate in azimuth is equal to the PRF, so Shannon's theorem means that the sampling rate must be larger than the signal Doppler bandwidth. The Doppler bandwidth is the difference between the Doppler frequencies at each border of the synthetic aperture length and can be written (Moreira et al., 2013):

$$B_D = \frac{2v \cdot \Theta_a}{\lambda} \tag{2.9}$$

With Θ_a the antenna beam width, which is linked to the size of the antenna d_a by:

$$\Theta_a = \frac{\lambda}{d_a} \tag{2.10}$$

Thus, the Nyquist theorem can be written as :

$$PRF \geq B_D = \frac{2 \cdot v}{d_a} \tag{2.11}$$

which can be rearranged in terms of the spatial sample spacing as :

$$v \cdot PRI \leq \frac{d_a}{2} \tag{2.12}$$

which PRI being the Pulse Repetition Interval, the inverse of the PRF. This means that at least one transmission of one pulse is required each time the platform moves by a distance equals to half the antenna's synthetic aperture.

2.3.6 Range migration

The Range Cell Migration (RCM) is a property of the SAR images. RCM comes from the fact that the distance between the radar and any fixed point of the surface is changing during the observation. The RCM can be computed as :

$$RCM(t) = \Delta R(t) = R - R_0 = \sqrt{R_0^2 + (vt)^2} - R_0 \approx \frac{(vt)^2}{2R_0} \tag{2.13}$$

With R_0 the minimum slant range distance to the target, as illustrated in 2.3, v the platform velocity and t the time. Thus, the RCM is expressed as a parabola, as presented in figure 2.7. When

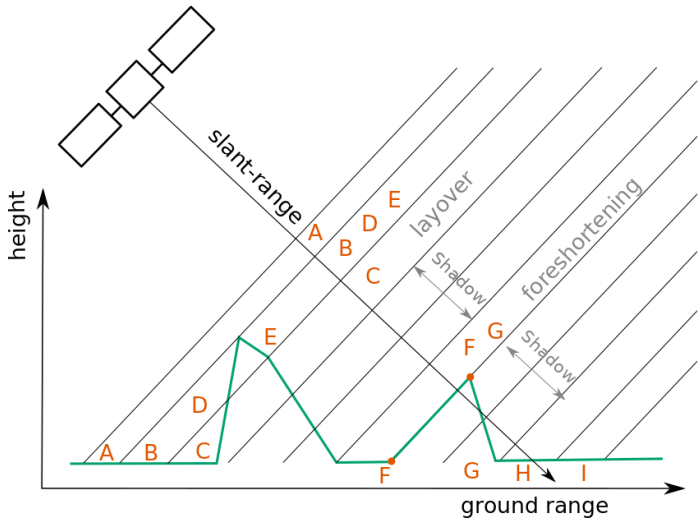

Figure 2.6: Examples of common SAR images distortions. Adapted from Schmitt et al. (2011)

the RCM spreads over several resolution cells, and is not corrected, this spread will cause an azimuth defocusing. Since the RCM depends on R_0, it can be corrected with a non-stationnary two dimensional reference function, which makes it a challenging aspect of SAR focusing.

The last years have marked an important transition in the application of SAR. Nowadays the public awareness of the usefulness of radar remote sensing beyond science is much higher, notably because of the Earth observation capabilities of these instruments and the communication carried out by several space agencies. As an example, radar satellites have been able to perform disaster monitoring and damage assessment due to their all-weather day-and-night imaging capability. SARs are thus widely used instruments, capable of achieving a high resolution in the azimuth direction using the SAR processing, and a high range resolution using the ultra-wideband technique.

2.4 UWB Radar

2.4.1 History

The development of Ultra-Wide-Band (UWB) radars, was a crucial evolution of radar instrumentation, and lead to high-resolution systems (Barrett & Vienna, 2001). It started in the 1960s with the work of Harmuth, who published a set of articles from 1969 to 1984 which defined the basic design for UWB transmitters and receivers. From 1972 to 1987, a series of patents from Ross and Robbins laid the base of the use of UWB signals in several domains such as telecommunications and radar, and in 1977 antenna concepts for UWB radar were designed. Thus, in the 1980s, the basic designs for UWB radar were available. From then, the advances came from improvements on existing subsystems but not on the UWB concept itself.

2.4.2 Description

Traditionally, radars use a signal with narrowband frequencies, which modulated a sinusoidal carrier signal (Taylor, 2000): indeed a sinus wave is the oscillation of an LC circuit, which is the most elementary oscillatory system and is thus easy to generate. However, as the amount of information transmitted in a unit of time is proportional to the signal's band, a narrowband waveform limits the information capability of the radar and leads to a poor resolution. Thus, to increase the system's information capacity, either the signal bandwidth or the information transmitting time must be enlarged. However, in order to improve the information transmitting time, the power needs to be increased as

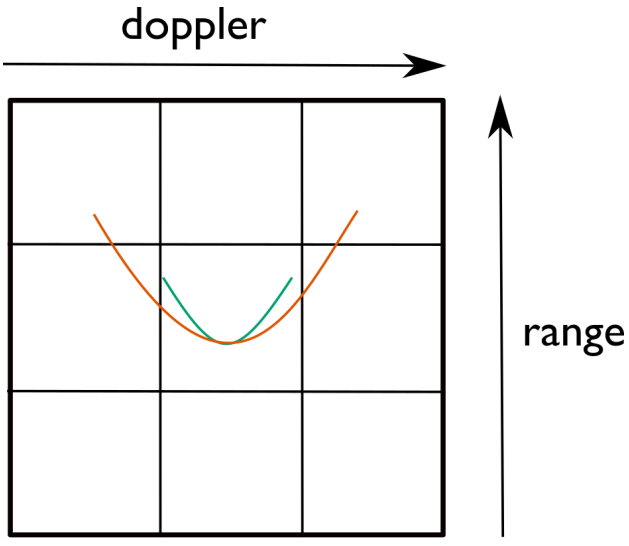

Figure 2.7: Illustration of the range cell migration. When the variation of slant range during the observation does not vary out of the range cell (blue curve), the energy of the point target is well identified in a single range cell. When the variation of slant range varies more during the observation (orange curve) and the parabola crosses several range cells, the RCM must be corrected.

well, which cannot always be wished. Hence, the research to improve the information capability of the instrument has focused on the research for enlargement of the bandwidth.
The denomination of UWB radars is regulated by the Federal Communications Commission (FCC) and the International Telecommunication Union Radiocommunication Sector (ITU-R). It is defined as a system for which the signal's bandwidth is larger than 500 MHz, or larger than 20% of the center frequency (Sabath et al., 2005).
UWB radars have a wide range of use such as in medicine (Panzer et al., 2013), humans or landmine detection (Staderini, 2002), Earth Observation (Breed, 2005), or vehicular collisions avoidance (Gresham et al., 2004). However, they can be complicated to design since each of the system components has to process the entire bandwidth. This limitation can be overcome by using a step frequency waveform where the signal's frequency is increased step by step.

2.4.3 Step-frequency radars

The ultra-wideband radar technique leads to a high resolution in the range direction. However, the wide bandwidth required for high resolution is actually difficult to achieve. An effective way to increase the bandwidth of a train of coherent pulses, and avoid building devices working on a wide bandwidth, is to add a frequency step Δf between consecutive pulses, as presented in figure 2.8. Thus, a wide bandwidth is achieved over several pulses instead of one large bandwidth pulse. The effective bandwidth of a stepped frequency waveform is the product of the number of pulses with Δf. The entire bandwidth is achieved in one sounding, and soundings are repeated on the whole synthetic aperture. Step frequency waveforms have several advantages:

- Each frequency generated by a stepped-frequency synthesizer is highly stable and uniformly spaced across a wide bandwidth.
- The pulse instantaneous frequency remains narrow, which is important because of simpler hardware involved in the narrow-band radar technique.
- By emitting pulses with different wavelengths, the radar received spectrum contains the contribution of every frequency: this way, any singular behavior of one frequency will be averaged. Thus, a large interval of radar responses can be registered from the asteroid: this is why step frequency radars are called versatile.

UWB SARs are thus high-resolution radars, which are easily designed using the step frequency waveform. The development of the UWB technology allowed the spread of radars, and the variety of usage it knows today.

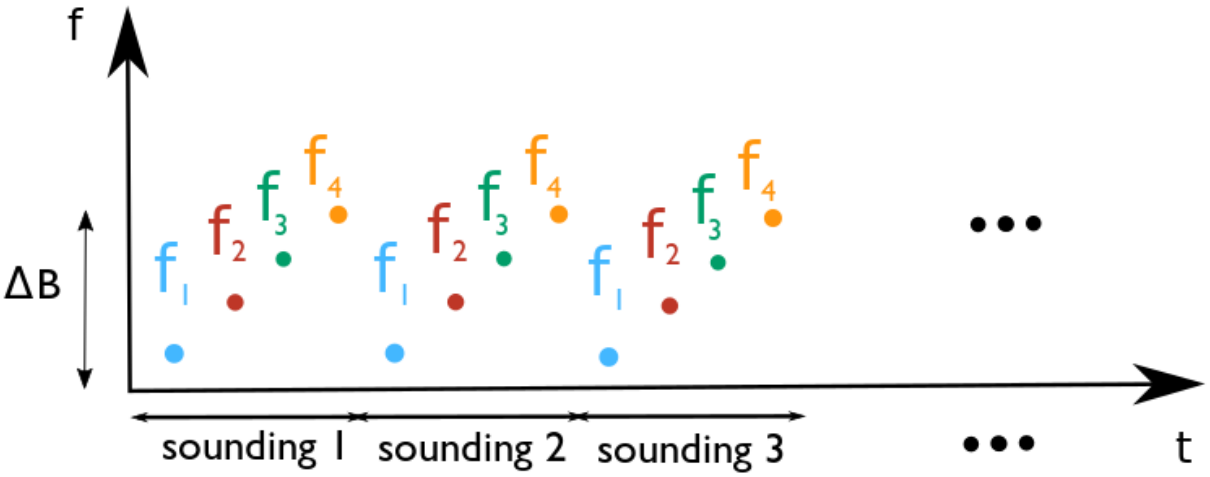

Figure 2.8: Step frequency radar.

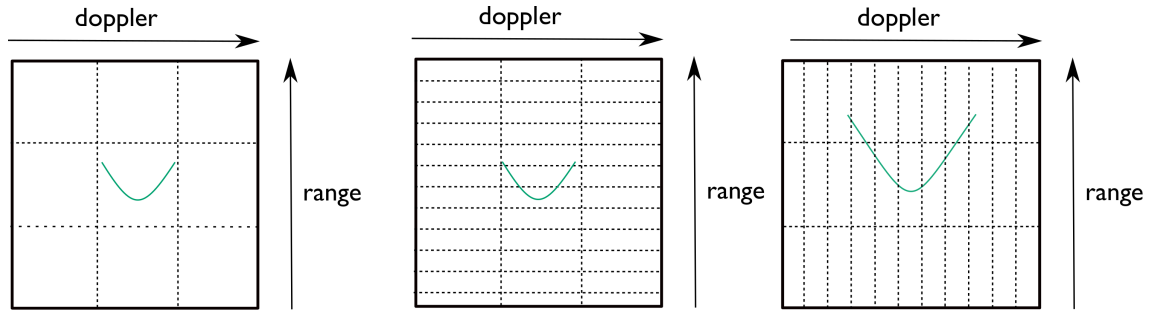

Figure 2.9: Illustration of the range cell migration. When the variation of slant range during the observation does not vary out of the range cell (left), the energy of the point target is well identified in a single range cell. When the resolution cell size is reduced in the range direction, the same target RCM might cross the range resolution cell limits (middle). When the Doppler bandwidth is enlarged, the parabola describing the RCM is larger (right), and thus the RCM might cross the range resolution cell limits.

2.4.4 UWB radars in Doppler

UWB radars can also be developed by considering the Doppler bandwidth. By observing the object with a larger aperture, the Doppler band will be widened and thus the azimuth resolution will be improved.

2.4.5 Correction of the migration

One major aspect of SAR imaging is the range migration. Indeed, the range migration must not exceed the size of the resolution or the RCM will have to be corrected. For UWB radars, the range resolution cell size is reduced and the RCM will more easily extend the resolution cell size. For radars UWB in doppler, the target is illuminated for a longer time, so the variation of the RCM is larger, as illustrated in figure 2.9. Thus, UWB radars require in a more frequent way RCM correction than classical narrowband radars or will suffer from azimuth defocusing.

2.5 SARs in space missions

The first exploitations of radars on planetary bodies were conducted by observing the Moon in 1946 from Earth, not long after the invention of the radar technique. After studying the Moon, the next accessible targets were the solar system planets. While the 300 meters Earth-based antenna at Arecibo in Porto Rico, and the 34m Earth-based dish of the Goldstone Observatory in the United States, provide numerous observations of space bodies, their accuracy remains a limit. Thus, since the 1980s, many radars have been operated on orbit around the planetary bodies they studied. Spaceborne radars have been collecting information about the structure of the surface of planetary bodies hidden by atmospheres impenetrable for optical instruments such as on Venus or Titan and probed the subsurfaces of planets, such as on the Moon or Mars, such as presented in table 2.1 and 2.2.

SARs have been used for several decades to map natural or anthropic surfaces on the Earth and more lately, probe the surface and subsurface of planetary bodies from orbit with a high azimuth resolution, while a high range resolution can be achieved using UWB waveforms. Yet, no spaceborne radars have been dedicated to the study of the surface and structure of asteroids, and thus questions linked to the formation and evolution of these bodies remains without an answer. Lately, several missions were proposed to investigate this question, including the mission AIM (Michel et al., 2016), which was proposed to the European ministerial council in 2016 and boarded in radar called HFR, whose objective was to probe the subsurface of an asteroid.

Target	Space Agency	Mission	Date	Radar	Center frequency	Objectives	References
The Moon	NASA	Apollo 17	1972	ALSE	5, 15, 150 MHz	Detect lunar subsurface geological and tectonic structure.	(Phillips et al., 1973)
	ISRO	Chandrayaan	2007	Mini-SAR	2.5 GHz	Characterize physical properties of the lunar surface such as the roughness, permittivity and porosity.	(Spudis et al., 2010)
	JAXA	Selene	2007	LRS	5 MHz	Study of the geological thermal history of the lunar surface region relating to a time scale of several hundreds of millions of years.	(Ono et al., 2008)
	NASA	LRO	2010	Mini-RF	2389 / 7140 MHz	Map the lunar poles and search for water ice.	(Nozette et al., 2010)
Venus	NASA	Pioneer Venus	1978	ORAD	1.757 GHz	Get information on the surface topography and estimate surface electrical conductivity.	(Pettengill et al., 1979)
	Soviet Agency	Venera 15-16	1983		3.75 GHz	Map the surface of Venus and identify geological characteristics.	(Stofan et al., 1991)
	NASA	MAGELLAN	1989		2.3 GHz	Built a map of the elevation for the whole planet and image tectonic structures.	(Ford et al., 1989)
Titan	ESA	CASSINI	1997		13.78 GHz	Image Titan's surface and its tectonic structures.	(Elachi et al., 2005)
Mars	ESA	Mars-Express	2003	MARSIS	2-5 MHz	Map the distribution of solid and liquid water in the first kilometers of Mars subsurface, probe geological features and study the ionosphere.	(Picardi et al., 2005)
	NASA	MRO	2003	SHARAD	20MHz	Map selected locations to at least several hundred meters depth in the Martian subsurface and analyse its composition in rock, water and ice.	(Seu et al., 2007)

Table 2.1: SARs in space missions part 1

Jupiter's satellites	ESA	JUICE	2022	RIME	9 MHz	Study the subsurface of Jovian satellites up to a depth of 9km to study the subsurface geology and geophysics of the icy moons, and detect possible subsurface water.	(Bruzzone et al., 2013)
Europa	NASA	Europa-Clipper	2022	REASON	9MHz, 60 MHz	Mapping Europa's vertical crustal structure, search for subsurface water, study the distribution of shallow subsurface water and search for an ice-ocean interface.	(Blankenship et al., 2018)
Comets	ESA	Rosetta	2014	CONSERT	90MHz	investigate the deep interior of the nucleus of comet 67/P Churyumov-Gerasimenko.	(Kofman et al., 2007)

Table 2.2: SARs in space missions part 2

Chapter 3

HFR, a radar dedicated to probe the surface and subsurface of asteroids

With its high performances, and its capabilities to differentiate between a large variety of different medium, a radar operating remotely from a spacecraft is the most mature instrument capable of achieving the science objective to characterize the internal structure and heterogeneity of an asteroid, from sub-metric to global scale (Herique et al., 2018) (Hérique et al., 2019).

3.1 AIM : Asteroid Impact Mission

The joint mission AIDA (Asteroid Impact and Deflection Assesment) consisted of a cooperation between NASA Double Asteroid Redirection Test, DART, described in Cheng et al. (2015), and ESA Asteroid Impact Mission, AIM (Michel et al., 2016). AIDA was designed to be the first test to use a kinetic impactor to deflect an asteroid and targeted the 180-meter large moon of the binary asteroid (65803) Didymos. While DART's objective is to impact the asteroid, AIM was designed to measure the physical and dynamical properties of the asteroid Didymos and detect the changes resulting from the impact, using measurements of key physical properties such as surface, subsurface and internal structure of the asteroid. The main objectives of the AIM mission were :

- Characterizing the mass, size, morphology, and density of the natural satellite of a binary asteroid.
- Determining the dynamical properties of the binary system.
- Determining surface and subsurface properties of the natural satellite of a binary asteroid.
- Determining the thermophysical properties of the natural satellite of a binary system.

In order to characterise the surface and subsurface properties of the main asteroid of (65803) Didymos, AIM boarded two radars: a bistastic, low-frequency radar (LFR) designed to observe the deep structure of the system structure and a monostatic, high-frequency radar (HFR) designed to probe the first tens of meters of the asteroid subsurface with a metric resolution, to identify layering and link surface measurements to the surface structure (Hérique et al., 2019).

3.2 HFR

3.2.1 Presentation

HFR is an ultra-wideband, step frequency SAR operating with frequencies ranging from 300 MHz to 800 MHz in nominal mode and up to 3 GHz in an optional mode. HFR's frequencies are a trade-off between the penetration depth, the range resolution, and technical constraints, especially

the antenna size. Indeed, a deep investigation requires low frequencies to reduce the dielectric and scattering loss and subsurface probing requires a high resolution, achieved with a wide band, and thus high frequencies. HFR's band of 300-800 MHz combined with the geometry of observation of a small asteroid geometry provides a resolution in the horizontal direction better than one meter. The instrument was designed to probe the top ten meters of the asteroid subsurface, determine the regolith depth and detect buried impact craters, while the 3 GHz mode allows probing the near surface with a higher range resolution.
One of the primary objectives of HFR within the AIM mission was the characterization of the regolith of the Didymos system's secondary body, Didymoon. HFR was supposed to study Didymoon before and after the DART impact and determine its structure and layering down to a few meters. Then, the tomography of the crater of the DART impact performed with HFR's data would have provided an estimate of the mass ejected by the impact, in order to model the momentum transfer efficiency of the impactor. With a single-pass orbit, Didymoon's mapping would have provided the 2D distribution of rocks embedded in the subsurface, and a multipass acquisition and processing would have been required to obtain the 3D tomography of the regolith. Another primary objective of HFR is the determination of the dielectric properties of the subsurface of Didymoon, which can be retrieved by analyzing the amplitude of the backscattered surface echoes.

3.2.2 Future missions embarking instruments related to HFR

HFR was one of the payload of AIM, however, the mission was not funded in ESA's ministerial council in 2016. Yet, different versions of HFR were proposed as payload for two additional missions: Hera, an updated version of AIM, and Chimera, a mission from the Discovery program proposed by NASA.

Hera

HERA is a small mission of opportunity built on the AIM concept, to investigate a binary asteroid, observe the outcome of a kinematic impactor, and provide information for asteroid impact thread mitigation, asteroid mining, and science. Hera is an optimized version of AIM, keeping its main objectives and its target, and providing crucial data for the interpretation of the DART impact, but reducing risks and costs by simplifying the spacecraft design and relaxing different constraints. Hera's main objectives are :

- Assessing momentum transfer efficiency of the hypervelocity asteroid impact
- Determining global asteroid parameters that drive the momentum transfer efficiency
- Determining local variation of parameters that drive the momentum transfer efficiency
- Demonstrating close proximity operations around a 163m diameter asteroid

To perform these objectives, and study the consequences of the DART impact on the asteroid structure, Hera will embark the Juventas CubeSat, which boards a monostatic low-frequency radar, which should reach about one hundred meters down the asteroid subsurface. Juventas' radar is a low frequency radar with frequencies ranging from 50 to 70 MHz, which would be flying in the same geometry of observation than HFR, and would thus benefit from the work carried out for HFR.

Chimera

Chimera (Harris et al., 2019) is a Discovery mission concept to visit the centaur 29P/ Schwassmann-Wachmann 1 (SW1). Chimera was designed to study the evolution, chemistry, and mechanisms driving the activity of a Centaur. As Centaurs are unknown objects, with properties of both Trans-Neptunian Objects and Jupiter-Family Comets, understanding their structure, chemistry, and processes that drive their activity is key to understanding the formation and evolution of icy planetesimals and inform us about the origin of the solar system.
SW1 was discovered in 1927, has a persistent coma and has been observed for about 90 years from Earth. With its intensive activity, SW1 is thus a perfect target to investigate Centaurs. Chimera

was supposed to board GRIFIN, a radar dedicated to measuring the near-subsurface structure and permittivity, in connection to topography and activity patterns. GRIFIN would have been crucial to reconnect the surface and coma observations with subsurface structure, and based on the design of HFR. It was supposed to use frequencies ranging from 400 to 420 MHz, with a mode at 3.0 GHz. However, Chimera was not founded by NASA in 2020.

3.3 Specificity of a UWB radar instrument imaging a small body

Among existing radar instruments, several ultra-wideband SAR have flown in order to study the surface of the Earth, such as depicted in section 2.3, some SAR have studied small bodies such as depicted in section 1.3 but no UWB SAR has studied small bodies.
However, the Earth Observation geometry is a standard geometry, different from the small body geometry by several characteristics :

- While in Earth observation the radar's trajectory can be considered as rectilinear during the illumination time, in the observation of Didymos with HFR, the spacecraft is motionless in an inertial frame. Thus, in a frame centered and linked to the asteroid, the trajectory is dominated by the Didymos' rotation, and cannot be considered rectilinear.

- For Earth-observing radars, the surface observed by the radar can be considered as planar in a first approximation due to the narrow antenna pattern. However, HFR's antenna beam covers the whole observed body, and the hypothesis of a plane surface for Didymos does not stand.

- HFR is an ultra-wideband radar, which means that its band Δf is not negligible with respect to its central frequency f_c : $\frac{\Delta f}{f_c} = 0.91$. The radar's wavelength almost triples during the observation, from 0.375 m to 1m, which is a larger variation than for classical UWB SARs.

- Earth-observing radars observe surfaces at distances sufficiently large to consider that the slant range distances between the spacecraft and a given point of the scene are close to be constant during the entire observation. For narrowband radars, the same assumption can be laid on the incidence angles. However, the geometry of observation of Didymos is dominated by the body's rotation, and the whole asteroid is small enough so that it is seen entirely by HFR's antenna beam. Thus, the incidence angles and the slant-range distance cannot be considered at all constant during the observation.

- In classical Earth observation radar, the separability between the range and Doppler delays can be assumed at a first-order, or can be obtained by performing range migration processing (Curlander & McDonough, 1991). However, in a small body geometry, the separability between the range and Doppler cannot be considered.

Because of these differences with the Earth observation, the radar performances cannot be deduced from known results, and simulations are needed to assess the radar performances.

Furthermore, for UWB radars, the classic speckle approach used for the computation of the field scattered by the surface, which is based on a distribution of point scatterers is no longer relevant: When the resolution cell becomes small enough, we cannot consider that it contains an infinite number of scatterers. Consequently, the Central Limit theorem (CLT) can no longer be applied. In this case, the speckle of the clutter deviates from Gaussian statistics, and the speckle is called not fully developed speckle. (Gao, 2010) (Billingsley et al., 1999), (Lampropoulos et al., 1999).
Plus, in small resolution cells, scatterers can no longer be considered isotropic and white. This means that the reflectivity of the scatterer depends on the aspect angle and the frequency. Thus, the source coherence has no reason to be assumed over the full bandwidth for both Doppler frequencies and RF. Because of the not fully developed speckle, ultra-wideband scattering performances may deviate from known performances.

3.4 Summary

HFR is the first SAR designed to image a small body, which requires observing the target in a specific geometry largely different from the Earth observation geometry where most spaceborne SARs have flown. Moreover, as a UWB SAR, HFR will be observing an asteroid with a high resolution, in both range and azimuth. Thus, because of its unique design, the classical SAR observation geometry is not reproduced, and the radar's return needs to be studied in order to assess the instrument's performances, and the applicability of different signal processing techniques such as autofocus (Xi et al., 1999), or tomography (Reigber & Moreira, 2000) to improve the radar science return. As the radar performances depend on the geometry and the radar design, each scenario of observation for any mission must be carefully studied in order to assess the instrument's science return and its interest within a space mission. The performances and design analysis of the instruments must thus be clearly defined before launching the mission, are performed using simulations of the instrument signal in a realistic geometry of observation.

Chapter 4

Estimating the radar performance in a small body geometry

As studying a small body with a UWB radar is a new approach, simulations are needed to estimate the radar performances, and determine the quality of the data the instrument will provide. The simulations of the signal propagation and scattering are performed with simulations of the Maxwell equation (described in appendix A), and simulation of the radar results are performed with the SPRATS toolbox (described in appendix B). However, before simulating the radar signal, the geometry of observation must be defined, which includes selecting a model for the targeted asteroid to be studied and setting its physical parameters.

4.1 Asteroid model

In order to simulate the signal scattered by an asteroid's surface and its subsurface, the asteroid physical model must be defined. Several asteroids have been studied from Earth with different asteroid research programs (as presented in 1.2.1) and have thus known shape and orbital parameters. However, the permittivity of asteroids has never been measured, which means that the dielectric model will be based on the analysis of rocky materials on Earth, meteoretical analogs, and inferences from surface or global in-situ measurements conducted on asteroids.

4.1.1 Target

Our simulations will focus on asteroids that are about 1km large, probable rubble pile, and with known orbitographic parameters. Two asteroid systems were considered : (65803) Didymos and 1994KW4.

(65603) Didymos

Didymos is an Apollo asteroid, a type of NEA with the semimajor axis of their orbit $>$ 1AU and a perihelion distance $<$ 1.017 AU. It is a binary asteroid, consisting of a main body, called Didymain, which is about 800 meters large, and its moon, called Didymoon, which is about 180 meters large. Didymain has a rotation speed of a little more than 2.2 hours, which is just above the limit of disruption for kilometric asteroids (Walsh et al., 2008), which makes it probably a rubble pile. Some of Didymos' physical orbital and dynamical properties are presented in table 4.1. The only parameters directly measured by observations are the orbital period of the secondary around the primary, their orbit separation, the rotation period of the primary, and the size ratio of the secondary. All other quantities are derived from these measured parameters, as described in Michel et al. (2016). A preliminary shape model was derived using observations from the radars Arecibo and Goldstone and photometric data; and is presented in figure 4.1. We can note from these parameters that Didymos's albedo is typical from S-type asteroids, which is consistent with the radar albedo that agrees with the presented of

silicates. Based on models on binary asteroids, we assume a 1:1 resonance, meaning that the same hemispheres of Didymos and Didymain will always be facing each other, like the Earth and the Moon.

As the target of the AIM mission, the Didymos system was a logical target for the study of HFR's performances. Its shape, dynamical and orbital parameters are well known and it has an available terrain model as presented in figure 4.1. However, the model's resolution is too poor. Thus another asteroid with an available high-resolution shape model needs to be investigated.

1999KW4

1999 KW4 is a Near Earth Asteroid discovered in 1999 by Lincoln Near-Earth Asteroid Research (LINEAR). It is approximately 1.3 km large and has a rotation period of 2.7 hours, which is just above the limit of disruption for kilometric asteroids (Walsh et al., 2008), which makes it probably a rubble pile. 1999 KW4 has a moon of 360 m in diameter, which orbits the main body with a period of 16 hours at a mean distance of 2.6 km. KW4's well-known physical properties make it a good reference for small NEA (as depicted in table 4.2, and in figure 4.3). 1999 KW4 has an available shape model with a good resolution, depicted in figure 4.2, which makes it a good target for our simulations.

The final asteroid model we will be using in our parameters will be the main asteroid of the Didymos system. However, since no DTM of Didymain is available with an acceptable resolution for our

Aphelion	2.2760 AU
Perihelion	1.013 AU
Semi-major axis	1.6446 AU
Orbital period	770 days
Primary rotation period	2.26 hours
Mean diameter of the primary	0.780 ± 10 % km
Mean diameter of the secondary	0.163 km ± 0.018 km
Bulk density of the primary ρ_P	2100 kg m^{-3}
Total system mass	$5.28 \pm 0.54 \times 10^{11}$ kg
Mean absolute magnitude H	18.16 ± 0.04
Geometric albedo	0.15 ± 0.04
Radar albedo	0.27 ± 25 %
Taxonomic Type	S / Xk

Table 4.1: (65603) Didymos physical properties (Dell'Elce et al., 2017; Michel et al., 2016)

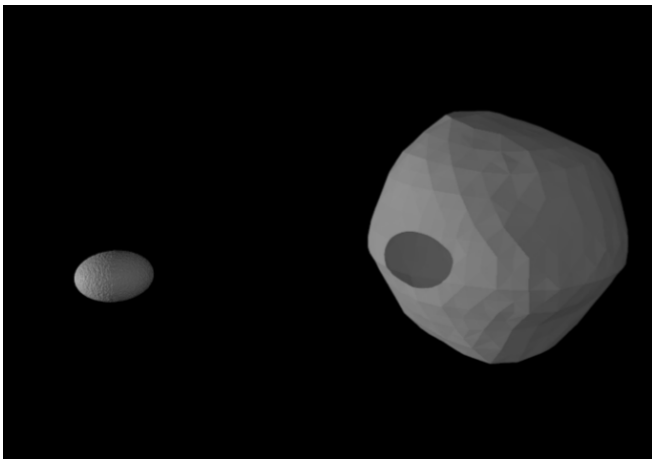

Figure 4.1: Didymos system shape model (Michel et al., 2016)

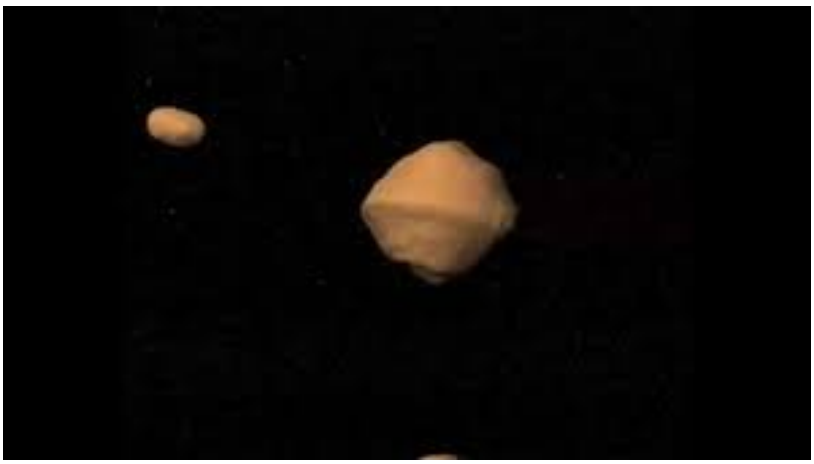

Figure 4.2: The binary asteroid 1999KW4. Credit: E.M. DeJong, S. Suzuki, and S.J. Ostro at JPL, and D.J. Scheeres and E.G. Fahnestock from Univ. of Michigan.

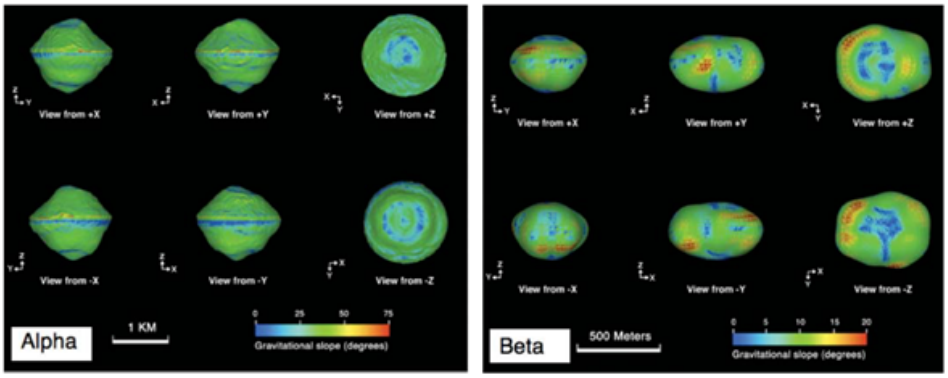

Fig. 3. Principal-axis views of the Alpha (**left**) and Beta (**right**) shape models. Colors indicate effective gravitational slope (the angular deviation from the local downward normal of the total acceleration vector due to gravity and rotation), calculated with the model densities (Table 2). Alpha's slopes average 28° with a maximum of 70°, whereas Beta's average 9° with a maximum of 18°. Beta's +*x* axis points toward Alpha.

Figure 4.3: 1999 KW4 and its moon (Ostro et al., 2006).

Aphelion	1.084 AU
Perihelion	0.2 AU
Semi-major axis	1.6446 AU
Orbital period	188 days
Primary rotation period	2.76 hours
Mean diameter of the primary	1.317 ± 0.04 km
Mean diameter of the secondary	0.360 km
Bulk density of the primary ρ_P	1970 kg m^{-3}
Total system mass	2.488 ± 0.124 × 10^{11} kg
Mean absolute magnitude H	18.16 ± 0.04
Geometric albedo	0.26
Taxonomic Type	S / Xk

Table 4.2: KW4 physical properties (Ostro et al., 2006).

simulations, we will use the DTM of 1999KW4 that will be rescaled to a size of 1 km. Approximating the shape of Didymos by the one of KW4 is not a restrictive hypothesis, since KW4 and Didymain have similar orbital, dynamical and physical parameters and seem representative of the small asteroid population. In this way, our simulations will still be representative of the observation geometry of Didymos. Yet, even the DTM of KW4 is not precise enough to picture the asteroid's roughness, which

will have to be modeled numerically randomly.

4.1.2 Asteroid dielectric model

In order to model the wave propagation at the surface and in the subsurface of an asteroid, a coherent dielectric model must be defined: having a reliable dielectric model for the asteroid is fundamental in order to define the radar's specification and later for data interpretation.
The relative dielectric permittivity $\epsilon = \epsilon' - i \cdot \epsilon''$ drives the wave's propagation in a material. The real part of the electrical permittivity relates to the amount of energy re-radiated by the material, whereas the imaginary part, usually represented by the loss tangent $\tan\delta = \frac{\epsilon''_r}{\epsilon'_r}$ relates to how much energy is lost in the scattering.

To create the asteroid dielectric model, the dielectric composition of rocky materials on Earth was analyzed, which gives a first idea of their range of values: ϵ_r' is constrained within the range $3 \leq \epsilon \leq 10$ (Herique et al., 2018), for compact rocks with low porosity. The loss tangent varies between $10^{-3} \leq \tan\delta \leq 10^{-2}$, and depends on the metallic content of the rocks, as presented in table 4.3. This range can be used to describe most dry rocks with few metallic contents, which correspond to the kind of materials expected from an asteroid.

However, the real nature of asteroid constitutive materials is still lacking. In order to fill the gap, several measurements of the permittivity and porosity were conducted on meteorites. Yet, it is not clearly understood how meteorites can relate to their parent body, as they may have experienced terrestrial weathering. Plus there is bias in considering that meteorites are representative of asteroids, since not all meteorites may survive the entry in the Earth atmosphere without disintegrating. Finally, measurements were done on a limited number of samples and may not reflect the compositional variability observed in a parent body family. This explains why the variability of the measured permittivity, which is presented in table 4.4 is so large.

Our asteroid model will be associated with a real permittivity of 3.0, the permittivity of dry sand (Dechambre et al., 2012). Indeed, a sand texture is similar to the texture of regolith found on the moon and on small asteroids, according to IR measurements.
To summarize, our small body model thus consists of the Didymos asteroid geometry, Didymos' shape model replaced by 1999 KW4's shape model, rescaled to 1 kilometer. The surface and interior permittivity of the asteroid is considered constant and equal to 3.0, and the asteroid roughness will be modeled as a random rough surface, whose parameters will have to be defined.
With this asteroid model, consisting of a geometry of observation and a permittivity model, HFR's behavior can now be simulated.

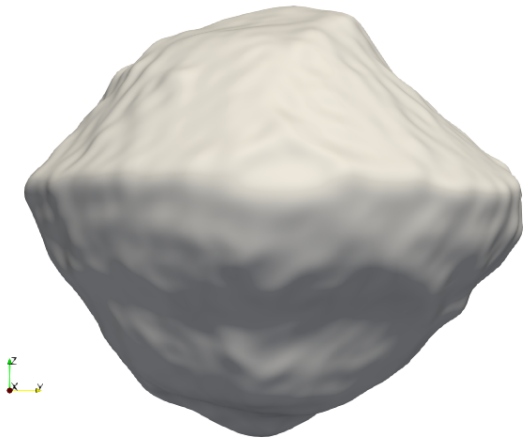

Figure 4.4: KW4 shape model

4.2 Radar performances

From HFR's SAR synthesis, several parameters can be computed to estimate the radar performances. The image resolution and peak to side lobe ratio can be deduced from the SAR image. The link budget is the accounting of all power and losses that the radar signal will experience and is necessary to assess the signal to noise ratio, which must be high enough for good image quality.

4.2.1 Resolution

The radar resolution is the radar's capability to distinguish between two targets. It is measured from the impulse response, as depicted in figure 4.5. The resolution is the width of the 3dB contour around the main peak power. If two targets are separated by a distance that is smaller than the resolution, then they will not be separated, as pictured in figure 4.6.

Table 4.3: Permittivity of relevant minerals and organics. Adapted from Herique et al. (2018).

Classification	Name	ϵ	$\tan\delta$
Silicates	Olivine (measurement 1)	7.1	$4\ 10^{-3}$
	Olivine (measurement 1)	7.3	$4\ 10^{-3}$
	Pyroxene (measurement 2)	7.9	$8\ 10^{-3}$
Phyllosilicates	Serpentine (measurement 1)	6.4	$4\ 10^{-2}$
	Serpentine (measurement 2)	6.4	$6\ 10^{-2}$
	Montmorillonite	4.2 - 4.8	-
Carbon	Graphite	15-23	0.5-0.85
	Pure Carbon	23-30	0.35-0.4
	Carbon Black	6.0-9.0	0.4
	Coal (with H-S-O-N)	1.94-2.21	0.02-0.2
Metal	Hematite + Magnetite	15.0	0.2

Table 4.4: Dielectric permittivity of meteoritic samples from the literature. Adapted from Herique et al. (2018).

Classification	Name	ϵ	$\tan\delta$
CR2	NWA 801	3.5-4.0	-
CM	NWA 5797	4.0-4.7	-
LL5	MAC99122	6.9-12.2	$4.0\ 10^{-3}$
L5	MET01260	8.4-20.4	$4.0\ 10^{-3}$
L6	Holbrook	7.8	$1.5\ 10^{-2}$
	Burderheim	9.0-11.9	$4\ 10^{-2}$
	Colby	10.6-11.8	$5\ 10^{-2}$
	Leedy (sample 1)	10.4-11.1	$3\text{-}6\ 10^{-2}$
	Leedy (sample 2)	11.2 -13.9	$3\text{-}4\ 10^{-2}$
H5	LEW 85320	8.6-21.4	$2.0\ 10^{-2}$
	Forest City	16-33	0.11
	Plainview (sample 1)	25.4-30.4	0.1-0.2
	Plainview (sample 2)	32.1-45.9	0.1-0.2
	Bonita Springs	43-81	0.13-0.19
EH4	Indarch	130-150	0.065-0.117
Mesosiderite	RKP 17015	12.3-..	$3\ 10^{-3}$

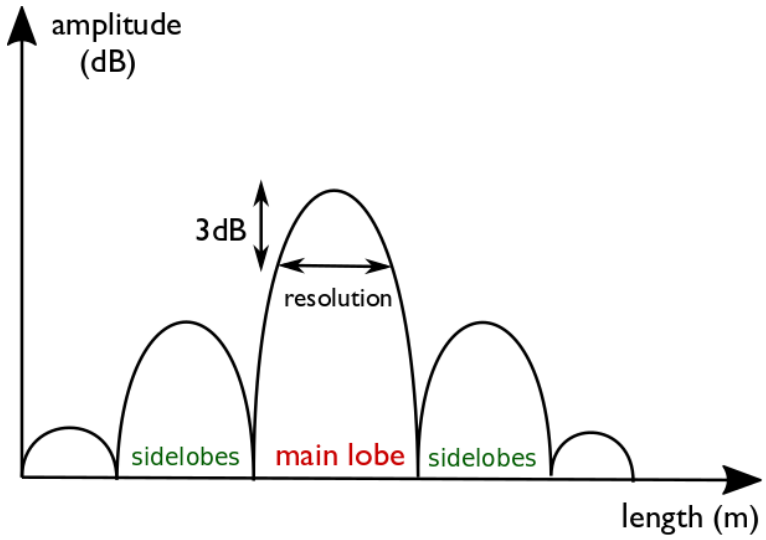

Figure 4.5: Impulse response of a point target.

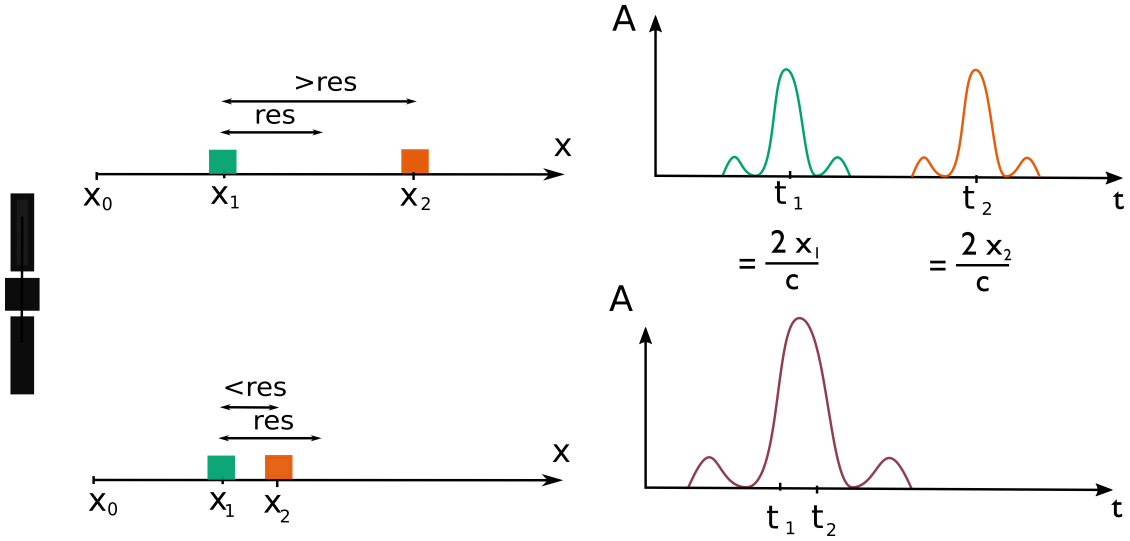

Figure 4.6: Illustration of how two targets separated by a distance larger than the resolution are imaged as one target by the radar.

The radar range resolution δ_r can be expressed :

$$\delta_r = \frac{c}{2B \cdot \sin(\theta)} \tag{4.1}$$

with c the velocity of light in the void, and B the radar bandwidth, and θ the incident angle.

The radar azimuth resolution is :

$$\delta_a = \frac{\lambda \cdot r_0}{2 \cdot v} \cdot \frac{1}{T_{ill}} \tag{4.2}$$

with r_0 the range to the target, v being the spacecraft velocity, and T_{ill} the length during which one point is seen by the radar. However, the expression of the azimuth resolution is only valid in an Earth observation geometry. In the small body observation geometry, the azimuth resolution will have to be computed using simulations.

4.2.2 Peak to sidelobe ratio

The Peak to sidelobe ratio is the ratio of the power of the largest level of sidelobes P_s to the power of the main lobe P_m of the target. It represents the quality of a SAR image since a strong PSLR

indicates strong sidelobes compared to the main lobe, which means that a weak target can be hidden by strong target sidelobes. The PSLR is computed such that :

$$PSLR = 10 \log_{10} \frac{P_s}{P_m} \tag{4.3}$$

The PSLR can be improved by windowing the SAR signal in the range and doppler directions, at the cost of the resolution.

4.2.3 Link budget

The link budget is used to estimate the power budget of the radar. Indeed, a wave must be emitted with power high enough so that it can be registered after its two-way travel, without being hidden by the noise level. The link budget can be expressed in the form of the radar equation which writes, for a monostatic radar (Curlander & McDonough, 1991):

$$P_{Rx} = \frac{P_{Tx} \cdot G_{Tx}^2 \cdot \lambda^2 \sigma}{(4\pi)^3 \cdot R^4 \cdot L_{FS} \cdot L_M} \tag{4.4}$$

With :

- P_{Rx} the received power
- P_{Tx} the transmitted power
- G_{Tx} the transmitter antenna gain, taking into account the transmitter loss
- L_{FS} the loss in free space
- L_M other, miscellaneous losses
- σ the RCS
- R the distance between the emitter and the receiver

The Signal to Noise Ratio (SNR) is written as $\frac{P_{Rx}}{N}$ with N the power of the noise. The SNR must be as high as possible to guarantee sufficient image quality.

4.3 Objectives of my Ph.D. thesis

My Ph.D. began in 2017 within the frame of the AIM mission and the design of HFR. As HFR was developed to fly in a specific geometry, the performances of HFR on realistic rough asteroids surfaces, and the applicability of tomography on asteroids need to be assessed. The objective of my Ph.D. is to study UWB SAR tomography in an asteroid observation geometry. This shall be achieved through:

- Development and implementation of a surface backscattering model for rocky terrains adapted to ultra-wideband radar signals.
- Development and implementation of a volume backscattering model adapted to ultra-wideband radar signals.
- Development/adaptation of a SAR simulator.
- Development of a tomographic SAR simulator for dry rocky terrain.

The study will be performed by analyzing, simulating and processing the radar signal. These steps are performed using the SPRATS toolbox, an IDL software that provides the tools to evaluate radar concepts, evaluate the processing performances and validate data processing techniques. SPRATS is further described in appendix B. However, in order to validate the performances and the results

of the models developed, these steps will also be performed in an Earth observation geometry. Indeed, the Earth observation can be considered simpler than the small body geometry, because of the range/Doppler separability or the availability of the analytical expressions for the range, azimuth and elevation resolutions.
As SPRATS provided tools to measure the spectrum of a point target only, my Ph.D. thesis will be consisting of developing new methods to widen the range of scenarios SPRATS can cover, and analyze the resulting radar performances.

In the first part of this manuscript, different surface backscattering models are reviewed, and the development of the surface backscatter model is introduced, validated and its results on a realistic asteroid surface are presented. In a second part, different volume backscattering models are reviewed, a volume backscatter model is introduced and validated. In the third part, different tomography models are reviewed, one tomography model is selected, implemented and validated. Finally, in the fourth part, the validity of the hypotheses of the SAR syntheses in UWB scattering are investigated and their impacts on the resulting resolution are presented.

Part II

Rocky Surface Scattering Model Selection

In the following part, we review different surface scattering models used to simulate the signals backscattered from random rough surfaces. The models are presented and their domains of validity are compared with the roughness parameters of existing asteroids' surfaces, in order to select the most suitable model. The reviewed models have to cover simulation of the full radar signal (amplitude and phase) as opposed to static models which provide only the backscattering coefficient σ_0. In this way, the phase coherence is preserved, and additional signal processing techniques could further be applied. Moreover, the reviewed models are analytical and not statistical. From this review, the backscattering model most adapted to our study is implemented, validated and applied to simulate the spectrum scattered by a rough surface on an asteroid.

In the first chapter, we introduce what a rough roughness is, how a random rough surface can be described and implemented, and how electromagnetic waves react when hitting a rough surface. Then, we describe the topology of an asteroid's surface, by taking as an example the asteroid Itokawa, observed by the mission Hayabusa (JAXA), which was the only asteroid closely observed when this work was started in 2017. An insight into Itokawa's roughness will give us an insight into the roughness domain the scattering models will have to cover. Next, we describe four promising surface models : the Small-Perturbation Method (SPM), the Kirchhoff Approximation (KA), the Small-Slope Approximation (SSA) and the Weighted Curvature Approximation (WCA). Finally the implementation of the KA is presented, validated in an Earth observation geometry, and applied in a small body geometry.

Contents

Chapter 5

Random rough surfaces

5.1 Definition

The surface of a workpiece has been defined in international standards (ISO 17450-1) as *a set of features which physically exist and separate the workpiece from the surrounding medium.*
No real surface can be perfectly smooth, even manufactured surfaces. The deviation from a nominal, smooth plane is what we call the surface topography (Blunt & Jiang, 2003). As part of this topography, the roughness is measured as the variation of height from the nominal reference plane. In the case of natural rocky surfaces, this deviation can originate from boulders, dust or other particles and have been built during the full history of the surface from its formation to its current state.
Most natural surfaces can be described as random rough surfaces and are usually characterized using a height distribution function, the variance, or RMS height. These processes are spatially random, and invariant in time, like many artificial surfaces or terrestrial surfaces. Others are random in space and time, as the interfaces between the air and fluid or desert surfaces. They are thus called stochastic rough surfaces. In the case of asteroid surfaces, we consider the temporal variation to be sufficiently small on the radar acquisition time to consider the surface as invariant in time. In the following, we will call a random rough surface one realization of a random process. The resulting realization is however, itself, deterministic.

A random rough surface is defined by its height ζ, a realization of a random variable, which depends on the position on the surface $\vec{r} = (x, y)$. The surface can be entirely characterized by the variability of its heights and their correlation, which are described by the probability density of heights, representing the statistic distribution of heights of the surface and the height autocorrelation function, representing the surface correlation between its points.

5.1.1 Probability density function

The probability density function p_h contains two major information about the surface: its mean value, here the mean height of the surface ζ_0 and its random mean square σ_h, which provides information about the variation of height. Random surfaces are often characterized by a Gaussian probability density :

$$p_h = \frac{1}{\sigma_h \sqrt{2\pi}} \cdot e^{\frac{1}{2}(\frac{\zeta - \zeta_0}{\sigma_h})^2} \tag{5.1}$$

For these surfaces, 99.73% of the surface heights are located between -$3\sigma_h$ and +$3\sigma_h$.
The probability density function checks :

$$\int_{-\infty}^{\infty} p_h(\zeta) d\zeta = 1 \tag{5.2}$$

$$< \zeta > = \int_{-\infty}^{\infty} \zeta p_h(\zeta) d\zeta = \zeta_0 \tag{5.3}$$

$< \zeta >$ is the first central moment, where ζ_0 is the mean height of the surface, chosen to be 0 here for simplicity. In this case, the second-order moment, or variance $< \zeta^2 >$, is the statistical mean of the square height, and is called in the following the root mean square (RMS) height :

$$< \zeta^2 >= \int_{-\infty}^{\infty} \zeta^2 p_h(\zeta) d\zeta = \sigma_h^2 \tag{5.4}$$

5.1.2 Autocorrelation function

The autocorrelation between two points $\vec{r_1}$ and $\vec{r_2}$ of the surface represents the statistical correlation between these points, namely how much the height at point $\vec{r_2}$ is similar to the height at point $\vec{r_1}$. Thus, the function's maximum is reached when $\vec{r_2} = \vec{r_1}$. This function allows accessing the surface correlation length c_L, which describes the correlation of the heights.

The autocorrelation is expressed by :

$$W_h(\vec{r_1}, \vec{r_2}) =< \zeta(\vec{r_1})\zeta(\vec{r_2}) >= \lim_{X,Y\to\infty} \frac{1}{XY} \int_{\frac{-X}{2}}^{\frac{X}{2}} \int_{\frac{-Y}{2}}^{\frac{Y}{2}} \zeta(\vec{r_1})\zeta(\vec{r_2}) dX dY \tag{5.5}$$

with

$$W_h(\vec{r_1}, \vec{r_1}) = W_h(\vec{r_2}, \vec{r_2}) = {\sigma_h}^2 \tag{5.6}$$

where X and Y are the surface length on the $\hat{x}$ and $\hat{y}$ axis respectively. For a stationary surface, we can note that if $\vec{r_2} - \vec{r_1} = \vec{r_d}$, then $W_h(\vec{r_1}, \vec{r_2}) = W_h(\vec{r_d}) =< \zeta(\vec{r_1})\zeta(\vec{r_1} + \vec{r_d}) >$.

The correlation length c_L determines the roughness scale of the surface and corresponds to the distance x_d between two points of the surface for which the auto-correlation coefficient is $\frac{1}{e}$, as illustrated in figure 5.1.

The probability density of heights and the autocorrelation function of heights allow describing completely the rough surface: for example, Gaussian surfaces have the property to have all of their moments connected to the first two moments (the mean and the variance), and the correlation length defines the correlation of the surface.

In addition to σ_h^2 and c_L, other statistical parameters allow characterizing a rough surface, such as the standard deviation of the surface's slopes σ_s defined by :

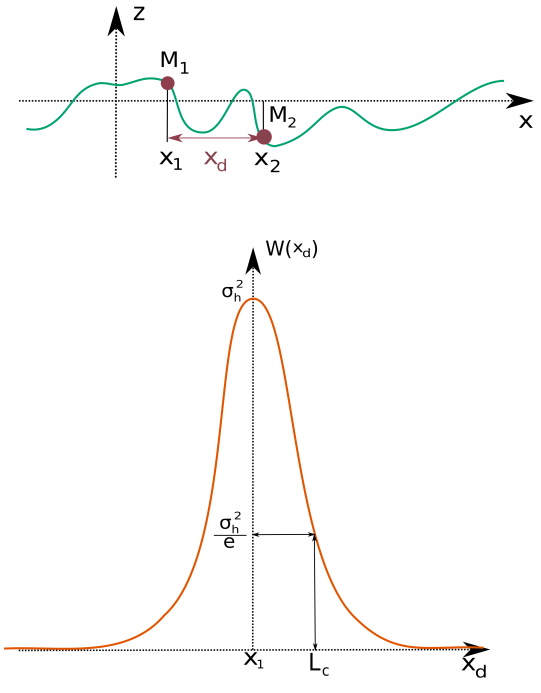

Figure 5.1: Autocorrelation function.

$$\sigma_s = \sqrt{<\zeta'(\vec{r})^2>} = \sqrt{\int_{-\infty}^{\infty} \frac{dk}{2\pi} k^2 S(k)} = \sqrt{-W_h''(0)} \tag{5.7}$$

For a Gaussian surface, the standard deviation of slopes is linked to the standard deviation of heights and to the correlation length by the relation :

$$\sigma_s = \sqrt{2} \cdot \frac{\sigma_h}{c_L} \tag{5.8}$$

For 2D surfaces, the distribution of heights may different on the $\hat{x}$ and $\hat{y}$ axis, so $\sigma_{s,x}$ is expressed using $c_{L,x}$ (the correlation length on the $\hat{x}$ axis) and $\sigma_{s,y}$ with $c_{L,y}$, (the correlation length on the $\hat{y}$ axis).

5.2 Generation of a random rough surface

5.2.1 Description of the random rough surface generator

In order to model a natural rough surface, one realization of a Gaussian random rough process is carried out. We will use the method detailed in Garcia and Stoll (1984), where a white Gaussian noise is convolved with a Gaussian filter to generate a correlated Gaussian surface. The convolution is carried out by a Fourier transform, and since the Fourier transform of a Gaussian is a Gaussian, the resulting surface will thus have a Gaussian behavior, with the RMS height and correlation specified in the filter.

The Gaussian filter $F(x_d, y_d) = F(\vec{r_d})$ is defined by the variance σ_h of the surface height, and the correlation length c_L :

$$F(\vec{r_d}) = \sigma_h^2 \exp\Big(- \frac{x_d^2 + y_d^2}{c_L^2/2} \Big) \tag{5.9}$$

The convolution between the Gaussian filter and the unitary white Gaussian noise N is performed using the 2D discrete Fast Fourier Transform (FFT) algorithm, and the surface can thus be described as :

$$\zeta(\vec{r_d}) = \frac{2}{\pi} \times \frac{L}{N_s} \times \frac{1}{c_L} \times FFT^{-1}[FFT(N) \times FFT(F(\vec{r_d})] \tag{5.10}$$

With N_s the number of points on one dimension of the surface, L the length of the surface of the surface and FFT^{-1} denotes the inverse fast Fourier transform.

This random rough surface generator is inserted into SPRATS (described in appendix B) in order to simulate surfaces with different roughness parameters and will be used as an entry to the selected surface scattering model. However, before describing these models, we will illustrate here how electromagnetic waves are scattered by a rough surface.

5.3 Wave scattering from rough surfaces

Wave scattering from rough surfaces has been largely studied: Rayleigh first considered the problem of a monochromatic wave incident on a sinusoidal surface, and developed the Rayleigh criterion, which determines the degree of roughness of a surface.

Let us consider a monochromatic wave incident on a rough surface with an angle θ_i, and scattered with an angle θ_t at two positions x_1 and x_2 on a surface, as presented in figure 5.3. The phase difference between the two scattered waves is given by (Ogilvy & Merklinger, 1991) :

$$\Delta\phi = k[(h_1 - h_2)(\cos\theta_1 + \cos\theta_2) + (x_2 - x_1)(\sin\theta_1 - \sin\theta_2)] \tag{5.11}$$

where k is the modulus of the wave vector and h_1 and h_2 are the heights of the surface at points x_1 and x_2.

For specular scattering, where $\theta_1 = \theta_2$ this equation becomes :

$$\Delta\phi = 2k \cdot \Delta h(\cos\theta_1) \tag{5.12}$$

The interference between these two waves will depend on the difference in their phases. For $\Delta\phi << \pi$, the two waves will be almost in-phase and will interfere constructively, and for $\Delta\phi \approx \pi$, the waves will

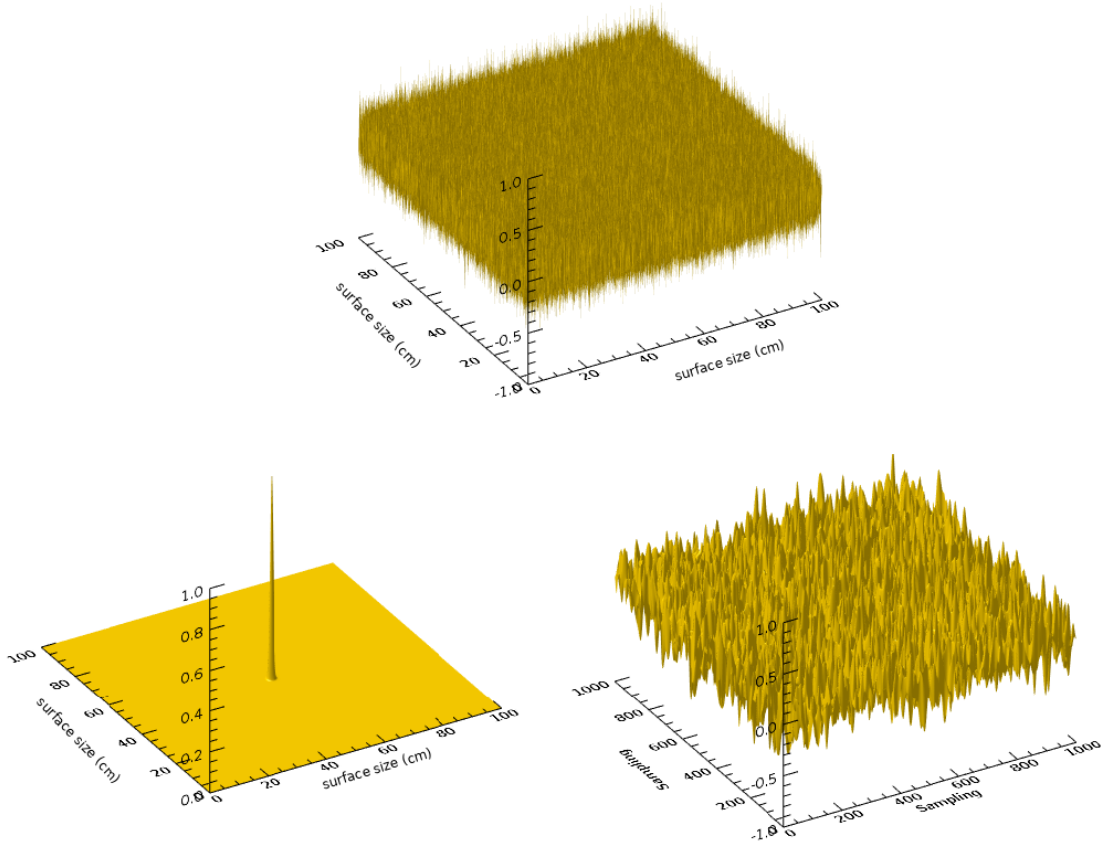

Figure 5.2: Generation of a random rough surface: a Gaussian white noise (top), the generated Gaussian filter (left) and the resulting Gaussian perturbation (right) for a surface of 1000 × 1000 samples and a correlation length of 1 cm.

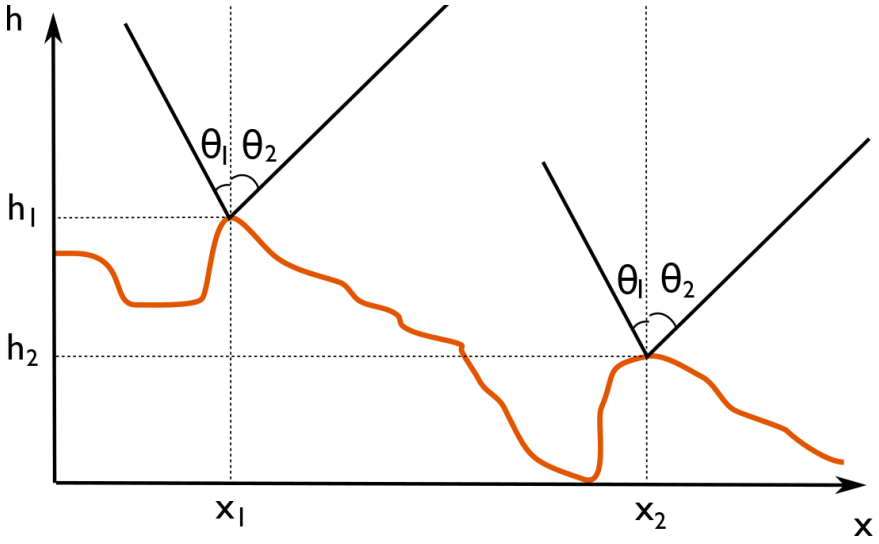

Figure 5.3: Configuration for determining the phase difference between two parallel rays scattered from different points on a rough surface.

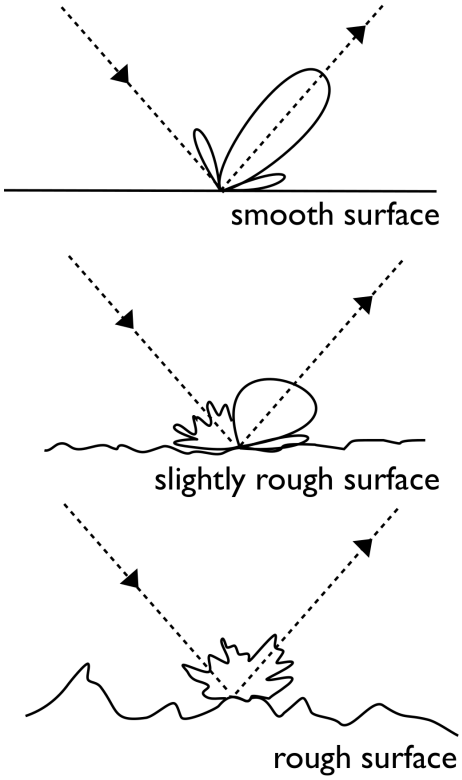

Figure 5.4: Change in the scattered energy from the surface as the surface roughness increases (smooth surface, slightly rough surface and rough surface). The amplitude of the strong specular field is reduced and a scattered, widely spread diffuse field appears. Adapted from Ogilvy and Merklinger (1991).

interfere destructively, leading to no contribution in the specular direction.
Thus, the Rayleigh criterion states that if $\Delta\phi < \pi/2$, the surface can be considered as smooth, and scattering will always occur in the specular direction. If this restriction is averaged on the whole surface, we can replace Δh by the rms height σ_h and the criterion becomes :

$$R_a = k\sigma_h \cos(\theta_i) < \frac{\pi}{4} \tag{5.13}$$

This criterion is however arbitrary and depends on both the frequency and the angle of observation. It determines how rough a surface appears to be from the instrument. A surface thus appears rough when observed with a small incident wavelength or with an incident angle close to the normal, while it may look smooth with a higher incident wavelength or a low incident angle.

For a smooth surface, the phase difference becomes :

$$\Delta\phi = k(x_2 - x_1)(\sin(\theta_1) - \sin(\theta_2)) \tag{5.14}$$

In the specular direction, $\Delta\phi = 0$ for all sources, and the wavelets will interfere constructively, which gives a strong field scattered in the specular direction. Away from the specular direction, the phase difference becomes larger and destructive inference will lead to less energy scattered.
Thus, a smooth, infinite plane will lead to a wave scattered in the specular direction only. Smooth, finite surfaces will have a strong scattering around the specular direction, with the main lobe's width dependent on the size of the surface relative to the wavelength. For rough surfaces, where $h_1 \neq h_2$, the interference of the waves will depend on the surface height. If the phase difference is smaller than π the surface will be seen as virtually smooth. If not, destructive interference will occur, reducing the amplitude of the scattered field in the specular direction. The influence of surface roughness on the scattered field is summarized in figure 5.4.

The apparent roughness of a surface is thus dependent on the wavelength of the radar observing the target and has major consequences on the resulting SAR image. A smooth surface with regards

to the observing frequencies will scatter energy mainly in the specular direction, while a rough surface scatters electromagnetic waves in all directions. Because of the waves interferences that are due to the roughness of the surface, a SAR image of a rough surface will have a random-like variation of power, which is called speckle (Goodman, 1976).

5.4 Summary

A rough surface can thus be described mainly by two parameters: its RMS height and its correlation length. We can consider in a simple way that the RMS height describes the variation of height in the vertical direction, while the correlation length describes the variation of height in the horizontal direction. Using the correlation between white noise and a Gaussian filter, a random rough surface generator was implemented and inserted into SPRATS in order to generate rough surface that will be used to study the radar's return. The rms height and the correlation length have major influences on the resulting SAR images of a rough surface, as a rough surface scatters energy in a different way that a smooth surface would.
Thus, in order to simulate the scattering of electromagnetic in a small body geometry, realistic asteroid surfaces need to be generated, so the RMS height and correlation of real asteroid surfaces must be investigated

Chapter 6

Asteroids' surfaces definition

In order to simulate the radar signal scattered by the surface of sub-kilometric asteroids, a precise knowledge of their typical surface is necessary. Then, we can set the digital terrain model (DTM) of the asteroids' surfaces which we will use in our simulations and have a more precise glimpse of the domain of validity the reviewed scattering models will have to cover. As detailed in the introduction, few small asteroids were closely observed: one of them is the asteroid Itokawa, explored in 2010 by the spacecraft Hayabusa (JAXA).

6.1 Hayabusa and Itokawa

The Hayabusa mission was developed by the Japan Aerospace Exploration Agency (JAXA) to return an asteroid's sample to the Earth, and targeted the asteroid 25143 Itokawa, a small Apollo asteroid. Hayabusa embarked several instruments to perform a global characterization of Itokawa, among which a LiDAR (LIght Detection And Ranging). The LiDAR uses ultraviolet, visible, or near-infrared light to image objects, in a similar way that a radar does with radio-frequency waves. It illuminates the target with pulsed light and registers the reflected pulses. Digital 3-D representations of the target can then be computed by converting the delay of the reflected light to the distance between the instrument and the target. The purpose of the Hayabusa's LiDAR was to establish the distance between the spacecraft and the surface of the asteroid but was also used to analyze Itokawa's surface topography.

The LiDAR's results were interpreted by Mazrouei et al. (2014) and Barnouin-Jha et al. (2008). It resulted that Itokawa, shown in figure 6.1 is a small asteroid of $535 \times 294 \times 209$ m, with a surface of 0,4011 km^2, a low density of 1,9 $g.cm^{-3}$, a porosity of 40%, and is thus considered a rubble pile. Itokawa is composed of two distinct attached masses, called the Head and the Body, both easily

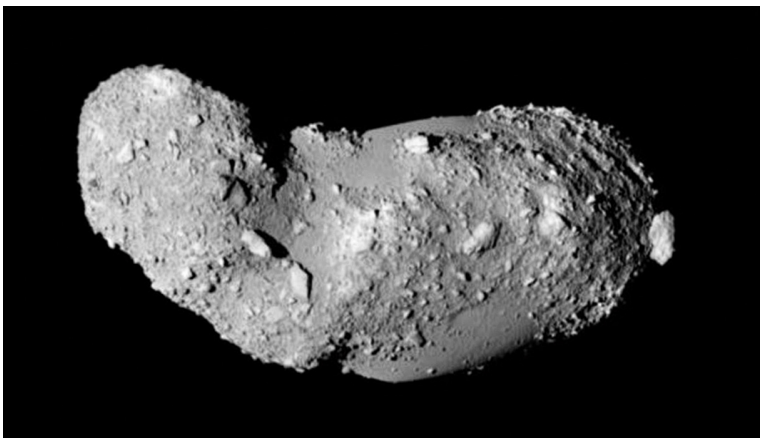

Figure 6.1: Generic view of the asteroid Itokawa (Mazrouei et al., 2014).

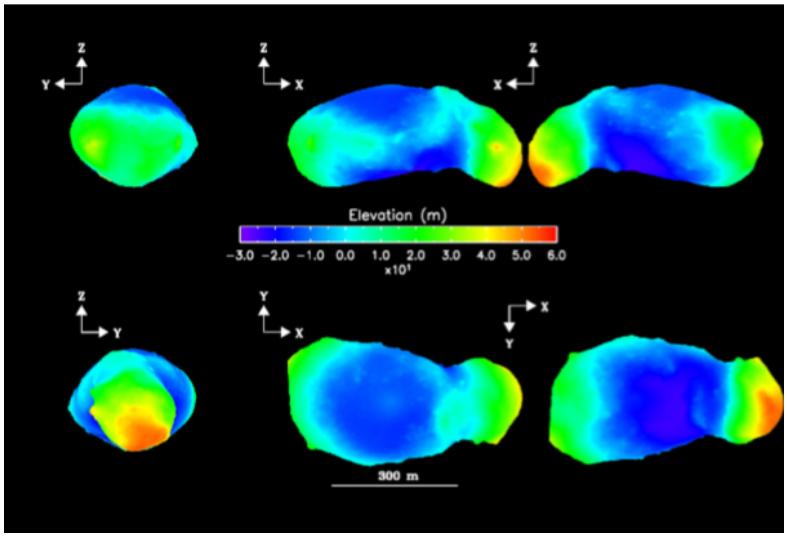

Figure 6.2: Itokawa's elevation compared to a local gravitational equipotential surface (Barnouin-Jha et al., 2008).

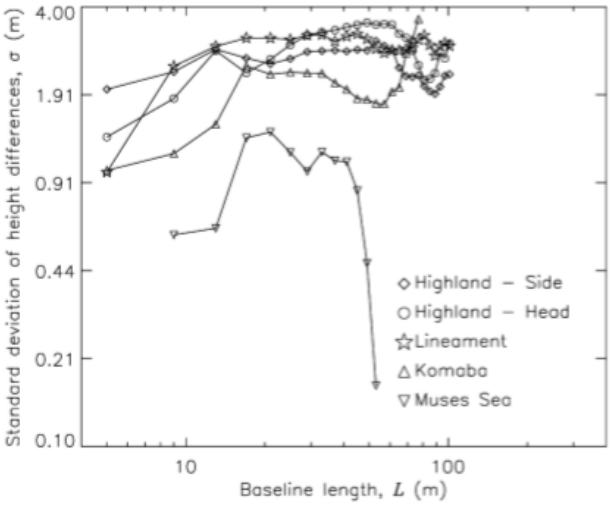

Figure 6.3: RMS height of the different regions of Itokawa (Barnouin-Jha et al., 2008).

identified in figure 6.1. The whole asteroid is covered by regolith, which is expected to be about 3 meters deep in the smoothest areas of the asteroid.
80% of Itokawa's surface is rough terrain dominated by large boulders, that are called the Highlands. The 20% remaining are smooth surfaces called the Lowlands. The Highlands are regions with higher elevation compared to a local equipotential surface such as represented in figure 6.2, and a much thinner regolith depth than the Lowlands.

6.2 The Highlands

Itokawa's Highlands were studied by Hayabusa's LiDAR, which followed the trajectory depicted in figure 6.4. The LiDAR results are detailed in figure 6.5. The Highlands were found to be rough surfaces, dominated with large rocky blocks, larger than 6 meters. Their typical variation in elevation ranges from 2 – 4m over small lateral distances as presented in figure 6.5, while broader variations of height on the Highlands reflect either the presence of a large block or a non-compensated motion of the instrument footprint across the surface of the asteroid. Thus we can consider that the Highlands have a metric RMS height. In total, 1430 blocks were identified on the entire asteroid's surface, distributed all over Itokawa as depicted in figure 6.6. Their distribution is dependent on their size, as shown on

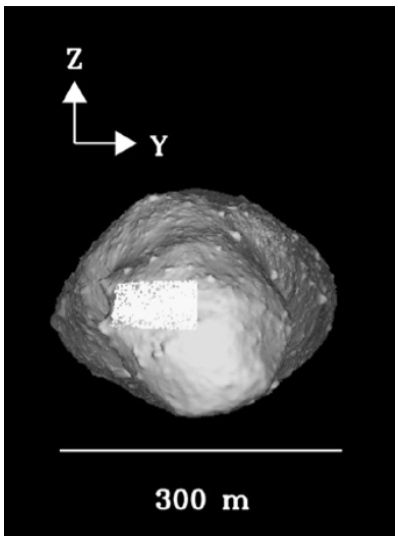

Figure 6.4: Surface of the Highlands studied by the LiDAR (Barnouin-Jha et al., 2008).

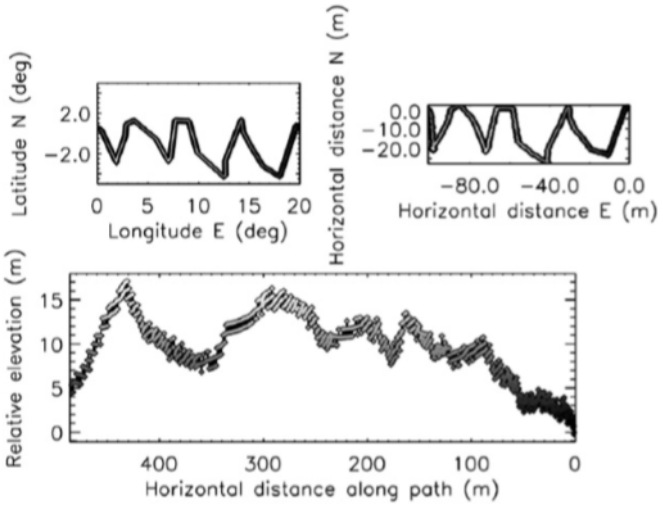

Figure 6.5: LiDAR measurements relative to Itokawa's gravity field on the Highland (Mazrouei et al., 2014).

figure 6.7, with the larger block, Yoshinodai, being 27 meters large. On a smaller scale, the Highlands are also made of particles, which size was detected by the LiDAR if larger than tens of centimeters. Figure 6.5 shows the large-scale roughness of the Highlands with a meters size correlation length, combined with a smaller-scale roughness of less than one meter, with a correlation length of the order of the centimeter.
The few smooth regions of the Highlands are craters, of 2 meters deep maximum, and of a diameter of 20 meters maximum. Their flat floor is covered by smooth regolith and surrounded by blocks typical of the Highlands. The RMS height of the areas is estimated to be about 2.2 meters in the Tsukuba region (represented in figure 6.8), as depicted in figure 6.3, with the instability of the instrument to be taken into account.

6.3 The Lowlands

The Lowlands are flat and smooth regions of Itokawa. They are areas with the lowest elevation, as illustrated in figure 6.2. Because of their low elevation, the regolith is filling these areas in priority, which explains their smoothness, but probing in the regolith depth could reveal more boulders. The Lowlands have small-scale and almost no medium-scale roughness and the central regions of the

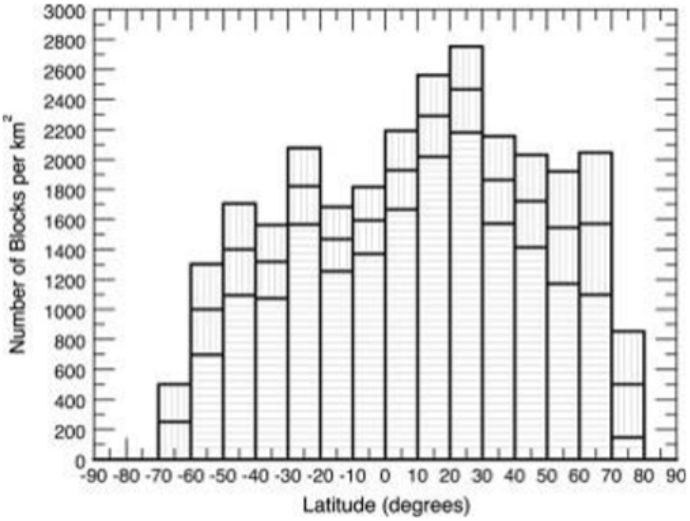

Figure 6.6: Block distribution on Itokawa (Mazrouei et al., 2014).

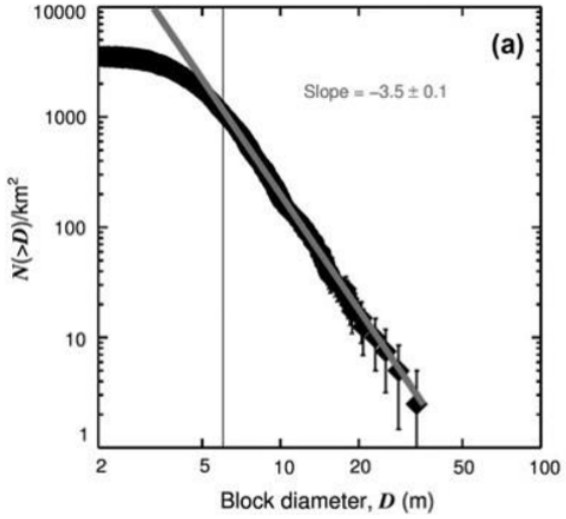

Figure 6.7: Itokawa block size distribution with respect to diameter (Mazrouei et al., 2014).

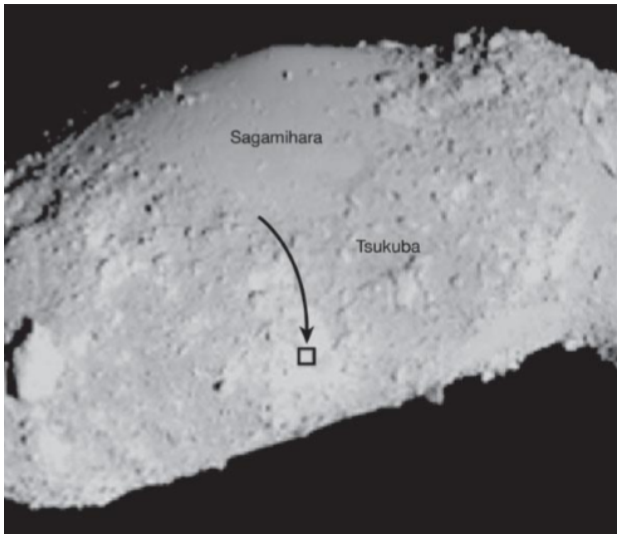

Figure 6.8: Tsukuba region on Itokawa (JAXA).

Lowlands are devoid of boulders. Over short distances, the variation in height is detected to be 0.5 m, as depicted in Figure 6.9 and figure 6.10. However, the LIDAR precision is estimated to be 1 meter (Mukai et al., 2002), so we will consider that these surfaces have a correlation length of about tens of centimeters. As the borders of the Lowlands are approaching, the variation of the height reaches 1 to 2 meters, as pictured in figure 6.9, due to an increasing number of Highland's boulders. The correlation length of the roughness is estimated to be a few tens of centimeters (Abe et al., 2006).

6.4 Summary

From this study of the surface of Itokawa, the roughness parameters of the Highlands and the Lowlands are used to model rough surfaces representative of the different areas of the asteroids. A third surface is modeled as well, representative of the change of roughness that occurs at the frontier between the Highlands and the Lowlands.

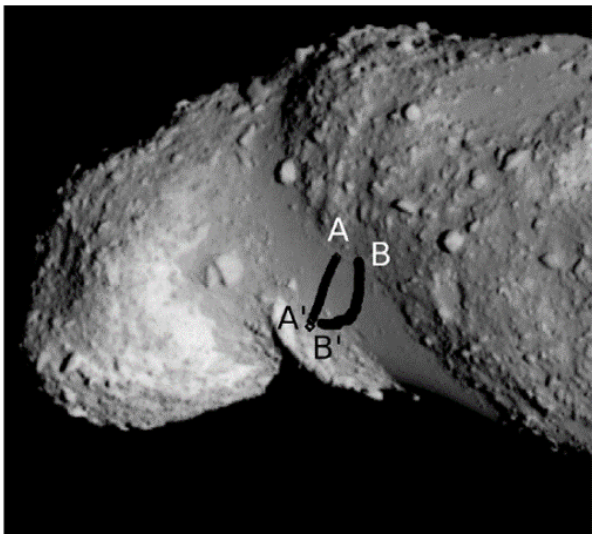

Figure 6.9: LIDAR's path on Itokawa's Lowlands (Barnouin-Jha et al., 2008).

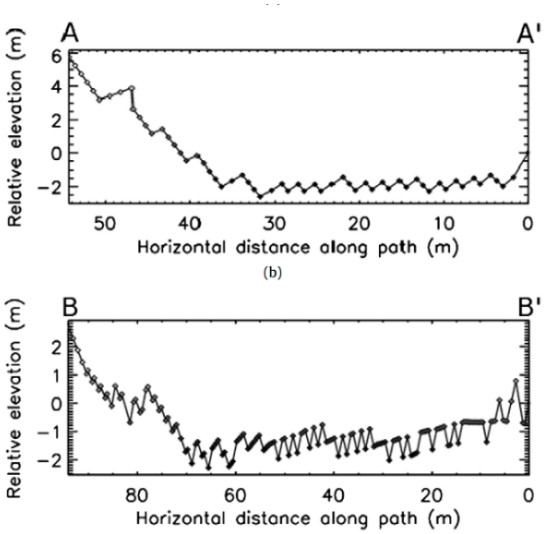

Figure 6.10: LIDAR's measurements on Itokawa's Lowlands (Barnouin-Jha et al., 2008) compared to a local gravitational equipotential surface

6.4.1 The Highlands

The roughness parameters used to generate the Highlands rough surface are presented in table 6.1. To this large scale roughness, a small scale roughness will be added with the parameters described in table 6.2. In order to avoid any edge effects, windowing will be applied to the patch's roughness and its permittivity. In this way, the variation of height and the permittivity of the borders of the patch are respectively equal to zero and one. The resulting Highland patch constituted of both roughness scales is presented in figure 6.11.

6.4.2 The Lowlands

The roughness parameters used to generate the Lowlands DTM are presented in table 6.3. In order to avoid any edge effects, windowing will be applied to the patch's roughness and its permittivity. In this way, the variation of height and the permittivity of the borders of the patch are respectively equal to zero and one. The resulting Lowland patch is presented in figure 6.12.

6.4.3 Mix of roughness

The Lowlands and Highlands are two distinct areas on Itokawa, but as some region on Itokawa constitute progress from Lowlands to Highlands, we need to model a surface with varying roughness. To represent these areas, we consider a terrain where the roughness varies from an almost completely

Table 6.1: Highlands' rougher scale physical parameters used for the generation of the DTM.

RMS height	2.2 m
Correlation Length	6 m
DTM size	20m
Maximum Permittivity	3
Continuity assured by	Hanning Weighting

Table 6.2: Highlands' smaller scale physical parameters used for the generation of the DTM.

RMS height	15 cm
Correlation Length	1 m
DTM size	20m
Maximum Permittivity	3
Continuity assured by	Hanning Weighting

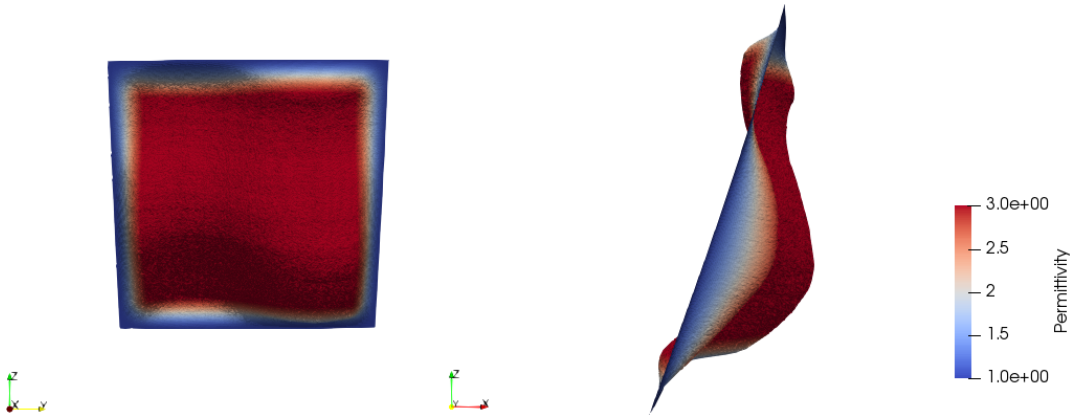

Figure 6.11: Highland DTM of 20mx20m. View from front (left) and side (right).

Table 6.3: Lowlands physical parameters used for the generation of the DTM.

RMS height	1.5 cm
Correlation Length	10 cm
Maximum Permittivity	3
Continuity assured by	Hanning Weighting

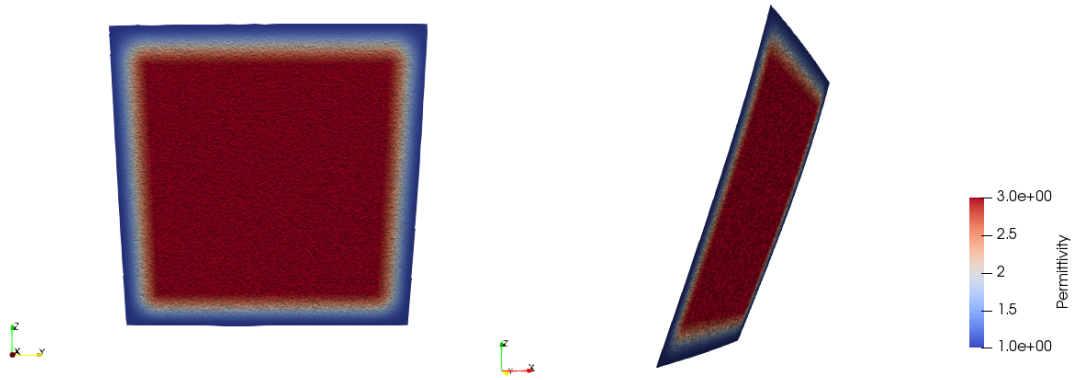

Figure 6.12: Lowland DTM of 20mx20m. View from front (left) and side (right).

Table 6.4: Mixed terrain parameters used for the generation of the DTM.

RMS height	15 cm
Correlation Length	10 cm
DTM size	20m
Maximum Permittivity	3
Continuity assured by	Hanning Weighting

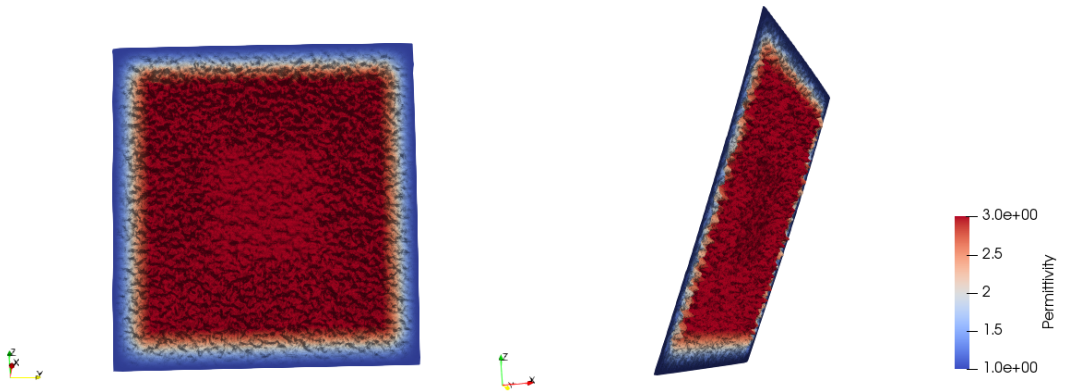

Figure 6.13: DTM of 20mx20m. View from the front (left) and side (right).

smooth surface to a rougher one. The resulting surface parameters are summed up in table 6.4. In the center of the area, the RMS height is reduced by 75% which makes it almost smooth. In order to avoid any edge effects, windowing will be applied on the patch's roughness and on its permittivity. In this way, the variation of height and the permittivity of the borders of the patch are respectively equal to zero and one. The resulting patch is presented in figure 6.13

The rough surface scattering model selected needs to be efficient for rough surfaces covered in with

boulders, as well as for smoother surfaces composed of centimeter-sized particles. The RMS height of the different surfaces of Itokawa are summed up in figure 6.3, with different baselines of the LIDAR for different regions: the rough Highlands, the smooth Lowlands (for the Muses C region), and a crater, Komaba, which gives us a good insight into the roughness variation between the Lowlands and the Highlands. The main difficulty the selected scattering model will have to overcome is to correctly reconstruct both roughness scales, since analytical scattering models are often adapted to one type of roughness. The boulders may be also challenging to correctly reconstruct because of their abrupt slope.

After this study of Itokawa's surface, we have an idea of the roughness of a standard asteroid's surface. With this knowledge, we can review the different scattering models available, which would be suited to model the field scattered by our DTM.

Chapter 7

State of the art of rocky surface scattering models

Wave scattering by rough surfaces is a major issue in different scientific domains such as medicine, optics, acoustics, communication, and remote sensing. Exact computation of the scattering problem is often unachievable because of the numerical complexity of the problems, especially in the realistic 3D geometry. Thus, faster but approximate of the solutions of the scattering problem began to be developed and compared with the results of numerical, exact solutions of the Maxwell equations, such as the method of moments (MoM) (Gibson, 2014) or the finite domain time difference FDTD (Schneider, 2010).

7.1 Analytical scattering models

Analytical models are approximate models derived from the Maxwell equations. Even if their limited domain of validity, the lack of precise characterization of it, and the long computation times that are required for evaluating high expansion terms are major drawbacks that can limit their application, these models have been largely developed and applied to solve the scattering problem. Indeed, more than twenty analytical scattering models can be found in the literature, but only four will be presented here.

In this review, we focus on the solving of Maxwell's equations at a random rough surface with analytical methods. T. M. Elfouhaily et al. (2004) reviews some analytical methods, which we will present and sort from the most approximate and fast to the most accurate and computationally intensive.

7.1.1 Definitions and notations

In the following, we will note :

- $\vec{A}$ a vector
- A its norm
- $\hat{A}$, a unitary vector

We consider a surface Σ separating the vacuum from a homogeneous medium associated with a given permittivity $\epsilon \neq 1.0$. We work in the Cartesian coordinate system (x, y, z), with the $\vec{z}$-axis directed upward, and the surface Σ is represented by $\zeta(\vec{r}) = \zeta(x, y)$. The position vector describing the position of a point in 3 dimensions is $\vec{R} = (\vec{r}, z)$.
We consider a surface Σ separating the vacuum from a homogeneous medium associated with a given permittivity $\epsilon \neq 1.0$. We work in the Cartesian coordinate system (x, y, z), with the $\vec{z}$-axis directed upward, and the surface Σ is represented by $\zeta(\vec{r}) = \zeta(x, y)$. The position vector describing the position of a point in 3 dimensions is $\vec{R} = (\vec{r}, z)$.

We consider that an electromagnetic wave propagating downwards with a wave vector $\vec{K_0} = (\vec{k_0}, \vec{q_0})$ and wave number $K = \frac{2 \cdot \pi}{\lambda}$ is incident on the surface and gives rise to upward scattered waves with wave-vectors in the direction $\vec{K} = (\vec{k}, q)$.

The vectors $\vec{k_0}$ and $\vec{k}$ are the horizontal components of the incident and scattered waves, while q_0 and q are the vertical components, as presented in figure 7.1. They are linked by the relation :

$$k^2 + q^2 = k_0^2 + q_0^2 \tag{7.1}$$

We note :

$$Q_H = \vec{k} - \vec{k_0} \tag{7.2}$$

$$Q_z = q - q_0 \tag{7.3}$$

The field scattered away from the surface is written $\vec{E_s}(\vec{R})$, where $\vec{R}$ is the position of the radar antenna. $\vec{E_s}(\vec{R})$ is related to the incident field $\vec{E_0}$ through an operator called the scattering amplitude $\mathbb{S}$. For a unitary field in the far field approximation (R $\rightarrow \infty$), we have :

$$\vec{E_s}(\vec{R}) = \frac{e^{ikR}}{iR} \cdot \mathbb{S}(\vec{K}, \vec{K_0}) \cdot \hat{E_0} \tag{7.4}$$

The scattered field is decomposed over a polarization basis, usually HH, VV, VH, and HV. $\mathbb{S}(\vec{k}, \vec{k_0})$ then becomes a 2x2 matrix. With this definition, the scattering amplitude takes the dimension of a wavelength in meters. An implicit time dependence $e^{i\omega t}$ is always assumed.

Physically, the scattering amplitude has to satisfy 3 fundamental geometrical properties: the reciprocity, which is the time-reversal invariance of the wave, the shift invariance, and the tilt invariance, which express the frame independence of the scattering mechanism. Different mathematical simplifications in the calculation of the scattering amplitude could lead to a scattering model that does not fulfill these criteria, thus their validation or not can lead to a good hint about the precision of the scattering models studied. These 3 properties are detailed below:

- The reciprocity is the time-reversal invariance of the wave in the harmonic regime, as presented in figure 7.2.

$$\mathbb{S}(\vec{K}, \vec{K_0}) = \mathbb{S}^T(-\vec{K_0}, -\vec{K}) \tag{7.5}$$

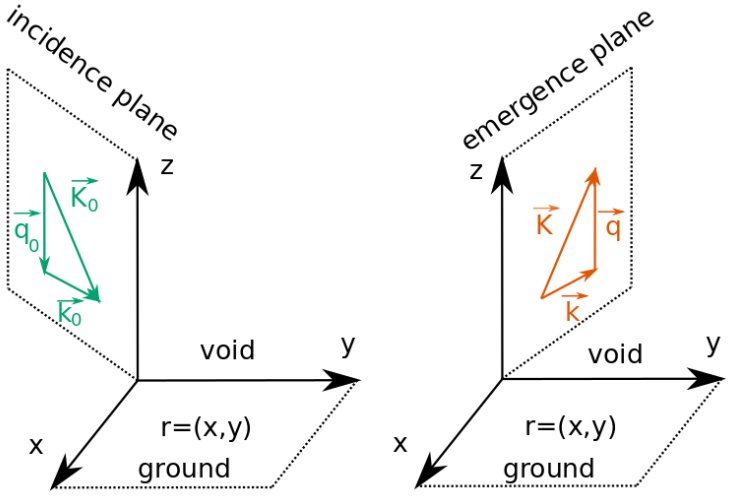

Figure 7.1: Geometry of the scattering problem.

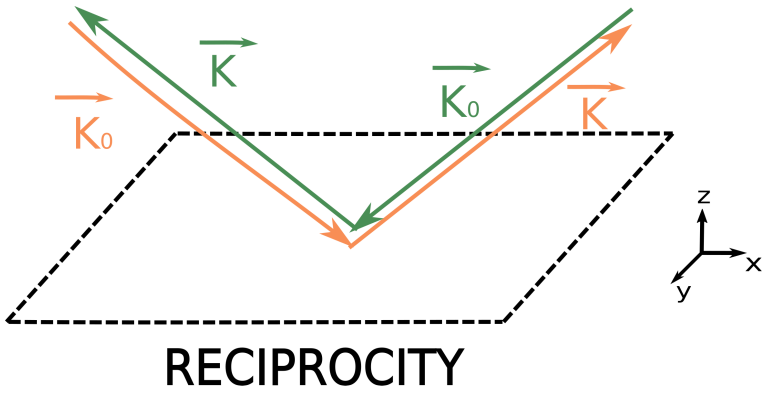

Figure 7.2: Illustration of the reciprocity.

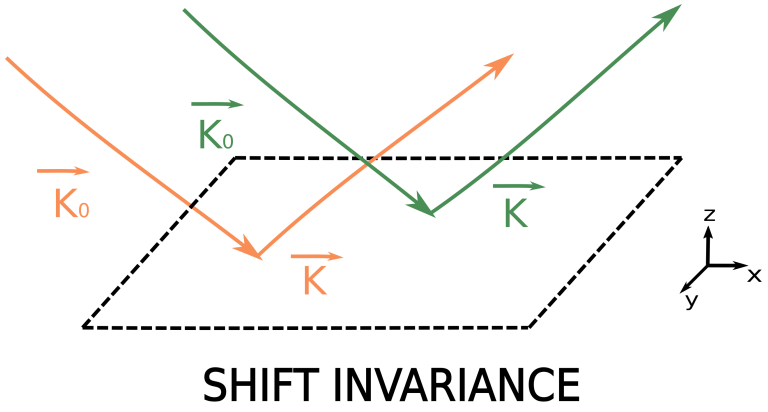

Figure 7.3: Illustration of the shift invariance.

- The shift-invariance is the phase-shifting (or delay, in the time domain) resulting from horizontal and vertical translations of the surface, as pictured in figure 7.3.

$$\mathbb{S}(\vec{K},\vec{K_0})_{|h(r-d)+D} = e^{-iQ_H d}e^{-iQ_z D}\mathbb{S}(\vec{K},\vec{K_0}) \tag{7.6}$$

- The tilt invariance is the fact that the scattering amplitude should not depend on the choice of the reference plane and the coordinate system related to it.

$$\mathbb{S}(\vec{K},\vec{K_0})_{|\mathbb{R}(\Sigma)} = \mathbb{S}(\vec{\tilde{K}},\vec{\tilde{K_0}})_{|\Sigma} \tag{7.7}$$

  Where $\mathbb{R}$ is a rotation of the surface and $\vec{\tilde{K}}$ and $\vec{\tilde{K_0}}$ are the horizontal components of the inversely rotated wave vectors $\mathbb{R}^{-1}(\mathrm{K})$ and $\mathbb{R}^{-1}(K_0)$. In general, we only use the tilt invariance to the first order.

$$\mathbb{S}(\vec{K},\vec{K_0})_{|h+ar} = \mathbb{S}(\vec{\tilde{K}},\vec{\tilde{K_0}})_h + O(a^2) \tag{7.8}$$

  With $\vec{\tilde{K}} = \vec{k} + \vec{q_k}\vec{a}$ and $\vec{\tilde{K_0}} = \vec{k_0} - \vec{q_0}\vec{a}$

  This last property is difficult to check analytically thus it is often checked only in the limit of small roughness.

Besides these physical properties, the scattering models ideally need to satisfy seven other criteria in order to be fully applicable. They are summed up below, along with the three previous criteria we just described. Thus, an ideal scattering model must be :

1. Applicable to dielectric types of surfaces

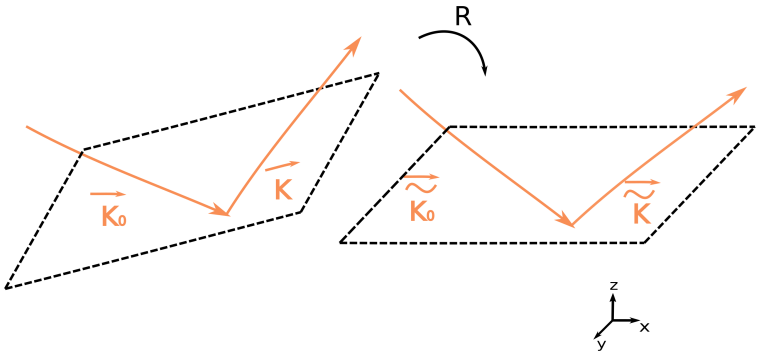

Figure 7.4: Illustration of the tilt invariance.

2. Applicable to 2D surfaces
3. Reciprocal
4. Shift invariant
5. Tilt invariant
6. Numerically fast and stable
7. Not restricted to large correlation lengths
8. Not restricted to small surface height
9. In agreement with the small frequency limit (SPM1 limit, see below)
10. In agreement with the high frequency limit (KA limit, see below)

However, in reality, the scattering models do not satisfy all of these criteria because of the approximations carried out to compute them. An investigation on the realization of each of these criteria can thus be investigated to assess the quality of the model.

All the investigated scattering models can as well be regrouped in families, depending on the type of approximation carried out to obtain them.

7.1.2 Families of Approximation

All surface analytical scattering theories can be classified in these two families :

- The first family works by estimating a closed (first or second kind) integral equation of the surface field or its derivatives.
- The second family computes the scattering amplitude directly by setting requirements we wish the scattering amplitude to satisfy.

Different techniques are then applied to derive the approximation, either on the scattering amplitude or on the surface currents, depending on the family under study :

1. The approximation is found by making hypotheses on either the surface current or on the scattering amplitude. In this way, the structure of the surface currents or the scattering amplitude is guessed by making physical or geometrical assumptions (e.g. supposing that a geometrical parameter is small, making a Taylor expansion and neglecting the higher orders terms, or writing the surface current or the scattering amplitude as an unknown multiplicative term of a reference problem). The unknowns of the model are found by setting boundary limits.

2. The results of the model when $f \to 0$ are set equal with one reference model, the Small Perturbation Method.

3. A particular Green function is used for computing the field, such as the Weyl representation or half-spaces Green functions. This allows making some simplifications for the computation or to enforce different properties.

4. A Fredholm integral equation of the first kind $f(x) = \int_a^b K(x,t)\Phi(t)dt$, where K(x,t) is called the kernel, and $\Phi(t)$ is an unknown function to be solved for, is used to express the result.

5. A Fredholm integral equation of the second kind $\Phi(x) = f(x) + \lambda \int_{-\infty}^{\infty} K(x,t)\Phi(t)dt$ is used to express the result.

6. The stationary phase approximation is used. We consider a function of the type $F(x,t) = \int e^{-ik\psi(\omega)}F(\omega)d\omega$, $k \to \infty$, where $F(\omega)$ is slowly varying. The rapid oscillations of $e^{-ik\psi(\omega)}$ over most of the range of integration means that the integrand averages to almost zero. Exceptions to this occur only at points where $\psi(\omega)$ is stationary. The integral can therefore be estimated by finding all the points where $\psi(\omega)$ has a zero derivative, evaluating the integral in the neighborhood of each of these points, and summing the contributions. For high frequencies, this allows a simplification of the computation and thus a faster and simpler implementation of the model.

We will now present the different scattering models investigated. The Small Perturbation Method and the Kirchhoff Approximation are two classical, simple reference methods, able to model the electromagnetic field scattered by surfaces with a small scale, and a large scale roughness, respectively. However, they are applicable to the two extremes of the roughness domains. In order to have models covering surfaces for which roughness scales are less extreme, and thus which include more natural rough surfaces domains, unifying models were later developed such as the Small Slope Approximation or the Weighted Curvature Approximation.

7.1.3 The Small Perturbation Method

The Small Perturbation Method (SPM) is the oldest method in scattering from rough surfaces. It computes the electromagnetic field scattered by a surface defined as a perturbation in height of a reference, often plane, surface.

History

The Small Perturbation Method was first implemented by Rayleigh (1896) to model the scattering of acoustic waves from a surface altered with small height perturbations. Rice (1951) updated the model and developed the first and second order of the model for one-dimensional conducting surfaces. Further works have been devoted to expanding further orders of the model to all surfaces, such as Demir et al. (2003) who developed the work described in J. T. Johnson (1999) to expand the model up to the fourth order and higher on two-dimensional dielectric surfaces. The SPM is still notably used to derive the electromagnetic scattering of natural stratified structures (Afifi et al., 2012), (Wu & Zhang, 2015), (Sanamzadeh et al., 2017). As any models described by an expansion of a characteristic of the surface, the SPM is more accurate when its higher orders are derived, but becomes heavier to compute. SPM is denoted SPMn, where n indicates the maximum order implemented.

Description

The principle of SPM is to write the scattering amplitude as a Taylor expansion of the surface height from a flat reference surface, such that (A. Voronovich, 1999) :

$$\begin{aligned}\mathbb{S}(\vec{K},\vec{K_0}) = V_0(\vec{K},\vec{K_0})\delta(\vec{k}-\vec{k_0}) + \int\int C_1(\vec{K},\vec{K_0},\vec{r_1})h(\vec{r_1})d\vec{r_1} \\ + \int\int C_2(\vec{K},\vec{K_0},\vec{r_1},\vec{r_2})h(\vec{r_1})h(\vec{r_2})d\vec{r_1}d\vec{r_2}\end{aligned} \tag{7.9}$$

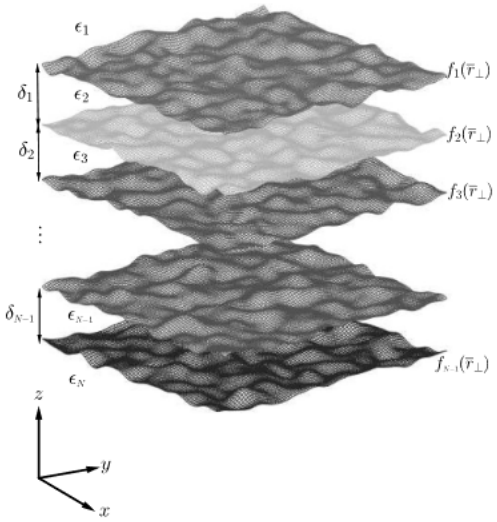

Figure 7.5: Geometry of Sanamzadeh et al. (2017) multilayer structure with random rough interfaces.

With $V_0(\vec{K})$ being the reflection coefficient, in which $\mathbb{S}$ reduces to in the absence of roughness, and C_1 and C_2 are unknown coefficients used to describe the first and second order of the model.

Limits

The SPM assumes that the representation of the electromagnetic field in terms of outgoing waves is valid on the surfaces. Thus, the SPM neglects multiple scattering. The SPM is also only valid for small perturbations compared to the wavelength : when the Rayleigh parameter, $\mathrm{R}_a = \mathrm{k}\sigma_h \cdot cos(\theta) \ll 0.3$ (Ogilvy & Merklinger, 1991), or else the hypothesis of small h necessary to set the expansion fails. Thus, the SPM is regarded as a true solution of the scattering problem for low frequencies.

Results

Sanamzadeh et al. (2017) implemented the second-order of the small perturbation method to a multilayer configuration, consisting of multiple small rough surfaces, as presented in figure 7.5. He computed the coherent and incoherent fields scattered and transmitted by each layer, which have a weak contrast between them, a random layer thickness and randomly generated permittivity profiles. Sanamzadeh then computed reflected and transmitted powers of the configuration to show that the SPM2 kernel functions obey energy conservation independent of the roughness statistics of the surface, and found out that SPM2 is adapted to computing scattering from layered rough surfaces, when a large number of rough interfaces have a small roughness.

The SPM is thus a fast and simple model but fails to fulfill most scattering amplitude physical criteria (as presented in the summary in section 7.2) and is limited to the narrow case of small roughness. Thus, additional models can be investigated, which could be more adapted to the surfaces we are interested in.

7.1.4 The Kirchhoff Approximation

The Kirchhoff Approximation (Ogilvy & Merklinger, 1991) is the second oldest method and one of the most largely used scattering model. The model considers that the field on the surface is equal to the one produced by a tangent plane at the same point of the surface, as reviewed in Beckmann and Spizzichino (1987).

History

The Kirchhoff approximation was initially developed as a solution to acoustic or electromagnetic scalar wave scattering from periodic or rough surfaces. In 1956, Meecham (1956) wrote the Kirchhoff approximation as the solution of the zeroth iteration of the integral equation governing the surface current, when considering scattering of scalar acoustic waves or electromagnetic waves from perfectly conducting surfaces. In 1963, the model was validated by comparing its results with observations, which allowed to observe and understand the effect of the surface roughness on the scattered field. Later, Bass and Fuks (1979) included in the model surface shadowing, as well as multiple scattering by considering perturbation theory, and Fortuin (1970) compared the Kirchhoff approximation to observations of sea surface scattering to estimate its domain of validity. Fung and Eom (1981) compared the Kirchhoff results to computer-simulated results for a perfectly conducting surface with λ= 4.5 m and λ= 9.5 m and found a correct reconstruction of the backscattering coefficient. Then, E. I. Thorsos (1988) provided an exact solution for Meecham's equations and computed the scattered far field intensity for 50 randomly generated surfaces, compared with the Kirchhoff results, and refined the domain of applicability of the method. Liszka and McCoy (1982) later refined the model and used the stationary phase approximation to provide a high frequency solution of the Kirchhoff approximation.

The Kirchhoff method is still largely used today, such as Tabatabaeenejad et al. (2013), who computed an analytical solution for coherent scattering of electromagnetic waves from a two-layer structure and especially with the development of the facet method, such as Zhang et al. (2011) who developed a feasible model to evaluate the scattered field by large 2D oceans, or Nouvel (2003) and Berquin et al. (2015), who computed the electromagnetic field scattered by the lunar and martian surfaces.

Description

The Kirchhoff Approximation is an approximate solution of the Maxwell equations, valid for locally smooth surfaces and is also known as the tangent plane approximation (TPA) and physical optics (PO) in its high-frequency form. For each point of the surface, the surface is replaced by its tangent plane and thus the electromagnetic field, computed by applying the Snell-Descartes law on the tangent plane, is reflected or transmitted by the plane in the specular direction.
This approximation is exact for infinite, smooth, plane scatterers, but is only an approximation for scatterers that are finite-sized, non-planar, or too rough. Used in conjunction with an integral formula, it gives an expression for the scattered field in terms of the approximated surface field. This model yields the geometric optics limit, which is the limit of rough surface scattering for high frequencies, but not the low frequencies limit, which is the SPM limit (Guerin & Sentenac, 2004).
The facet method uses the Kirchhoff Approximation by approximating the surface by planar facet and computes the field scattered by each of the facets.

Limits

The Kirchhoff Approximation makes several assumptions in its derivation :

- The incident wave is plane.
- No point on the surface has an infinite gradient.
- The surface can be locally approximated by a smooth plane.
- No conservation of energy was stated. Propagating modes such as surface waves and multiple scattering effects are ignored.

Plus, KA is a local approximation, which means that the field at a point of the surface does not depend on other points on the surface. The approximation will also be poor near-surface edge, where diffraction will not be adequately modeled: thus smaller surfaces will lead to greater inaccuracies. Thus, the Kirchhoff theory is regarded as a high frequency approximation. Indeed, the smaller λ, the smaller the distance over which the surface is restricted to being quasi-planar, and the more accurate the approximation is.

Results

Berquin et al. (2015) used the facet method with KA to simulate the electromagnetic field scattered by planetary surfaces, and thus to discriminate the surface echoes from subsurface echoes in real radar data.
First, Berquin reproduced results obtained with LRS (Lunar Radar Sounder, described in Ono et al. (2009)), which studied the surface and subsurface of the Moon. Using DTM of the Moon and considering that the surface and subsurface permittivity were constant, the simulation of LRS data was able to reconstruct radar signals accurately enough from a qualitative point of view in order to reproduce the main structures, such as seen in figure 7.6. However, the real data seem to contain a diffused signal which was not reproduced by the simulation. It is likely that this signal is due to surface and subsurface scattering occurring at much smaller scales than the terrain resolution.
The same work was done for the SHARAD instrument (Seu et al., 2007) that studied the surface and the shallow subsurface of the Martian surface. The surface and subsurface permittivity were also assumed to be constant over the areas in both cases. Although the main structures were reproduced, as seen in figure 7.6, the results obtained with the SHARAD instrument are not as satisfying as the ones with LRS instrument. This can be explained by a coarser terrain resolution with regards to the signal wavelength as well as possible atmospheric effects and an overall smaller signal to noise ratio.

The Kirchhoff approximation is thus a model based on a concept easy to implemented that fulfills more scattering amplitude physical criteria than the SPM, as presented in section 7.2, which is why it is such a popular model. However, the Kirchhoff approximation covers only the scattering of large scale roughness. Thus we will investigate newer, more complex models, and examine their domain of validity.

7.1.5 The Small-Slope Approximation

The Small-Slope Approximation, developed in A. Voronovich (1994) is a unifying theory set up to bind the Kirchhoff approximation and the Small Perturbation Method. It requires the slope of the surface to be sufficiently small to write the wave scattering amplitude as an expansion in slope : $\nabla h \ll \frac{q}{k}$. SSA uses the structure of the Kirchhoff approximation so that the scattering amplitude satisfies the shift invariance property and associates it with the limits of the SPM.

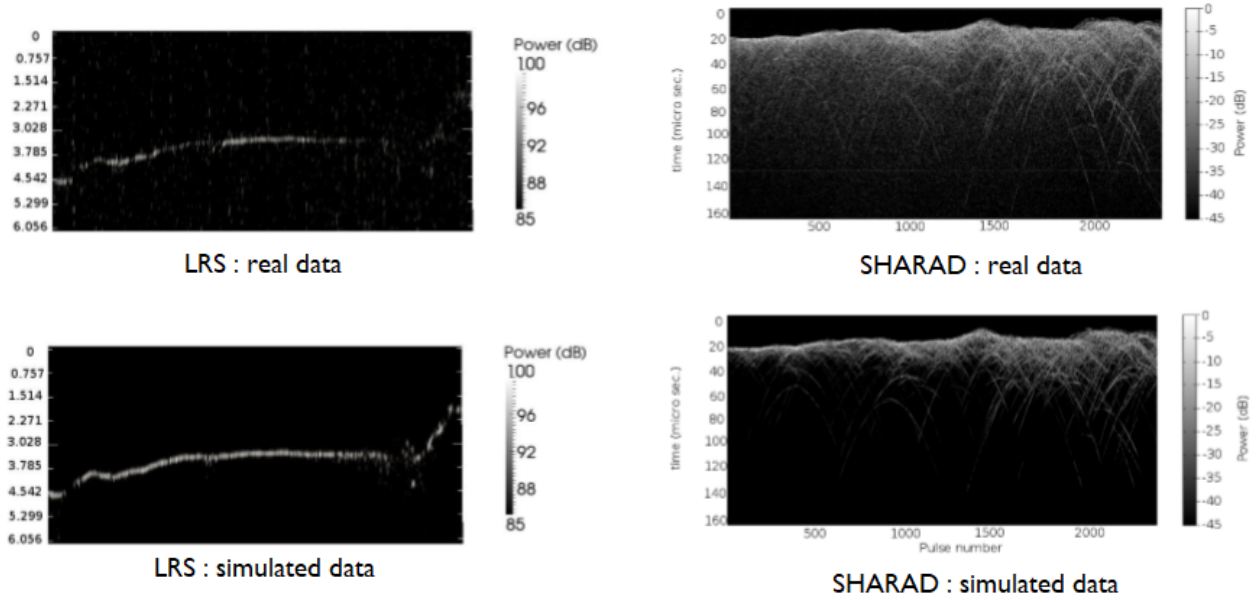

Figure 7.6: Comparison of LRS (left) and SHARAD (right) real (top) and simulated (bottom) data (Berquin et al., 2015).

History

The KA and the SPM have long been two simple and efficient models but covering two distinct domains of validity. Thus, several models have been designed with the objective to overcome the limits of the KA and the SPM and to bind them, such as the Two-Scale Model (TSM) developed by Wright (1968) to better model the sea clutter echo. However, these unifying models have the drawback of setting an arbitrary parameter that divides the roughness into two classes: large-scale and small-scale roughness. Because that parameter cannot be uniquely derived, its choice affects the results. The Small-Slope Approximation (SSA) was developed by A. Voronovich (1994) to overcome this limit as it was made to be a continuous transition between the Kirchhoff Approximation and the SPM. Thorsos et al. (1995) detailed the method derivation and compared the SSA results with the exact field scattered by one-dimensional surfaces with Gaussian statistics and spectrum. He found that the SSA is accurate for surfaces having small to moderate slope angles. The SSA is still used today to model the electromagnetic field scattered by ocean surfaces such as in Voronovich and Zavorotny (2012), Guérin and Johnson (2015) and H. Zhang et al. (2016).

Description

The Small-Slope Approximation is based on a Taylor expansion of the slope of the surface. In the case of a Gaussian rough surface, the slope parameter is defined as the ratio of the RMS height to the surface correlation length. Treating the slope of the surface allows considering both small and large scales roughness, providing that the surface has small slopes. Voronovich uses the shape of the Kirchhoff Approximation scattering amplitude, and uses the kernel in the integral to make the SSA coherent with the SPM at low frequencies. The kernel is further modified to impose the geometrical properties we want the scattering amplitude to satisfy a priori. Thus, as the SSA replaced the Kirchhoff kernel by that of the SPM1, it recovers by construction the low frequency limits, and it respects as well the shift invariance and reciprocity but does not recover any longer the Kirchhoff limit. In practice, the slope expansion is performed at the lowest two orders only, the higher order being too complex to compute for the accuracy it provides. The second order of SSA (SSA-2) was shown to reproduce the Kirchhoff limit and to feature the tilt invariance. However, it is very cumbersome to implement numerically due to the complicated second-order kernel and due to numerical instability in the evaluation of the double Fourier integral in the kernel. In the following, SSA is denoted SSA-n, where n indicates the maximum order implemented.

Limits

The validity of SSA is related to the size of the slopes compared with the incident angle and the scattering angles. SSA-n can be used for the case of small elevation when the following condition is fulfilled:

$$\nabla h \ll \frac{q}{k} \tag{7.10}$$

It means that the slopes should be small enough and be at least smaller than the grazing angles of the incident and scattered waves.

SSA numerical and experimental results were studied and compared for anisotropic sea spectra (Soriano & Saillard, 2001), (Berginc, 2002). SSA-1 considerably extends the validity domain of SPM but remains outperformed by KA for large roughness in its domain of validity.
The second order kernel, SSA-2 reduces to the Kirchhoff theory in the high frequency limit, and accounts for large-scale effects. However, its main limitation is its numerical complexity. For this reason, SSA-1 remains mostly employed.

Results

H. Zhang et al. (2016) compared the results of the SSA-1 to calculate the RCS of a ship wake surfaces. Zhang considered a surface of size 25m × 25m which contains part of the ship wake. The SSA was

simulated with an incident wave with a frequency of 1.3GHz and an incident angle of 45°. The results were compared with the method of moment and are depicted in figure 7.7. The SSA reconstructs the MoM results with good precision at small scattering angle but drives away from numerical results when the incident angle exceeds 60°.

Thus, SSA is an improvement of SPM, as it recovers and extends the domain of validity of the SPM, fulfills 8 of the 10 physical scattering amplitude criteria when SPM fulfilled only 6 (as presented in the summary in section 7.2). However, SSA1 is still not efficient for both small frequencies and high frequencies and remains outperformed by the KA for high frequencies, while SSA2 is computationally intense. Thus, further unifying scattering models can be investigated.

7.1.6 Weighted Curvature Approximation

The Weighted Curvature Approximation is a model based on theoretical considerations, designed as an improvement of the Small-Slope Approximation. It applies a second-order kernel for correcting the local curvature and was designed heuristically to satisfy the SPM and KA limits.

History

The WCA was developed in Elfouhaily et al. (1999) and is based on a fusion between the KA and the Local Weight Approximation (LWA), a model developed by Dashen and Wurmser (1991). The LWA is written as a Kirchhoff integral with a local kernel taking into account curvature effects and can be applied at KA and SPM limits. However, its main limitation is its inapplicability to dielectric surfaces, which is why it is not developed in this study. Guerin and Sentenac (2004) compared the WCA with a numerical method, the method of moments, and showed that the WCA remained extremely accurate in a roughness range where KA and SSA failed. Guerin et al. (2010) then refined the WCA to make its analytical expression simpler and compared the new formula with the method of moments.

Description

The WCA is strictly based on mathematical derivations of the scattering amplitude of different existing models. The WCA's integrand constructed in a similar way than the SSA-1 and thus the Kirchhoff integrand. It has the structure of a Kirchhoff integral with an unknown local kernel with the structure of the LWA. Elfouhaily builds this kernel with all the properties wished: reciprocity, compatibility with SPM of the first order (SPM1) and KA, with tilt and shift invariance and includes the curvature

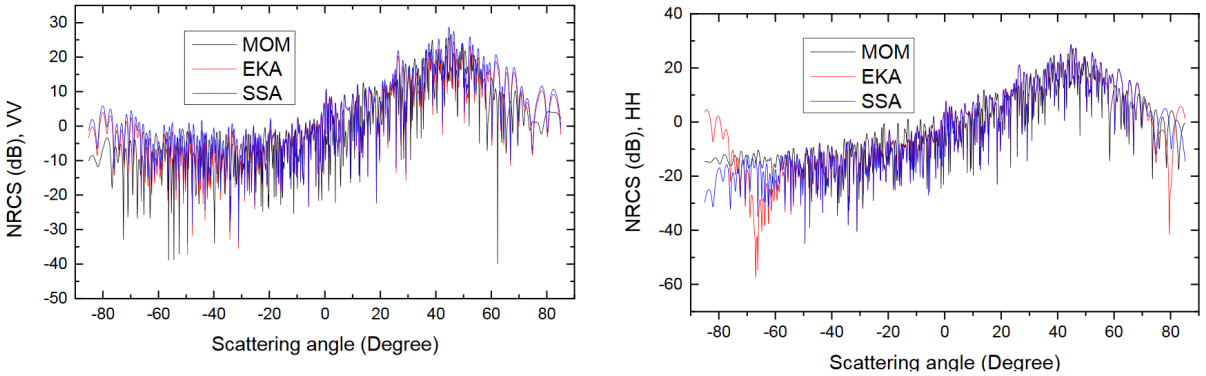

Figure 7.7: Comparison of VV (top) and HH (bottom) components of the RCS of a partial wake surface, between the SSA, an numerical method (MOM) and an other analytical method (Extended Kirchhoff Approximation) (H. Zhang et al., 2016).

effects. The kernel is a simple difference between the low-frequency SPM1 and KA kernels expressed in a local frame of reference, to take into account curvature effects. This ensures that both SPM and Kirchhoff limits are reached.

Limits

The WCA is the most developed model presented by the works of T. M. Elfouhaily et al. (2004). It only has a few limits: the statistical formulas are not easily obtained if we need them, and the model is quite complex, for both a theoretical and numerical point of view.
In our case, the applicability of the WCA is still unsure since the WCA requires integration on the mean plane of the surface. The model was initially developed for sea scattering, where the mean reference plan was simpler to compute. In our case, we are not fully certain that the model would work on a sphere or ellipsoid of reference. It could also work on small mean planes of reference, but the continuity of planes would be hard to guarantee.

Results

Guerin et al. (2010) refined the WCA to a universal form and compared it with the method of moments. The scattering problem in the off specular region was evaluated for λ=25cm at L-band. A 2-dimensional Gaussian sea surface was generated with a 7 m/s wind speed. The surface is sampled at 3cm, and the incoherence radar RCS is obtained with Monte Carlo simulation. Guerin showed that the normalized RCS (NRCS) results fit well with the MoM results, as presented in figure 7.8, with the visible oscillation of the MoM due to insufficient sampling of the surface. However, the MoM values for large angles ($\geq 80°$) are stated to be not reliable, and around the specular region (25°), the involved spectrum diverges because only the off-specular component of the scattered field was simulated.

The WCA seems to fulfill all scattering amplitude physical criteria (presented in the summary in section 7.2) and thus seems to be the most adapted model. However, it remains more complex to implement than other models, such as the KA, and does not seem to be applicable in a small body geometry, where the mean surface can not be considered as a plane.

7.1.7 Domain of validity of analytic surface methods

G. Soriano et al. (2002) compared the performances of the KA and the SSA with the MoM in order to define their domain of validity. The surfaces investigated have Gaussian correlation, and are thus

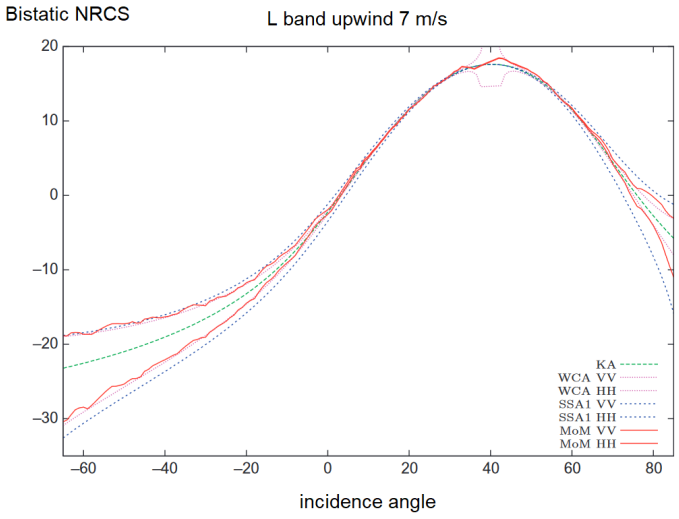

Figure 7.8: Comparison of the normalized RCS (NRCS) computed with KA, SSA1, WCA, and MoM (Guerin et al., 2010).

Table 7.1: Surface parameters used for the generation of rough surfaces to compare the performances of each surface scattering models. The unit is the electromagnetic wavelength. The minimum value of correlation length 0.5 is fixed by the numerical limitations of the MoM, for memory storage and computation time (G. Soriano et al., 2002).

Surface	σ	c_L	RMS slope
1	0.25	3.15	0.112 (6.4°)
2	0.05	0.63	0.112 (6.4°)
3	0.5	3	0.24 (13.3°)
4	0.25	1.5	0.24 (13.3°)
5	0.167	1	0.24 (13.3°)
6	0.125	0.75	0.24 (13.3°)
7	0.083	0.5	0.24 (13.3°)
8	0.5	2	0.35 (19.5°)
9	0.5	1.5	0.47 (25.2°)
10	0.25	0.75	0.47 (25.2°)
11	1	2	0.71 (35.3°)

characterized by their RMS height σ and their correlation length c_L. The study was carried out on 11 surfaces numbered from 1 to 11, with different roughness parameters presented in table 7.1.

A Monte Carlo simulation over 500 sampled surfaces was performed. The first surfaces correspond to the SPM domain, where the SSA is accurate as opposed to KA. This was expected, since SSA covers the SPM1 limit. As the RMS height is increased to leave the domain of validity of the SPM (surface 3), the SSA is still better than the KA and is accurate in the forward direction but starts deteriorating in the backward direction. Increasing the correlation length while keeping the slope constant (=13.3°) (surfaces 3 to 7), the KA becomes continuously the most accurate method, the turning point being surface 5. For higher values of the RMS slope (surfaces 8 to 11), the SSA is never reliable while the KA remains good up to RMS slope value of 19.5° for large correlation length (surface 8). Note that for large correlation length, the SSA is accurate only for very small values of slope (like surface 1).

The validity domains of the approximation are represented on a diagram represented in figure 7.9 with dimensionless parameters $(K\cdot l, K\cdot\sigma)$, which represents the product of the correlation length and the RMS height with the radar's wavelength, for the surfaces investigated in table 7.1.

To summarize, we can state that:

- SPM is valid for small perturbation when the Rayleigh Parameter is small $k\sigma \ll 0.3$ (Ogilvy & Merklinger, 1991).
- KA is valid for $K \cdot R_c \cdot \cos(\theta_i) \gg 1$, where R_c is the radius of curvature, which is : $R_c = \frac{c_L^2}{2\cdot\sigma\sqrt{3}}\left(1 + \frac{2\sigma^2}{c_L^2}\right)^{3/2}$ for Gaussian surfaces Papa and Lennon (1988).
- KA is not valid if the condition $K \cdot l$ is not respected, $K \cdot l \geq 6$ according to E. I. Thorsos (1988). Under this limit, the tangent plane approximation fails. The approximation is still a method for small roughness, so the domain of validity of the KA is the largest for small roughness and decreases as the roughness gets larger. Sorianos' work shows the validity of the KA until the surface 8 with a RMS slope s of $s \leq 0.35$.
- SSA recovers the SPM domain but remains outperformed by KA in its domain. Its domain of validity was also investigated in Broschat et al. (1997).
- WCA is investigated in Guerin and Sentenac (2004) on a constant line of RMS slope of $s = 0.353$, corresponding to a slope angle of 20°. This is a zone where none of the other models were valid. The WCA was found to be efficient on this limit, however, additional works are still needed to investigate it further the limit of the domain of validity.

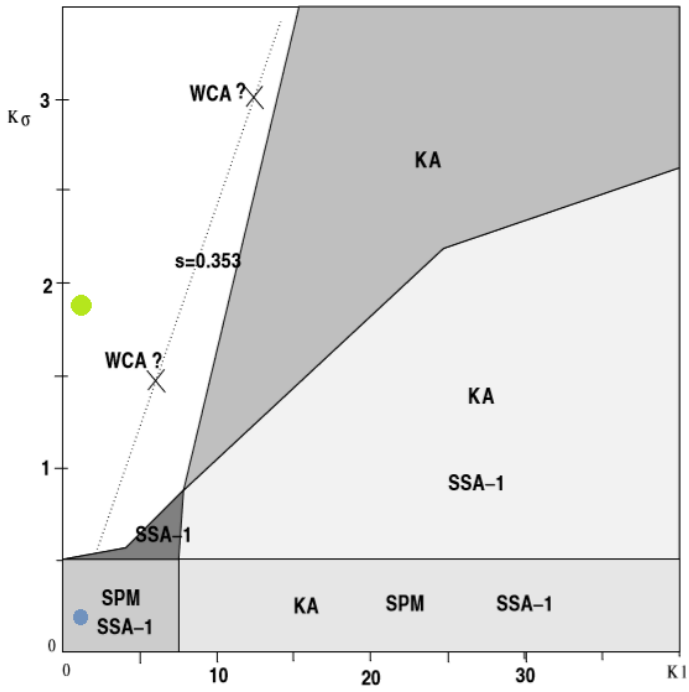

Figure 7.9: Domain of validity of the different surface methods depicted in table 7.1 (G. Soriano et al., 2002): Small Perturbation Method (SPM), Kirchhoff Approximation (KA), Small Slope Approximation (SSA), and Weighted Curvature Approximation (WCA). The blue and green points depict the position of our simulated surfaces.

7.2 Summary

Each of these methods has their advantages and drawbacks, as presented in table 7.4. As explained in the first part, the model chosen will need to reconstruct both small and high scales of roughness. However, all the models described above have similar limitations: they do not include shadowing or multiple scattering and would need corrections to give better results. Their performances are detailed in table 7.4.

For the Highlands scenario, the surface parameters $K \cdot l = 69$, $K \cdot \sigma = 25$ are out of the range displayed by figure 7.9. However, we can compute that $K \cdot R_c \cdot \cos(\theta_i)$ varies from 3.0 to 5.0 considering the range of incidence angles between the spacecraft and the surface (from 30° to 60° in our simulations): this is superior than 1.0, but not largely, so the surface is at the limit of validity for the Kirchhoff approximation. However, if we imagine the WCA limit of figure 7.9 extending to $K \cdot l = 69$, $K \cdot \sigma = 25$, the surface also falls out of the theoretical domain of validity of the WCA.

The position of the lowland surface is located as a blue spot in figure 7.9 with $K \cdot l = 1.15$ and $K \cdot \sigma = 0.17$, and falls out of the theoretical domain of validity of the KA.

The position of the mix roughness surface is indicated by a green point on figure 7.9 with $K \cdot l = 1.15$ and $K \cdot \sigma = 1.72$, away from the domain of validity of any model.

Thus, no existing analytical scattering model can be applied to model exactly the field scattered by the surface of an asteroid. As the WCA is a model complex to implement, and the KA has been successfully applied to model to field scattered by rough planetary surfaces, it will be applied to simulate the field scattered by both scales roughness of an asteroid's surface. It seems for now that it is the best compromise between computational charge and precision even if not ideal for our study. Moreover, since the observation of the asteroids Bennu and Ryugu in 2018, asteroids may be much rougher than what was previously thought, and straying away from the domain of validity of the SPM and the SSA. Thus, the Kirchhoff approximation will be implemented to model the scattering of the electromagnetic field by asteroids' surfaces.

Table 7.2: Summary of the classification of all scattering models (T. M. Elfouhaily et al., 2004).

Method	1	2	3	4	5	6	7	8	9
SPM		x	x	x	x		x		
KA		x							x
SSA		x	x	x	x				
WCA		x	x		x				x

Where :
1. Proceeds via estimation of a surface current
2. Works directly on the scattering amplitude
3. Makes a structure hypothesis for the surface current or the scattering amplitude
4. Uses a functional expansion of some quantity in surface height
5. Requires consistency with SPM for the identification of some unknown series
6. Uses a particular choice of Green's function
7. Uses second-kind Fredholm integral equation
8. Uses first-kind Fredholm integral equation
9. Uses the stationary phase approximation

Table 7.3: Summary of the physical criteria fulfilled by all scattering models (T. M. Elfouhaily et al., 2004).

Property	1	2	3	4	5	6	7	8	9	10
SPM	■	■	□	\	\	■	□	\	■	\
KA	■	■	□	■	■	■	\	■	\	□
SSA	■	■	■	■	\	■	■	■	■	\
WCA	■	■	■	■	■	■	□	■	■	■

Where:
1. Applicable to dielectric types of surfaces
2. Applicable to 2D surfaces
3. Reciprocal
4. Shift invariant
5. Tilt invariant
6. Numerically fast and stable
7. Not restricted to large correlation lengths
8. Not restricted to small surface height
9. In agreement with the small frequency limit (SPM1 limit, see below)
10. In agreement with the high frequency limit (KA limit, see below)

And where:
■ = satisfied by construction
□ = satisfied upon inspection
\= not satisfied

Table 7.4: Table of performances of the analytical methods (T. M. Elfouhaily et al., 2004).

Property	Computational burden	Domain of Validity	Complexity
SPM	Low	Short	Low
KA	Low	Medium	Low
SSA	Medium	Large	Medium
WCA	Medium	Large	High

Chapter 8

The Kirchhoff Approximation and the facet method

The Kirchhoff Approximation is a scattering model that computes the field scattered by a surface by cutting the surface into a set a planes and apply the Fresnel coefficients to get the scattered field. Since infinite planes are unreachable in reality, instead of computing the field scattered by an infinite plane tangent to the surface, we compute the field scattered by planes of finite size. This implementation is called the facet method and was covered in Nouvel (2003) and Berquin (2014). In the first part, the facet method implementation will be reviewed, then we will present the results of the model when confronted with a small body observation geometry.

8.1 Implementing the Kirchhoff approximation using a meshed surface

In a similar way than the Kirchhoff approximation, the facet method assumes that the total electromagnetic field scattered by a surface, characterized by its heights ξ, is identical to the electromagnetic field scattered by finite planar facets, that are tangent to the surface and which form a mesh that describe the surface. Each facet thus has a diffraction pattern, that depends on its size compared to the wavelength.
We consider that $\vec{r_0}$ corresponds to the position of the radar antenna, and $\vec{r}$ corresponds to a point on the surface. Once the fields scattered by each facet $\vec{E_{s_\alpha}}(\vec{r_0})$ are computed, the resulted total scattered field $\vec{E_{s_{tot}}}$ is obtained by summing the contribution of each facet :

$$\vec{E_{s_{tot}}}(\vec{r_0}) = \sum_{\alpha} \vec{E_{s_\alpha}}(\vec{r_0}). \tag{8.1}$$

To compute the field scattered by a facet, Nouvel (2003) and Berquin (2014) follow the work of Kong (2000) which is presented in the following.

8.1.1 Application of the Huygens-Fresnel principle

First, Kong considers a plane wave incident upon a random rough surface observed by a radar, described by its interface S. If the surface is located in the far field of the antenna, the electric field generated by the incident wave is given by:

$$\vec{E_i}(\vec{r_0}, \vec{x}) = E_0 \cdot e^{-i \cdot \vec{k_i} \cdot (\vec{r} - \vec{r_0})} \cdot \vec{e_i} \tag{8.2}$$

Where $\vec{k_i}$ is the incident wave vector and $\vec{e_i}$ is the incident wave polarization.
Using Huygens principles, the field reflected by an interface can be written from the fields at its surface, $\vec{n} \times \vec{E}(\vec{r})$ and $\vec{n} \times \vec{H}(\vec{r})$. Thus, in the far field assumption, the field scattered by a surface $\vec{E_s}$ can

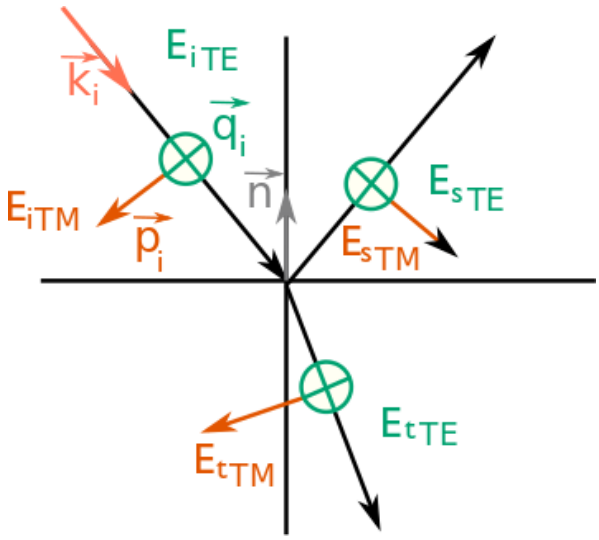

Figure 8.1: Illustration of TE and TM waves polarisation.

be written as:

$$\vec{E}_s(\vec{r_0},\vec{r}) = \int_{S'}[i\omega\mu_0\bar{\bar{G}}(\vec{r_0},\vec{r})\cdot[\vec{n}\times\vec{H}(\vec{r})] + \nabla\times\bar{\bar{G}}(\vec{r_0},\vec{r})\cdot[\vec{n}\times\vec{E}(\vec{r})]]dS' \tag{8.3}$$

where S' is the surface on which to perform the integral, ω is the wave pulsation, μ_0 the vacuum permeability, and $\vec{n}$ is the normal.
$\bar{\bar{G}}$ is the dyadic green function for the homogeneous space and is written:

$$\bar{\bar{G}}(\vec{r_0},\vec{r}) = (\bar{\bar{I}} - \vec{k_s}\vec{k_s})\cdot\frac{e^{-i\cdot\vec{k_s}\cdot(\vec{r_0}-\vec{r})}}{4\pi|\vec{r_0}-\vec{r}|} \tag{8.4}$$

With k_s being the scattered wave vector.
Thus we can write the electromagnetic field scattered by a surface as:

$$\vec{E}_s(\vec{r_0},\vec{r}) = i\cdot k_s\cdot(\bar{\bar{I}} - \vec{k_s}\vec{k_s})\cdot\int_S[\vec{k_s}\times(\vec{n}\times\vec{E}(\vec{r_0},\vec{r})) + \eta\times(\vec{n}\times\vec{H}(\vec{r_0},\vec{r}))]\cdot\frac{e^{-i\cdot\vec{k_s}\cdot(\vec{r_0}-\vec{r})}}{4\pi\cdot|\vec{r_0}-\vec{r}|}dS' \tag{8.5}$$

With $\eta = \sqrt{\mu/\epsilon}$ is the medium impedance.

Then, the surface fields can be written with the Fresnel coefficients by decomposing the total field into Transverse Electric (TE) and Transverse Magnetic (TM) waves. This is presented in figure 8.1, using an orthogonal base $(\vec{q_i},\vec{p_i},\vec{k_i})$ at a point $\vec{r}'$.

$$\vec{q_i} = \frac{\vec{k_i}\times\vec{n}}{|\vec{k_i}\times\vec{n}|} \tag{8.6}$$

$$\vec{p_i} = \vec{q_i}\times\vec{k_i} \tag{8.7}$$

The TE component of the wave then is:

$$\vec{E}_{TE}(\vec{r_0},\vec{r}) = E_0 e^{-i\vec{k_i}\cdot(\vec{r}-\vec{r_0})}(\vec{e_i}\cdot\vec{q_i})\vec{q_i} \tag{8.8}$$

And thus, the reflected TE wave is:

$$\vec{E}_{s_{TE}}(\vec{r_0},\vec{r}) = R_{TE}\cdot E_0 e^{-i\vec{k_i}\cdot(\vec{r}-\vec{r_0})}(\vec{e_i}\cdot\vec{q_i})\vec{q_i} \tag{8.9}$$

With RTE, the Fresnel reflection coefficient, which can be written:

$$R_{TE} = \frac{\cos(\theta_i) - \sqrt{\epsilon_a} \cdot \cos(\theta_t)}{\cos(\theta_i) + \sqrt{\epsilon_a} \cdot \cos(\theta_t)} \tag{8.10}$$

$$\vec{E}_{TM}(\vec{r_0}, \vec{r}) = E_0 e^{-i\vec{k_i} \cdot (\vec{r} - \vec{r_0})} (\vec{e_i} \cdot \vec{p_i}) \vec{p_i} \tag{8.11}$$

Thus, the reflected TM wave is:

$$\vec{E}_{s_{TM}}(\vec{r_0}, \vec{x}) = R_{TM} \cdot E_0 e^{-i\vec{k_i} \cdot (\vec{r} - \vec{r_0})} (\vec{e_i} \cdot \vec{p_i}) \vec{p_i} \tag{8.12}$$

With RTM the Fresnel reflection coefficient, which can be written:

$$R_{TM} = \frac{\cos(\theta_t) - \sqrt{\epsilon_a} \cdot \cos(\theta_i)}{\cos(\theta_t) + \sqrt{\epsilon_a} \cdot \cos(\theta_i)} \tag{8.13}$$

After some manipulations the surface fields then becomes:

$$\vec{E}_{surf}(\vec{r_0}, \vec{r}) = [(\vec{n} \times \vec{q_i}) \cdot (\vec{e_i} \cdot \vec{q_i}) \cdot (1 + R^{TE}) + \vec{q_i} \cdot (\vec{n} \cdot \vec{k_i}) \cdot (\vec{e_i} \cdot \vec{p_i}) \cdot (1 - R^{TM})] \cdot E_0 \cdot e^{-i\vec{k_i} \cdot (\vec{r} - \vec{r_0})} \tag{8.14}$$

$$\vec{n} \times \vec{H}(\vec{r_0}, \vec{r}) = [-(\vec{n} \times \vec{k_i}) \cdot (\vec{e_i} \cdot \vec{q_i}) \cdot \vec{q_i} \cdot (1 - R^{TE}) + (\vec{n} \cdot \vec{q_i}) \cdot (\vec{e_i} \cdot \vec{p_i}) \cdot (1 + R^{TM})] \cdot \frac{E_0}{\eta} \cdot e^{-i\vec{k_i} \cdot (\vec{r} - \vec{r_0})} \tag{8.15}$$

If we note the local slopes α and β on the $\vec{x}$ and $\vec{y}$ axes:

$$\alpha = \frac{\partial \xi(x', y')}{\partial x'} \tag{8.16}$$

$$\beta = \frac{\partial \xi(x', y')}{\partial y'} \tag{8.17}$$

Then, in the monostatic case where $\vec{k_i} = -\vec{k_s}$, the total reflected fields at a point can be written:

$$\vec{E_s}(\vec{r_0}, \vec{r}) = i \cdot k_s \cdot E_0 (\bar{\bar{I}} - \vec{k_s}\vec{k_s}) \cdot \int_S F(\alpha, \beta) \frac{e^{-2 \cdot i\vec{k_i} \cdot (\vec{r} - \vec{r_0})}}{4\pi \cdot |\vec{r_0} - \vec{r}|} dS' \tag{8.18}$$

With :

$$\begin{aligned} F(\alpha, \beta) = \frac{1}{\sqrt{1 + \alpha^2 + \beta^2}} \cdot [& -(\vec{e_i} \cdot \vec{q_i}) \cdot (\vec{n} \cdot \vec{k_i}) \cdot \vec{q_i} \cdot (1 - R^{TE}) \\ & + (\vec{e_i} \cdot \vec{p_i}) \cdot (\vec{n} \times \vec{q_i}) \cdot (1 + R^{TM}) \\ & + (\vec{e_i} \cdot \vec{q_i}) (\vec{k_s} \times (\vec{n} \times \vec{q_i})) \cdot (1 + R^{TE}) \\ & + (\vec{e_i} \cdot \vec{p_i}) \cdot (\vec{n} \cdot \vec{k_i}) \cdot (\vec{k_s} \times \vec{q_i}) \cdot (1 - R^{TM})] \end{aligned} \tag{8.19}$$

On equation 8.18, the expressions on the integrand are not dependent on r', except for the phase factor. Thus, the phase integral, which we call the phase factor, needs to be computed.

8.1.2 Computation of the phase factor

Nouvel (2003) computed the total reflected field analytical formula for square facets. However, square facets cannot allow complete continuous coverage of a spherical surface, which explains why a decomposition of the surface into triangular facets is needed (Plettemeier et al., 2009). Berquin et al. (2015) cut down facets with a triangular mesh and expanded the phase, using both a zeroth-order development, where the phase is computed as constant on each facet, and first order development, where the phase is written as linear on the facet.

Constant phase function

This simple approach considers that the phase is constant over the facet. Thus, by noting $\vec{r_c}$ the position of the center of the facet, the integrand can be written:

$$\int_S e^{-2i\vec{k}_i\cdot(\vec{r}-\vec{r_0})}dS' = S\cdot e^{-2i\vec{k}_i\cdot(\vec{r_c}-\vec{r_0})} \tag{8.20}$$

In this way, the surface is approached by a set of elementary surfaces. This formulation is right but requires a large number of point facets to describe extended surfaces. Namely, a facet will have to be largely smaller than the wavelength in order to be considered as a point target. Thus, this derivation has an extensive computational load.

Linear phase function

In order to reduce the computational load of the facet method, Berquin computed the first order development of the phase, in order to overcome the size limit of the facets. The phase is thus written such that:

$$e^{-2i\vec{k}_i\cdot(\vec{r}-\vec{r_0})} = e^{-2i\vec{k}_i\cdot(-a_0\cdot x-b_0\cdot y+d_0)} \tag{8.21}$$

With a_0, b_0 and d_0 the coefficient of the equation of the plan where the facet lies.
After a series of manipulation described, in Berquin et al. (2015), the phase is then written :

$$\begin{aligned}\int_S e^{-2ik(-a_0\cdot x-b_0\cdot y+d_0)}d\sigma(\vec{x}) = J\cdot\frac{e^{2ik\cdot d_0}}{(2ik)^2 b_0}\Bigg[&\frac{e^{-2ik\cdot b_0\beta_1}}{a_0+b_0\alpha_1}\left(e^{-2ik\cdot D'_{x'}(a_0+b_0\alpha_1)}-e^{-2ik\cdot A'_{x'}(a_0+b_0\alpha_1)}\right)\\&+\frac{e^{-2ik\cdot b_0\beta_2}}{a_0+b_0\alpha_2}\left(e^{-2ik\cdot B'_{x'}(a_0+b_0\alpha_2)}-e^{-2ik\cdot D'_{x'}(a_0+b_0\alpha_2)}\right)\\&+\frac{e^{-2ik(b_0\cdot D'_{y'}+A'_{x'}a_0)}-e^{-2ik(b\cdot D'_{y'}+B'_{x'}a_0)}}{a_0}\Bigg]\end{aligned} \tag{8.22}$$

With A'$_*$, B'$_*$, C'$_*$ being facet points after a change of frame to the local frame of facet, D'$_*$ being the point on $\vec{AB}$, which cuts the facet into two right triangles, and

$$J = \sqrt{a^2+b^2+1} \tag{8.23}$$

$$\alpha_1 = \frac{A'_{y'}-C'_{y'}}{A'_{x'}-C'_{x'}} \tag{8.24}$$

$$\beta_1 = C'_{y'}-\alpha_1 C'_{x'} \tag{8.25}$$

$$\alpha_2 = \frac{B'_{y'}-C'_{y'}}{B'_{x'}-C'_{x'}} \tag{8.26}$$

$$\beta_1 = C'_{y'}-\alpha_2 C'_{x'} \tag{8.27}$$

8.1.3 Validation of SEPO: observation of a point target in the Earth observation geometry

The facet method implementation with triangular facets, Surface Echo PO (SEPO) has been applied by Berquin et al. (2015) to reconstruct radargrams from Mars and the Moon and thus validated the method. Hence, we integrated SEPO into the SPRATS toolbox, which allowed the computation of the scattered electromagnetic field from an extended rough surface. In order to validate the integration, we will compare two results :

- The results of the SAR synthesis of the spectrum of a point target obtained with SEPO
- The results of the SAR synthesis of the spectrum of a point target obtained with the spectrum module of SPRATS, as presented in appendix B.

The resulting SAR images will be associated with low scattered power, that may be lower than minus few hundreds of dB. Indeed, the simulations do not cover any process gain, antenna gain or synthesis gain. Moreover, they do not consider any gain that may be reached with the range/Doppler compression.

First, SEPO will be applied to a point target observed in the Earth observation geometry, as presented in scenario EO-SP-1, described in appendix D. This scenario consists of observing a point target in an Earth observation geometry, at an altitude of 510 km for a distance of 10 km, with an incidence angle of 24° and a band of 1.0 GHz. Indeed, SEPO performances can be easily validated in the Earth observation geometry, where the point target cardinal sine pattern is well known, compared to the small body geometry where the point target response will be highly dependent on the geometry of observation.

The 2D SAR synthesis of scenario EO-SP-1 obtained with the point target computation module of SPRATS is pictured on the left side of figure 8.2 and compared with the SAR image obtained from the spectrum of the same scenario, computed with SEPO, on the right side of figure 8.2. The location of the point target scattering the electromagnetic field is indicated by a white sphere.
SEPO results agree with SPRATS point target outcome: since the range and Doppler delays can be considered separable, the pattern of the point target response corresponds to a product of two cardinal sines, with its maximum power at the center of the frame which indicates that SEPO correctly locates the target. The performances of the point target are coherent with SPRATS point target results, as depicted in table 8.1: the resolutions are alike up to a sampling error and the PSLR are equal. The PSLR level is -13dB because no windowing has been applied on the target spectrum, in order to observe the raw performances of SEPO. The two images main power difference is explained because SPRATS' point target spectrum does not take into account the attenuation of the power due to the distance, or the surface of the target that scatters the power back to the radar.

The 3D SAR synthesis results of scenario EO-SP-1 computed with SPRATS spectrum are presented on the left side of figure 8.3 and compared with the 3D synthesis obtained with SEPO point target spectrum on the right side of figure 8.3.
The target position is well identified at the center of the frame, since the high power portion of the SAR image crosses the white sphere position. However, figure 8.3 depicts a major characteristic observed in SAR images, which is the ambiguity of the target location in the third dimension of space, that occurs because only one trajectory with a single elevation is flown. Indeed the target location in range is well identified because of the wide band of frequencies used by the radar, its position in azimuth is localized because of the large amount of time the target is illuminated by the radar. However because the target is imaged with a single track in elevation, the target position is ambiguous and the radar cannot resolve the target location in the elevation direction, the direction normal to the slant range and the azimuth direction. From now on, this characteristic will be called the elevation ambiguity, since it depicts the ambiguous localization of the target in the elevation direction.

8.1.4 Summary

The surface scattering model Surface Echo PO is an implementation of the Kirchhoff approximation with a discretization of the surface using triangular facets. The model was initially validated by

Table 8.1: Performance summary of SurfaceEchoPO.

Performance	Point target	SEPO
3 dB Range resolution (m)	1.88	1.88
3 dB Doppler resolution (m)	1.46	1.46
Main lobe power (dB)	-230.6	-390.9
PSLR (dB)	-13.4	-13.9

comparing SEPO's results with actual Martian or Lunar radargram (Berquin et al., 2015), and was thus associated with SPRATS in order to compute SAR syntheses of extended, rough surfaces. In order to validate the integration of SEPO with SPRATS, a SAR synthesis of a spectrum of a point target obtained with SEPO was simulated and was found out to be coherent with the known SAR synthesis results of a point target in the Earth Observation geometry. Thus we can consider that the insertion of SEPO into SPRATS is validated, and the model can be applied to a small body geometry to compute the SAR image of extended surfaces.

8.2 Result of the facet method in a small body geometry

As the radar returns depend on the geometry of observation, the SAR synthesis pattern of a point target is not known in complex geometries, and will differ from the well known Earth observation patterns. Thus, the results of the SAR synthesis cannot be known in advance and customized simulations are necessary to analyze the instrument's performances for each scenario for our asteroid target.

As detailed in 8.1.3, the resulting SAR images will be associated with low scattered power, that may be lower than minus few hundreds of dB. Indeed, the simulations do not cover any process gain, antenna gain, or synthesis gain. Moreover, they do not consider any gain that may be reached with the range/Doppler compression.

First, the simulation of a point target is computed to establish the performances of HFR in the Didymos geometry and analyze the point target patterns. Then, we will compute SAR syntheses of different rough surfaces applied on the asteroid surface to visualize the behavior of HFR when observing rough, asteroid-like surfaces.

8.2.1 Simulation of a point target

First, a point target study was performed to analyze the SAR image properties in the small body geometry, following the scenario SB-SP-1 described in appendix E. This scenario considers the observation of a point target located at the surface of the asteroid KW4, at $[0°, 0°]$ lat lon, with the 500MHz band of HFR. The pattern of the point target in the small body geometry is expected to be highly different from the pattern in the Earth observation geometry. Indeed, since the range and Doppler delays cannot be considered separable in the small body observation geometry, the point target pattern will differ from the product of the cardinal sines. Furthermore, the image range resolution is expected to be similar from the theoretical range resolution, but the azimuth resolution should differ since the

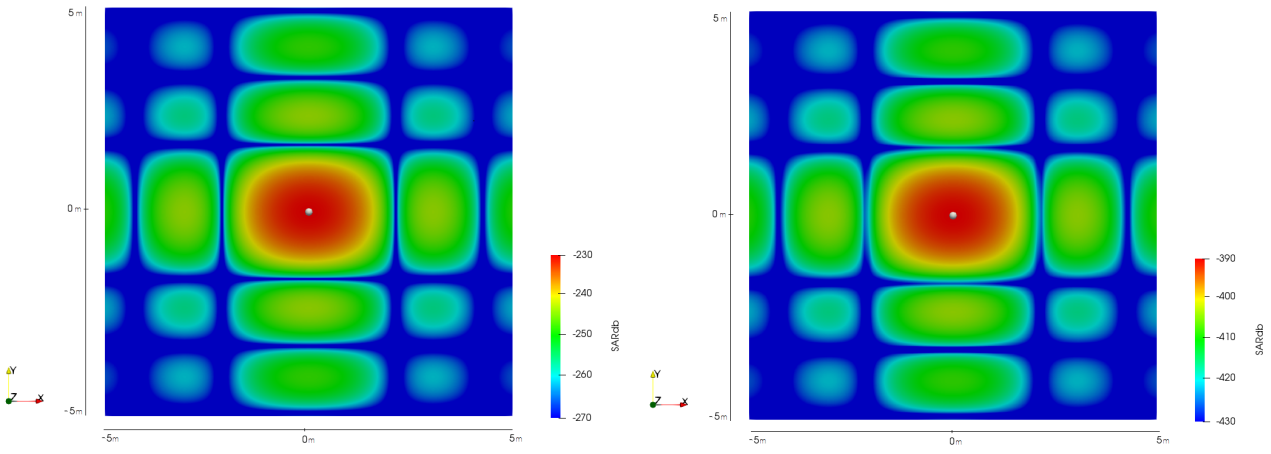

Figure 8.2: SAR Synthesis of scenario EO-SP-1 on the 2D SAR surface, obtained with SPRATS point target spectrum (left) and with a point target spectrum computed with SEPO (right).

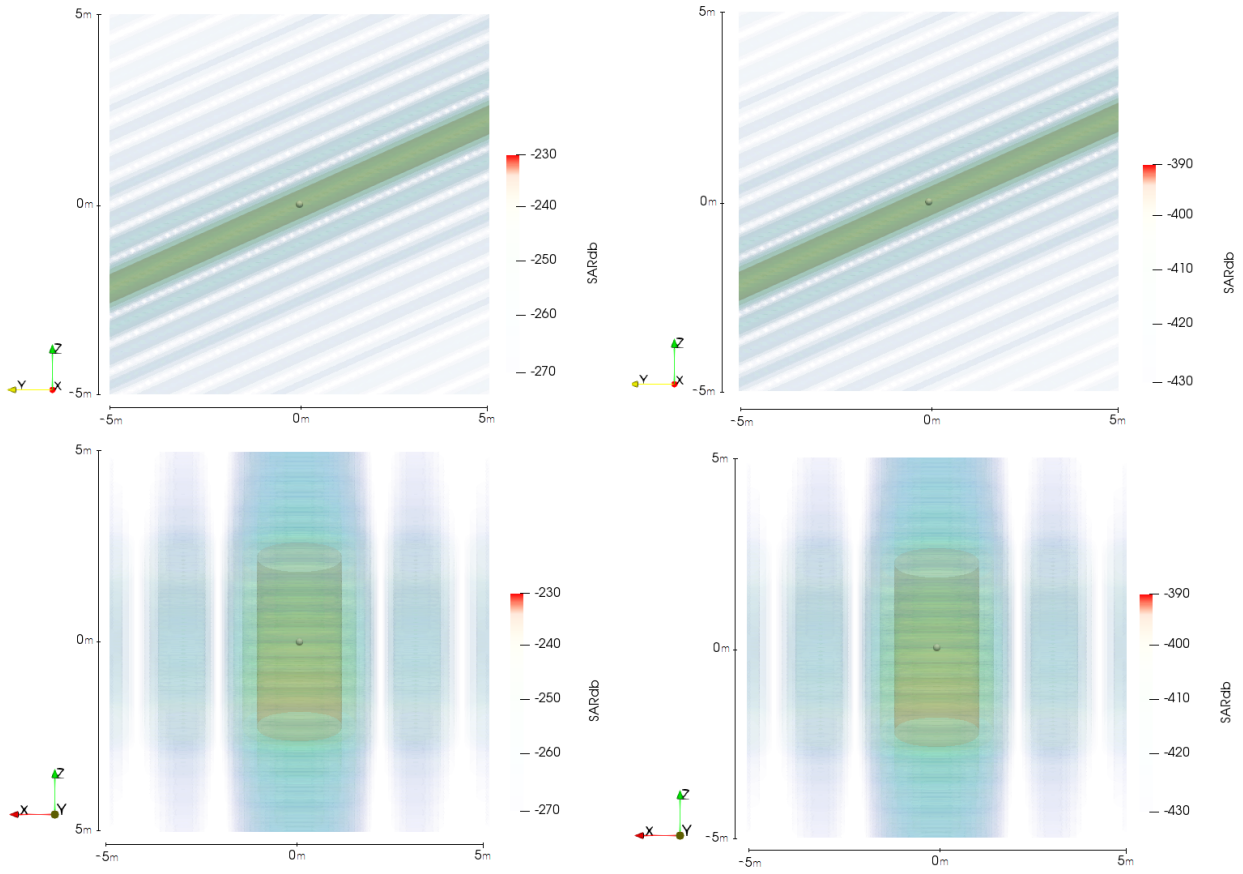

Figure 8.3: SAR Synthesis of scenario EO-SP-1 on the 3D SAR volume obtained with SPRATS point target spectrum (left) and with a point target spectrum computed with SEPO (right). The radar's trajectory follow the $\vec{x}$ direction. Top: view from the side. Bottom: View from the front.

azimuth resolution formula is not adapted to the small body observation geometry.
The result of the 2D SAR synthesis is presented in figure 8.4 and the result of the 3D SAR synthesis is presented in figure 8.5.
The 2D SAR synthesis presents the pattern of the point target in the small body geometry. Since the characteristic of the image with the highest associated power is located at the position of the target, we can conclude that SEPO correctly locates the target at the center of the frame, with the performances presented in table 8.2. As expected, the range and doppler sidelobes highly differ from the cardinal sine Earth observation pattern. Figure 8.4 presents that even though the range sidelobes lie in the range direction, the Doppler sidelobes do not lie in the azimuth direction.
The origin of the orientation of the Doppler sidelobes is pictured in figure 8.6, which presents the evolution of the SAR synthesis of three soundings on the beginning (blue), middle (grey) and end (red) of the trajectory, on a whole 1999KW4 hemisphere, where the position of the point target is indicated by a white sphere. Since all three syntheses are performed with HFR's entire RF bandwidth but at only one position on the trajectory, the position of the target is identified in range, but ambiguous in Doppler. Figure 8.6 thus pictures in bright red the points on the asteroid surface having the same range delay than the target, which are the Doppler ambiguities. The true position of the target will be obtained by averaging the results from all soundings building the trajectory, reducing the power of the ambiguity at all points except at the target's position. However, because of the pattern of the ambiguity, the Doppler ambiguities of the two soundings making the trajectory border will be less affected than other soundings. Indeed, figure 8.7 depicts on a closer area the effects on the SAR image of the averaging of the Doppler ambiguities associated with different soundings. Thus, the final Doppler sidelobes will be shaped as the Doppler ambiguities of the two soundings of the border of the

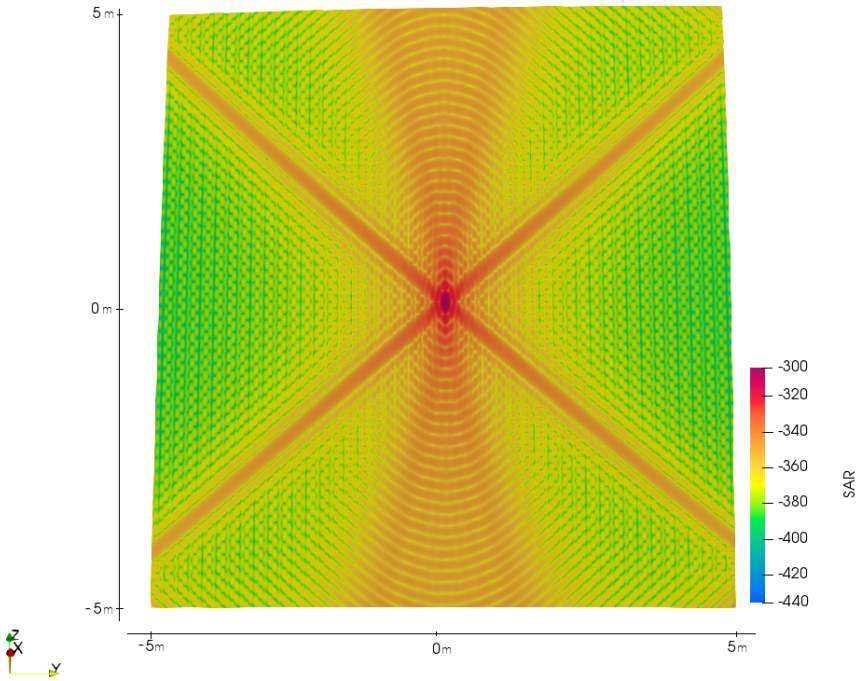

Figure 8.4: KW4 point target SAR synthesis on a 2D surface.

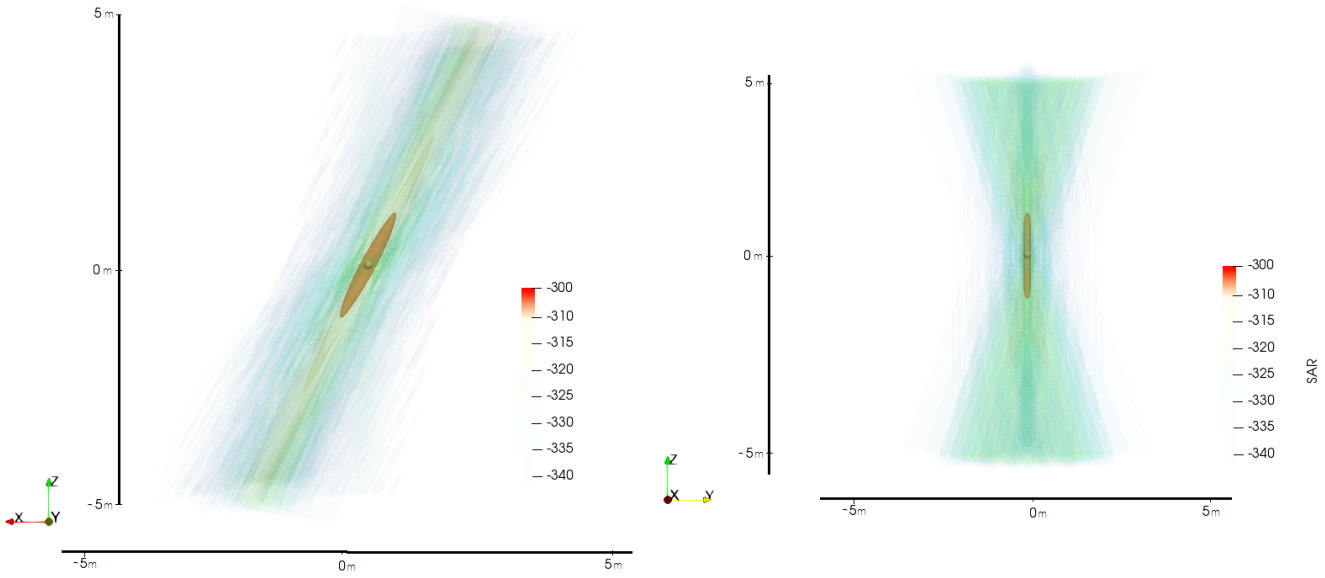

Figure 8.5: KW4 point target SAR synthesis on a 3D surface. The white sphere indicate the target theoretical location.

trajectory, as a "cross", as presented in figure 8.4.

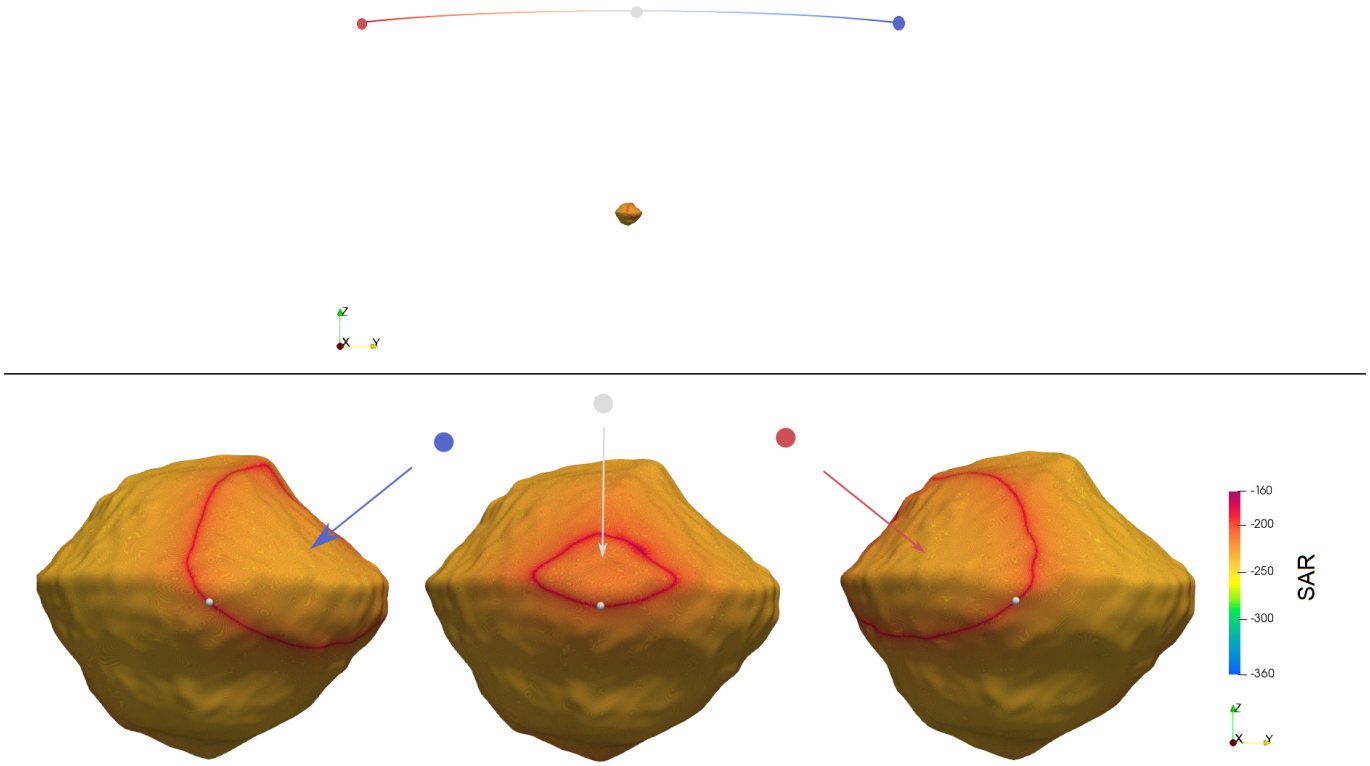

Figure 8.6: Illustration of the origin of the Doppler borders, with the SAR synthesis of HFR from a single sounding locating at the right border of the trajectory. By simulating all soundings, the Doppler borders will be averaged, except for both soundings at the ends of the trajectory.

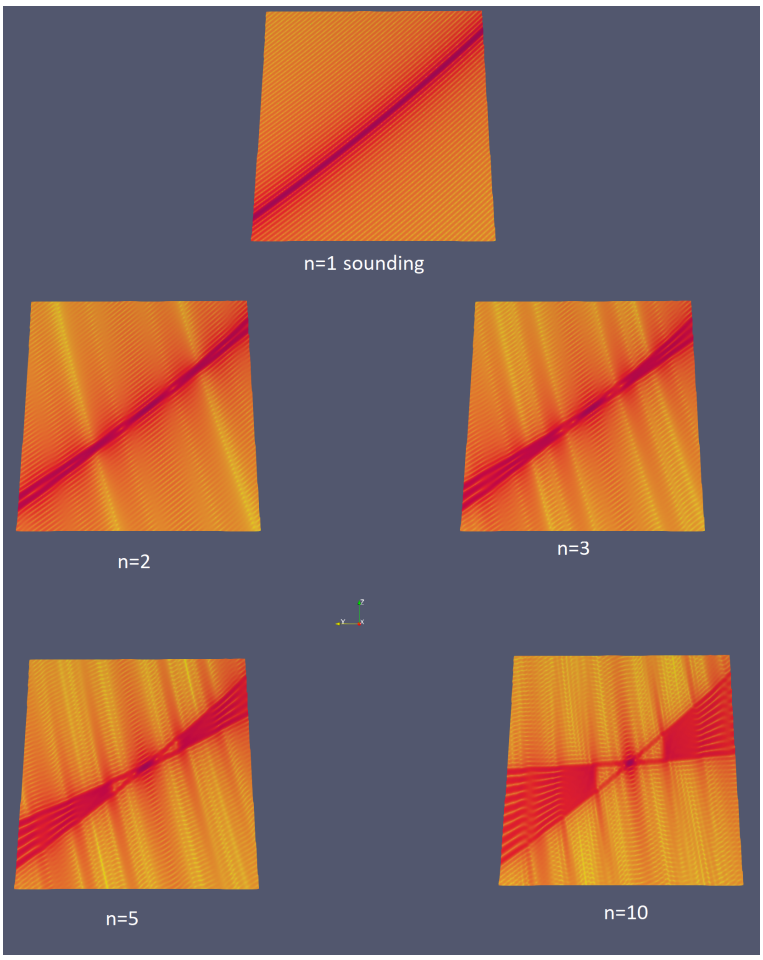

Figure 8.7: Illustration of the origin of the Doppler patterns, when the SAR synthesis is performed with 1, 2, 3, 5 and 10 soundings. The Doppler ambiguities of the final soundings of the trajectory have a higher power than the ambiguities of the other soundings.

The azimuth and range resolutions of HFR are computed from the 3-dB width of the main lobe of the point target pattern and are presented in table 8.2. The range resolution corresponds exactly to the theoretical range resolution of 37 cm, while the azimuth resolution differs a bit from the theoretical azimuth resolution of 21 cm, as expected. Yet, the range and azimuth resolution are both below one meter, which corresponds to the specification of the instrument. The main lobe power and the PSLR levels are presented in table 8.2. As in the Earth observation geometry, no windowing has been performed to reduce the PSLR ratio, in order to observe the raw performance of HFR in a small body observation geometry.

The 3D SAR synthesis shows in figure 8.5 the elevation ambiguity. Compared to the results of Earth observation radars, the ambiguity is defocused at all points except at the position of the target and is not shaped like a straight tube. This is due to the fact that the radar's trajectory is not rectilinear, so the Doppler ambiguities vary during the illumination of the target and the ambiguity tube position is not constant during the whole observation, as illustrated in figure 8.7.
Because of the elevation ambiguity, the location of the target in the elevation direction is ambiguous. However, since the trajectory is not rectilinear, the target position can be resolved in the elevation direction, but with a poor resolution: only 2.2 meters, largely over the range and Doppler resolutions, and over the sub-meter specification of the radar.

Scenario SB-SP-2, described in appendix E, considers the observation of the same point target than SB-SP-1, but the SAR synthesis is pictured on a whole hemisphere of 1999KW4 hemisphere, as presented in figure 8.8. One can identify two different characteristics:

- The projection of the elevation ambiguity on the asteroid surface as depicted in figure 8.5, which

Table 8.2: Performances of HFR in a small body geometry.

Range resolution (m)	0.36
Doppler resolution (m)	0.21
Elevation resolution (m)	2.2
Main lobe power (dB)	-305
PSLR (dB)	-14

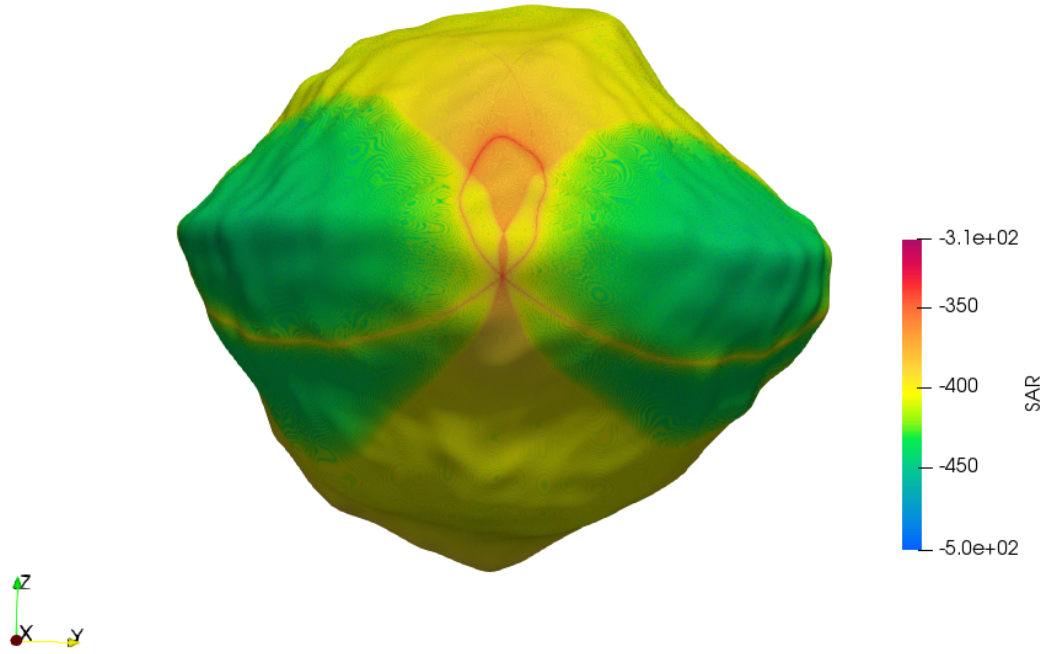

Figure 8.8: KW4 point target response on an entire KW4 hemisphere, following scenario SB-SP-2.

is the area that has the second-highest power after the detected position of the target. On the north hemisphere of the asteroid, this north/south ambiguity has a level of about 15 dB lower than the power associated with the target position.

- The second observable characteristic is the Doppler limit. They are observed at a power about 30 dB lower than the power associated with the target position. The Doppler limits' power could be further reduced by windowing the received spectrum.

Both of these characteristics are artifacts due to the signal processing and lead to unexpected large power corresponding to areas on the surface that do not have any physical characteristics. Thus, they must be reduced as much as possible or must be taken into account in the analysis of SAR images of rough surfaces. While the Doppler sidelobes can easily be reduced by windowing the spectrum, the power of the projection of the elevation ambiguity will be an issue.

Now that the different effects induced by the geometry on the radar image have been understood, the SAR synthesis of extended surface can be computed and HFR results on rough terrains can be analyzed.

8.2.2 Simulation of rough surfaces

Here, we will apply SEPO over rough surfaces created by our random rough surface generator, from roughness parameters motivated by the study of the surface of the asteroid Itokawa.

Lowlands

The Lowlands are small-roughness areas of Itokawa, with a decimetric correlation length and a decimetric RMS height. We present here the result of the simulation applied with scenario SB-SP-3,

described in appendix E. Scenario SB-SP-3 describes the observation of a terrain with the characteristics of Itokawa's Lowlands in a small body geometry. Figure 8.10 pictures the Lowlands DTM generated (left), and the resulting SAR image (right).

The patch form, size, and location are perfectly reconstructed on the SAR image, with the scattered power falling at the edges of the patch when the permittivity becomes smaller than 3.0 and then equal to 1.0. We can conclude from this image that the observed surface has a roughness that seems constant on the whole patch, with a low correlation length. This description corresponds to the DTM that we used for this simulation, which thus confirms the validity of SEPO to image Lowlands surfaces.

Highlands

The Highlands are areas of Itokawa associated with a larger scale roughness, with a metric correlation length and a metric rms height, with an additional smaller-scale roughness, that is representative of the Lowlands. We present here the results of the simulation applied with scenario SB-SP-4, described in appendix E, which considers the observation of a terrain with the Highlands characteristics, in the small body geometry.

Figure 8.11 pictures the used generated DTM (left), and the resulting SAR image (right), and figure 8.12 presents the patch orientation compared to the trajectory (not to scale). The patch form, size, and location are well reconstructed if we take into account the fact that the bottom right portion of the patch scatter almost no energy back to the radar. Indeed, Figure 8.12 presents that the facets building this bottom right portion do not face the radar's trajectory. Figure 8.11 also presented a thin line associated with a high returned power. This power can be explained by taking into account the

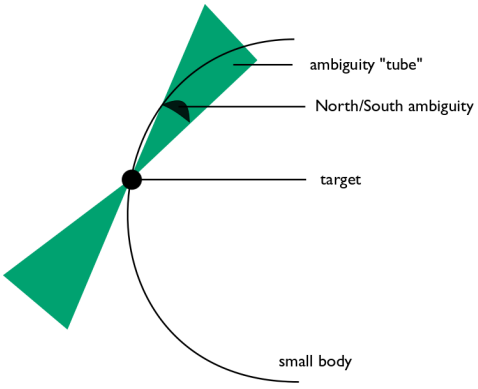

Figure 8.9: Illustration of the elevation ambiguity, occuring because only one pass in elevation is flown.

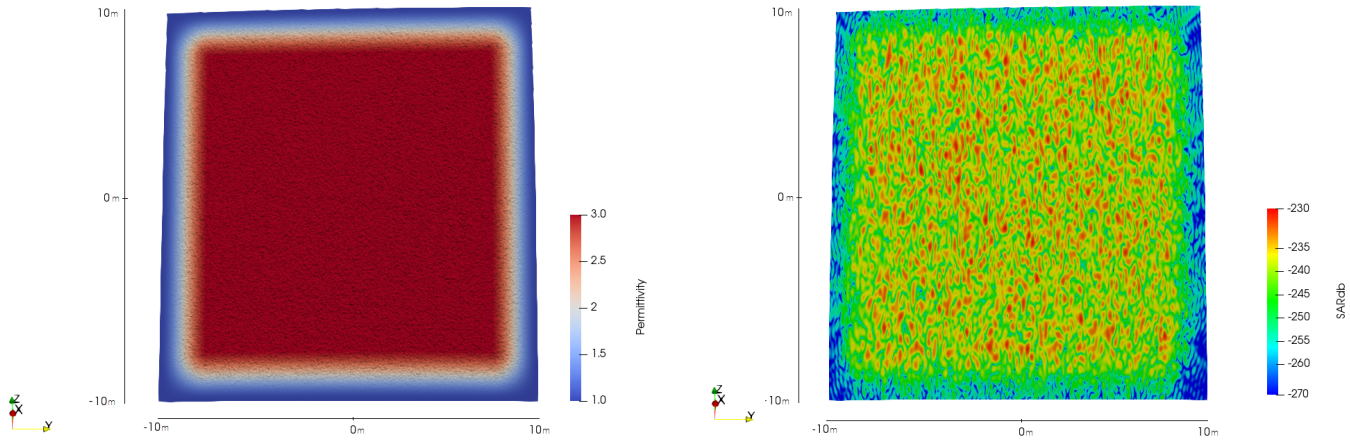

Figure 8.10: Lowland patch (left) and SAR synthesis of scenario SB-SP-3 on the Lowland patch (right).

orientation of the concerned facets, whose normals are aligned with the radar nadir direction. Thus, a larger portion of power is returned to the radar because of specular scattering, and these facets are associated with a large power on the SAR image.
The small-scale roughness of the patch is identified by the lower-powered, rapidly varying, fluctuations of received power, such as pictured on figure 8.10, and the large-scale roughness can be recognized by the slow varying but higher-power variations. Thus, SEPO succeeds in retrieving the characteristics of the surface associated with a large scale roughness.

Mix roughness

SEPO was applied to a surface associated with a large scale roughness and a surface associated with a small scale roughness. However, to experience how SEPO deals with the change of roughness, the DTM of a surface with both a large-scale roughness, associated with a high RMS height, and small-scale roughness associated with a small RMS height was generated. We present here the SAR synthesis' results of scenario SB-SP-5, described in appendix E. Scenario SB-SP-5 considers the observation of a terrain with a mixed roughness. Figure 8.13 (left) presents the DTM used as a rough surface, and

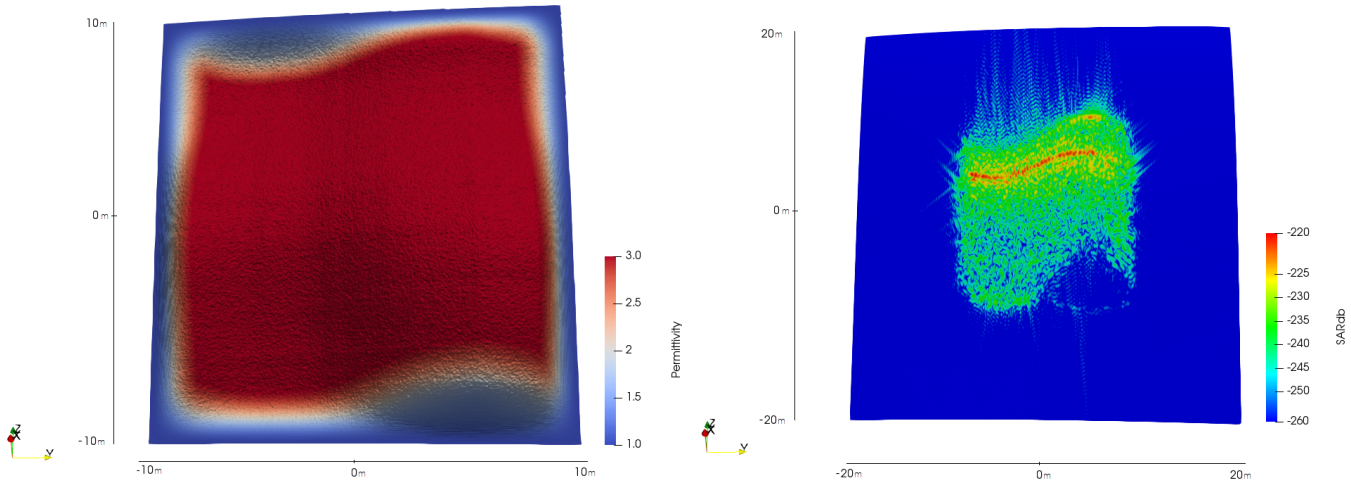

Figure 8.11: Highland patch (left) and SAR synthesis of scenario SB-SP-4 on the Highlands patch (right).

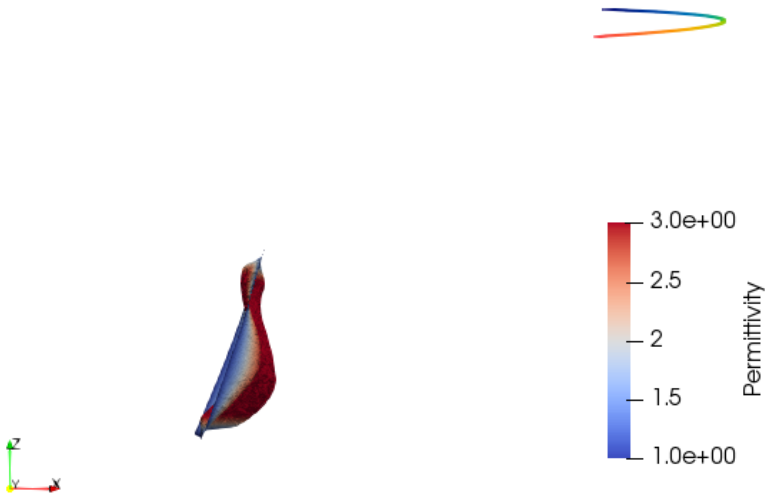

Figure 8.12: Orientation of the Highland patch (left) compared to the trajectory (blue: beginning of the trajectory, red: end of the trajectory). Not to scale.

(right) depicts the SAR image of scenario SB-SP-5 with a range dynamic of 40 dB.

The patch location, form, and size are correctly reconstructed by SEPO. The two different scales of roughness can be identified on the patch, with the power of the smoothest, centered part being lower than the power associated with the external roughest parts. Indeed, the mean power of the smoothest part is about 3dB lower than the roughest part, as depicted in table 8.3. This is expected, since the smoothest areas scatter more energy in the specular direction, and the roughest parts scatter energy in every direction.

In order to observe the behavior of the north/south ambiguity and the Doppler limits than will perturb the global SAR image of the asteroid, the SAR synthesis is performed as well on a whole half hemisphere on an asteroid, which is presented in figure 8.14. The power of the Doppler limits is more than 40 dB below the power of the patch intensity, and their effects can be easily ignored. However, the power of the north/south ambiguity area, recognizable by the high power hyperbola on the North hemisphere, is 13dB below the main patch power, as presented in table 8.4, which is too high to be ignored.

HFR's performances were thus established using the point target measurements and HFR's capacities have been tested on rough surfaces with different roughness parameters. However, the power associated with the north/south ambiguity may be problematic since it is only 13 dB below the mean power of the target. One way to resolve the problem and reduce the power associated with the

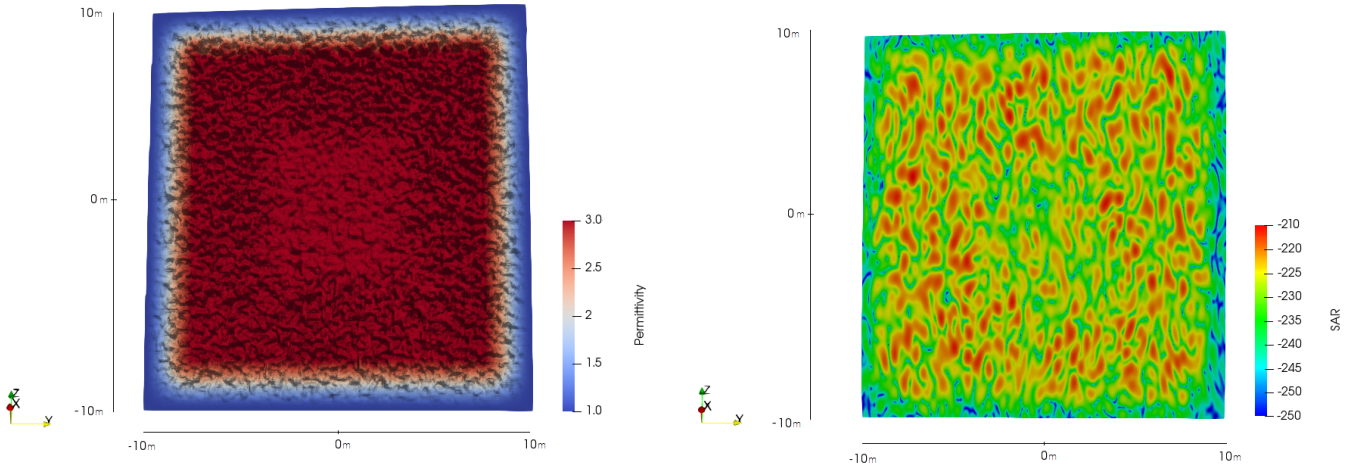

Figure 8.13: Mixed roughness rough patch (left) and the SAR synthesis of scenario SB-SP-5 on a 20m patch (right).

Table 8.3: Difference of power between rough and smooth areas of the mix-roughness patch.

Mean Intensity of the rough parts of the patch	-226 dB
Mean Intensity of the smooth parts of the patch	-229 dB
Difference	3dB

Table 8.4: Difference of power between the patch and the ambiguity.

Mean Intensity of the patch	-226 dB
Mean Intensity of the ambiguity	-239 dB
Difference	13dB

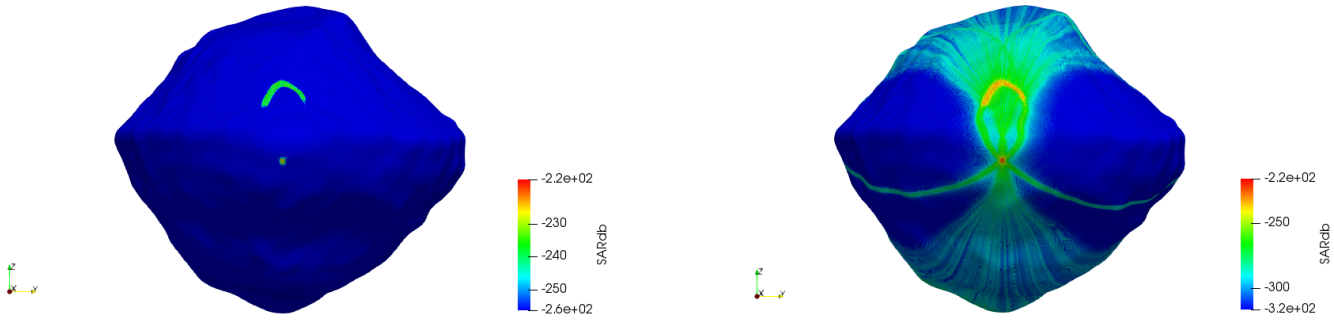

Figure 8.14: SAR synthesis for the mixed roughness patch pictured on a whole KW4 hemisphere with a 40 dB range dynamic (left) and a 100 dB range dynamic (right).

Table 8.5: Difference of power between the main patch and the ambiguity, using a multipass geometry.

Mean Intensity of the patch	-226 dB
Mean Intensity of the ambiguity	-244 dB
Difference	18dB

north/south ambiguity is the use of a multipass orbitography.

Multipass geometry

In order to reduce the power associated with the north/south ambiguity, a multipass orbitography can be implemented. Indeed, the elevation ambiguity's location depends on the radar's position, as it is the direction normal to the slant range direction and the azimuth direction. Thus, by shifting the position of the orbit, the ambiguity position will change, while the target position will not. With a multipass geometry, several SAR images will be acquired, each with a north/south ambiguity at a different position on the asteroid. Thus, by averaging each SAR image synthesis, the mean power of the ambiguity will be reduced. The multipass geometry will thus be applied, following scenario SB-MP-1, described in annex. Scenario SB-MP-1 considers the observation of a terrain with a varying roughness in a multipass, small body geometry.
Figure 8.15 presents the SAR simulation on KW4 half hemisphere with a range dynamic of 100 dB, and figure 8.16 presents the same results with a range dynamic of 40 dB.

Figure 8.15 pictures the 20 north/south ambiguities associated to each flown track, on the North hemisphere. Figure 8.15 thus presents that the power of the ambiguity is largely reduced compared to the single pass orbitography: the maximum power of the ambiguity is about 18 dB lower than the mean power of the patch, as presented in table 8.5 compared to 13 dB with only one track.

8.2.3 Summary

The Kirchhoff Approximation was applied with Surface Echo PO to simulate the field scattered by a rough surface of an asteroid surface, using the digital terrain model of the asteroid 1999 KW4. The rough surface was generated to represent the asteroid's surface with a sampling much smaller than the radar resolution cell, which is about 1 meter. The surface roughness was generated in order to represent the asteroid Itokawa smooth surfaces, rough surfaces, and a mix of both roughness. The facet method was proven to be efficient for simulating the electromagnetic field of an asteroid surface. The size and shape of these different surfaces have been correctly reconstructed, both small-scale and large-scale roughness can be identified from the resulting SAR images, and the difference of roughness of a surface can be identified. Finally, thanks to a multipass geometry, the signal processing artifacts

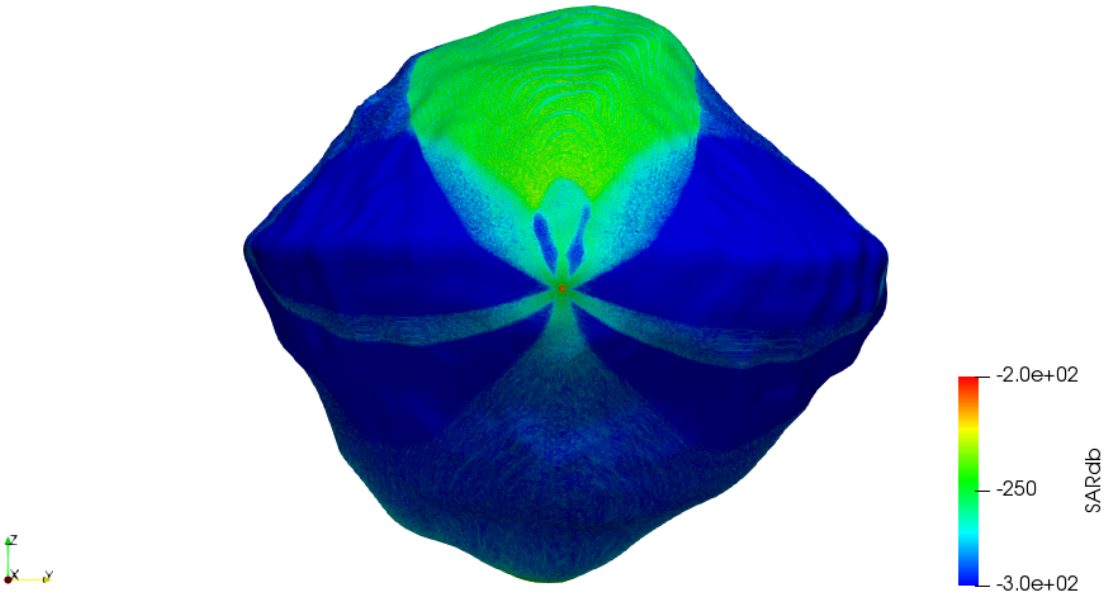

Figure 8.15: SAR image on KW4 using scenario SB-MP-1 with a range dynamic of 100dB.

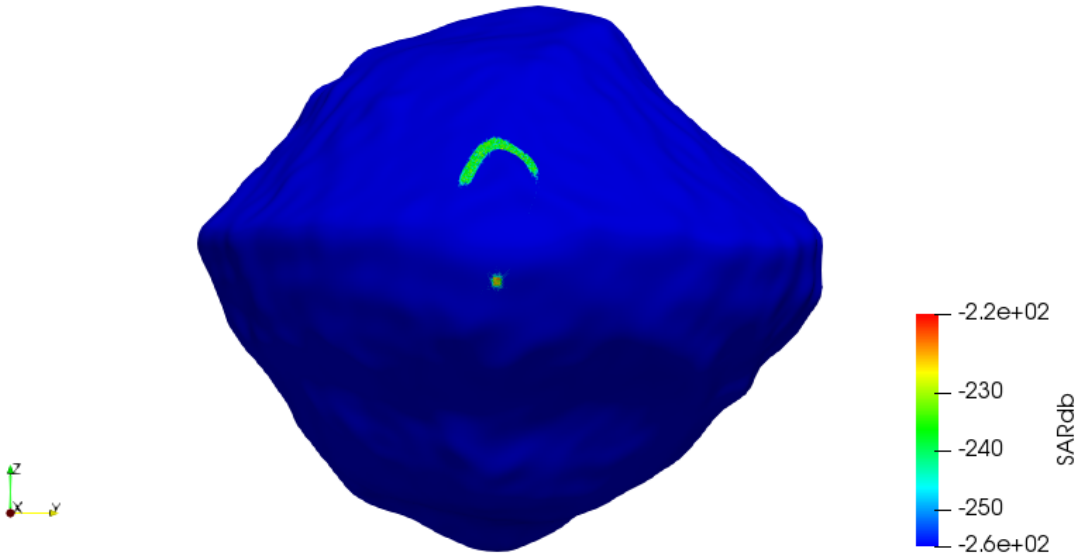

Figure 8.16: SAR image on KW4 using scenario SB-MP-1 with a range dynamic of 40 dB.

power became sufficiently low not to alter the SAR image in a troubling way. From now, the facet method will thus be used for simulation of the electromagnetic field scattered by different surfaces of ab asteroids. However, as the objectives of HFR are to perform the tomography of the first ten meters of the asteroid subsurface, a different model is needed to simulate the field scattered by the subsurface of the asteroids, which is performed by volume scattering models.

Part III

Rocky Volume Scattering Model Selection

This part covers the review of different volume scattering models, and their application to simulate the electromagnetic field scattering by an inclusion embedded in an asteroid subsurface. Computations are carried out in the frequency domain by analogy with the surface models and because of the faster computations. Scattering from 3D volumes has been less studied than for surface scattering, because of the rapidly increasing computational load when the size of the simulated area increases, which makes impossible the simulation of the scattering from large, meaningful volumes. Volume scattering can be modeled as a superposition of surfaces, representing layered media, over which 2D scattering models are applied. However, we will consider only models covering volume scattering.

In the first chapter, we describe two volume scattering models, the Born approximation and the volume SPM. Then the implementation of the Born Approximation is presented, and its results are presented in an Earth observation geometry in order to validate the results and in a small body geometry to study the model's performance.

Contents

Chapter 9

Review of volume scattering models

Several methods have been carried out in order to compute the electromagnetic field scattered by volume media. Numerical solutions to the Maxwell equations, such as the FDTD (Finite Time Domain Difference (Schneider, 2010)) or the MoM (Method Of Moments (Gibson, 2014)) provide rigorous expressions of the scattered field but are computationally intensive. Another method consists in describing the volume under study by a superposition of different layers and applying the surface scattering model to each of the layers, such as described in Tabatabaeenejad et al. (2013). However, we will consider strictly volume scattering models in this study. These models can rely on two main approaches :

- The first approach consists in building a Born series from a volume-integral equation involving the Green's tensor of a medium. The Born approximation and its derivation follow this approach.
- The second studies layered surfaces and consists in deriving a height-perturbative expansion of the surface boundary conditions written under the Rayleigh hypothesis. This approach is close to the SPM but with a volume integral instead.

The Born approximation is a traditional volume scattering method, which considers the electromagnetic field scattered by a weak contrast of permittivity in a volume. However, Guérin et al. (2004) studied the electromagnetic field scattered by rough surfaces on layered surfaces, overcoming the limit of permittivity but restraining to a given geometry.

9.1 The Born approximation

9.1.1 History

The Born Approximation was originally used for describing scattering in quantum mechanics, but it used now as a deterministic, analytical approximate solution of scattering problems in electromagnetics. Hill (1988) used the Born approximation to derive the plane-wave scattering matrix for objects of low contrast, conducted analytical expression for scatterers with general shapes (sphere, cylinders, and box), and included the phase expression for each of these extended targets. These results were conducted in the near and far field and were largely used for ground penetrating radar simulations. Numerical simulations have been conducted in Bucci et al. (2001) with two separate bodies of relative permittivity 4.005 and 4.01 respectively, embedded in a domain of investigation of 1×1 m^2, partitioned into 32×32 square cells. The Born Approximation results were found to restore the model with a permittivity reconstruction error of about 10^{-3}. Li et al. (2004) conducted another set of numerical experiments by reconstructing two anomalies in a volume of 10cm $\times$ 10cm, divided into $23 \times 23 \times 23$ subcubs with an operating frequency of 1 GHz. The reconstruction relative error of the permittivity after performing the inverse problem is less than 0.4. Further work has been conducted on extensions of the Born Approximation, such as Salucci et al. (2014), who used the Born approximation at a second order with a linearization tool call the inexact Newton method to reconstruct buried cylinders.

9.1.2 Description

The Born Approximation considers scatterers (called inclusions) embedded inside a background medium, defined in the following with the index b, such as presented in figure 9.1.

Scattering from the object is described by a volume distribution of currents induced inside the scatterer. Thus, the scattering is described by the following equation:

$$\nabla \times \nabla \times \vec{E}(\vec{R}) - k_b^2 \vec{E}(\vec{R}) = Q(\vec{R})\vec{E}(\vec{R}) + i\omega\mu_0 \vec{J}_s(\vec{R}) - \nabla \times \vec{M}_s(\vec{R}) \tag{9.1}$$

With :

- $\vec{R} = (x, y, z)$ the 3 dimensional position vector
- ϵ and σ' the permittivity and conductivity distributions
- k_b the wave number of the medium: $k_b^2 = i\omega\mu_0\sigma_b' + \omega^2\mu_0\epsilon_b$
- Q the change in the materials properties :
  $Q(r) = i\omega\mu_0[\sigma'(\vec{R}) - \sigma_b'] + \omega^2\mu_0[\epsilon(\vec{R}) - \epsilon_b] = i\omega\mu_0[\sigma(\vec{R}) - \sigma_b] = i\omega\mu_0\Delta\sigma(\vec{R})$
- $\vec{J}_s$ and $\vec{M}_s$ are the impressed electric and magnetic sources

The solution of this equation can be expressed with a dyadic Green's function with the appropriate boundary conditions:

$$\nabla \times \nabla \times \bar{\bar{G}}(\vec{R}, \vec{R}') - k_b^2 \bar{\bar{G}}(\vec{R}, \vec{R}') = \bar{\bar{I}}\delta(\vec{R} - \vec{R}') \tag{9.2}$$

With $\bar{\bar{I}}$, the identity dyadic.
Using the far field approximation, the solution of this equation is:

$$\bar{\bar{G}}(\vec{R}, \vec{R}') = \left[\bar{\bar{I}} + \frac{1}{k_b^2}\nabla\nabla\right] g(\vec{R}, \vec{R}') \tag{9.3}$$

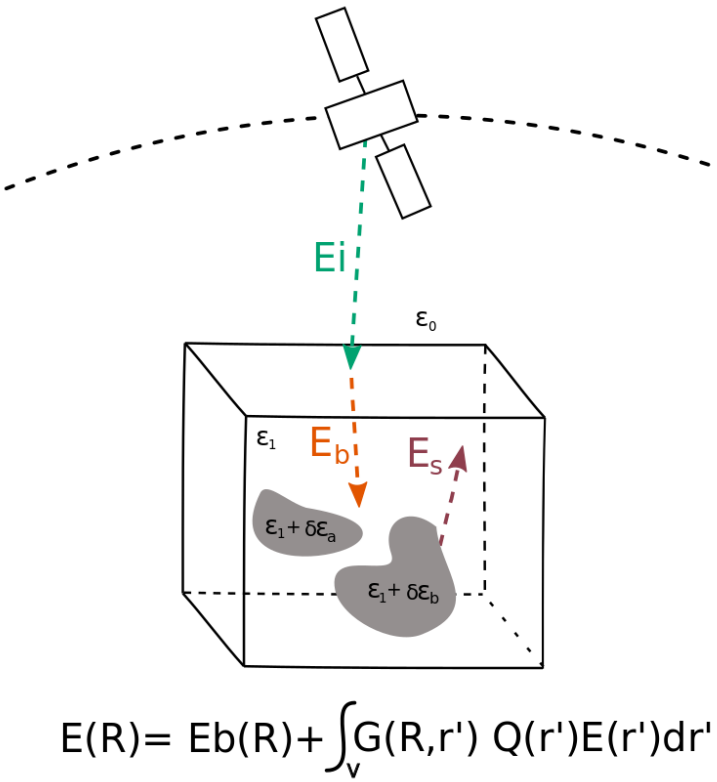

Figure 9.1: Illustration of the Born Approximation geometry.

With :

$$g(\vec{R},\vec{R}') = \frac{e^{ik_b|\vec{R}-\vec{R}'|}}{4\pi|\vec{R}-\vec{R}'|} \tag{9.4}$$

The solution of the equation is given by :

$$\left\{ \vec{E_{vol}}(\vec{R}) = \vec{E}_b(\vec{R}) + \left[\bar{\bar{I}} + \frac{1}{k_b^2}\nabla\nabla\right] \int_{V_s} d\vec{R}' g(\vec{R},\vec{R}') \cdot Q(\vec{R}') \vec{E_{vol}}(\vec{R}') \qquad R \in V_s \right. \tag{9.5}$$

Where V_s is the support of $Q(\vec{R})$ and $\vec{E}_b$ is the solution of the wave equation :

$$\nabla \times \nabla \vec{E}_b(\vec{R}) - k_b^2 \vec{E}_b(\vec{R}) = i\omega\mu_0 \vec{J}_s(\vec{R}) - \nabla \times \vec{M}_s(\vec{R}) \tag{9.6}$$

Since the electromagnetic field inside the integral of equation 9.5 $\vec{E_{vol}}$ is unknown, the integral cannot be computed. In order to overcome this limit, the Born approximation considers that the change in the materials properties Q is sufficiently small to consider that in the homogeneous background, $\vec{E_{vol}}(\vec{R}) \simeq \vec{E}_b(\vec{R})$.
Thus, $\vec{E_{vol}}$ is represented as the sum of the background field $\vec{E}_b$ and the scattered field, generated by the scattering currents (and charges) induced inside the scatterer by the interaction of the field $\vec{E}_b(\vec{R})$ with material variation $Q(\vec{R})$.

The Born approximation relies on the hypothesis that the total field of the volume is equal to the field in the volume without the inclusions. The hypothesis is valid only when the permittivity of the inclusions is small compared to the permittivity of the volume. However, this limit can be overcome, as Chew et al. (1990) imagined by considering the Born approximation as an iterative method where, for its zeroth order, $\vec{E_{vol}}$ is computed as the field of the volume plus the one scattered by the inclusion. Then, further orders would require that the $\vec{E_{vol}}$ is the field computed at the previous iteration. However, when the iterative Born approximation is applied to a media where the variation of permittivity is large, the convergence of the Born approximation is not assured.

9.1.3 Limits

The main hypothesis of the Born approximation is the hypothesis of the low refracting power of the inclusions. This approximation is necessary to the assumption that the total field is equal to the background field inside the integral. The validity of this hypothesis is difficult to assess because we have a limited knowledge on the asteroid's structure. However, this limit can be overcome by an iterative approach. Finally, as any 3D scattering model, the Born Approximation suffers from its large computational load and will be used to model the behavior of small areas only.

9.2 Volume SPM

In order to model 3D volume scattering from substrates located on a layered surface, Guerin and Sentenac (2004) derived a height perturbative expansion from the surface boundary conditions. The method is easily applied to stratified media and is considered as a volume SPM since it performs the same expansion of small heights.

9.2.1 Description

In the volume SPM, the interface between the volume and the void is described with a permittivity ϵ_{ml}, perturbed with different deposits of permittivity ϵ_h, as depicted in figure 9.2.

The permittivity is thus :

$$\epsilon^{ref}(\vec{R}) = \epsilon^{ref}(z) = \begin{cases} 1 & \text{if} \quad z \geq h(r) \\ \epsilon_h & \text{if} \quad 0 \leq z \leq h(r) \\ \epsilon_{ml(z)} & \text{if} \quad z \leq 0 \end{cases} \tag{9.7}$$

The scattering amplitude is found with a perturbative expansion in height and can be written at the second order :

$$\mathbb{S}(\vec{K},\vec{K_0}) = \mathbb{R}(\vec{K_0})\delta(\vec{K}-\vec{K_0}) + TF_\zeta(\vec{K}-\vec{K_0})\mathbb{B}_1(\vec{K},\vec{K_0}) + \int TF_\zeta(\vec{K}-\xi)TF_\zeta(\xi-\vec{K_0})\mathbb{B}_2(\vec{K},\vec{K_0},\xi) \quad (9.8)$$

where $\mathbb{R}$ is the same matrix used for the zeroth-order of the surface SPM, $\mathbb{B}_1$ and $\mathbb{B}_2$ are the first and second order Kernel of the SPM method, developed in T. M. Elfouhaily et al. (2004), and TF indicates the Fourier transform.
Guerin also presented the results for heterogeneous deposits located on a layered surface, as depicted on figure 9.3 for which the analytical computation can be found in Guerin and Sentenac (2004) and does not differ much from the homogeneous case.

9.2.2 Limits

As the SPM method, the volume SPM was designed for substrates with a small thickness compared to the wavelength, since it performs an expansion in height. This means than the method would be adapted to model inclusions that are a few centimeters thick, and located on the surface, which do not correspond to our need.

9.2.3 Results

Guerin and Sentenac (2004) numerically tested the method for one dimensional surfaces, compared the results with rigorous Born approximation results and validated the approach. The method was tested with both an homogeneous and hetereogeneous geometry. An agreement between the SPM and the Born approximation for dielectric surfaces was achieved for homogeneous surfaces, as presented on figure 9.4, but the results differs from optical metallic surfaces, as shown on figure 9.5, because the Born Approximation does not account for multiple scattering.

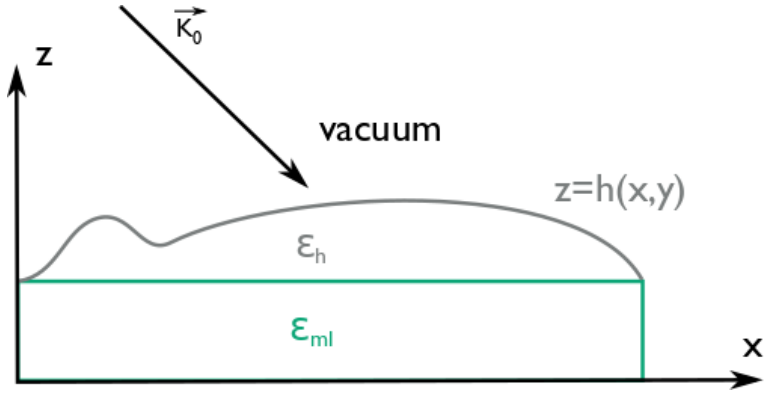

Figure 9.2: Geometry of homogeneous deposits on a multilayer substrate (Guerin & Sentenac, 2004).

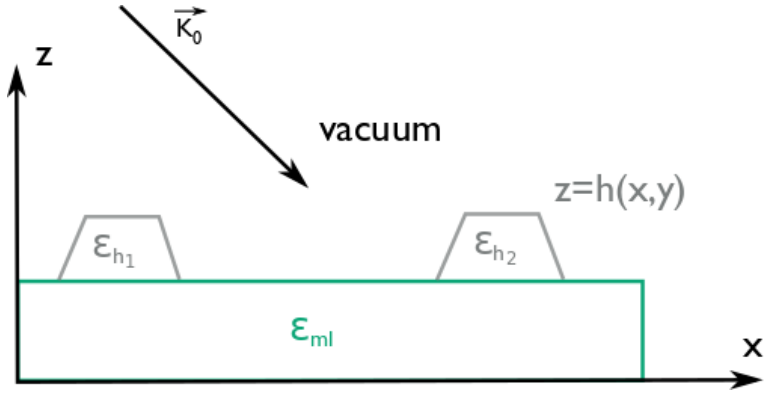

Figure 9.3: Geometry of heterogeneous deposits on a multilayer substrate (Guerin & Sentenac, 2004).

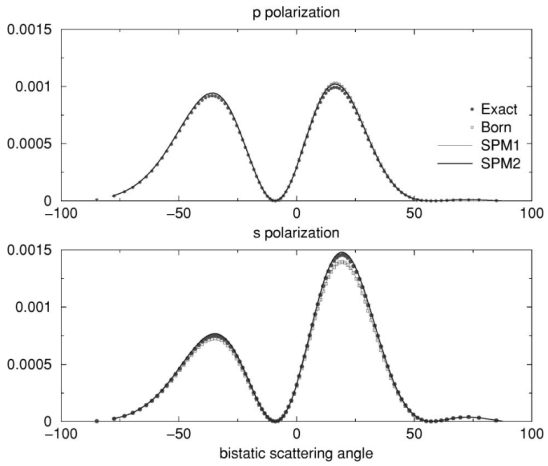

Figure 9.4: Scattering cross section at 20° incidence for the geometry of $\epsilon_h = \epsilon_{ml} = 2.25$ (glass on glass) (Guerin & Sentenac, 2004).

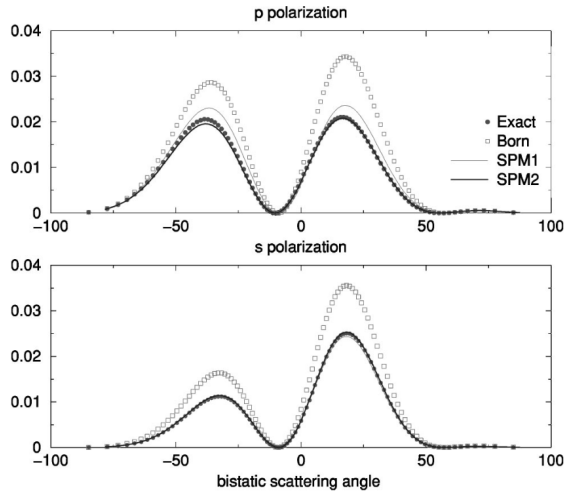

Figure 9.5: Scattering cross section at 20° incidence for the geometry of $\epsilon_h = \epsilon_{ml} =$ -3+0.8i (metal on metal) (Guerin & Sentenac, 2004).

9.3 Summary

This review of existing volume scattering models covered promising models applicable for use in a UWB radar simulator. We considered in this part:

- The Born Approximation
- The Volume SPM

Both volume scattering models under study are based on restrictive hypotheses: in the Born approximation, the inclusions need to have low refracting power, while in the volume SPM, the layers must be homogeneous. As the volume SPM requires homogeneous layers and considering that the Born approximation has been successfully implemented for performing tomography, we will consider applying the Born approximation as a volume scattering model to the small body geometry in order to model the electromagnetic field scattered by inclusion embedded below an asteroid surface, in its zeroth-order. As presented, the main limitation of this method is its computational load. The model will thus be implemented only to small areas, with a small number of inclusions.

Chapter 10

Application of the Born approximation to recover inclusions embedded in a subsurface

The Born Approximation (BA) is a volume scattering method, used to simulate the field scattered by a volume perturbed with inclusions. The BA will be applied to image inclusions located in the asteroid's subsurface.
The volume of subsurface studied is described as a cube volume, called the background volume associated with a homogeneous permittivity ϵ_a, which is perturbed by inclusions, described as subcubs, associated with a permittivity $\epsilon = \epsilon_a + \epsilon_f$. This background volume is separated from the void by an interface, associated with a permittivity ϵ_a described as a mesh of triangular facets.
The Kirchhoff Approximation, with SEPO for the reflection part (described in chapter 5), is applied to compute the field reflected from the interface back to the radar's antenna, as well as the field transmitted from the surface to each center of the subcubs. The field scattered by each volume subcub is then computed, and evaluated at the position of the radar's antenna.

The Born approximation algorithm is thus separated into three main parts:

- The reflection of an incident wave by the surface
- The transmission of this incident wave by the surface
- The transmission of the wave scattered by the inclusion to the radar

After computing these three steps, the spectrum of the field scattered by the inclusions and the surface is obtained and can be further treated by the SAR processor.

The implementation of the Born approximation is described in the following sections. The implementation of the BA is inspired by SEPO architecture and will be using similar notations: $\vec{r_0}$ corresponds to the position of the radar antenna, $\vec{r_1}$ corresponds to the position of the scattering inclusion in the volume and $\vec{r}$ corresponds to the position of the point scattering the wave at the surface of the background volume. α corresponds to the denomination of one of the facet describing the surface.

10.1 Implementing the Born approximation using a meshed boundary surface

10.1.1 Reflection by the surface

The reflection by the interface between the void and our volume of investigation is computed with the facet method, implemented with SEPO (Berquin, 2014), described in part II. The phase is developed linearly on each facet.

10.1.2 Transmission by the surface

The second step, transmission by the surface to the volume is also handled with the facet method but was not computed by SEPO. Thus, we describe in the following section the implementation of the transmission of a wave by a surface, using the Kirchhoff approximation.

As for the fields reflected by the interface, the transmitted fields are computed using the Huygens-Fresnel principle, stating that the fields at any point in space can be expressed from the field at the scattering surface S'. For the reflection case, surface fields were computed with the local Fresnel coefficients. Since the tangential component of the electric field is continuous, the surface field is computed in the same way for the reflection step. This step gives $\vec{n} \times \vec{H}(\vec{r})$ and $\vec{n} \times \vec{E}(\vec{r})$ at the surface of the background cube.
Then, the field transmitted to each subcubs with fluctuating permittivity $\epsilon_f \neq 0$ are computed :

$$\vec{E}_b(\vec{r}) = \int_S [i\omega\mu_0 \bar{\bar{G}}(\vec{r_0}, \vec{r}) \cdot [\vec{n} \times \vec{H}(\vec{r})] + \nabla \times \bar{\bar{G}}(\vec{r_0}, \vec{r}) \cdot [\vec{n} \times \vec{E}(\vec{r})]] dS \tag{10.1}$$

Where S is the surface of the facet, and $\vec{n}$ the normal to the facet. $\bar{\bar{G}}(\vec{r_0}, \vec{r})$ is the dyadic Green function for the homogeneous space, and can be written in the far field:

$$\bar{\bar{G}}(\vec{r_0}, \vec{r}) = (\bar{\bar{I}} - \vec{k_t}\vec{k_t}) \cdot \frac{-e^{i \cdot k_t |\vec{r_1} - \vec{r}|}}{4\pi |\vec{r_1} - \vec{r}|} \tag{10.2}$$

Where $\vec{k_t}$ is the transmitted wave vector.
Considering that the incident wave can be written :

$$\vec{E_i}(\vec{r_0}, \vec{r}) = E_0 \cdot e^{i \cdot \vec{k_i} \cdot (\vec{r} - \vec{r_0})} \cdot \vec{e_i} \tag{10.3}$$

Thus the electromagnetic transmitted field can be written :

$$\vec{E}_b(\vec{r_1}, \vec{r_0}) = i \cdot k_t \cdot (\bar{\bar{I}} - \vec{k_t}\vec{k_t}) \cdot \int_S [\vec{k_t} \times (\vec{n} \times \vec{E}(\vec{r})) + \eta \times (\vec{n} \times \vec{H}(\vec{x}))] \cdot \frac{e^{-i \cdot (k_i \cdot |\vec{r} - \vec{r_0}| + k_t \cdot |\vec{r} - \vec{r_1}|)}}{4\pi \cdot (|\vec{r} - \vec{r_0}| + |\vec{r} - \vec{r_1}|)} dS' \tag{10.4}$$

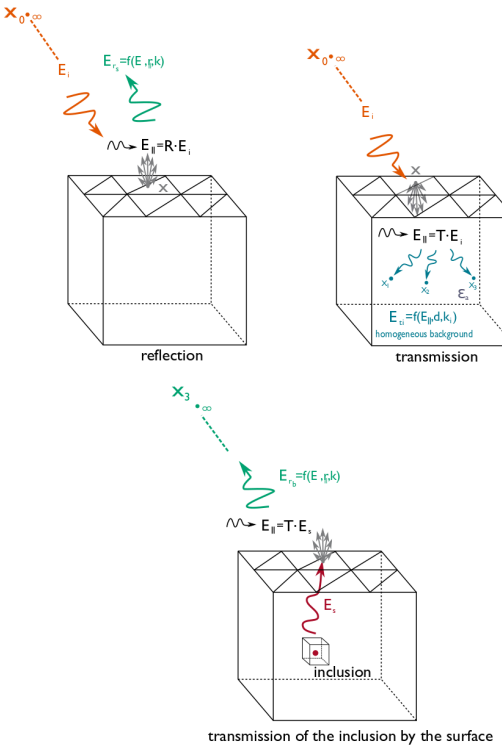

Figure 10.1: Illustration of the different steps of the Born Approximation algorithm.

Given that $\vec{n} \times \vec{E}(\vec{r})$ and $\vec{n} \times \vec{H}(\vec{r})$ are given using the Fresnel coefficients, they are constant for each facet. Thus, the surface field can be expressed as a product of a geometrical term $\mathrm{F}^{\alpha}(r_0, \vec{r})$, constant over each surface facet, and a phase term $e^{i\phi_{\alpha}(\vec{r_0},\vec{r_1},\vec{r})}$ such that :

$$\vec{E_b}(\vec{r_1}, \vec{r_0}) = F(\vec{r_0}, \vec{r})^{\alpha} \cdot \int_{\alpha} e^{\phi_{\alpha}(\vec{r_0},\vec{r_1},\vec{r})} dS' \tag{10.5}$$

The constant term $\mathrm{F}^{\alpha}(\vec{r_0}, \vec{r^{\alpha}})$ is the same than for the reflection phase, taking into account that the wave vector becomes $\vec{k_t}$, but the phase term has changed and needs to be developed :

$$\phi(\vec{r_0}, \vec{r_1}, \vec{r}) = k_i \cdot |\vec{r} - \vec{r_0}| + k_t \cdot |\vec{r_1} - \vec{r}| \tag{10.6}$$

Consider than HFR's maximum wavelength is about one meter, and will be probing the first ten meters of an asteroid the BA will consider targets embedded at distances less than fifteen wavelengths from the surface. Thus, to keep the far field hypothesis, each facet must behave as like a point target, and thus the surface sampling must be large enough. This means that the phase term can be supposed to be constant on the entire facet, which is equivalent to developing the phase at the zeroth order. Thus, the phase can be written :

$$\phi(\vec{x_0}, \vec{x_1}, \vec{x}) = k_i \cdot |\vec{r_c} - \vec{r_0}| + k_t \cdot |\vec{r_1} - \vec{r_c}| \tag{10.7}$$

With $\vec{r_c}$ the center of each inclusion.

10.1.3 Scattering of the inclusion back to the radar

For the third and final step, we consider that each inclusion is the emitter of an incident field $\vec{E}_{incl}$ that is transmitted by the interface to the radar :

$$\vec{E}_{incl} = \int_V \frac{\Delta\epsilon \cdot \vec{E_b}}{4\pi|\vec{r_1} - \vec{r}|} e^{-ik_s \cdot |\vec{r_1} - \vec{r}|} dV \tag{10.8}$$

With, $\Delta\epsilon$ the difference between the inclusions' permittivity and the background volume permittivity ϵ_a, V the volume of each subcubs and $\vec{E_b}$ is the transmitted electromagnetic field inside the background volume.

In order to compute the integral term, the subcubs will have to be point targets, and thus small in regards to the incident wavelength. Thus, equation 10.8 can be rewritten:

$$\vec{E}_{incl} = \frac{\Delta\epsilon \cdot \vec{E_b}}{4\pi|\vec{r_c} - \vec{r_1}|} e^{-ik_s \cdot |\vec{r_c} - \vec{r_1}|} \cdot V \tag{10.9}$$

With $\vec{r_c}$ is the position of the center of each subcubs, and V is the volume of each subcub. In our implementation of the Born approximation, V is supposed to be very small, in order to correspond to point targets. This step is thus an inversion of the transmission step: an incident field, $\vec{E}_{incl}$, the field scattered by the inclusion, propagates in a medium of permittivity ϵ_a, hits a surface with a permittivity ϵ_a and propagates in the void to a receiver at the position $\vec{r_0}$. Since the surface is the same as in the transmission case, the phase development is similar to the transmission case. The surface fields are recomputed, the far field dyadic green function of a wave propagating in the void is applied, and the field at position $\vec{r_0}$ is calculated.

These three steps are repeated for each inclusion for a given facet, and the resulted spectra are summed to obtain the spectrum of the facet. The computation is then repeated for all the facets of the surface and summed to obtain the spectrum of the entire interface. Once the algorithm is finished, a spectrum is obtained and can be treated with SAR processing. However, we have to keep in mind that some hypotheses were made in the derivation of the algorithm, which are detailed in the next section.

10.1.4 Limits

Several hypotheses were set for the derivation of the Born approximation, which lead to the following restrictions:

1. The model does not take into account multiple scattering.
2. Inclusions are only described as point targets, shaped a cube facets in our 3D geometry.
3. Inclusions must be small enough to be considered as point targets.
4. Inclusions must not be located on the borders of the volume under study. Indeed, our implementation considers that each subcub is seen by a large number of facets meshing the surface. If a subcub is located on the border of the volume, it will only be seen by facets at one of its side. Thus this geometry would not constitute a physical scenario and its results would be meaningless.
5. Facets describing the surface must be small enough to act like point targets.
6. The variation of permittivity $\Delta\epsilon$ must be small.

However, we assume that these limitations are sufficiently negligible to have an impact on our first results. Some of these limits are simple to overcome, such as the fact that the inclusion must not be at the borders of the volume, and were only impose to reduce the computational load of our algorithm. Other limits, such as the size of the inclusion, their shape and the size of the surface facets, would require some further study to decide whether or not they can be overcome, while the fact that multiple scattering is not taking into account is part of the Born Approximation concept and will have to be taken into account. Finally, the limitation of small permittivity could be overcome by performing the Born approximation in its iterative form, assuming the convergence of the results.

The algorithm is implemented on IDL and applied to different scenarios in order to test its results.

10.2 Validation of the Born approximation

In order to validate our implementation of the Born approximation, we will apply the BA to four different scenarios :

1. Scenario EO-SP-2: First we will consider the scenario of a point target surrounded by void, in the Earth Observation geometry. The Earth Observation geometry is adopted because of the simple and characteristic cardinal sine of a point target, which allow us to validate the method easily.
2. Scenario EO-SP-3: Then, we will consider the scenario of a point target embedded in a medium with a permittivity of 3.0, in the Earth Observation geometry. The inclusion should then have a point target behaviour.
3. Scenario SB-SP-6: Once the scenarios in the Earth Observation geometry are validated, we will consider the scenario of a point target surrounded by void in the small body geometry. This scenario will be used to analyze the BA applicability and performances in a small body geometry.
4. Scenario SB-SP-7: Finally we will consider the case of a point target, embedded in a medium with a permittivity of 3.0, in the small body geometry. The inclusion should then have a point target behavior. This scenario corresponds to the most realistic case the BA will be able to perform for now.

As each of these scenarios should have responses similar to the response of a point target, we will compare the BA SAR synthesis of each scenario to the SAR synthesis of a point target obtained with SEPO. The SAR synthesis pattern and performances of both models should be identical, such as their

resolution.
As detailed in 8.1.3, the resulting SAR images will be associated with low scattered power, that may be lower than minus few hundreds of dB. Indeed, the simulations do not cover any process gain, antenna gain, or synthesis gain. Moreover, they do not consider any gain that may be reached with the range/Doppler compression.

Additionally, the main power of the spectrum obtained with the BA will be much lower than the spectrum obtained with SEPO. Indeed, if we take into account the power losses that are due to the transmission of the small interface, the scattering of a point inclusion, a cube with a very small volume and the retransmission of the wave by the first interface, the power of the scattered spectrum of the inclusion will be very low. However, the goal of this chapter is to validate the point target pattern with the BA and not estimate how it can reconstruct a physical model. Further work will have to be carried out on the Born approximation in order to compute realistic scenarios and analyze the physical meaning of the scattered powers.

10.2.1 Earth Observation geometry

Scenario EO-SP-2: Point target in the void

We present here the SAR synthesis results of the scenario EO-SP-2, which is described in appendix D.

In order to verify that the BA results are correct, we will compare the results of the scenario EO-SP-2, with the response of a point target obtained with SEPO. Indeed, both SAR syntheses should have similar patterns, ignoring some power normalization factor. Figure 10.2 depicts the SAR synthesis obtained with a point target spectrum computed with SEPO (left), and the SAR synthesis obtained with the BA spectrum (right). In figure 10.3, the elevation ambiguity is plotted with a 40 dB range dynamic for a point target spectrum computed with SEPO (left) and for the scenario computed with the BA (right), while the theoretical location of the inclusion is represented as a white sphere. The performance comparison between the Born Approximation and Surface Echo PO are summarized in table 10.1.

The BA correctly locates the target at the center of the frame and in the center of the ambiguity tube. The cardinal sine of the point target pattern is recovered, as well as the values of the range, Doppler, and elevation resolutions, as presented in table 10.1. Thus the BA achieves to model the field scattered by a point target in the void.

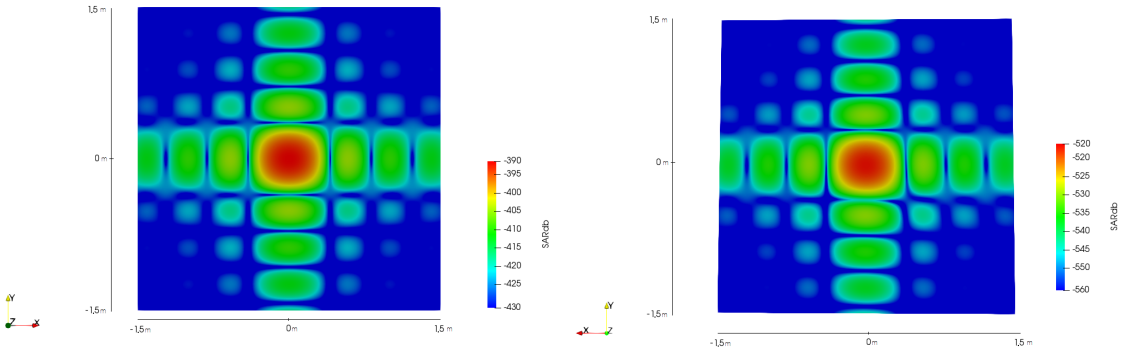

Figure 10.2: Scenario EP-SP-2: SAR image of a point target whose spectrum was computed using SEPO (left) and using the BA (right) on a 2D surface.

Scenario EO-SP-3: Point inclusion in a background volume of permittivity equal to 3.0

We present here the SAR synthesis results of the scenario EO-SP-3 presented in appendix D.

We expect that the BA results of scenario EO-SP-3 will be similar to the response of a point target obtained with SEPO. Figure 10.4 represents the SAR synthesis of a point target whose spectrum was obtained with SEPO (left) and the results of scenario EO-SP-3 computed with the Born approximation (right). Figure 10.5 depicts the SAR volume synthesis and the elevation ambiguity of SEPO (left) and of the BA (right) and depicts the theoretical position of the target with a white sphere. The performances of both SAR synthesis are presented in table 10.2.

The SAR synthesis of the BA in figure 10.4 (right presents that the classical SAR cardinal sine point target pattern is reconstructed by the BA. The volume SAR syntheses present that the BA correctly reconstructs the pattern of the SAR synthesis, but does not correctly locate the target. This location error is induced by a phase error generated by the background permittivity ϵ_a, which is not compensated by the SAR synthesis, which considers that the signal is propagating in a medium with a permittivity of 1. Finally, table 10.2 demonstrates that the resolution and the peak-sidelobe ratios of the BA are close to those achieved with SEPO. The difference in the resolution is superior to the sampling of 0.6 cm, and could be explained by the defocalization of the signal since the propagation in a media with a permittivity different than 1 is not compensated by the SAR synthesis

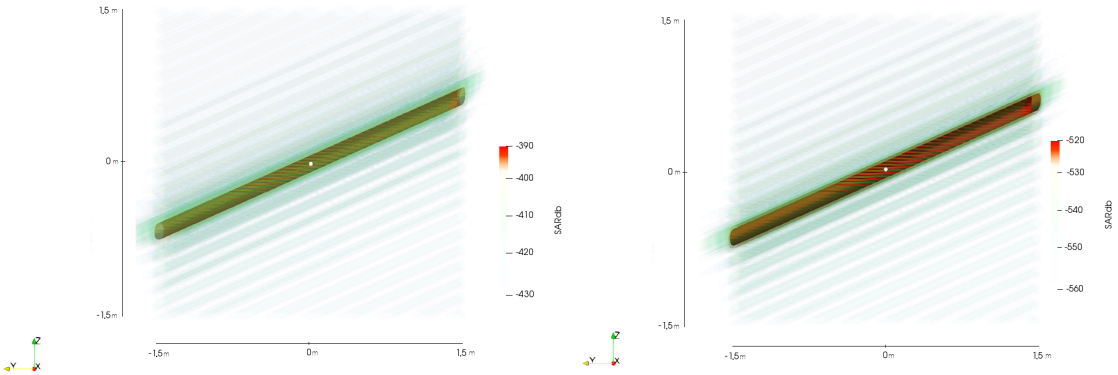

Figure 10.3: Scenario EP-SP-2: SAR image of a point target whose spectrum was computed using SEPO (left) and using the BA (right) on a 3D volume. The target theoretical position is indicated with a white sphere.

Table 10.1: Scenario EP-SP-2: Performances comparison between SEPO and the BA.

	Born Approximation	Surface Echo PO
Range resolution (m)	0.31	0.31
Doppler resolution (m)	0.35	0.35
Elevation resolution (m)	-	-
Peak to Side-lobe ration (dB)	-13	-13

Table 10.2: Scenario EO-SP-3: Performances comparison between SEPO and the BA

	Born Approximation	Surface Echo PO
Range resolution (m)	0.32	0.31
Doppler resolution (m)	0.36	0.35
Elevation resolution (m)	-	-
Peak to Side-lobe ration (dB)	-13	-13

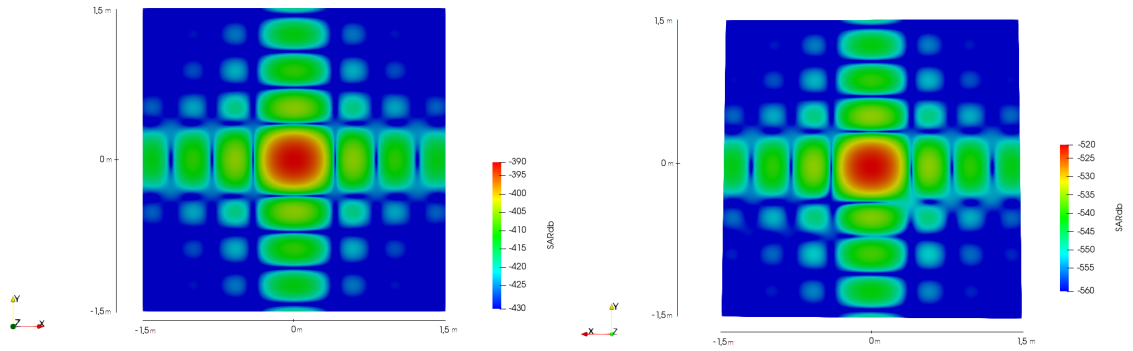

Figure 10.4: Scenario EO-SP-3 :SAR image of a point target spectrum computed with SEPO (left) and with the BA (right) on a 2D surface.

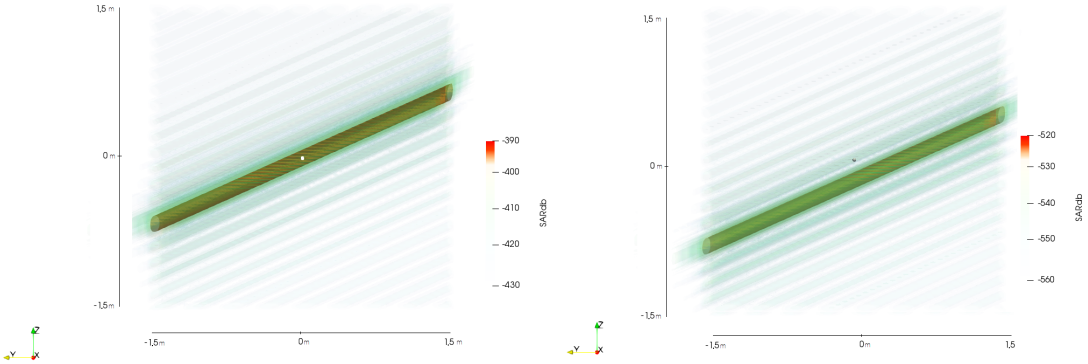

Figure 10.5: Scenario EO-SP-3 :Results of a point target spectrum computed with SEPO (left) and with the BA (right) visualized in a volume area. The target theoretical position is indicated with a white sphere.

Thus, the BA was found to reproduce the point target behavior in an Earth observation geometry and reproduced the performances achieved by SEPO. However, these scenarios focus on the scattering of one single inclusion and do not take into account the presence of several inclusions. Since the scattered field of each inclusion is computed in an independent manner and summed for each facet, the behavior of the Born approximation with several inclusions should be recovered. A further study should be performed in order to confirm this hypothesis but such simulations could not be done before having GPU computations, in order to compute the BA on larger volumes.

A further step in the validation of our results is to confront the Born approximation to the small body geometry and estimate the performances of the Born approximation for the study of the sub-surface of asteroids.

10.2.2 Small-body geometry

Scenario SB-SP-6: Point target in the void

We present here the SAR synthesis results of the scenario SB-SP-6 presented in appendix E.

We expect that the SAR synthesis computed from the BA results of scenario SB-SP-6 will be similar to the response of a point target obtained with SEPO. We expect both SAR syntheses to have similar patterns, ignoring some power normalization factor, that is due to the geometry of the BA. We present below the first results of our simulations: Figure 10.6 represents the SAR synthesis obtained with the

spectrum computed with SEPO (left), and the SAR synthesis obtained with the spectrum computed by the BA (right) obtained using the same geometry. In figure 10.7 the elevation ambiguity is plotted with a 40 dB range dynamic for SAR images computed using SEPO (left) and the BA (right), and the theoretical location of the inclusion is represented as a white sphere. The performances' comparison between the BA and SEPO is summarized in table 10.3.

The resolutions of the two SAR syntheses are the same in the range and azimuth direction, with the measurement accuracy available, and the sidelobes levels difference of both responses are very similar. The resolutions are also comparable in the elevation direction, up to the sampling measurement error. The orientation of the sidelobes pattern are respected, are 1dB higher with the Born approximation

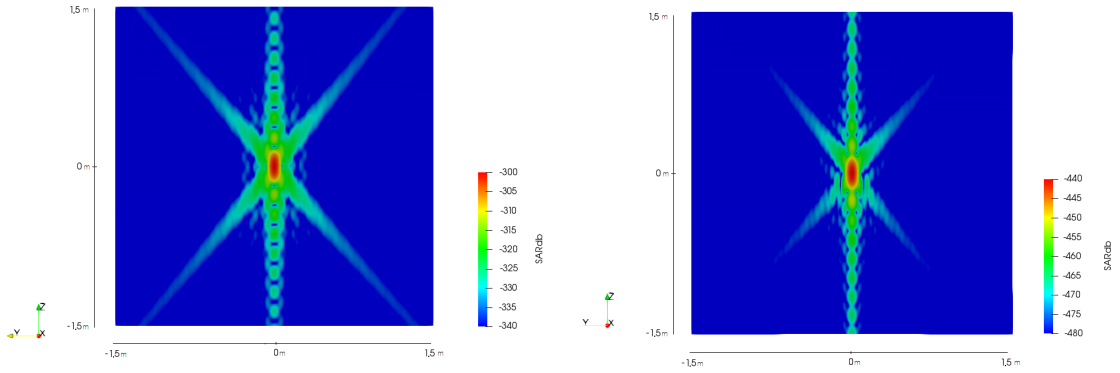

Figure 10.6: Scenario SB-SP-6: SAR image of a point target spectrum computed with SEPO (left) and with the BA (right) on a 2D surface.

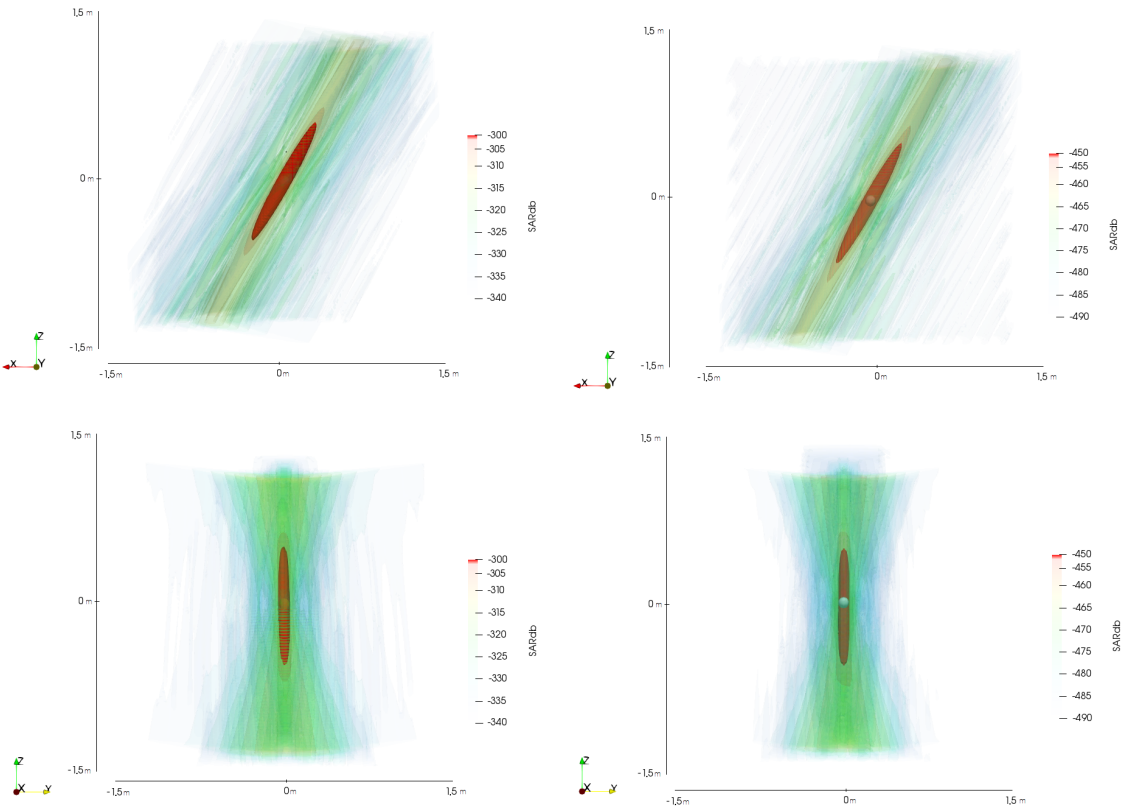

Figure 10.7: Scenario SB-SP-6: Results of a point target spectrum computed with SEPO (left) and with the BA (right) visualized in a volume area. The target theoretical position is indicated with a white sphere.

than with a point target, but this difference is negligible. However, even though the global "star" patterns of both SAR syntheses are similar, they are not exactly the same, and the extension of the Doppler patterns are shortened with the Born approximation, which seems to act as a windowing effect on the Doppler sidelobes. This effect may be caused by the different approximations carried out by the BA. Namely, in the Born Approximation, the incident waves are propagating to the surface before being transmitted to the inclusion. However, the surface has a finite size: and the inclusion is not seen by an infinite number of facets. Scenario SB-SP-6 thus would be equivalent to the observation of a point target if the surface was an infinite plane, as illustrated in figure 10.8, which is not the case.

From this comparison, the Born approximation was found to reproduce the SAR synthesis pattern from a point target surrounded by the void in a small body geometry with acceptable precision. The next step is to validate the BA in the small body geometry, but with an interface and a background volume different from the void.

Scenario SB-SP-7: Simulation scenario of a point target in a background volume of permittivity equal to 3.0

We present here the SAR synthesis results of the scenario SB-SP-7 presented in appendix E.

We expect that the BA results of scenario SB-SP-7 will be similar to the response of a point target obtained with SEPO. Thus, both SAR syntheses should have similar patterns, ignoring some power normalization factor. We present below the first results of our simulations: Figure 10.9 represents the SAR synthesis obtained with the spectrum of a point target using SEPO (left), and the SAR synthesis obtained with a spectrum computed the BA using the same configuration (right). In figure 10.10 the elevation ambiguity is plotted with a 40 dB range dynamic using SEPO (left), and using the BA (right), and the theoretical location of the inclusion is represented as a white sphere.

Table 10.3: Scenario SB-SP-6: Performances comparison between SEPO and the BA.

	Born Approximation	Surface Echo PO
Range resolution (m)	0.54	0.54
Doppler resolution (m)	0.21	0.21
Elevation resolution (m)	2.3	2.3
Peak to Side-lobe ration (dB)	-12	-13

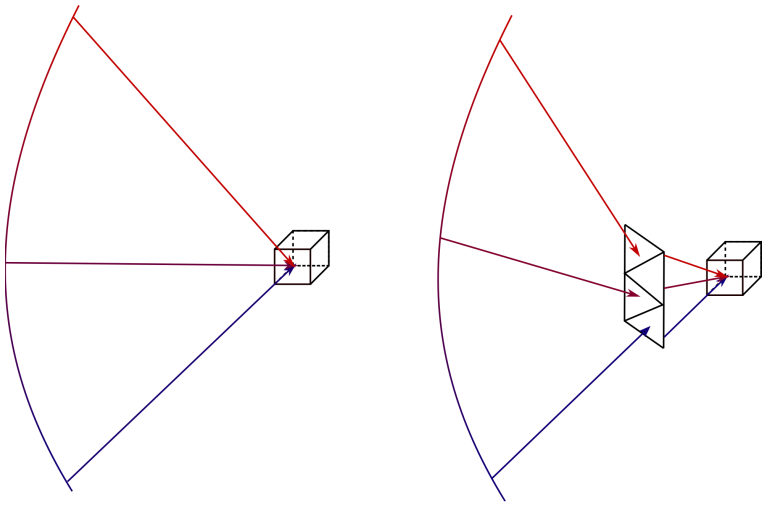

Figure 10.8: Scenario SB-SP-6: Difference between the observation of a point target and a point inclusion with the BA. When the length of the surface is too small, the geometry differs largely with the observation of a point target in the void.

The performance comparison between the Born Approximation and Surface Echo PO are summarized in table 10.4.

The resolution and sidelobes levels of both responses are very similar, close up to a sampling error. The difference between the BA and SEPO resolutions may be due to the defocalization of the point target response when the wave is propagating in a medium with a permittivity different than 1. The sidelobes are 1dB lower with the BA than with SEPO but the difference is negligible. The global patterns of each response are similar, and the orientations of the sidelobes tubes are respected. Even if the extensions of the Doppler sidelobes are shorten with the BA, for the same reasons as explained in scenario EO-SP-3.

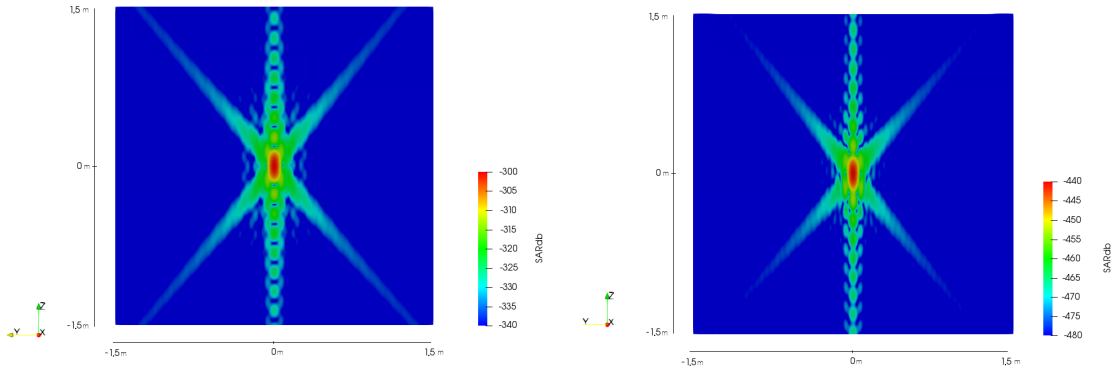

Figure 10.9: Scenario SB-SP-7: SAR Image of a point target with a spectrum computed with SEPO (left) and with the BA (right) on a 2D surface.

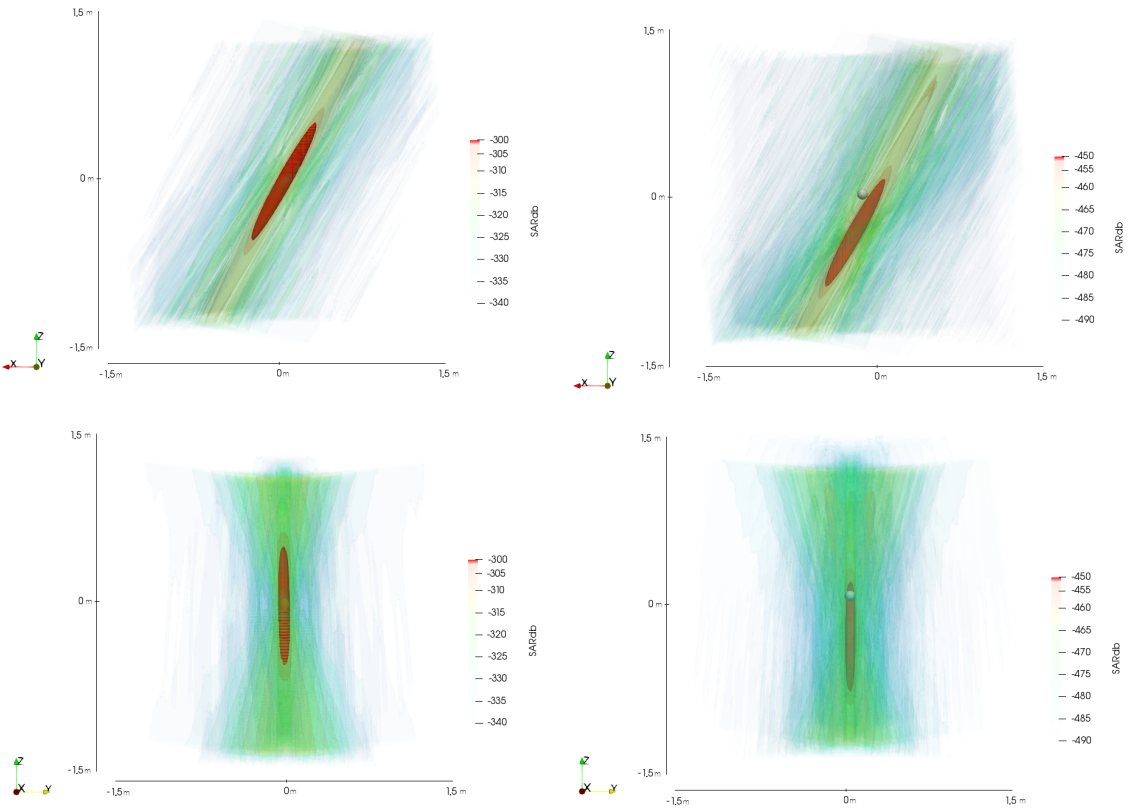

Figure 10.10: Scenario SB-SP-7: SAR Image of a point target with a spectrum computed with SEPO (left) and with the BA (right) visualized in a volume area. The target theoretical position is indicated with a white sphere.

The main pattern of the 3D synthesis ambiguity structure of "hourglass" is recovered. As expected, the phase measurement error brings a position error in the range direction, as well as in the elevation direction, which explains why the target is not correctly located.

Thus, the Born approximation was found out to reproduce the point target behavior for a small body geometry, except from a location error that is expected and physically explainable. A further study would require the simulation of the behavior of several targets and verify that the results of the SAR synthesis are coherent to our physical. However, the computational load of the Born approximation is high, and such simulations would be more easily performed when having access to GPU computations.

10.3 Conclusion

The Born approximation was implemented, in association with the Kirchhoff approximation to compute the field transmitted to a surface. The model was then applied in the Earth geometry, where the point target's response is well-known, for two different scenarios: when the target is surrounded by the void, and when the target is embedded in a medium with a permittivity of 3.0. The results of the BA have been validated, first by comparing the results of the BA with the results of SEPO, then by approving that the target has been reconstructed at the correct depth. After obtaining these results, the Born approximation was implemented in a small body geometry, for a target surrounded by the void, and for a target embedded in a medium with a permittivity of 3.0. The results were validated by comparing them with SEPO and assessing that the position of the target is reconstructed at the correct depth. In both geometries, the BA retrieves the point target response, with only an alteration of the point target pattern in the small body geometry noticeable at -30 dB that is due to small size of the surface compared to the wavelength. As the SAR synthesis does not compensate the medium permittivity, the BA does not reconstruct the correct position of the target. These results validate the implementation of the Born Approximation and confirm that it is well suited to simulate the field scattered by inclusions embedded in a sand-like medium.
However, the computational load of the BA does not allow us to compute the simulation of a volume that contains several inclusions separated by a distance larger than the resolution. Furthermore, the small size of the surface associated with the small size of the inclusion leads to a weak scattered power, which has few physical sense. Paralleling the code and implementing it on CPU or GPU nodes would reduce the BA's load and allow us to simulate several targets, larger volumes or larger targets, and thus simulate scenarios where the subsurface would scatter electromagnetic waves with a higher power.

Thus, the Born approximation allows us to compute the field scattered by an inclusion embedded in an asteroid's subsurface. However, the resulting resolution in the elevation direction is 2.4 meters in a small body geometry, which is too large if we take into account the fact that the incident wave will be penetrating the asteroid first ten meters.
Tomography methods can be applied to the results of the Born approximation in order to improve its performances: by multiplying the number of observations for different positions in space, the resolution in elevation can be improved.

Table 10.4: Scenario SB-SP-7: Performances comparison between SEPO and the BA.

	Born Approximation	Surface Echo PO
Range resolution (m)	0.54	0.53
Doppler resolution (m)	0.22	0.21
Elevation resolution (m)	2.41	2.42
Peak to Side-lobe ration (dB)	-12	-13

Part IV

SAR Tomography

Radars are instruments that have the unique ability to probe a planetary body surface and its subsurface. However, when a SAR uses a single-pass orbitography, where only one trajectory with a single elevation position is flown, the resolution in the elevation ambiguity will be poor. As HFR aims at probing the first ten meters of the asteroid subsurface, and HFR's resolution in the third dimension was measured to be larger than two meters, the standard SAR synthesis performances become limited. A solution to improve the radar's resolution in the third dimension of space is to perform tomography with a multipass orbitography. Tomography techniques were initially developed for medical applications, and are based on the idea that observing an object with a multitude of angles of observation can be used to recover the 3D shape of this object. Tomography can thus be applied to recover the 3D structure of embedded scatterers with an optimal resolution by observing the scene with a diversity of incidence angles, with a so-called multipass geometry.
The first chapter of this part will cover the description of different existing SAR tomography (TomoSAR) algorithms, which are reviewed with more details in appendix C. From this study, the TomoSAR algorithm most adapted to the observation of a small body will be selected. The second chapter will cover the implementation of the chosen model, and present its validation in an Earth observation geometry, as well as its performances in a small body geometry.

Contents

Chapter 11

A first SAR Tomography method: the FDBP

11.1 General presentation of SAR tomography algorithms

In 2D SAR image processing, a high spatial resolution along the range direction is achieved by sending high bandwidth pulses, and along the azimuth direction by regularly sending pulses to create an antenna synthetic aperture longer than the real antenna aperture.
However, no processing forms a high elevation resolution, and a SAR image pixel corresponds to the sum of the contribution of all scatterers in the same elevation direction, as a projection of a 3D scattering volume to a 2D surface. Thus, image distortions may happen, degrade the 3D reconstruction of the scene and alter the imaged geometry.
Interferometric SAR (InSAR) was thought to be an answer to this problem since it can determine the height of a target by measuring the phase difference between several observations separated in space and/or in time. However, the measured height is the height of the phase center of all the scatterers in the same range-azimuth cell, and the position of each individual scatterer still cannot be resolved.
Polarimetric SAR Interferometry (PolInSAR) was then developed to separate between surface and volume scattering effects within the same resolution cell and estimate their associated height. However, this technique remains limited because it is not possible to discriminate between the contributions of the same scattering mechanism over different heights.
SAR tomography (or TomoSAR) was thus developed to overcome these limits. Its principle is to extension the synthetic aperture principle used in the azimuth direction to the elevation direction, using standard SAR images obtained with different geometries of observation. In this way, SAR tomography allows the reconstruction of the scene reflectivity profile along the elevation direction, which was not possible in conventional 2D SAR imaging. The geometry of observation of TomoSAR is presented in figure 11.1. The elevation direction $\vec{s}$ is defined as the vector normal to the range direction $\vec{r}$ and to the azimuth direction. The objectives of TomoSAR are to retrieve the position of the scatterers of structures in the elevation direction with an extend of Δs.

Generally, SAR Tomography algorithms are classified into three families:

- Methods modified from the traditional 2D SAR imaging algorithms.
- Polarimetric coherence tomography.
- Spectral estimation.

Each method is characterized by a trade-off between simplicity, computational efficiency, side-lobe reduction, and super resolving capability. Different TomoSAR algorithms are presented here, with a deeper review detailed in appendix C. This review was revisited from the works of Du and Fa (2016), from which I included an analysis of the impact of the knowledge of the ground permittivity on the reconstruction of the target position.

The first category of TomoSAR algorithms, the traditional 2D SAR imaging methods applied in the 3D domain, can be divided into frequency and time domain algorithms:

- The frequency-domain methods, such as the SPECAN (SPECtral ANalysis, (Reigber & Moreira, 2000)), operate a Fourier transform to focus the received signal along the elevation direction. Their main appeal is their low computational burden. However, it is challenging to observe a scene with evenly distributed flight tracks: because the received data are always undersampled due to the small number of observations, an additional interpolation procedure is always needed, which increases the computational burden and reduces the interest of these methods. However, the method cannot be applied when the range migration caused by the multiple orbits exceeds half the resolution cell.

- The time-domain methods, such as the TDBP (Time-Domain Back Projection) method (Nannini & Scheiber, 2006) directly focus the signal in elevation with an ad hoc function. These methods do not rely on a regular distribution of flight tracks. However, they are time244 consuming. The TDBP can be expressed in the frequency-domain, and is then called FDBP (Frequency Domain Back Projection, Soumekh (1999)).

This method uses POLInSAR data to derive the elevation reflectivity function, characterized by the Fourier Legendre series. Using a single or dual baseline architecture, the PCT method has been implemented to derive the elevation profile of the radar scattering intensity, while avoiding any flight track control (Cloude, 2006). However, PCT relies on a priori knowledge on the height of the scattering volume and the phase of the ground, which adds some additional procedures when this knowledge is not available and increases its computational load. Finally, due to the small number of baselines, the spatial resolution of the PCT tomogram is not as good as different tomography methods

Finally, Spectral Estimation methods are high-resolution TomoSAR algorithms, which are based on an inversion problem between the measurement vector and a matrix called the mapping matrix to retrieve the vector reflectivity profile. They can be classified as parametric or non-parametric models:

- Parametric models, such as the MUSIC (MUltiple SIgnal Classification) algorithm (Nannini et al., 2011) are easily implemented but require a priori information on the surface to be imaged, such as the number of scatterers.

- Non-parametric models, such as the CS (Compressive Sensing) algorithm (Zhu et al., 2010) are more flexible but rely on hypotheses on the investigated geometry that may be hard to satisfy.

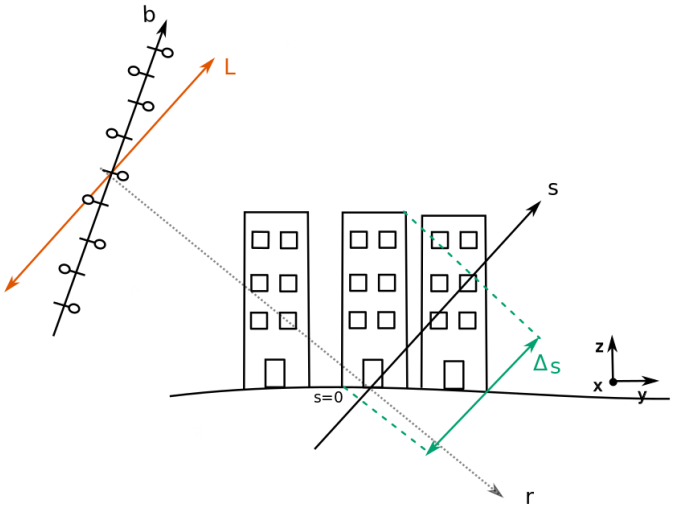

Figure 11.1: Illustration of a multipass geometry.

Table 11.1: Tomography method performances summary.

	Computational burden	Resolution	Complexity	Adaptability to a change of ϵ
SPECAN	Medium	Medium	High	Low
TDBP	High	Medium	Medium	Low
PCT	Low	Low	Low	Medium
MUSIC	Medium	High	High	Low
CS	Medium	High	Medium	Medium

However, the SE methods cannot be applied when the range migration caused by the multiple orbits exceeds half the resolution cell.

Ultimately, the choice of one model instead of another relies on the characteristics and requirements of the study, since each of these models has its advantages and drawbacks. Table 11.1, which is built from the description of each model, classifies the different methods depending on their computational burden, their resulting spatial resolution, the operation complexity (the difficulty to carry on the observation in a nominal way), and the adaptability of the algorithm to correct the delay induced by the permittivity of the subsurface.

Given the high resolution provided by the radar, the range migration caused by the different orbits will exceed half the resolution cell size in small body observation geometries, which excludes frequency domain methods as well as spectral estimation methods for a correct reconstruction of the reflectivity profile. Since we applied the SAR processor of SPRATS, which uses the FDBP to compute the 2D SAR synthesis, its 3D-domain application a natural first choice to be applied in tomography.

11.2 Application of the FDBP to TomoSAR imaging

11.2.1 Description

The FDBP is presented in 2D imaging in Soumekh (1999) and achieves focusing by using the geometry between the sensor and the imaged volume: every resolution cell of the 3D SAR image is focused based on the true acquisition geometry and a reference function. The TomoSAR FDBP is based on the same principle and considers 3D SAR images $s_n(\vec{r}_l)$ already focused on the range/Doppler plan. For each track, the image s_n corresponds to the n-th flight track :

$$s_n(\vec{r}_l) = \sum_{j=a_n}^{b_n} S(f_m) \cdot \exp\left(i4\pi f_m \frac{R_{n_{ij}}}{c}\right) \tag{11.1}$$

With:

S: the measured spectrum
$\vec{r}_l$: the position of the scatterer
a_n, b_n: the indexes of the first and last azimuth position of the sensor
$r_{\vec{S}_{jn}}$: the position vector of the sensor of the n-th track
$R_{n_{ij}} = |\vec{r}_l - r_{\vec{S}_{jn}}|$: the range distance
f_m: the frequency

The TomoSAR image v is then the sum of all spectra for all tracks, and can be written at the position $\vec{r}_l$:

$$v(\vec{r}_l) = \sum_{n=1}^{N} \sum_{j=a_n}^{b_n} S(f_m) \cdot \exp\left(i4\pi f_m \frac{R_{n_{ij}}}{c}\right) \tag{11.2}$$

As a TomoSAR algorithm, the resolution expected from FDBP can be obtained by Reigber and

Moreira (2000) :

$$\delta_e = \frac{\lambda r_0}{2L} \tag{11.3}$$

11.2.2 Numerical results

First, the FDBP was applied to an Earth observation geometry, following scenario EO-MP-1, described in appendix E. This scenario consists in observing a point target with a permittivity of 3.1 embedded in a medium with a permittivity of 3.0 in an Earth observation geometry. The results are presented in figure 11.2 with a range dynamic of 40 dB, with the position of the target highlighted by a white sphere. The spherical reddish portion depicts the 3dB width of the pattern, where the inclusion is imaged. As expected, a range measurement error prevents the recovery of the true position of the target, but the resolution achieved with the FDBP reaches 20 cm, which is equal to the 19.6 theoretical resolution expected from TomoSAR algorithm. In the Earth observation geometry, ray tracing methods could be implemented to correct the delay induced by the propagation of the wave in the medium with the permittivity of 3.0.

The FDBP was then applied to a small body geometry, using scenario SB-MP-2, described in appendix E. The scenario consists in observing a point target with a permittivity of 3.1 embedded in a medium with a permittivity of 3.0 in the small body geometry. The results are presented in Figure 11.3, with the position of the target highlighted by a white sphere. The elevation resolution achieved with the multipass geometry is improved from 2.2 m and reaches 47 cm, which is comparable to the 39 cm theoretical resolution expected from TomoSAR algorithms but not equal. The theoretical resolution is not reached because its expression was carried out in the Earth observation geometry and not in our specific small body geometry. However, the position of the target cannot be retrieved by the FDBP. Indeed the SAR processor has no knowledge of the medium permittivity, and the position of the target is then shifted.
Traditionally, ray tracing methods are implemented to correct the delay induced by the propagation of the wave in a medium where the permittivity is different from 1.0. However, these methods are highly dependent on the shape models. Given the very rough surfaces of asteroids, ray tracing methods are not reliable in the small body geometry and will not be considered.

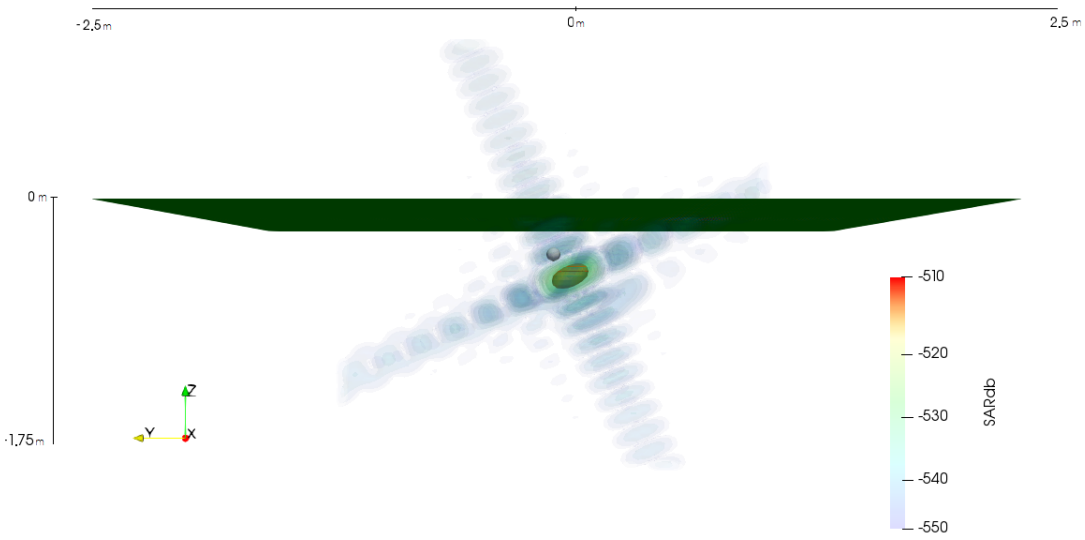

Figure 11.2: Scenario EO-MP-1: 3D SAR synthesis results of a point target embedded in a medium with a permittivity of 3.0 with a dynamic of 40 dB. The theoretical position of the target is indicated by a white sphere.

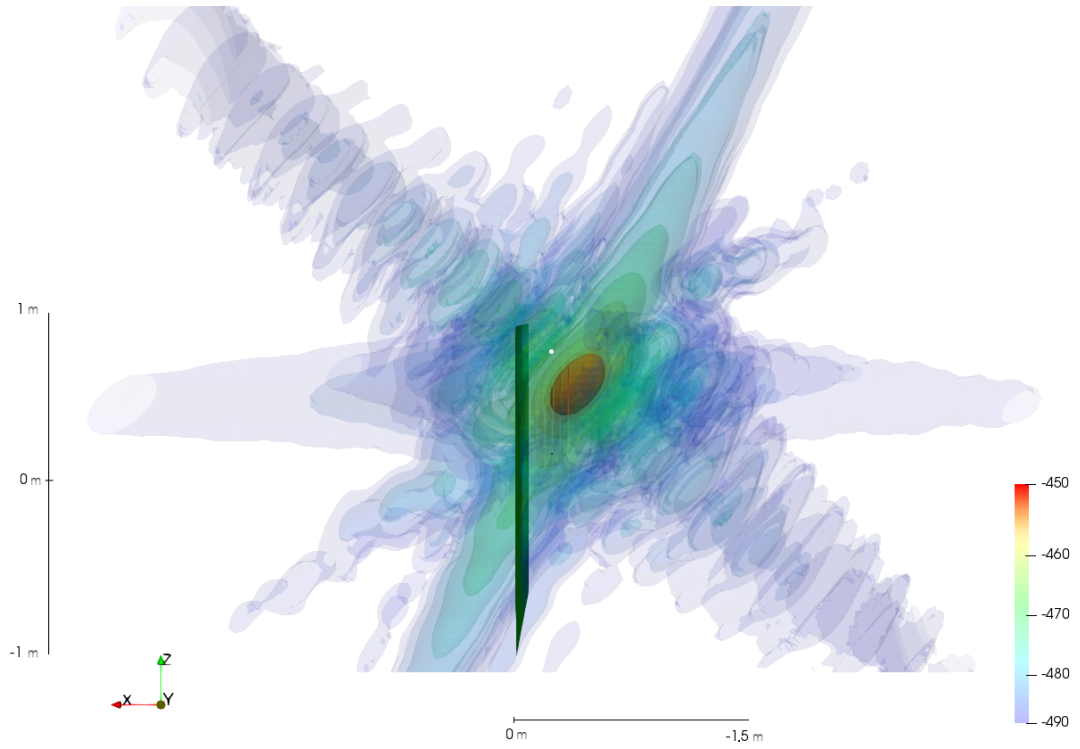

Figure 11.3: Scenario SB-MP-2: FDBP results of a point target embedded in a medium with a permittivity of 3.0 with a dynamic of 40 dB. The surface is indicated as a dark square to help visualize the geometry. The theoretical position of the target is indicated by a white sphere.

11.3 Reconstructing the true position of the target

To reconstruct the true position of the target, additional tomography methods can be considered. The Compressive Sensing (CS) is a spectral estimation method based on the computation of SAR images of the surface of the volume investigated, and on the retrieval of the reflectivity profile in the elevation direction if this reflectivity profile is sparse. This means that the CS treats the propagation of the waves in the void (by computing the SAR image at the surface) and the subsurface (by computing the reflectivity profile of the subsurface) separately. Thus, the compensation of the delay can be carried out more easily than by correcting the SAR processing.However, the CS is not entirely adapted in a geometry where the range migration exceeds the size of the resolution cell, which is the case in our small body geometry. As a consequence, the performances of the CS will deviate from the nominal performances and will not be as high as the performances achieved with the FDBP. Nevertheless, by treating the propagation of the wave in two steps, in the void and the subsurface, the CS can be applied to retrieve the true position of the scatterers.

Chapter 12

Compressive Sensing in TomoSAR imaging

12.1 Presentation of the Compressive Sensing

12.1.1 Description

The TomoSAR CS method, developed in Zhu et al. (2010), is a tomography method that can preserve the super-resolving capabilities of the SAR image along the range/azimuth dimensions and provide a very high resolution in the elevation direction. TomoSAR CS is based on the assumption that the reflectivity profile is sparse, which means that only a few stable targets lie in the elevation direction. It exploits the theory of compressive sampling (Candès & Wakin, 2008), which is used for analyzing data using only a few signal samples, with a high resolution and low computation times.

TomoSAR CS considers that in a single-pass SAR acquisition, the value of a SAR pixel g located at the range/azimuth position (r, x) corresponds to the integral of the reflected signal along the elevation direction :

$$g(x,r) = \int_{\Delta s} \gamma(s(x,r,s)) \exp(-\frac{4\pi}{\lambda} d_l(x,r,s))ds \tag{12.1}$$

- s is the elevation vector, sampled with L points
- γ is the reflectivity vector, sampled with L points
- d_l is the distance from the radar to each point in the elevation direction of the (x, r) pixel with l = 1...L
- λ is the wavelength.

By multiplying the number of observation with a multi-pass acquisition, the SAR image can then be obtained as :

$$g_n(x,r) = \int_{\Delta s} \gamma(s(x,r,s)) \exp(-\frac{4\pi}{\lambda} d_{l_n}(x,r,s))ds \tag{12.2}$$

With $n = 1....n$.

By discretizing this equation, we then find that

$$g = R \cdot \gamma \tag{12.3}$$

Where :

- g is the vector containing the value of the SAR image vectors
- R is a matrix composed of the coefficients $\exp(-\frac{4\pi}{\lambda} d_n(x,r,s))$, called the steering matrix
- γ is the reflectivity vector.

If the surface under study complies with the compressive sampling conditions, the elevation profile is reconstructed by L_0 norm minimization, which finds the solution of equation 12.3 with the minimum number of non-zero coefficients (Hyder & Mahata, 2009) :

$$\hat{s} = \arg\min\{\|\gamma\|_0\} \quad \text{s.t.} \quad g = R\gamma \tag{12.4}$$

For sparse signals, the L_0-norm minimization and the L_1-norm minimization, which is the minimization of the sum of the magnitudes of the vectors, lead to the same results (Candès & Wakin, 2008). Thus, s can be found using the L_1-norm minimization :

$$\hat{s} = \arg\min\{\|\gamma\|_1\} \quad \text{s.t.} \quad g = R\gamma \tag{12.5}$$

Which is a minimization easily achieved with basis pursuit methods (Van den Berg & Friedlander, 2011).
Since the CS can be applied on SAR images computed on the surface of a volume, and the position of the embedded scatterers are reconstructed from the surface, the portion of space with different permittivities can be separated, and the TomoSAR CS can easily be applied on a geometry with a change of permittivity. Thus, the TomoSAR CS can be applied to improve the reconstruction of buried target, with the knowledge of the ground permittivity.

12.1.2 Results of previous experiments

Zhu and Bamler used TerraSAR-X images of the Las Vegas convention center in order to compare the TomoSAR CS performances to other spectral estimation nonparametric and parametric methods, such as the Singular Value Decomposition (SVD) reconstruction, or the Wiener type regularization (SVD-Wiener). The targeted-building imaged has a height of 20m. Figure 12.1 shows the convention center visualized on Google Earth on the left and the TerraSAR-X intensity map of the area on the right. The bright blue line shows the position of the analyzed slice and the area marked by the red block is a layover area. Figure 12.2 shows the estimated reflectivity with SVD Wiener in the azimuth elevation plane. Even though these results demonstrate the validity of the SVD Wiener, the final resolution achieved is limited and blurs the reflectivity profile for each pixel. In contrast, 12.3 shows the same plot but estimated by the TomoSAR CS approach. Not only the layover area can be more clearly separated, but the elevation positions can be easily located in the reflectivity slices.

12.1.3 Sampling

As tomography methods adapt the synthetic aperture principle to the elevation direction, a given sampling of the trajectories must be respected in order to avoid aliasing in the Earth observation

Figure 12.1: Las Vegas Convention Center (left) and TerraSAR-X Intensity Map (right) (Zhu et al., 2010).

geometry. The unambiguous height of the simulation, which is the height over which no aliasing ambiguities will appear, is described in Reigber and Moreira (2000) as :

$$h = \frac{\lambda R_0}{\mu} \tag{12.6}$$

With R_0 the range distance to the target and μ is the elevation separation between the tracks. However, this evaluation has been performed from observations in the Earth observation geometry. Given the differences between the Earth observation geometry and the small body geometry observation geometry, this assessment is questioned for the observation of an asteroid.

12.2 Correction of the position of the target with Compressive Sensing

One of the main attractions of the Compressive Sensing is its potential to correct the delay induced by the propagation of the wave in the subsurface. The compensation of the delay of the signal can be understood by considering a target embedded under a surface. Because the SAR processor considers that the signal is always propagating in the void, the final SAR image sees any point below the surface located deeper than it actually is. This means that the elevation ambiguity in the void and in the subsurface will not have the same orientation, yet the SAR processor will consider the elevation ambiguity has always the orientation of the void's. Indeed, a target is imaged at a distance d_1 from the surface while it is actually embedded at a distance d_2, such that $d_1 = \sqrt{\epsilon_a} \cdot d_2$, as illustrated in figure 12.4. Thus, targets lying at an angle θ_2 from the point on the surface with the same range/azimuth delay, will be imaged at an angle θ_1.
The different angle between the medium ambiguity and the void ambiguity $\Delta\theta$ can be retrieved from

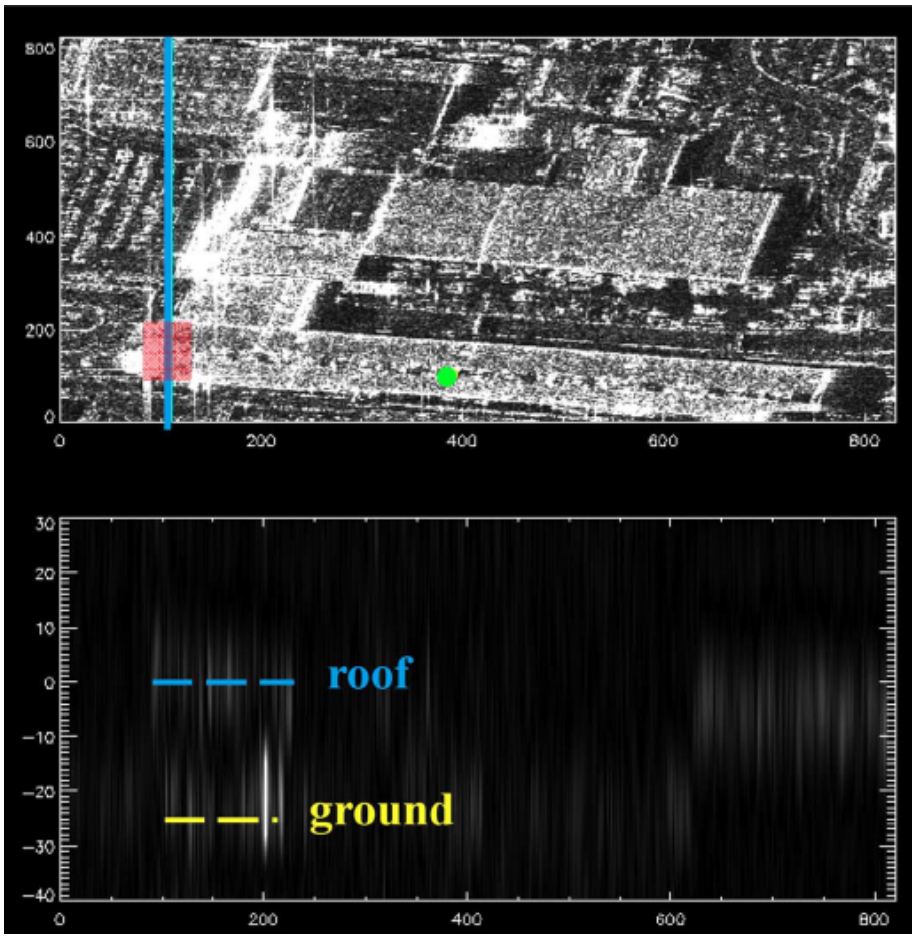

Figure 12.2: SVD radar image of the Las Vegas Convention Center (Zhu et al., 2010).

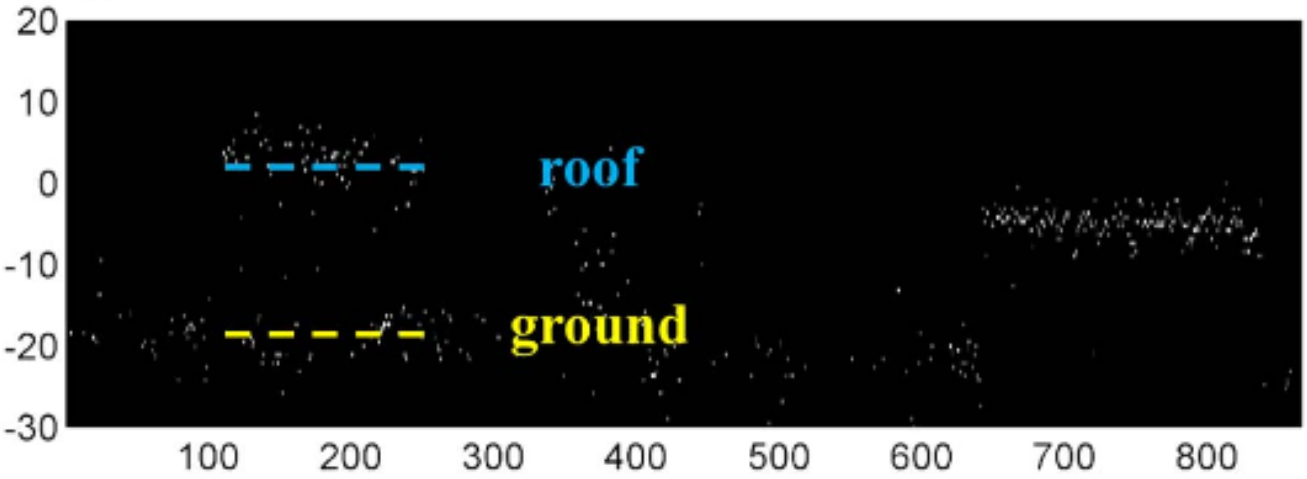

Figure 12.3: CS radar intensity of the Las Vegas Convention Center (Zhu et al., 2010).

the angle between the ambiguity and the surface θ_1 given that:

$$\tan \Delta\theta = \frac{\Delta d}{x} \tag{12.7}$$

$$\tan \theta_1 = \frac{d_1}{x} \tag{12.8}$$

Since:

$$\tan \Delta\theta = \frac{\Delta d \tan \theta_1}{d_1} \tag{12.9}$$

Then:

$$\Delta\theta = \arctan\left(1 - \frac{d_2}{d_1}\right) \cdot \tan \theta_1 \tag{12.10}$$

$$= \arctan\left(1 - \frac{1}{\sqrt{\epsilon_a}}\right) \cdot \tan \theta_1 \tag{12.11}$$

By performing a rotation of angle $\Delta\theta$ and a dilation of parameter $a = \frac{1}{cos(\Delta\theta)}$, the delay due to the permittivity of the medium can be compensated with the CS, first by recovering the position of the scatterers in the direction of the void ambiguity (as the original algorithm achieves) and then by reconstructing the true orientation of the elevation ambiguity.

In the next chapter, the application of the Compressive Sensing method and its results will be presented : the method will be applied on an Earth observation geometry in order to validate our implementation of the method, and in a small body geometry, in order to analyze the CS's performances. The performances of the CS in the Earth observation geometry are expected to be similar to the one achieved with the FDBP. However, since the range migration exceeds half the resolution cell size in the small body geometry, the resolution is expected to be worse than the one achieved by the FDBP.

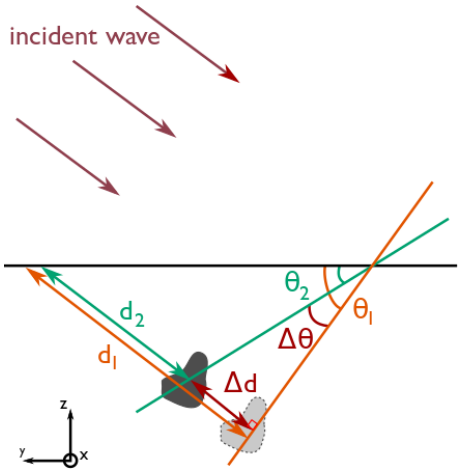

Figure 12.4: Illustration of the geometry to retrieve the true position of the scatterers. Orange illustrates the ambiguity in the void, and green illustrates the ambiguity in the medium.

Chapter 13

Application of the Compressive Sensing to retrieve the true position of the scatterers

13.1 Compressive sampling theory

13.1.1 Description

Compressive sampling is a technique adapted to the reconstruction of sparse signals, described in Candès and Wakin (2008). A signal x of length L is said K-sparse in an orthogonal basis ψ if the projection of x onto ψ, s= ψx has only K non-zero elements. If a measurement vector of size N y is obtained by projecting x onto a matrix ϕ, where ϕ is called the sensing matrix, then we can write :

$$y = \phi x = \phi \psi^H s = \Theta s \tag{13.1}$$

Where Θ is called the mapping matrix and ^{H} indicates the transpose operator.
Using the CS method, s can be reconstructed by L_0-norm minimization, which finds the solution of equation 13.1 with the minimum number of non-zero coefficients (Hyder & Mahata, 2009) :

$$\hat{s} = \arg\min\{||s||_0\} \quad \text{s.t.} \quad y = \Theta s \tag{13.2}$$

For sparse signals, the L_0-norm minimization and the L_1-norm minimization lead to the same results (Candès & Wakin, 2008). Thus, s can be found using the L_1-norm minimization, which is the minimization of the sum of the magnitudes of the vectors :

$$\hat{s} = \arg\min\{||s||_1\} \quad \text{s.t.} \quad y = \Theta s \tag{13.3}$$

In order to have a unique solution, two conditions must hold :

- The sensing matrix ϕ and the orthogonal basis ψ must be incoherent, in order not to bias the reconstruction of non-zero elements into certain positions. The incoherence can be computed as (Candès & Wakin, 2008) :

$$\mu(\phi, \psi) = \sqrt{n} \cdot \max | < \phi_k \psi_j > | \quad 1 < k, j < n \tag{13.4}$$

  With n the size of the signal s.

- The mapping matrix Θ must follow the Restricted Isometry Property (RIP), which guarantees a sufficiently sparse reconstruction in the presence of noise :

$$(1 - \delta_s)||v||^2 \leq ||\Theta v||_2^2 \leq (1 + \delta_s)||v||^2 \tag{13.5}$$

  Where v is any K-sparse vector, with non-zero coefficients at the same position as s, and δ_s is a small number. The smaller δ_s the better the sparse signal will be reconstructed in the presence

of noise. This property assures that Θ preserves approximately the Euclidean length of the sparse signals. This implies that these vectors cannot be in the null space of Θ and can thus always be recovered, and that all distances between sparse signals will be reconstructed in the measurement space.

Before applying the compressive sensing, these two conditions must thus be verified.

13.1.2 Applicability of the Compressive Sampling to the SAR Tomography of small bodies

By taking the notation followed in section 13.1, the Compressive Sensing method applied to TomoSAR imagery seeks to solve:

$$\hat{\gamma} = \arg\min \|\gamma\|_1 \quad \text{s.t.} \quad g = \gamma \cdot R \tag{13.6}$$

However, in order to apply CS, the three conditions of the compressive sampling must be verified:

- The signal γ is sparse. Considering that the medium under study contains only a few inclusions in each elevation direction of each pixel of the SAR image, we can consider that the hypothesis stating that γ is sparse is true in a first approximation.
- The orthogonal basis matrix Ψ is the identity matrix in our geometry. As the distance between the radar to each pixel is large compared to the wavelength, the R matrix can be considered as random. Thus, by definition, the matrix Φ and Ψ of the compressive sampling described in section 13.1.1 are incoherent, $\mu(\phi, \psi) = 0$, and the coherence does not have to be computed.
- The RIP property is verified: in the case of a single scatterer, the RIP property is automatically verified. When imaging several scatterers, the RIP is verified if the scatterers are separated by a distance larger than the resolution (Zhu et al., 2010). This allows to neglect the multiple scattering effects between points.

Thus, in a first approximation all CS hypotheses can be considered validated, and the CS can be applied to our study.

13.2 Description of the CS algorithm

The CS tomography algorithm begins with a stack of SAR images, each obtained with a different geometry using the Born approximation. The stack of images is computed at the surface of the volume investigated.
The first step of the algorithm is to provide an expression for the R matrix. By choosing a reference track among all flown trajectories, we define $b_{n\parallel}$ and $b_{n\perp}$ as the distance between the tracks in the range and in the elevation plane, as presented in figure 13.1 :

$$b_{n\parallel} = \vec{d_n} \cdot \vec{r} \tag{13.7}$$

$$b_{n\perp} = \vec{d_n} \cdot \vec{s} \tag{13.8}$$

With $\vec{d_n}$ the difference vector between each trajectory and the reference trajectory, $\vec{r}$ is the range vector and $\vec{s}$ is the elevation vector, normal to the velocity vector of the radar and $\vec{r}$.

Then from each track, the distance can be computed as:

$$d \approx \sqrt{(r - b_{n\parallel})^2 + (s - b_{n\perp})^2} \tag{13.9}$$

With r the range distance between the reference track and the pixel understudy, and s is the position of the scatterer in the elevation direction. According to Fornaro et al. (2003) derivation, the distance can be written as:

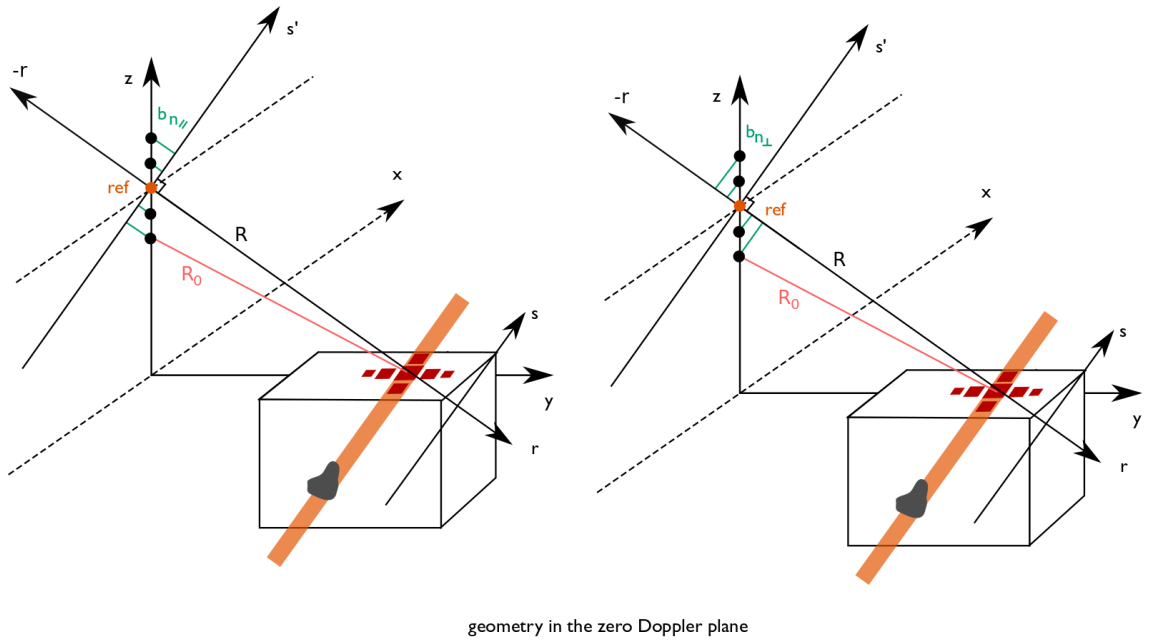

Figure 13.1: Geometry of the compressive sensing method. The inclusion is pictured in grey in the subsurface. The elevation ambiguity associated with the target is pictured in orange, and is parallel to the s direction. The position of the different trajectories are indicated by a black sphere, with the reference trajectory highlighted in orange.

$$d \approx \frac{-b_{n\perp} s}{(r - b_{n\parallel})} \tag{13.10}$$

Thus, by simplifying $\gamma(r, x, s)$ into $\gamma(s)$, we can rewrite equation 12.2:

$$g_n(x, r) = \int_{\Delta s} \gamma(s) \exp\left(2i\pi \frac{2}{\lambda} \frac{b_{n\perp}}{(r - b_{n\parallel})}\right) ds \tag{13.11}$$

Which can be simplified as:

$$g_n(x, r) = \int_{\Delta s} \gamma(s) \exp\left(2i\pi \frac{2}{\lambda} \frac{b_{n\perp}}{r}\right) ds \tag{13.12}$$

When $r >> b_{n\parallel}$, which is the case for Earth Observation.
Finally, we can write:

$$g = R\gamma \tag{13.13}$$

With γ the complex L-elements reflectivity vector along the elevation direction of size L and R is an $N \times L$ matrix, with :

$$R_{nl} = \exp(-2i\pi \cdot \frac{f_n}{c} \cdot s_l) \tag{13.14}$$

Where c the speed of light and:

$$f_n = -2f \cdot \frac{b_{n\perp} s}{(r - b_{n\parallel})} \tag{13.15}$$

Where f is the central frequency.

The compressive sensing will estimate for each pixel of the SAR image:

$$\hat{\gamma} = \arg\min\{\|\gamma\|_1\} \quad \text{s.t.} \quad g = \gamma \cdot R \tag{13.16}$$

With all γ profiles for each pixel of the SAR image are retrieved, we can then reconstruct a volume containing the reflectivity of all SAR image pixels.

The minimization can be easily achieved with basis pursuit methods. We use the spgl1 package, developed by Van den Berg and Friedlander (2011) on Python 3.7.

13.3 Results of the application of the compressive sensing

The CS was applied using a stack of SAR images obtained using the BA, first in an Earth Observation geometry in order to validate the results of the method, and in a small body observation geometry in order to analyze the applicability and the performances of the CS.

13.3.1 Earth Observation geometry: Scenario EO-MP-1

We will now present the results of the compressive sensing tomography obtained with the scenario EO-MP-1 described in appendix D. The scenario consists of a point target with a permittivity of 3.1 embedded in a medium with a permittivity of 3.0, as a sandy material in a sand background. The small variation of permittivity allows to apply the BA to the scenario and is reasonable to consider in a small volume of investigation.

The results of the CS are presented in figure 13.2 with a dynamic of 40 dB, with the 3dB portion highlighted in bright red, which indicates the measured position of the target. The theoretical position of the target is indicated with a white sphere. No sidelobes appear in the range and Doppler directions but are taken into account in the CS signal model. The surface is indicated to help to visualize the geometry. Table 13.1 is compared the resolutions achieved with a single-pass SAR synthesis, with the multi-pass SAR synthesis, with the CS without compensation of the delay (denoted as $\epsilon = 1$), with compensation of the delay (denoted as $\epsilon = 3$), and with the theoretical value expected from TomoSAR algorithms.

Figure 13.2 depicts that the target position is not reconstructed at its correct location, which is expected since the SAR synthesis does not compensate the delay that is due to the propagation of the wave. As the medium permittivity is $\epsilon_a = 3.0$, the theoretical range measurement error is $\Delta_d = d(\sqrt{(\epsilon_a - 1)} = 18.3$ cm. In our simulation, we measure a difference of range distance between the

Table 13.1: Scenario EO-MP-1: Performances.

	Single-pass synthesis	FDBP	CS ($\epsilon = 1$)	CS ($\epsilon = 3$)	Theoretical
Resolution (m)	-	0.20	0.22	0.22	0.196

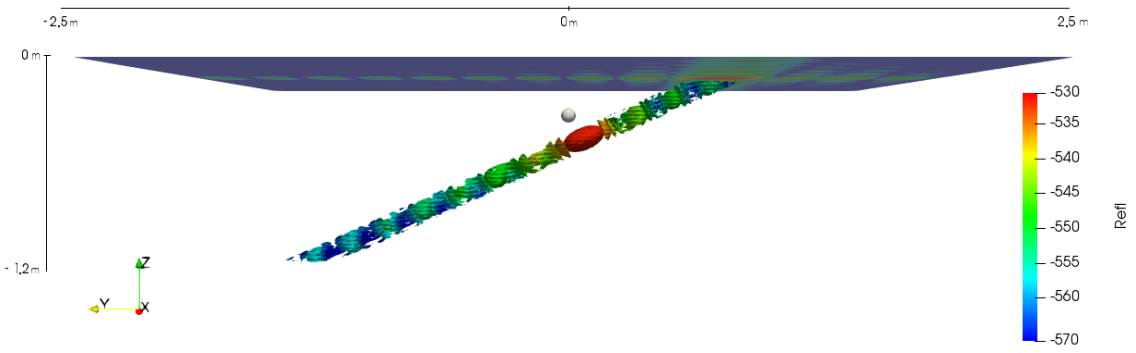

Figure 13.2: Scenario EO-MP-1: Compressive sensing results of a point target embedded in a medium with a permittivity of 3.0 with a dynamic range of 40 dB. The surface is indicated to help visualize the geometry.

theoretical target position and the retrieved tomography position of 19 cm. The difference between the theoretical target and the retrieved one is below the sampling precision of about 3.4 cm, thus we consider that the position of the target has been correctly retrieved.

Table 13.1 presents the resolution in elevation, which was improved from a width larger than 5 meters to a width of 22 cm, equal to the performances achieved with the FDBP by taking into account the sampling precision. The little difference of resolution is expected since the conditions of application of the CS are verified in the Earth observation geometry.

In order to overcome the measurement error induced by the permittivity ϵ_a, the CS was then carried out with the compensation of the delay. The results are presented in figure 13.3, where the target position is highlighted with a white sphere, and the CS results are depicted with transparency for a better visualization of the target position.
As expected, the compensation of the delay improves the localization of the target, which falls into the 3dB resolution spot.

The compressive sensing was thus proven to be efficient to recover the position of a target embedded under a surface in an Earth observation geometry, with the same performances as the FDBP, and compensates the delay induced by the propagation of the waves in a medium with a permittivity different than 1.0. The next step would be to test the method for the small-body geometry and assess the compressive sensing performance in this different and complex geometry.
Further Earth observation simulation on larger volumes would be necessary to assess the performances of the CS, with a larger number of inclusions, and how the method reconstructs the position of the target.

13.3.2 Small body geometry: Scenario SB-MP-2

Compressive sensing will now be applied to small body geometry. This geometry has various differences with the Earth observation geometry and considering that HFR characteristics are different from classical Earth observing radars, simulations are needed to validate the applicability and the performances of the CS in the small body geometry. We now present the results of the compressive sensing tomography obtained with the scenario SB-MP-2 described in appendix E. The scenario consists in observing a point target with a permittivity of 3.1 embedded in a medium with a permittivity of 3.0 in the small body geometry.

The CS results are presented in figure 13.4 with a dynamic of 40 dB, with the 3dB portion highlighted in bright red, which indicate the detected position of the target. The theoretical position of the target is indicated with a white sphere and the asteroid surface is indicated to help to visualize the geometry. No sidelobes appear in the range and Doppler directions, but are taken into account in the CS signal model. The resulting resolution of the tomography is presented in table 13.2, with

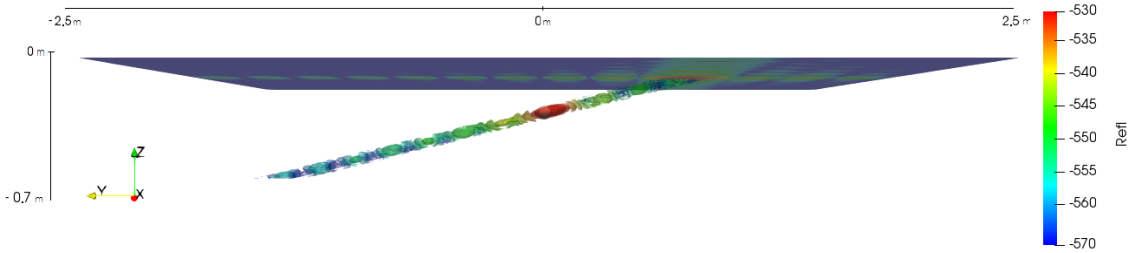

Figure 13.3: Scenario EO-MP-1: Compressive sensing results of a point target embedded in a medium with a permittivity of 3.0 with a dynamic range of 40 dB, with compensation of the delay. The position of the target is indicated by a white sphere. The surface is indicated to help visualize the geometry.

the CS without compensation of the delay (denoted as $\epsilon = 1$), and with compensation of the delay (denoted as $\epsilon = 3$) and compared with the resolution achieved with single-pass SAR synthesis, FDBP, and with the theoretical resolution of TomoSAR imaging.

Figure 13.4 presents that the target is not located at its correct location, which is expected since the SAR synthesis does not compensate for the delay that is due to the propagation of the wave in a medium with a permittivity $\epsilon_a \neq 1.0$. As the medium permittivity is $\epsilon_a = 3.0$, the theoretical range measurement error is $\Delta_d = d(\sqrt{\epsilon_a} - 1) = 18.3$ cm. In our simulation, we measure a difference in distance between the theoretical target position and the retrieved tomography position of 15 cm. The difference between the theoretical target position and the retrieved one is around the sampling precision of about 3.4 cm. However, the position of the target is considered to be correctly reconstructed.

Table 13.1 presents the evolution of the elevation resolution, for a single pass SAR synthesis, the FDBP, and the CS. The resolution in elevation was improved from a resolution of 2.2 meters with a single pass synthesis to a resolution of 60 cm with the CS, which is however worse than the resolution achieved by the FDBP of 47 cm. This difference is expected since the conditions of the application of the CS are not fully retrieved in our geometry.

In order to overcome the measurement error induced by the permittivity ϵ_a, the CS was then carried out with the compensation of the delay. The results are presented in figure 13.5.

Table 13.2: Scenario SB-MP-2 : Performances

	Single pass synthesis	FDBP	CS($\epsilon = 1$)	CS ($\epsilon = 3$)	Theoretical
Resolution (m)	2.22	0.47	0.6	0.6	0.39

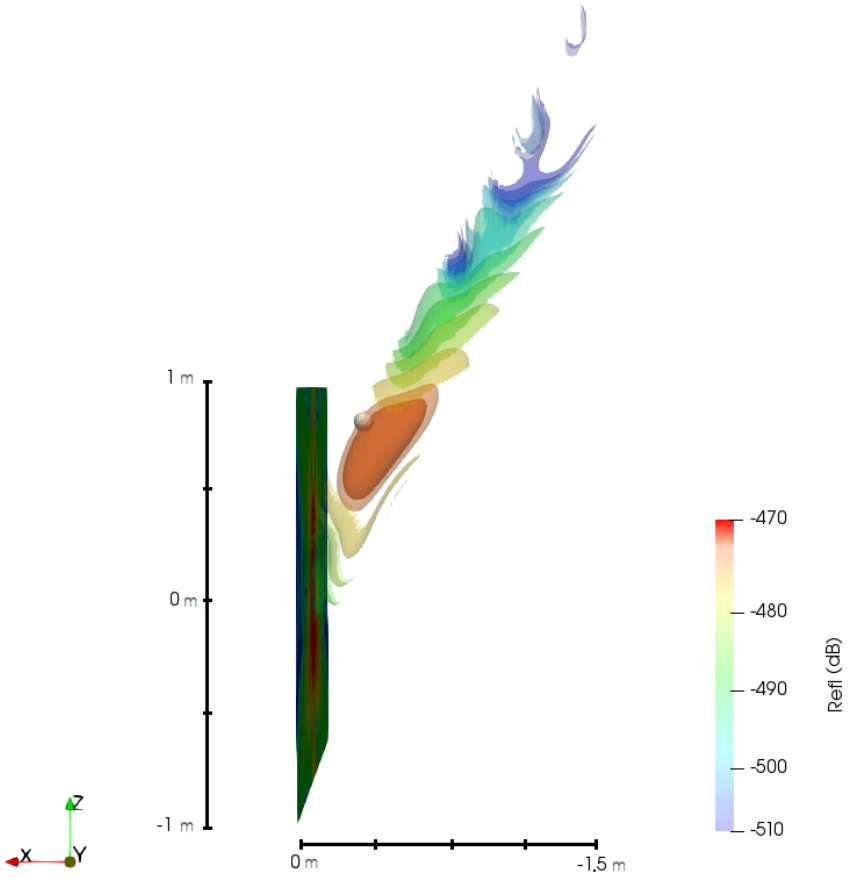

Figure 13.4: Scenario SB-MP-2: Compressive sensing results of a point target embedded in a medium with a permittivity of 3.0, with a dynamic range of 40 dB, without compensation of the delay. The surface is indicated to help visualize the geometry.

As expected, the compensation of the delay improves the locational of the target, which falls into the 3dB resolution spot.

The compressive sensing tomography method was found out to recover the position of buried targets in the small body geometry. The performances recovered from the compressive sensing are better than the resolutions retrieved from a single pass orbit, but not better than the one retrieved in the elevation direction, as summarized in tables 13.1 and 13.2. However, this loss in resolution is compensated by the fact the CS allows to compensate the delay induced by the permittivity ϵ_a.
This study proved that compressive sensing can also be applied in small body geometry to correctly locate the target when the subsurface permittivity is different than one. However, as the CS derivation makes different hypotheses that are valid in the Earth observation geometry, but not anymore in the small body, and scenarios with larger volume would be required to verify the CS is still valid to image inclusions in the small body geometry.

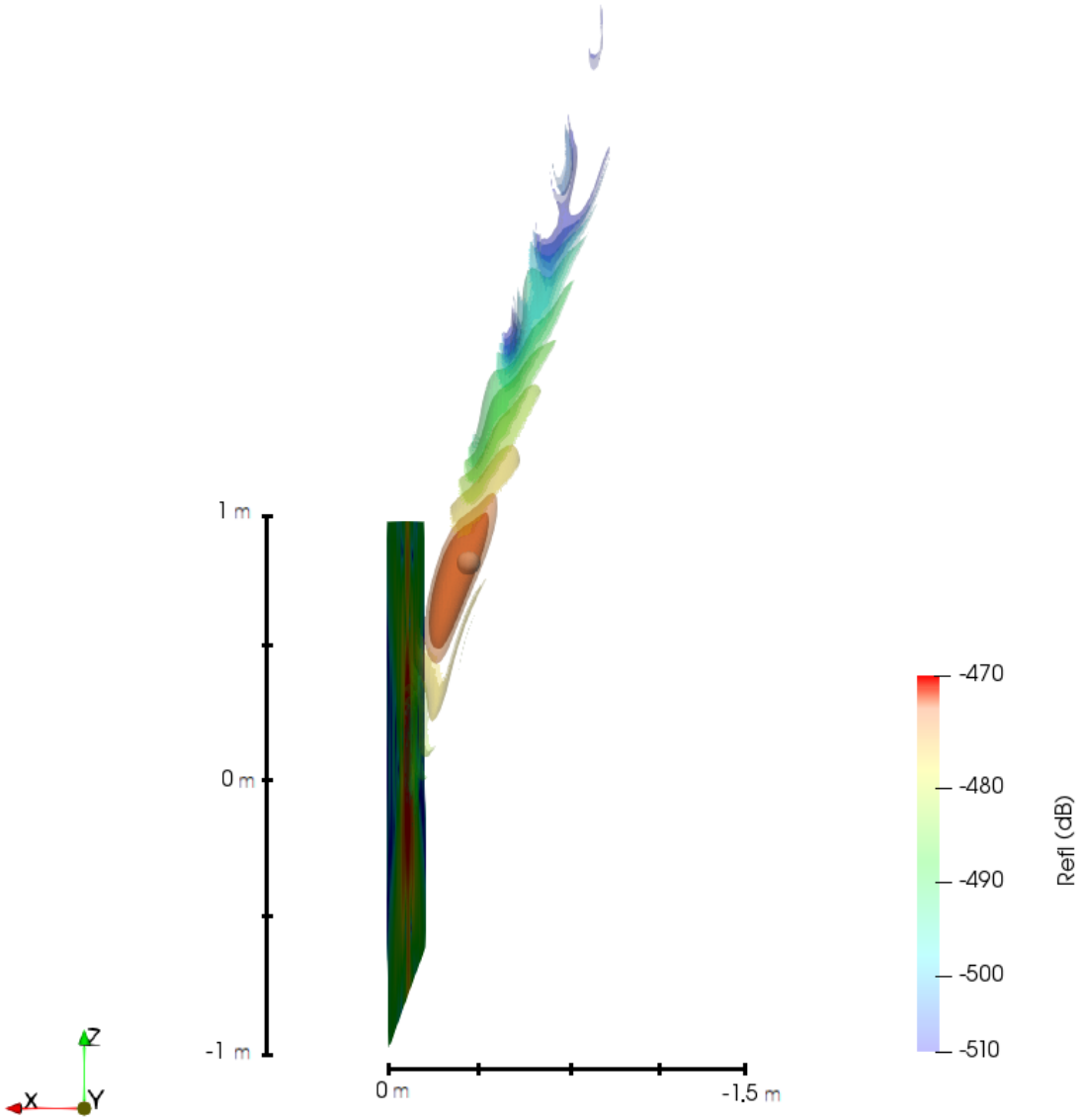

Figure 13.5: Scenario SB-MP-2: Compressive sensing results of a point target embedded in a medium with a permittivity of 3.0 with a dynamic range of 40 dB, with compensation of the delay. The position of the target is indicated by a white sphere.

13.4 Summary

SAR Tomography (TomoSAR) methods are imaging techniques that can be used to retrieve the 3D structure of scatterers by exploiting SAR data acquired in a multipass geometry. Different TomoSAR methods exist, each of them with their advantages and drawbacks. The Frequency-Domain-Back-Projection (FDBP) method was chosen to perform the 3D tomography of an asteroid. FDBP is based on the correction of the received spectrum by an ad-hoc function and was applied to improve the resolution in the elevation direction by a factor of 4. However, FDBP cannot be applied to retrive the true position of scatterers embedded in the asteroid surface. Thus, Compressive Sensing (CS) was investigated. CS is based on the hypothesis that the subsurface reflectivity profile is sparse, which is confirmed if only few inclusions lie in the subsurface. The CS was applied to an Earth observation geometry to validate the results and confirm the method's performances, and in a small body geometry to test the applicability of the method. Using a multipass geometry with 20 tracks, CS successfully recovers the depth of the inclusion with an improved resolution in the elevation direction from 2.4m in a single pass geometry to 60 cm with the CS. However the resolution achieved by the CS will be worse than the one achieved by the FDBP in the small body observation geometry, since the conditions of application of the method are not retrieved in this geometry.
However, the CS was performed with only one small inclusion, as it is linked to the large computational load of the Born approximation. Improving the computational load of the BA should allow working with more flexible scenarios and perform the tomography of several inclusions or inclusions with a size larger than the elevation resolution. These different studies could be used to validate the CS in more complex scenarios.

Part V

Limits of the UWB scattering

Standard, classical SAR syntheses are based on two main hypotheses on the surface investigated:

- The SAR resolution cell contains a large number of scatterer: thus, the central limit theorem can be applied and the statistics of the intensity of the resolution cell can be computed.
- Each scatterer is bright, which means that it scatters energy in the same manner for all angles and frequencies of observation.

However, when considering UWB scattering, the resolution cell size reduces and cannot be considered to contain a large number of scatterers. Thus, the central limit theorem cannot be applied and the statistics of the resolution cell will change. Moreover, in UWB, the Doppler and RF bands become large enough so that the coherence of the scatterer cannot be assumed on the whole RF and Doppler bands. Thus the brightness of the scatterers can no longer be assumed. As these two hypotheses are two major assumptions carried out to compute the SAR synthesis, the fact that they are not respected could have major consequences on the SAR image. If they have an influence on the performances, these effects must be registered and understood.
In this part, we investigate the validity of these two hypotheses. The first chapter considers the validity of the fully developed speckle model, the second chapter considers the validity of the bright point model and the third chapter studies the evolution of the radar resolution when the radar's RF and Doppler bands are increased and compared it with the theoretical values of the resolution. This part covers preliminary works, which would require more effort to be finalized.

Contents

Chapter 14

Limitation of the speckle model

Synthetic aperture radar remote sensing offers a number of advantages over optical remote sensing, mainly the all-day, all-weather acquisition capability. However, one drawback of SAR images is the presence of speckle, a granular noise, that visually degrades the appearance of images, as presented in figure 14.1. The model of the speckle has widely been studied over the years and is linked to signal's band.

14.1 The speckle model

14.1.1 Definition

As an active system, a SAR emits an electromagnetic wave and captures the complex signal backscattered from a small area of the imaged scene, delimited by the radar's resolution cell. If we assume that the resolution cell contains a certain number of scatterers and that none yields a reflected signal much stronger than the others, as it is the case for distributed targets, then the received signal can be viewed as the incoherent sum of several backscattered waves, and each individual scatterer cannot be resolved within a resolution cell, as presented in figure 14.2. The final signal, with its amplitude A and phase ϕ can be written as :

$$Ae^{j\phi} = \sum_i A_i e^{j\phi_i} \tag{14.1}$$

Where i denotes a scatterer in the resolution cell. The amplitudes A_i and phases ϕ_i are the results of several factors, including propagation attenuation, scattering of the illuminated targets, and antenna directivity. If we consider that the phases of each path are highly different, they interfere in a constructive or destructive way and the amplitude of the received signal varies randomly. So, even if the reflectivity of each scatterer making up the surface is constant, the SAR image appears as affected by the speckle. For classical Earth observation radars, two fundamental assumptions are made for modeling the well known speckle:

- The wavelength is much shorter than the resolution cell size and the observing distances, so ϕ_i are highly varying. Thus, ϕ may be considered as uniformly distributed in $[-\pi, \pi]$.
- The amplitude A_i and the phases ϕ_i of the scatterers are statistically independent of each other.

And thus the speckle can be treated as a random walk phenomenon.
Furthermore, if the number of scatterers in one resolution cell is sufficiently high, the central limit theorem applies (Gao, 2010), and the resolution cell imaginary and real amplitudes have a Gaussian distribution. This means that the resolution cell amplitude (squared intensity) has a Rayleigh distribution. Finally, if the surface has a constant RCS background, each resolution cell can be considered as a stochastic process, and each resolution cell intensity is independent of one another. This means that the whole image has a distribution identical to the one of a single resolution cell.

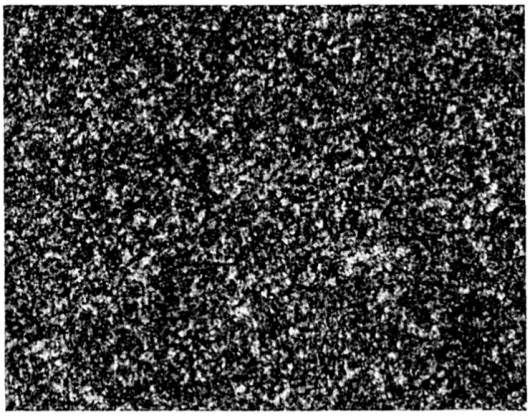

Figure 14.1: Typical speckle pattern (Goodman, 1976).

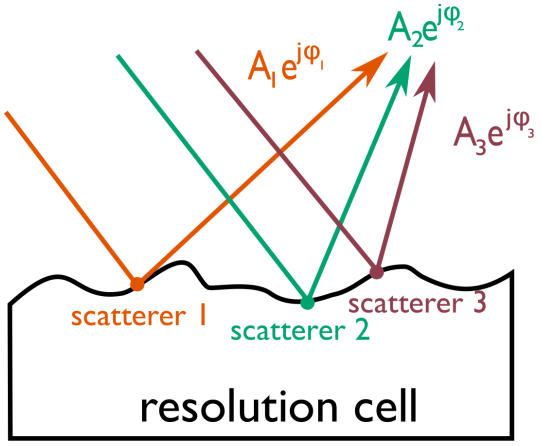

Figure 14.2: Illustration of the origin of speckle in one resolution cell.

With these considerations, the speckle is called "fully developed" (Argenti & Alparone, 2002). However, when either of the fully-developed speckle hypotheses is not filled, the speckle amplitude deviates from the Rayleigh behavior. This happens when a scatterer has a stronger response than the others in the resolution cell, when the number of scatterers per resolution cell itself follows a given probability density function (Jakeman, 1980), when the radar is observing a scene with low-grazing angles (Schleher, 1976) or low-depression angles (Boothe, 1969), or when the resolution cell becomes smaller because of the use of UWB radars. Then, the speckle fits a different distribution, which needs to be investigated.

14.1.2 Speckle statistics analysis

Speckle statistical analysis is a classical tool, used for speckle reduction (Novak et al., 1990) (Porcello et al., 1976), pattern recognition (Oliver & Quegan, 2004), or target classification (Nyoungui et al., 2002) and has been largely been studied over the years. The statistical speckle models can be divided into two groups:

- The parametric models, which use known probability distributions. The parameters of these probability density functions are unknown and will have to be estimated.
- Non parametric models, which don't assume any distribution. They are more flexible and can fit the data with more accuracy, but they are computationally intensive and are thus less used than the parametric models.

The model most widely used to model the speckle's statistics is the Rayleigh distribution, which describes the amplitude of a fully developed speckle. However, another popular parametric model was created to cope with the deviations from Rayleigh behavior: the product model (Ward, 1981).

Name	Expression	Use
Rayleigh	$p_R(x,a) = \frac{x}{a}\exp(-\frac{x^2}{a^2})$	Amplitude of a fully developed speckle.
Exponential	$p_E(x) = \frac{1}{a}\exp\Big(-\frac{x}{a}\Big)$	Intensity of a fully developed speckle.
Gamma	$p_G(x,k,a) = \frac{x^{b-1}\exp(-\frac{x}{a})}{\Gamma(b)a^b}$	Multilook averaged speckle or RCS in the product model (Ward, 1981).
Lognormal	$p_{ln}(x,\sigma,\nu) = \frac{1}{ax}\exp\Big(-\frac{(\ln(x)-\nu)^2}{a^2}\Big)$	Low grazing angle speckle (Trunk & George, 1970).
K-distribution	$p_K(x,a,\nu) = \frac{4}{a\Gamma(\nu)}\Big(\frac{x}{a}\Big)^{\nu}K_{\nu-1}\Big(2\frac{x}{a}\Big)$	Sea speckle with the product model (Jakeman & Pusey, 1976).
Weibull	$p_K(x,b,\rho) = \frac{b}{2\rho}\Big(\frac{x}{\rho}\Big)^{(b/2-1)}\exp\Big[\Big(-\frac{x}{\rho}\Big)^{b/2}\Big]$	Sea speckle with low elevation angles (Boothe, 1969).

Table 14.1: List of different known speckle models.

It was initially developed to analyze the non-Rayleigh behaviour of the sea echo by introducing the notion of texture, which appears when the RCS of the target is considered to be varying with its own probability density function. Thus, the SAR image statistics deviate from the statistics of its resolution cells. With the product model, the intensity I in a SAR image can be written:

$$I = \sigma \cdot n \tag{14.2}$$

With I the SAR image intensity, σ being the RCS component and n the speckle component. If the RCS is constant, then the image intensity will have the same behaviour as the speckle, retrieving the behavior of classical speckle models.

Several additional parametric models were then developed to describe speckle when the RCS has its own probability density such as the gamma distribution, the lognormal distribution, the Weibull distribution and the K-distribution are distributions that were used to model speckle deviating from Rayleigh statistics. All these probability density functions described in table 14.1 are pictured in figure 14.3.

To regroup all these distributions and model the speckle with increased simplicity, two families of distributions were developed, the GΓ- distribution and the GC-distribution.

GΓ distribution

The GΓ pdf is a three-parameter statistical model, developed in (Lampropoulos et al., 1999) to model the clutter. It is defined by the probability density function:

$$p_{G\Gamma}(x,a,b,\nu) = \frac{b}{a\Gamma(\nu)}\Big(\frac{x}{a}\Big)^{b\nu-1}\exp\Big[\Big(-\frac{x}{a}\Big)^{b}\Big] \tag{14.3}$$

where a is the scale parameter, b is the power parameter, ν is the shape parameter.

The main advantage of the GΓ-pdf is that it is a family of probability density functions. Indeed, the following statistical models can be obtained from the GΓ-pdf:

- b=1, ν=1 : Exponential pdf
- b≠1, ν=1: Weibull

- b≠1 : Gamma pdf
- b → 0 and $\nu \to \infty$: lognormal pdf

GC distribution

The GC-pdf is a five-parameter statistical model was developed in (Lampropoulos et al., 1999) to fit the product model, the interaction of the RCS variation with the speckle, with larger flexibility. The GC distribution considers that both the RCS and the speckle can be described with the GΓ distribution:

$$p_{GC}(x) = \int_0^\infty p_{G\Gamma}(x|s)p_{G\Gamma}(s)ds \tag{14.4}$$

The GC pdf can thus be written:

$$p_{GC}(x,a,b_1,b_2,\nu_1,\nu_2) = \frac{b_1 b_2}{\Gamma(\nu_1)\Gamma(\nu_2)} \frac{x^{b_1\nu_1-1}}{a^{b_2\nu_2}} \int_0^\infty s^{b_2\nu_2-b_1\nu_1-1} \exp\Big[-\Big(\frac{s}{a}\Big)^{b_2} - \Big(\frac{x}{s}\Big)^{b_1}\Big] ds \tag{14.5}$$

Where b_1, ν_1 describe the RCS behaviour and b_2, ν_2 describe the speckle's behaviour.

14.1.3 Deviation of the speckle model in UWB scattering

One characteristic of UWB SAR is the enlargement of the RF band, and in our case, the enlargement of the Foppler band as well: as a consequence, the resolution cell's size is reduced in both the range and azimuth directions. Thus, with UWB instruments, both conditions set for the fully developed speckle hypotheses are questioned:

- The resolution cell's size is not large compared to the wavelength: thus the phases of each scatterer are not highly varying and cannot be considered uniformly distributed.
- Only a few scatterers may lie in one resolution cell, and the central limit theorem cannot be applied.

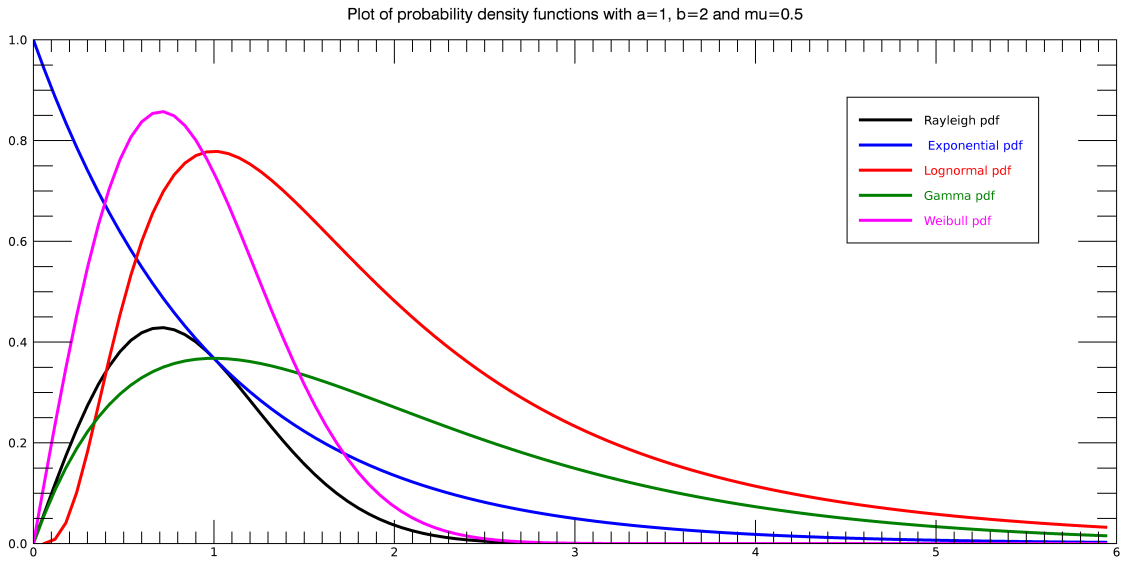

Figure 14.3: Illustration of different probability density functions.

The divergence of the Rayleigh behaviour for high resolution SAR images has been observed for several years, mostly for sea surfaces, where the speckle was found to be compliant with the K-distribution (Jakeman & Pusey, 1976), the Weibull distribution or the log-normal distribution when imaging sea surfaces with high resolution radars and low grazing angles (Schleher, 1976) (Trunk & George, 1970). Tison et al. (2004) applied the same work for urban areas observed with high resolution radars and observed that the speckle deviates from the Rayleigh distribution, either because the resolution cell becomes smaller or because of the appearance of a dominant scatterer. Lombardini (2005) analysed the influence of roughness parameters on simulated SAR speckle and found out that an increase of the SAR correlation length brings a deviation from Rayleigh clutter, and used the Weibull model to estimate the deviation from the Rayleigh distribution from X-band forest images. Lampropoulos et al. (1999) used the GC distribution to model speckle from high resolution sea SAR data in C-band and X-band and SAR land data. Even though sea data are found out to fit relatively closely the Rayleigh probability density function for the speckle (b_1=1.95 and ν_1=1.05 when the Rayleigh pdf is achieved for b_1=2.0 and ν_1=1.0), the land data were found out to largely differ from a Rayleigh behaviour (b_1=1.55 and ν_1=1.22).
Among all studies focused on modelling the speckle, none has concentrated on studying the model of the speckle when only the resolution cell is reduced, and often considered the high resolution speckle along with observation at low grazing angles, or the high resolution speckle along with the appearance of dominant scatterers.
In order to observe the influence of the reduction of the resolution cell alone, we will simulate SAR images on different random rough surfaces and observe the variation on the speckle distribution depending on the size of the resolution cell. We will perform this study first in the Earth observation geometry, and then with HFR, to observe the behaviour of the speckle in the small body geometry. To estimate the behaviour of the speckle, the data will be fitted to the known models with a Markov Chain Monte Carlo method.

14.1.4 MCMC-Markov Chain Monte Carlo

The Markov-Chain Monte Carlo (Hanson, 2000), or MCMC is a method for fitting models to data, little different from a linear χ^2 fit. The MCMC will compare models, generated by a set of parameters to data. The goal of the MCMC is to find the parameters that fit the model to the data the best. The MCMC has several advantages: it allows fitting models with large flexibility, allows to detect easily local minimums, and it has been widely used, which means that it can be implemented on a diversity of platforms. The MCMC process is called Bayesian, since it requires to impose what are called priors to the parameters. The priors contain a priori information about the data and computes the probability of the model given the data. The MCMC uses an ensemble of walkers, denoted as θ, which are vectors that contain the set of parameters used to generate the model. We can consider a grid of possible values for θ, based on the prior values established previously. Each walker will be exploring the parameter space by moving on a new value of the grid and generates a new model. Then, the model y_{model} will be compared to the data y_{data}, via a χ^2 test :

$$\delta = -\frac{1}{2}\sum\left(\frac{y_{data} - y_{model}}{y_{data,err}}\right)^2 \tag{14.6}$$

Where $y_{data,err}$ is the error of the data and δ is the likeliness. The MCMC then checks the ratio of the likeliness generated by the new model vs the likeliness generated by the older model. If the likeliness obtained with the new location is better, the walker moves there and repeats the process. If it is worse, the walker tries a new direction. Finally, all walkers end up in a region of highest likeliness. At the end of the process, each walker keeps the history of all achieved values, which create a chain. As a sampler, the MCMC doesn't tell which parameter θ is the best but indicates for a given number of walkers where the likeliness area stands.

The MCMC is implemented with the GΓ pdf as our model, while the data are the SAR image amplitude. The MCMC is implemented on python 3.7 package emcee, with about 500 walkers, and will be used to fit the image's amplitude, normalized with its mean: $A/ < A >$. We will present the results

of the MCMC with two figures: the first figures will picture the SAR image amplitude histogram, as well as the model with the retrieved parameters. The second figure will present the histogram of the retrieved parameters, and the 2D histograms of the model's different parameters.

14.2 Simulation of UWB speckle in an Earth Observation geometry

The SAR speckle statistics will first be analyzed in an Earth Observation geometry, the geometry where all speckle analyses have been performed, in order to compare our results with previous studies.

14.2.1 Comparison of the speckle statistics with a 100MHz band and a 900MHz band

In order to analyze the behaviour of the speckle originating from the scattering of random rough surfaces, the scenario EO-SP-4 is followed. In this scenario, the speckle statistics of SAR images obtained with different resolution cell sizes are computed, where both the RF band and the Doppler band are modified. For each band, 20 different rough surfaces are randomly generated, the field backscattered from these surfaces are simulated and the statistics of the SAR image are analyzed, averaging the 20 resulting histograms, and fitting them with the GΓ distribution with MCMC. Indeed, the RCS of the surfaces is supposed to be constant, so the fitting with the GC pdf would be unnecessarily complex. First, we compare the histograms obtained for SAR image with a theoretical resolution cell of 13.58m^2, obtained with a band of 100MHz and an illumination time of about 0.6 s, and of 0.17 m^2, obtained with a band of 900MHz and a theoretical illumination time of about 5.5 s.

The results of the MCMC fit of the histogram of a SAR image computed with a band of 100MHz are pictured in figure 14.4. The mean values of the fitted parameters are a=1.13, b=1.92 and ν=1.01, and we recall that the GΓ pdf has a Rayleigh behavior for b=2.0 and ν=1.0. The fit of the GΓ pdf to our model seems satisfying, thus, considering the error margin presented in the bottom of figure 14.4, we can consider than the SAR amplitude has a Rayleigh behaviour.

The results of the MCMC fit of the histogram of a SAR image computed with a band of 900MHz is pictured in figure 14.5. The mean values of the fitted parameters are a=0.15, b=0.74 and ν=3.03, which shows than the behaviour of the speckle is not Rayleigh, yet the model parameters do not correspond to any known probability density function. Moreover, the model obtained with these parameters fails to fit correctly the SAR image amplitude. This means that no probability density function from the GΓ family is suited to model the SAR image amplitude for SAR images obtained with a band of 900MHz, especially not the Rayleigh probability density function. Further probability density functions will need to be investigated in order to fit our data.

14.2.2 Evolution of the GΓ pdf parameters with an increase of the band

The fit of the histograms has been performed from 9 different RF band, from 100 MHz to 900MHz, and 9 different Doppler bandwidth. The sizes of the resolution cell associated with each of these bands are presented in table 14.2, where it is computed using the Earth observation range and azimuth resolution formulas. The 9 histograms resulting from each averaged histogram are pictured first in figure 14.6. A trend can be identified from this figure: the tail of the histogram grows longer as the size of the resolution cell decrease, the maximum of the histogram is increased and is displaced to the right.

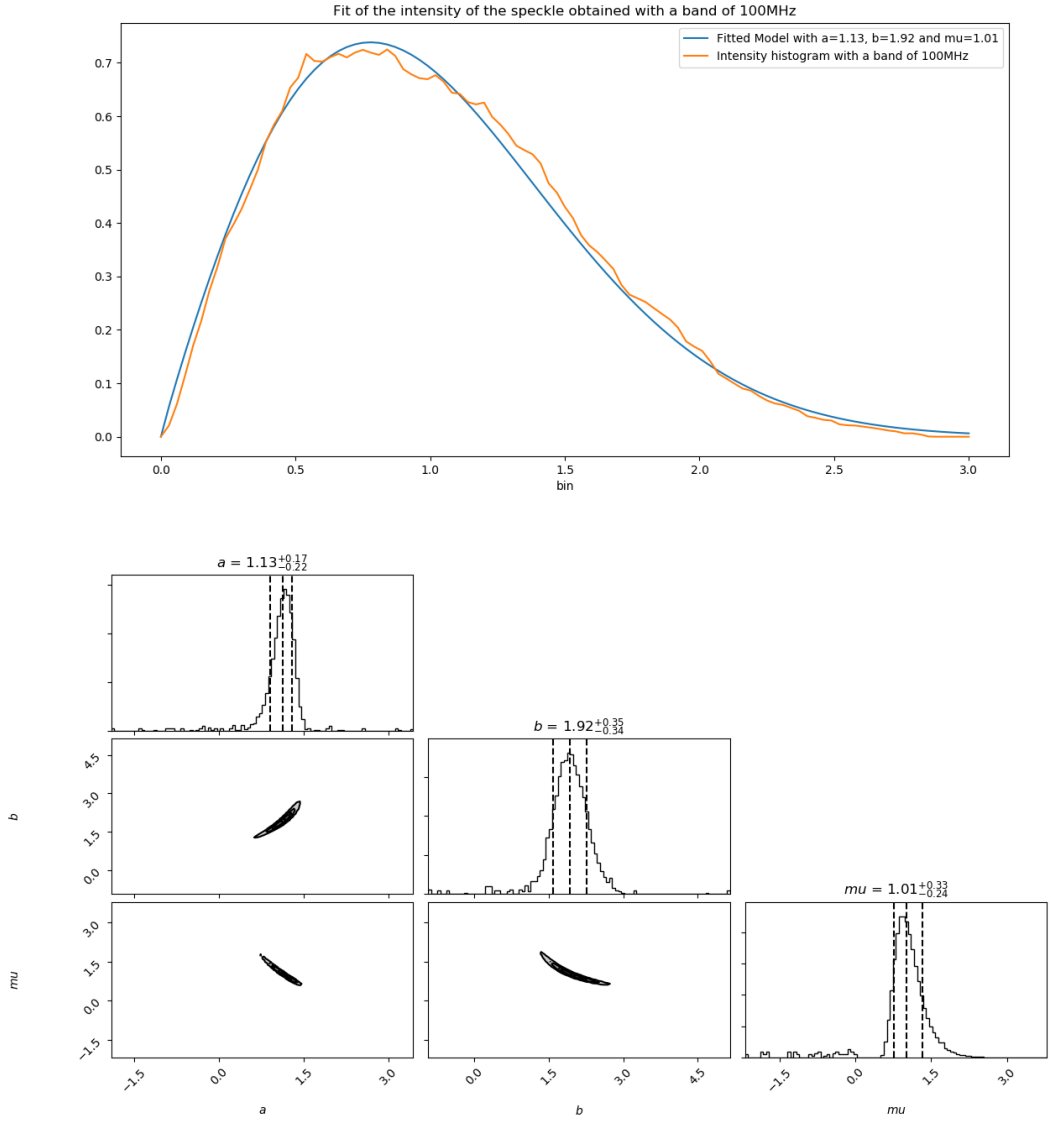

Figure 14.4: Results of the fit of the speckle obtained with a band of 100MHz, and a resolution cell size of 13.5m^2, with the GΓ distribution using MCMC (top) in an Earth Observation geometry, and histograms of the final value of the walkers (bottom).

Table 14.2: Theoretical resolution cell size depending on the RF and Doppler band.

nband	Resolution cell size (m^2)
1	13.58
2	3.39
3	1.51
4	0.85
5	0.54
6	0.38
7	0.28
8	0.21
9	0.17

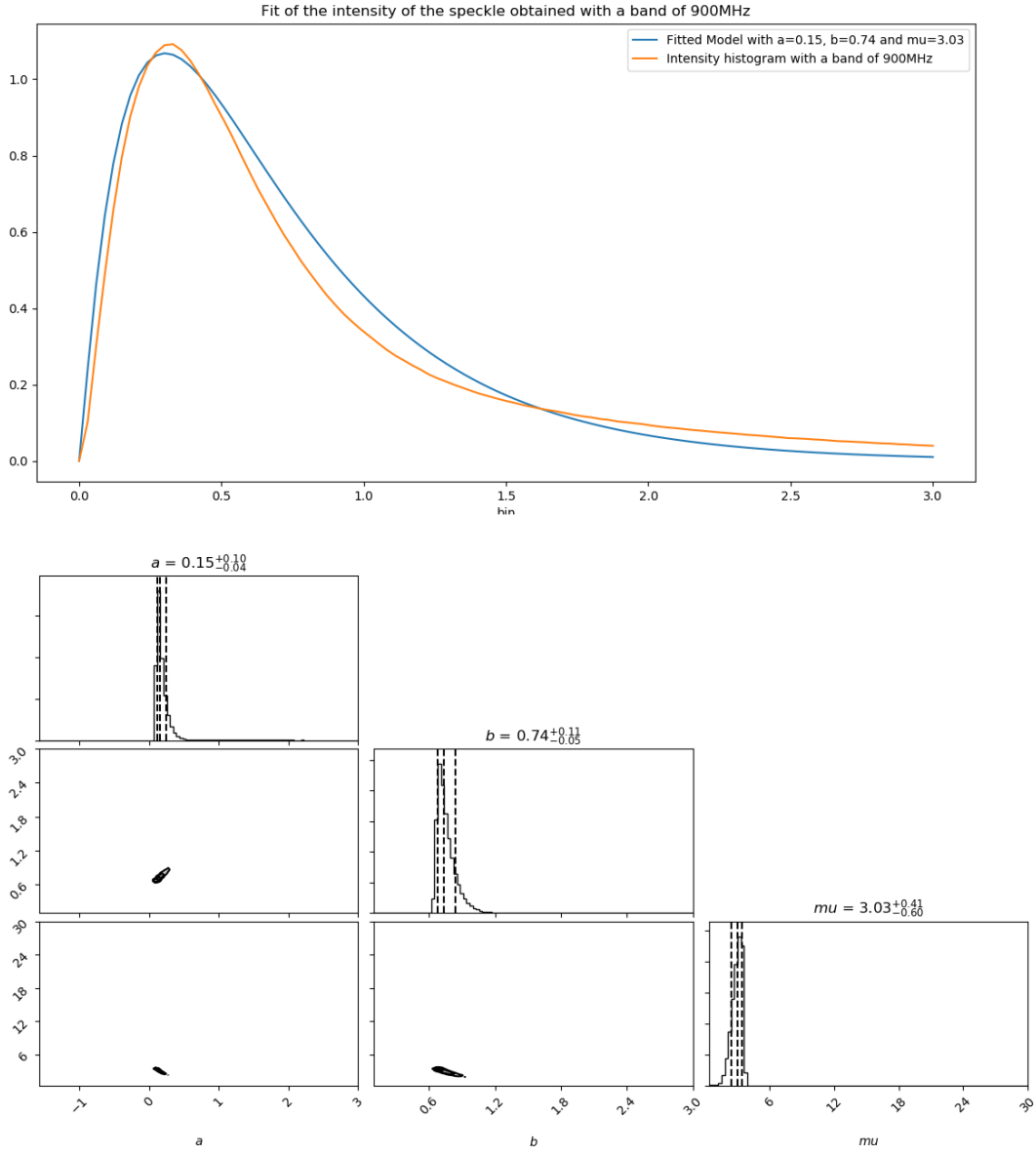

Figure 14.5: Results of the fit of the speckle obtained with a band of 900MHz, and a resolution cell size of 0.17m^2, with the GΓ distribution using MCMC (top) in an Earth Observation geometry, and histograms of the final value of the walkers (bottom).

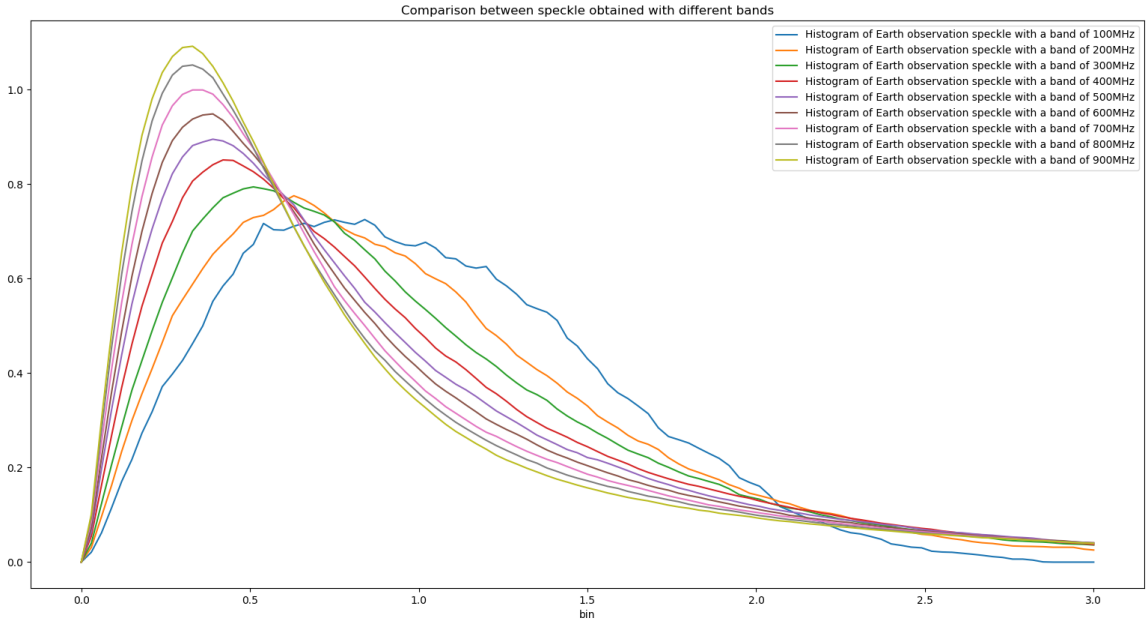

Figure 14.6: Comparison of the averaged histogram obtained with the 9 resolution cells.

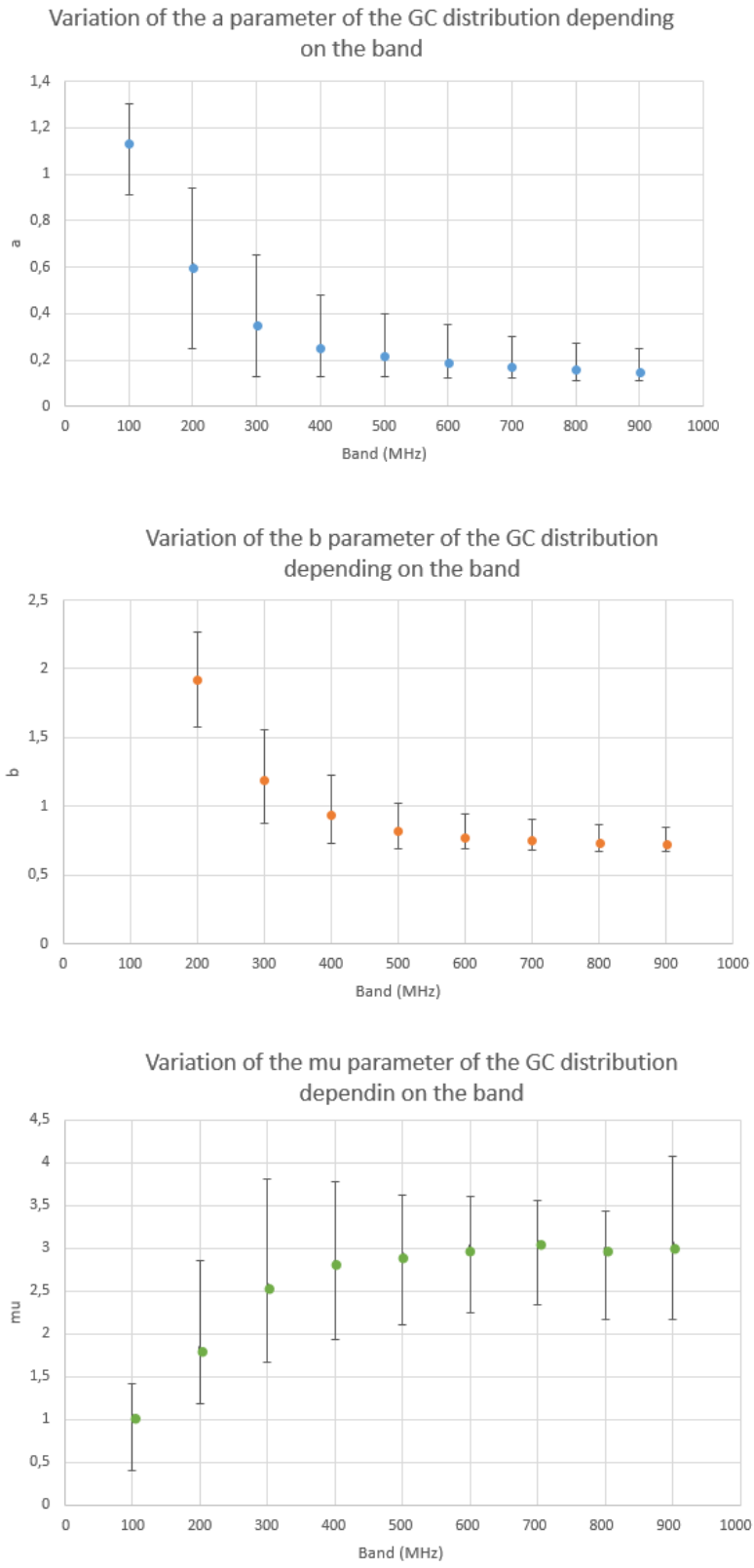

Figure 14.7: Variation of the estimation of the a parameter (top), b parameter (middle) ,and ν parameter (bottom) of the GC pdf with the MCMC depending on the resolution cell size.

The MCMC fit results are presented in appendix F. Figure 14.7 depicts the variation of the values of a, b and ν depending on the band and thus, the resolution cell size. The estimation of the a, b and ν parameters seems to follow a trend: the estimation of the a and b parameter both decrease as the band increase, before reaching a floor around nband=4 or 5. Meanwhile, the estimation of the ν parameter increases, until a floor at around nband=6. This means that the fit of the speckle in UWB in our simulations seems to reach a particular probability density function.
However, the GΓ pdf does not seem to reconstruct the speckle statistics with an acceptable level. Starting from nband=5, the floor the fit seems to indicate is not represented in our simulated data, as presented in figure 14.6. Further models, as well as non-parametric models, will need to be implemented in order to retrieve the type of distribution.

14.2.3 Summary

The speckle in an Earth Observation geometry has been analysed depending on the resolution cell's size. The behaviour of the speckle when the resolution cell is still large, for nband=1 was identified with a Rayleigh behaviour, as predicted by the speckle model. However, starting from nband=4, the speckle is not identified with a Rayleigh behaviour anymore. Furthermore, starting from nband=5, the quality of the GΓ fit becomes too poor, and we can consider that the GΓ pdf cannot be used to recover the speckle statistics. Additional speckle models will thus have to be reviewed in order to fit our data with acceptable precision.

The speckle will now be analysed when observing a small body with HFR in order to observe the statistics of the speckle behaviour in a different geometry.

14.3 Simulation of UWB speckle in a small body geometry

20 SAR images were now computed, following scenario SB-MP-8 using HFR in the Didymos observation geometry, with a range resolution of 54 cm, an azimuth resolution of 21 cm, which leads to a resolution cell size of 0.11 m^2. Each of the SAR image amplitude histograms was computed and averaged, and the resulting histogram amplitude was then fitted with the GΓ probability density function. The results of the fit are presented in figure 14.8 top, and the corner plot indicates the histogram of the final results obtained with each walker is presented in the bottom. The mean values of the fitted parameters are a=0.28, b=0.90 and ν=2.77, which does not correspond to a Rayleigh behaviour, obtained with b=2.0 and ν=1.0, even when considering the error bars. Moreover, the model fails to fit the SAR image amplitude with correct precision. This means that no probability density function from the GC family is suited to model the SAR Intensity for SAR images obtained with a band of 500MHz with HFR, especially not the Rayleigh probability density.

14.4 Conclusion

UWB imaging questions the hypotheses established in the case of classical SAR imaging. Indeed, when the RF and the Doppler bands get larger the resolution cell size decrease and the fully developed speckle hypotheses cannot be assessed. Thus, the speckle becomes in theory "not fully developed", and the speckle amplitude does not have a Rayleigh behaviour. Several studies have been carried out to investigate the speckle statistics in UWB, but always in the Earth Observation geometry, and they never considered the widening of the band only. Our simulation of the SAR images from random rough surfaces in an Earth Observation geometry confirmed that the speckle leaves a Rayleigh behaviour when the RF and Doppler band are increased, but the precise final UWB behaviour cannot be identified with the GΓ pdf. Then, simulations were carried out in the small body geometry using HFR's configuration. The speckle was also found to be different from a Rayleigh behaviour, but the GΓ pdf fails as well to model the speckle. A further study would be required to order to investigate further parametric models or non-parametric models, which would be adapted to the study of the UWB speckle.

However, the fully developed hypothesis of the speckle is not the only hypothesis of classical SAR imaging that UWB imaging questions. One of the main hypothesis of SAR imaging, which is the whiteness and isotropy of the scatterers, is questioned. Theoretically, this deviation from the classical hypotheses should have a major influence on the SAR image resolution.

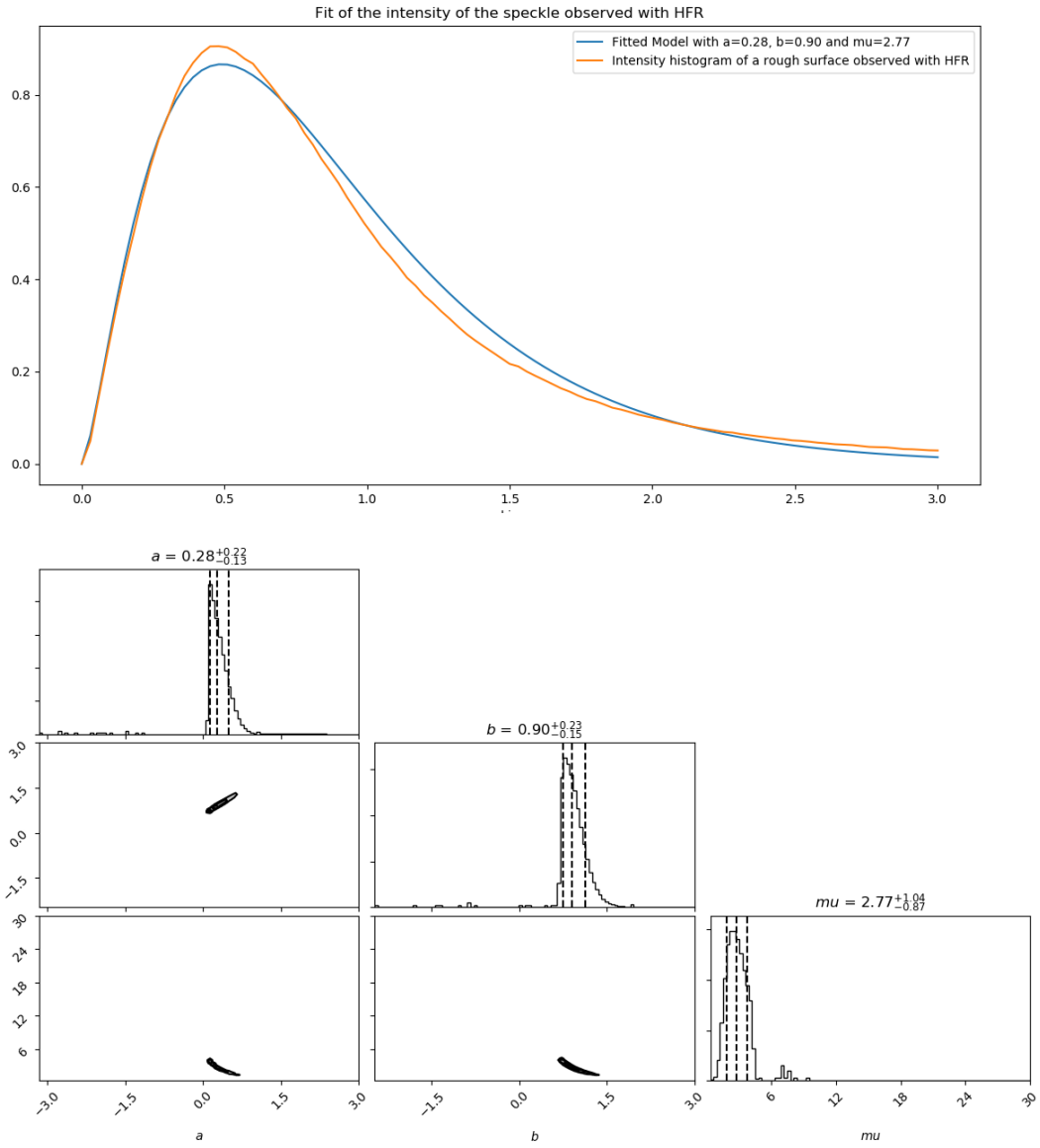

Figure 14.8: Results of the fit of the speckle obtained with HFR in a small body observation geometry with MCMC (top) and histogram of the final value of the walkers (bottom).

Chapter 15

Loss of brightness of the scatterers

15.1 The whiteness and isotropy of scatterers in the SAR synthesis model

Traditionally, SAR imaging follow the the model of bright points. A bright point scatters energy irrespective on the incident angle (such a point is then called isotropic) and irrespective on the incident frequency (such a point is called white). The resulting surface is described as :

$$I(\vec{r}) = \sum_{i=1}^{N} \gamma_i \delta(\vec{r} - \vec{r}_i) \tag{15.1}$$

With I being the surface model, γ_i being the reflectivity of each point and $\vec{r}$ the position of a scatterer in the 2-dimensional plane. γ_i is supposed to be independent on the angle of observation and the frequency : the scatterers are called isotropic and white and thus, bright. This hypothesis is valid for a narrow bandwidth and a small variety of angle of observations. However, with the development of ultra-wideband SAR, which observe targets with a wide range of observation angles and frequencies, the scatterers reflectivity $\gamma_i(\vec{k})$ may depend on the frequency and the angle of observation. Thus the resulting image $I(\vec{r}, \vec{k})$ also depends on f and θ.
The standard image spectrum can be written :

$$H(\vec{k}) = \int_S I(\vec{r}, \vec{k}) \exp(-i\vec{k} \cdot \vec{r}) dS = \int_S \sum_{n=1}^{N} \gamma_n(\vec{k}) \delta(r - r_n) \exp(-i\vec{k} \cdot \vec{r}) dS \tag{15.2}$$

And thus, the inversion of this model to retrieve the image I(r) cannot be obtained with a inverse Fourier transform since γ_n is dependent on $\vec{k}$ as well. As the SAR image is obtain by an inverse Fourier transform from the spectrum, it means that the SAR image in UWB scattering does not recover the true surface reflectivity.
Before analysing the effects of the dispersive and anisotropic behaviour of the scatterers on the resolution, this behaviour will first have to highlighted. In order to so, an hyperimage $I(r,\vec{k})$ can be developed, giving access to each scatterer response depending on the frequency and the angle of observation.

15.2 Time Frequency Method to investigate the whiteness and isotropy of scatterers

The angular/frequency response of each scatterer can be imaged using time frequency methods and building hyperimage an $I_H(\vec{r}, \vec{k})$, from the spectrum of a surface. The hyperimage concept was developed in Ovarlez et al. (2003), Tria (2005) and Duquenoy (2009) to analyse the dispersive and anisotropic behaviour of scatterers in high resolution SAR image. In these works, consequences on the resolution are implied, but have never been measured.
Hyperimages are built from the bilinear structure of the spectrum $H(\vec{k})$ scattered by an object :

$$I_H(\vec{r},\vec{k}) = \int K(\vec{k_1},\vec{k_2},\vec{r},\vec{k})H(\vec{k_1})H(\vec{k_2})d\vec{k_1}d\vec{k_2} \tag{15.3}$$

where K is an hermitian kernel. K can be determined by setting some constraints on the hyperimage, detailed in Tria (2005), with the most crucial being the principle of covariance, stating that $I_H(\vec{r},\vec{k})$ must be independent on the choice of the reference system. Thus, the first task is to identify the transformations connecting the different frames, which mostly consist of a change of origin because of the movement of the radar, and a change of unit in length and time because of the Doppler effect. However, the Doppler effect acts in a different way depending on the signal's band, as a translation for narrowband signals or as a compression when the signal is wideband. Thus, in order to respect the principle of covariance, two different operations will have to be performed on the spectrum in order to obtain an hyperimage, depending on whether the signal is narrowband, or ultra-wideband.

15.2.1 Narrowband signals and the short Fourier Transform

For narrowband signals, the Doppler effect acts only as a translation of the frequency. Thus, the transformation law from a spectrum H(f) obtained for a target located at a point x and at a frequency f, to the spectrum obtained for a target localised at a point x+b and at a frequency f_a can be written :

$$H(f) \to H_{(f_a,b)}(f) = H(f-f_a)\exp(-2i\pi b\cdot(f-f_a)/c) \tag{15.4}$$

The short term Fourier transform is an hyperimage construction method that respects the principle of covariance of narrowband signals. It starts from the fact that the spectrum H($\vec{k}$) can be recovered from the surface spectrum I($\vec{r}$) by an inverse Fourier transform :

$$I(\vec{r_0}) = \int_S H(\vec{k})e^{-2i\pi\cdot\vec{k}\vec{r_0}}d\vec{k} \tag{15.5}$$

To compute the hyperimage, we will thus add a windowing function $W(\vec{k}-\vec{k_0})$ which will be isolating the angle and frequency over which to perform the inverse Fourier transform.

$$I_H(\vec{r_0},\vec{k_0}) = \int_S H(\vec{k})W^*(\vec{k}-\vec{k_0})e^{-2i\pi\cdot\vec{k}\vec{r_0}}d\vec{k} \tag{15.6}$$

This hyperimage is also called a spectrogram, and can thus analyze for each scatterer their frequency and angular behaviour.

15.2.2 Wideband signals and the wavelet analysis

The transformations connecting all the reference frames for wideband signals consist of a change of origin, which accounts for the change of the observer position and a change of units of time and length to account for the dilatation effect due to the Doppler effect. The dilation effect is applied on frequencies, as well as on times to preserve the light velocity constant.
Thus, the transformation law from the spectrum H(f) obtained for a target located at a point x and at a frequency f, to the spectrum obtained for a target located at a point x+b and at a frequency $\frac{f}{a}$ can be written :

$$H(f) \to H_{(a,b)}(f) = a\exp(-4i\pi b\cdot f/c)H(af) \tag{15.7}$$

By taking into account that a dilatation in space $x \to ax$ is performed to keep the constancy of the speed of light Bertrand and Bertrand (1995).

Definition of the wavelet transform method

The bidimensional wavelet transform is an hyperimage formation algorithm that satisfies the covariance principle for wideband signals. It considers a wavelet $\Phi(\vec{k})$, called the mother wavelet, located at $\vec{r}=\vec{0}$, in the direction $\theta=0$ and at the frequency corresponding to k=$\frac{2f}{c}$. $\Phi(\vec{k})$ does not have to be representative of a target scattering but just needs to be easily located in frequency and in angle.

Then, the spectrum $\mathrm{H}(\vec{k})$ can be decomposed into elementary wavelets Φ, perfectly located at the point $(\vec{x},\vec{k})$. A family of functions $\Psi_{\vec{r_0},\vec{k_0}}$, located at $(\vec{x_0},\vec{k_0})$, is built from $\Phi(\vec{k})$ using the transformation described above as :

$$\Psi_{\vec{r_0},\vec{k_0}}(\vec{k}) = \frac{1}{k_0} e^{-j2\pi\cdot\vec{k}\cdot\vec{r_0}} \Phi\Big(\frac{k}{k_0}, \theta - \theta_0\Big) \tag{15.8}$$

In order to decompose the spectrum on this family of wavelet, we compute the wavelet coefficient $C_H(r_0,\vec{k_0})$ as the dot product between the spectrum $H(k)$ and the wavelet $\Psi_{r_0,\vec{k_0}}(\vec{k})$

$$C_H(\vec{r_0},\vec{k_0}) = \int_{\theta_{min}}^{\theta_{max}} \int_{k_{min}}^{k_{max}} kH(k,\theta) \frac{1}{k_0} e^{-j2\pi\cdot\vec{k}\cdot\vec{r_0}} \Phi^*(\frac{k}{k_0}, \theta - \theta_0) \tag{15.9}$$

and the hyperimage is built as

$$I_H(r_0,\vec{k_0}) = |C_H(r_0,\vec{k_0})|^2 \tag{15.10}$$

Definition of the mother wavelet

As the hyperimage depends on the surface spectrum and on the mother wavelet, the choice of the mother wavelet is crucial: indeed, a wavelet well localized in frequency and angle is necessary. The mother wavelet needs to satisfy the admissibility coefficient:

$$\int_{-\pi}^{\pi} \int_{0}^{+\infty} dk \frac{|\phi(k,\theta)|^2}{k} < +\infty \tag{15.11}$$

In time/frequency analysis, the Gaussian wavelet satisfies this admissibility coefficient :

$$\Phi(k,\theta) = \exp\Big(\Big(\frac{k-1}{\sigma_k}\Big)^2\Big) \cdot \exp\Big(\Big(\frac{\theta}{\sigma_\theta}\Big)^2\Big) \tag{15.12}$$

While the parameters σ_k and σ_θ define the wave spread in the frequency and angular domain.

15.3 Application of the time/frequency analysis methods

In order to observe the scatterers' angular and frequency behaviour, the short term Fourier transform and the wavelet analysis are applied to different signals, depending on their RF bandwidth and the domain of validity of each method.
In an X-band Earth observation geometry, using a radar with a central frequency of 9.8 GHz, the short term Fourier transform will be applied to signals having a bandwidth smaller than 450 MHz, while the wavelet transform will be applied for signals with a band larger than 450MHz.
For the small body geometry, HFR was designed to have a central frequency of 550MHz and a bandwidth of 500MHz. Thus, the narrowband hypothesis cannot be filled, which means that the wavelet transform will have to be applied to construct the scatterer's hyperimages.
The hyperimages are computed depending on the wavenumber k and the angle of incidence of the spacecraft with the target θ. Since the hyperimages of a single point are computed, the angle of incidence is linked to the position of the spacecraft on the trajectory and thus on the Doppler frequency. The hyperimages are thus presented depending on the frequency of the signal, and of the Doppler frequency of the scatterer since it might give an easier representation of the geometry.

15.3.1 Implementation of the short-term Fourier transform in an Earth observation geometry

The short-term Fourier transform was applied to observe the angular/frequency of the scatterers in different cases:

- On a point target, where the scatterer will be isotropic and white, and thus bright. This geometry is described by scenario EO-SP-5

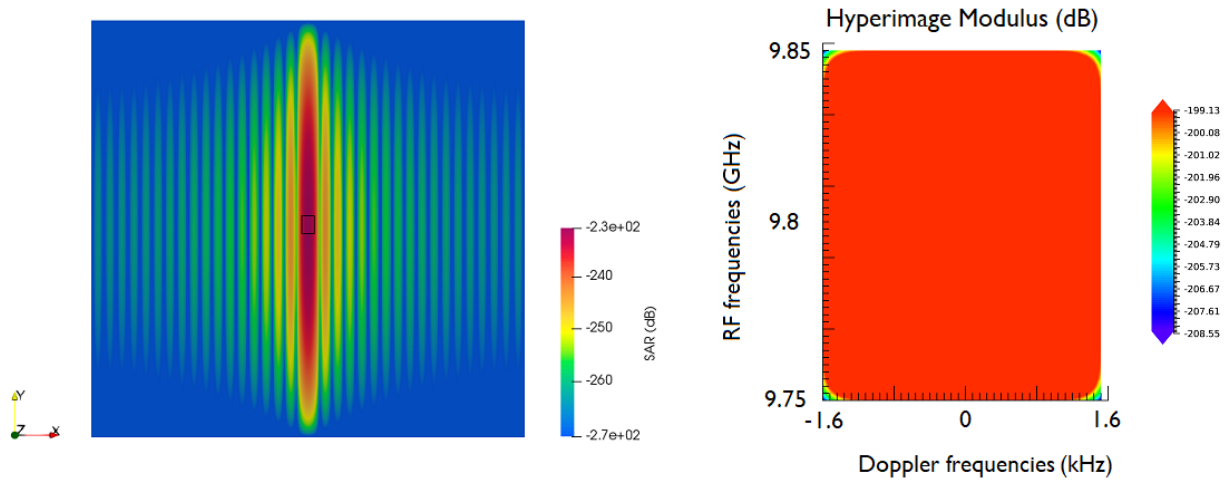

Figure 15.1: The SAR image obtained from scenario EO-SP-5 and the hyperimage associated with the pixel denoted by the black square.

- On a larger facet where the scatterer will be white, but anisotropic. This geometry is described by scenario EO-SP-6
- On an extended rough surface, composed of an association of facets, where the behaviour of the scatterers is unknown for now. This geometry is described by scenario EO-MP-2.

The short Fourier transform is applied with a Gaussian windowing function $W(\vec{k})$, defined as:

$$W(\vec{k}) = W(k,\theta) = \exp\Big(-\Big(\Big(\frac{k}{c_{lk}}\Big)^2 + \frac{\theta}{c_{l\theta}}\Big)^2\Big) \tag{15.13}$$

Where c_{lk} and $c_{l\theta}$ defines the spread of the windowing function in the frequency and angular domains.

Implementation on a point target

The simulated spectrum and the SAR image of a point target, corresponding to scenario EO-SP-5 were computed and the short term Fourier transform was applied at the position of the target. The SAR synthesis and the hyperimage computed are pictured in figure 15.1, with the black square indicating the position of the target $\vec{r_0}$ where the short term Fourier transform was calculated.

The hyperimage is constant on the range of frequencies and incidence angles used in the geometry, which means that the scatterer is bright, isotropic and non dispersive. The deviations on the image border occur because of the discontinuity of spectrum, which is equal to 0 outside of the domain $[k_{\min}, k_{\max}, \theta_{\min}, \theta_{\max}]$. Thus, we can consider the behaviour of a point scatterer is correctly recovered by the hyperimage.

Implementation on a larger facet

A second step in the application of the short term Fourier transform is to consider an extended facet. Scenario EO-SP-6 considers observing a 3m-large facet, which SAR synthesis has a cardinal sine pattern, depending on the incident angle of observation. The corresponding SAR synthesis, with the triangular facet pictured in white and the hyperimage is pictured in figure 15.2. The black square indicates the position of the center of the facet, at the position $\vec{r_0}$ where the hyperimage was computed.

The hyperimage is constant on the vertical axis, which means that the scatterer is non-dispersive. However, the hyperimage is not constant on the horizontal axis, which shows that the scatterer is

anisotropic, and reproduces the cardinal sine behaviour of a plane. Thus, the hyperimage reproduces the angular/frequency behaviour of a large facet.

Implementation on an extended surface

In order to analyse the behaviour of different scatterers forming a surface, the short Fourier transform is applied to a random rough surface consisting of 3-cm large facets, following scenario EO-MP-2. As the SAR images of rough surfaces are perturbed with speckle, that create a granular, random-like noise, the hyperimage of one realisation of a random rough surface will be associated with a random behaviour. In order to retrieve the mean behaviour of the hyperimage, the surface is imaged with a multipass geometry, and the hyperimages resulting from each pass are averaged, following scenario EO-MP-2. The random rough surface investigated and the SAR synthesis of the first trajectory is presented in figure 15.3, with the position of the three scatterers investigated highlighted in black, blue and green. The final hyperimages of each of these scatterers are pictured in figure 15.4.

These resulting hyperimages are averaged from 50 hyperimages computed from scenario EO-MP-2. Considering that the largest dynamic between points on the hyperimage reaches 2 dB, we can

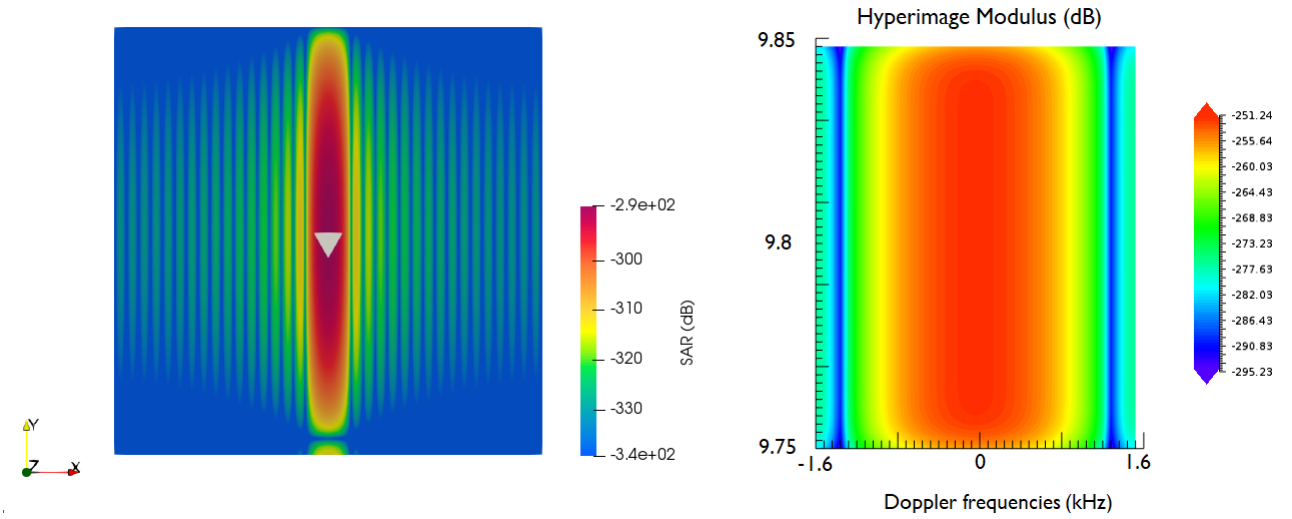

Figure 15.2: The SAR image of scenario EO-SP-6 with the position on the facet (left) and the hyperimage of an extended facet (right) associated with the position indicated by a black square.

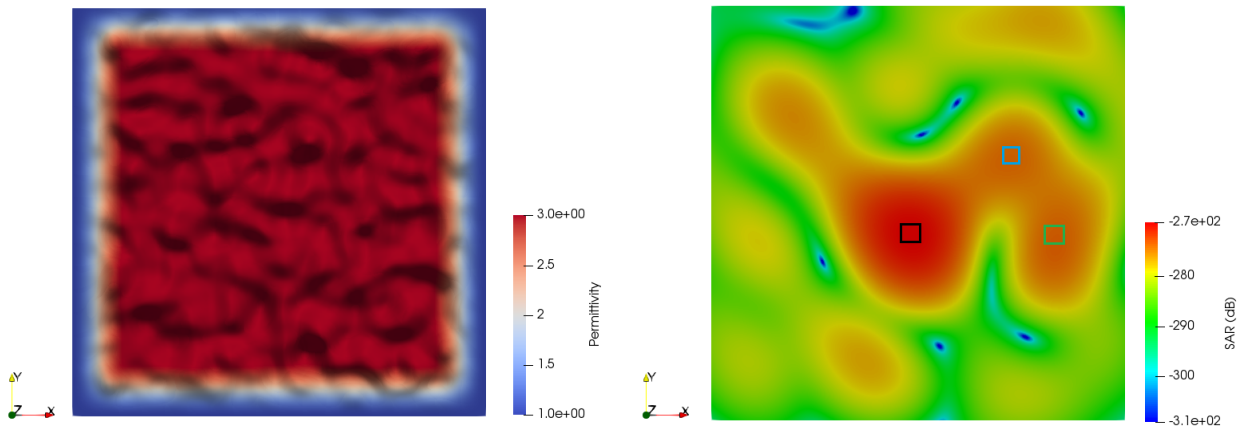

Figure 15.3: The rough surface generated from scenario EO-MP-2 and a SAR image processed from one trajectory of the multipass observation.

consider that the value of the hyperimage is constant, we can conclude that all scatterers have the same angular/frequency response. The hyperimage can be considered constant on the entire frequency and angular bands of each scatterer, except for different azimuth positions around the 10th and 95th soundings. However, this effect is only 1.5 dB below the power of the rest of the hyperimage and is thought to be due to the averaging, since only 50 hyperimages were computed.
Thus for an extended surface consisting of 3cm facets, the averaged behaviour of each scattered can be considered as white and isotropic, satisfy the bright point model, and the hypotheses considered for the SAR synthesis can be thought as valid.

15.3.2 Implementation of the wavelet analysis in an Earth observation geometry

In order to check the applicability of the wavelet transform on wideband signals, the method was applied to observe the angular/frequency behaviour of the scatterers in different cases:

- On a point target, where the scatterer will be isotropic and white, and thus bright. This geometry is described by scenario EO-SP-7
- On a larger facet where the scatterer will be white, but anisotropic. This geometry is described by scenario EO-SP-8.
- On an extended rough surface, composed of an association of facets, where the behaviour of the scatterers is unknown for now. This geometry is described by scenario EO-MP-3.

Point target

The simulated spectrum and the SAR image of a point target, corresponding to scenario SB-SP-7, were computed and the wavelet analysis was applied at the position of the target. The SAR synthesis and the hyperimage computed are pictured on figure 15.5, with the black square indicating the position of the target $\vec{r_0}$ where the hyperimage was computed.

The hyperimage is constant on the range of frequencies and incidence angles used in the geometry, which means that the scatterer is non-dispersive and isotropic, thus bright. The deviations of the hyperimage on the borders occur because of the discontinuity of spectrum, which is equal to 0 outside

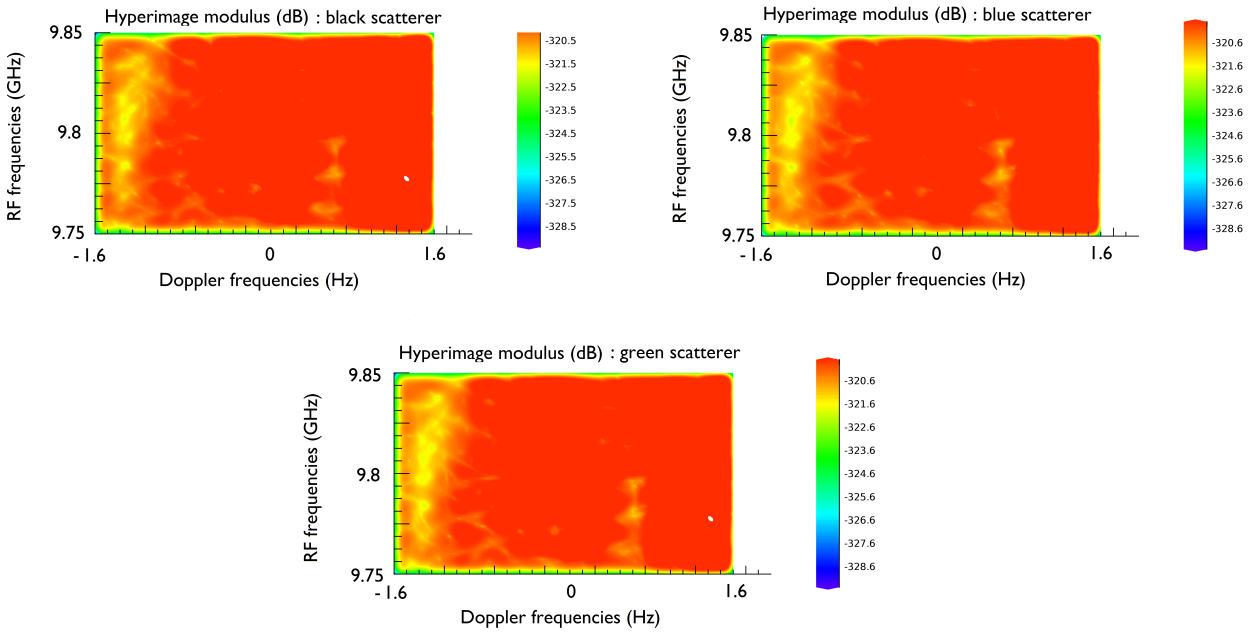

Figure 15.4: The 3 hyperimages obtained from the 3 scatterers positions (left, black; right, blue, bottom, red), with a dynamic of 8 dB.

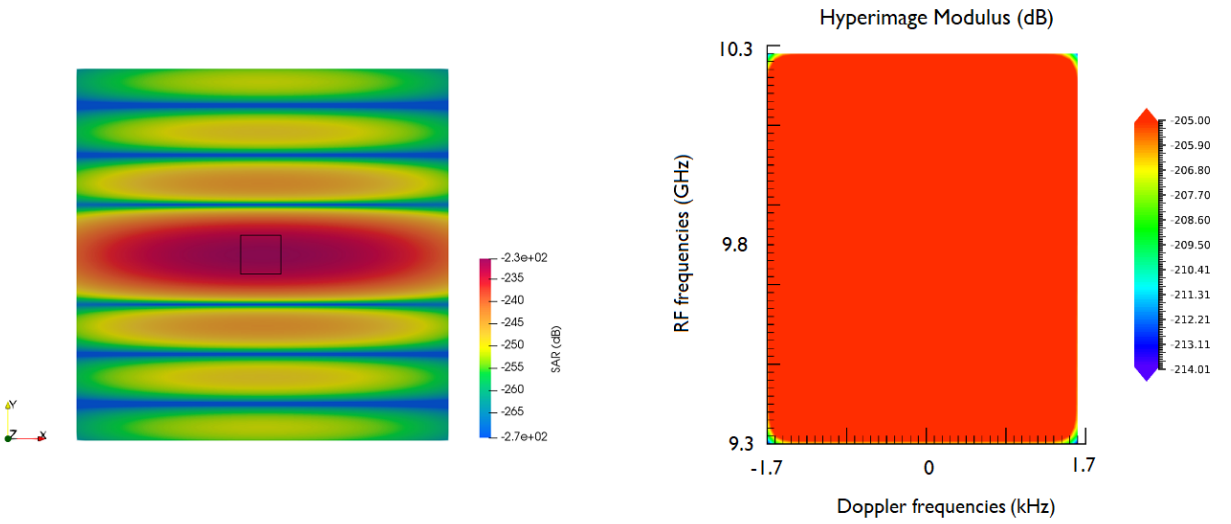

Figure 15.5: The SAR image of scenario EO-SP-7 of a point facet and the hyperimage corresponding the position of the facet, indicated by a black square.

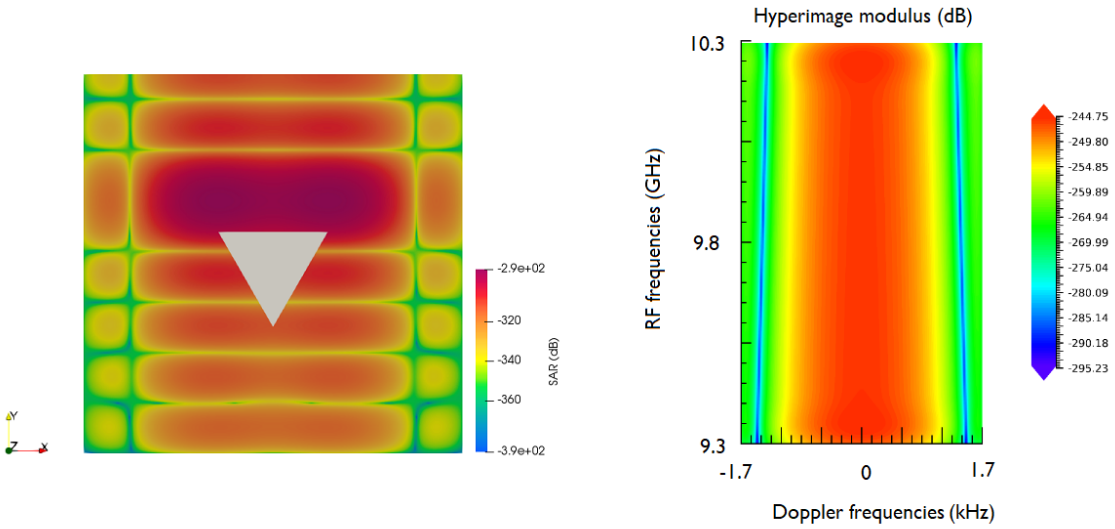

Figure 15.6: SAR image of scenario EO-SP-8, with the position on the facet (left) and the hyperimage of an extended facet (right) associated with the position of the center of the facet, indicated by a black square.

of the domain $[k_{\min}, k_{\max}, \theta_{\min}, \theta_{\max}]$. Thus the behaviour of a point scatterer is correctly recovered by the hyperimage.

Large facet

Scenario EO-SP-8 considers observing a 3m-large facet, which has a cardinal sine angular pattern. The SAR synthesis, with the triangular facet pictured in blue and the corresponding hyperimage are pictured on figure 15.6. The black square indicates the position of the center of the facet, at the position $\vec{r_0}$ where the hyperimage was computed.

The hyperimage is constant on the vertical axis, which means that the scatterer is non dispersive. However, the hyperimage is not constant on the horizontal axis, which shows that the scatterer is anisotropic, as it reproduces the cardinal sine behaviour of the facet. Thus, the hyperimage reproduces the anisotropic behaviour of a large facet.

Implementation on an extended surface

In order to analyst the behaviour of different scatterers forming a rough surface, the wavelet analysis will be applied to a random rough surface consisting of 3-cm large facets, following scenario EO-MP-3. As the SAR images of rough surfaces are perturbed with speckle, that creates a granular, random-like noise, the hyperimage of one realization of a random rough surface will be associated with a random behaviour. In order to retrieve the mean behaviour of the hyperimage, the surface will be imaged with a multipass geometry, and the different corresponding hyperimages will be averaged. The random rough surface investigated and the SAR syntheses of the first trajectory are presented in figure 15.7, with the position of the three scatterers investigated highlighted in black, blue and green. The final hyperimages of each of these scatterers are pictured in figure 15.8.

These resulting hyperimages are averaged from the 50 hyperimages computed from scenario EO-MP-3. All 3 hyperimages have a dynamic between points on the hyperimage of 4 dB maximum. Thus, the value of the hyperimages may be considered constant, but a pattern of straight lines following given directions seems to be standing out. For now, not much can be deduced for these results. The hyperimages of facet in different orientations will have to be studied more carefully in order to understand the scatterers' behaviour.

15.3.3 Implementation of the wavelet analysis in the small body geometry

In order to check the applicability of the wavelet analysis in the small body geometry, the method was applied to observe the angular/frequency behaviour of the scatterers in different cases:

- On a point target, where the scatterer will be isotropic and white and thus bright. This geometry is described by scenario SB-SP-8
- On a larger facet where the scatterer will be white, but anisotropic. This geometry is described by scenario SB-SP-9

Implementation on a point target

The SAR image corresponding to scenario SB-SP-8 was computed, and the wavelet analysis was implemented based on the simulated spectrum. The SAR synthesis and the hyperimage corresponding are pictured on figure 15.9, with the black square showing the position of the position $\vec{r_0}$ where the wavelet analysis transform is computed, which is the position of the point facet.

The hyperimage is constant on the range of frequencies and incidence angles used in the geometry, which means that the scatterer is isotropic and non dispersive, and thus bright. The deviations on the image border occur because of the discontinuity of spectrum, which is equal to 0 outside of the domain

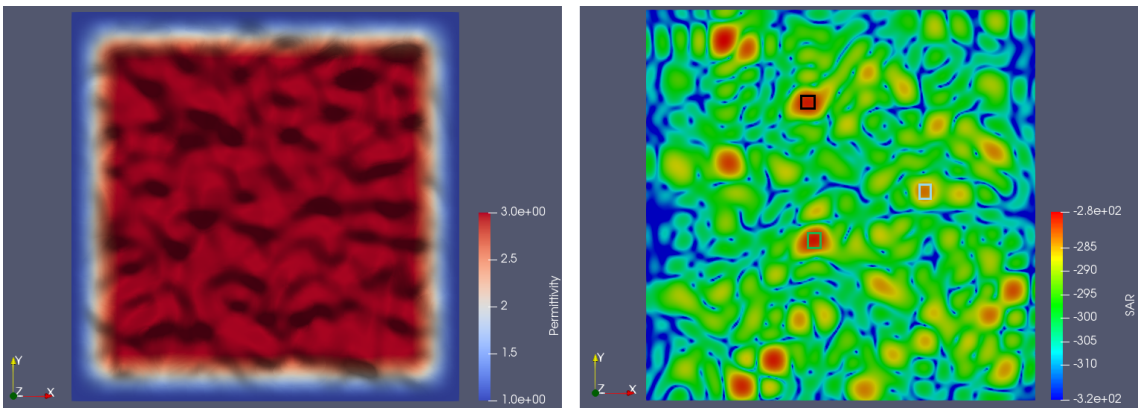

Figure 15.7: The rough surface generated from scenario EO-MP-3 and a SAR image processed from one trajectory of the multipass observation.

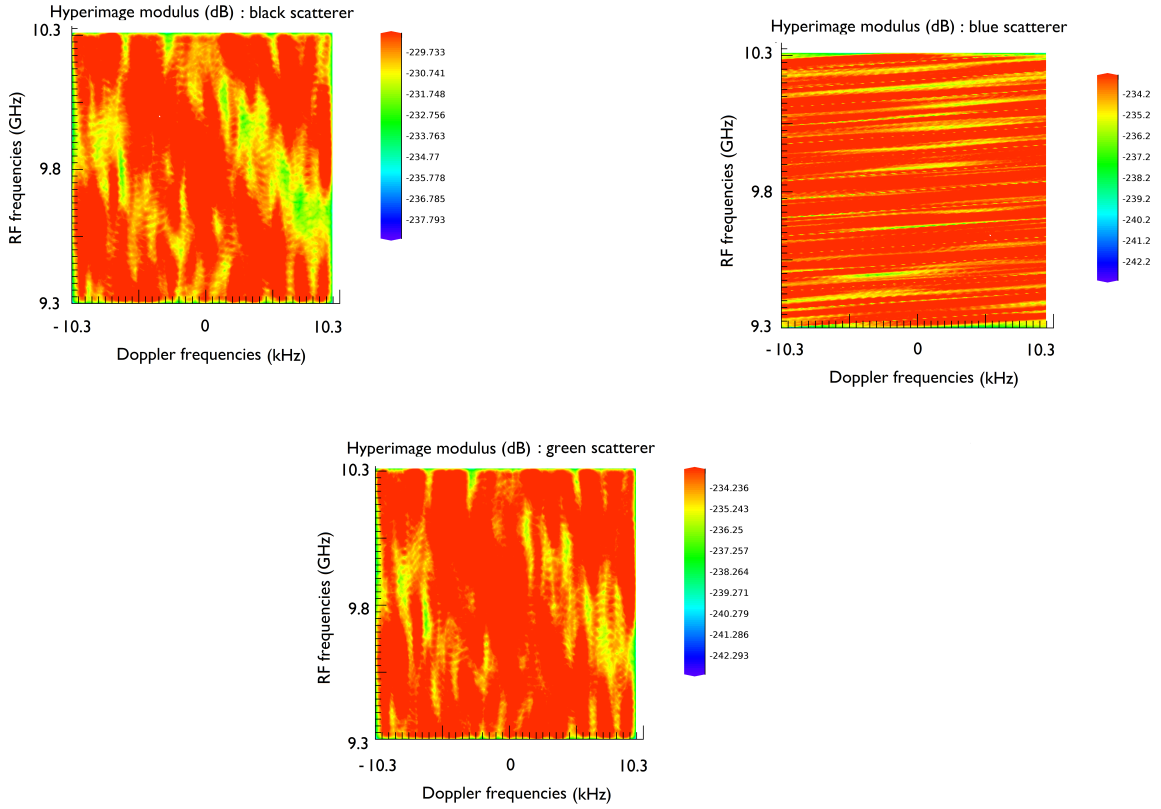

Figure 15.8: The 3 hyperimages obtained from the 3 positions on the image (left, black; right, blue; bottom, red), with a dynamic range of about 8 dB.

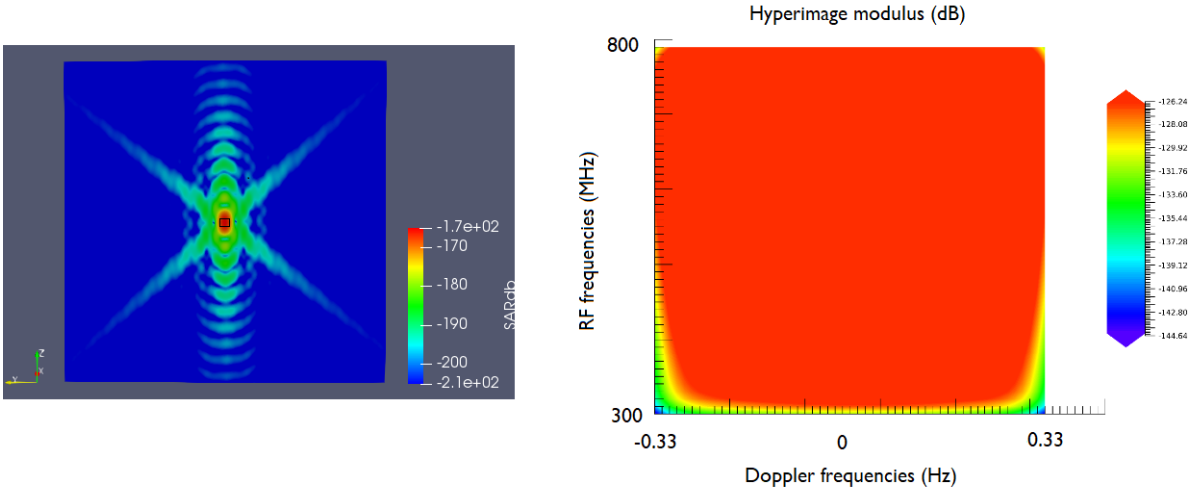

Figure 15.9: The SAR image obtained from scenario SB-SP-8 and the hyperimage associated with the center of the facet, denoted by the black square.

$[k_{\min}, k_{\max}, \theta_{\min}, \theta_{\max}]$. However, the hyperimage is not as symmetric as in the Earth Observation analysis, which makes us consider the applicability of the method. Thus, further inspection of results obtained from the wavelet analysis is required.

Large facet

A second step in the application of the wavelet analysis is to consider an extended facet. Scenario SB-SP-9 considers observing of a 3m-large facet, which has a cardinal sine angular pattern. The

SAR synthesis, with the triangular facet pictured in white and the hyperimage is pictured in figure 15.10. The black square indicates the position of the center of the facet, at the position $\vec{r}_0$ where the hyperimage was computed.

The hyperimage is not constant on the vertical axis, which means that the target is dispersive, while it is not anisotropic, but does not follow a cardinal sine pattern. The deviation from the non-dispersive behaviour goes beyond the limitation of the spectrum in angular angle and frequencies. Further analysis on the reasons for the deviations should be performed: either the wavelet analysis cannot be applied to the small body geometry, or the small body geometry makes large facets not white. The hyperimage of a large facet must be understood before studying the behaviour of different facets forming a random rough surface.

15.3.4 Summary

The hyperimage of different scatterers were computed, using the short Fourier transform for narrowband signals and the wavelet analysis for wideband signals. Both methods were able to reconstruct the white isotropic behaviour of point target, and the anisotropic behaviour of a large facet. The short Fourier transform was able to demonstrate that 3cm facets constituting a rough surface, in average, have a bright behaviour for narrowband signals, and thus that the SAR synthesis hypotheses of brightness are respected for narrowband signals, which complies with our expectations. However, the behaviour of 3cm facets constituting a rough surface imaged with wideband signals could not be clearly identified. The non-brightness could be due to a real change of behaviour of the scatterers, or to averaging effects due to the few numbers of surfaces generated for this study.
Furthermore, the behaviour of facets making a rough surface is computed in average, and we do not how it is linked to the mean behaviour of the scatterer.
Lastly, the wavelet analysis did not succeed in reproducing the angular/frequency in a small body with HFR. Further studies would need to be performed in order to understand whether this deviation is due to the fact that the wavelet analysis is not adapted to a small body geometry, or that the facets lose their bright behaviour in the small body geometry.

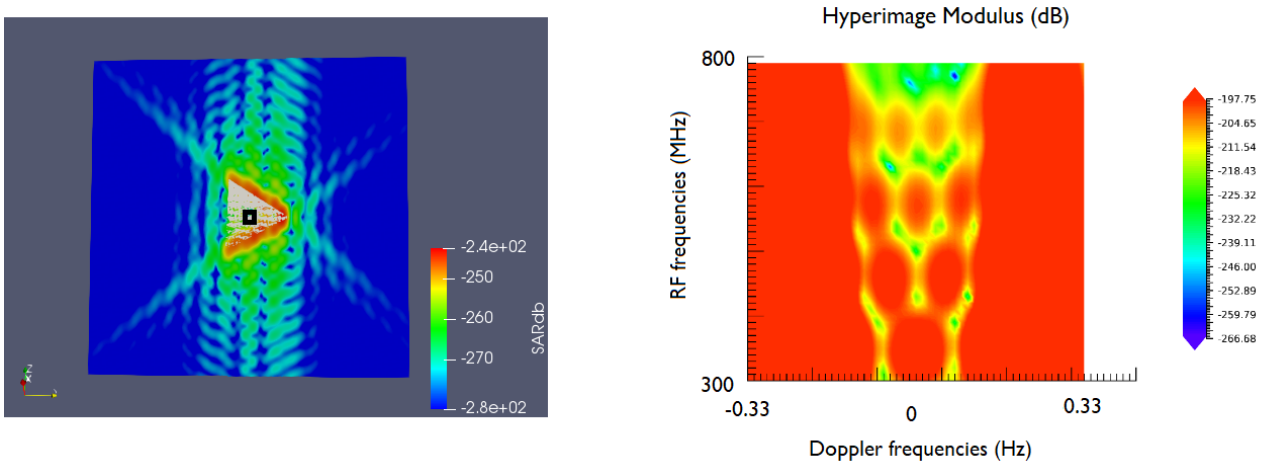

Figure 15.10: The SAR image of scenario SB-SP-9 with the position on the facet (left) and the hyperimage of an extended facet (right) associated with the position of the center of the facet, indicated by a black square.

Chapter 16

Impact on the resolution

UWB scattering challenges the hypotheses established for classical narrowband radars: the speckle does not have a fully developed behaviour and the whiteness and isotropy of the scatterers are questioned. As these two assumptions are carried out to perform the SAR synthesis, the effects of the UWB scattering on the performances of the SAR image, namely the range and azimuth resolution, thus need to be investigated and evaluated.

16.1 Measuring the resolution of extended surface

The resolution is a major indicator of the radar performance, classically measured on point targets, as the 3dB width of the point target response. However the deviation of the resolution caused by UWB scattering cannot be measured on a point target, since the scatterer is bright by definition, and does not lead to an image affected by speckle. Thus, a different way of measuring the resolution needs to be developed. F. Ulaby et al. (1986) studied analytical expressions to model the speckle and found out that the speckle associated with points separated by a distance larger than the resolution may be considered uncorrelated. Thus, by computing the speckle autocorrelation, access to the image resolution could be granted.

16.2 Variation of the resolution in an Earth Observation geometry

Simulations were carried out following scenario EO-SP-4, studying 20 different rough surfaces randomly generated, with 9 different range and Doppler bands, and thus with 9 different resolution cell sizes, as presented in table C.16. For each band, the 20 SAR images were computed, the SAR image autocorrelations were calculated and the 3dB width of the autocorrelation was measured.

The resulting range resolutions are averaged from the 20 different SAR images computed. The averaged resolution for each band are presented in figure 16.1 and compared with the theoretical range resolution.
Figure 16.2 depicts the differences between the measured and the theoretical range resolutions, expressed as :

$$\Delta_{rr} = \frac{rr_{th} - rr_{mes}}{rr_{th}} \tag{16.1}$$

The resulting Doppler resolutions are averaged from the 20 different SAR images computed. The averaged resolution for each band are presented in figure 16.3 and compared with the theoretical doppler resolution.
Figure 16.4 depicts the difference between the measured and the theoretical Doppler resolutions, such that :

$$\Delta_{rd} = \frac{rd_{th} - rd_{mes}}{rd_{th}} \tag{16.2}$$

The measured range and Doppler resolution both follow the theoretical trend. However the difference between the theoretical and measured resolution increases when the band increases: while the measurement difference in the doppler resolution is only 2% when studying an image obtained with a band of 100MHz, the difference increases up to almost 10% when studying an image obtained with a band of 900MHz. The evolution is less major when considering the range resolution, since the measurement difference in the range resolution is 5% when considering an image obtained with a band of 100 MHz and 9% when studying an image obtained with a band of 500MHz. The difference measurement of the Doppler resolution seems to decrease starting from 600MHz when the band is increased, but this may be an effect due to the small number of surfaces since only 20 surfaces were computed.

Table 16.1: Resolution cell's size depending on the RF and Doppler band.

nband	Resolution cell size (m^2)
1	13.58
2	3.39
3	1.51
4	0.85
5	0.54
6	0.38
7	0.28
8	0.21
9	0.17

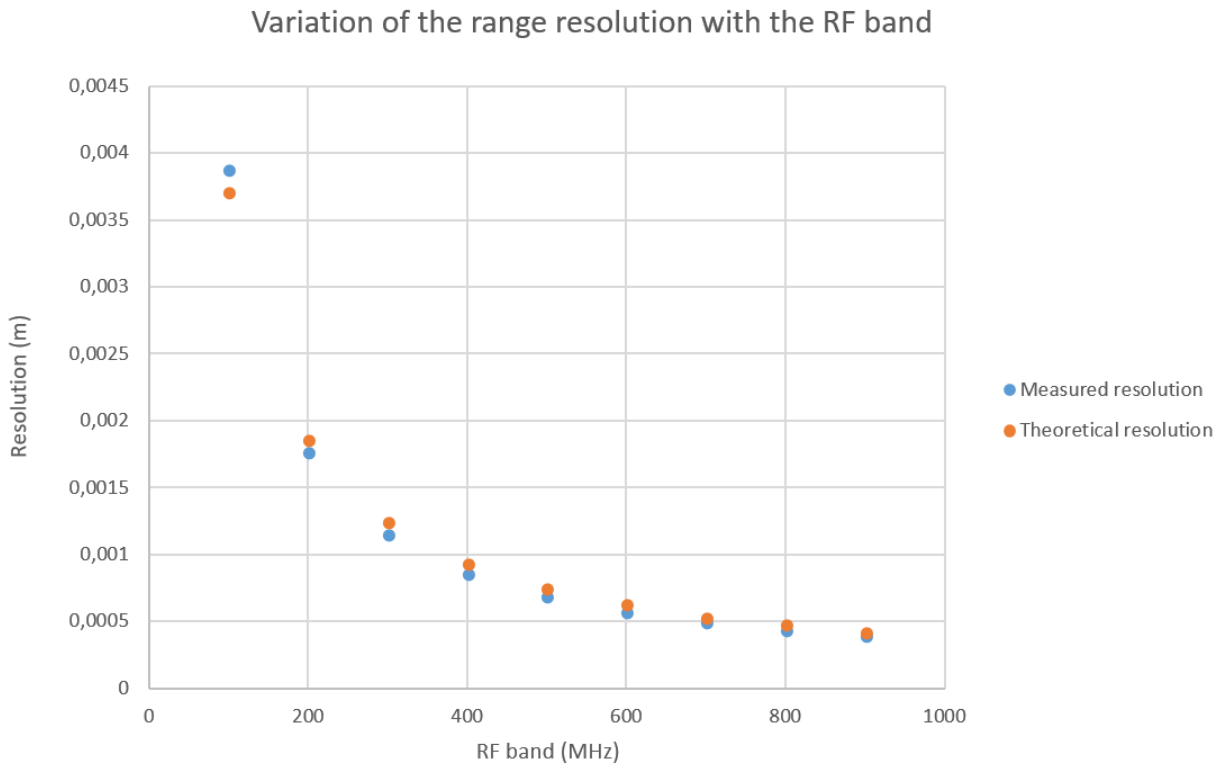

Figure 16.1: Variation of the theoretical range resolution (orange) and the measured range resolution (blue) depending on the RF band.

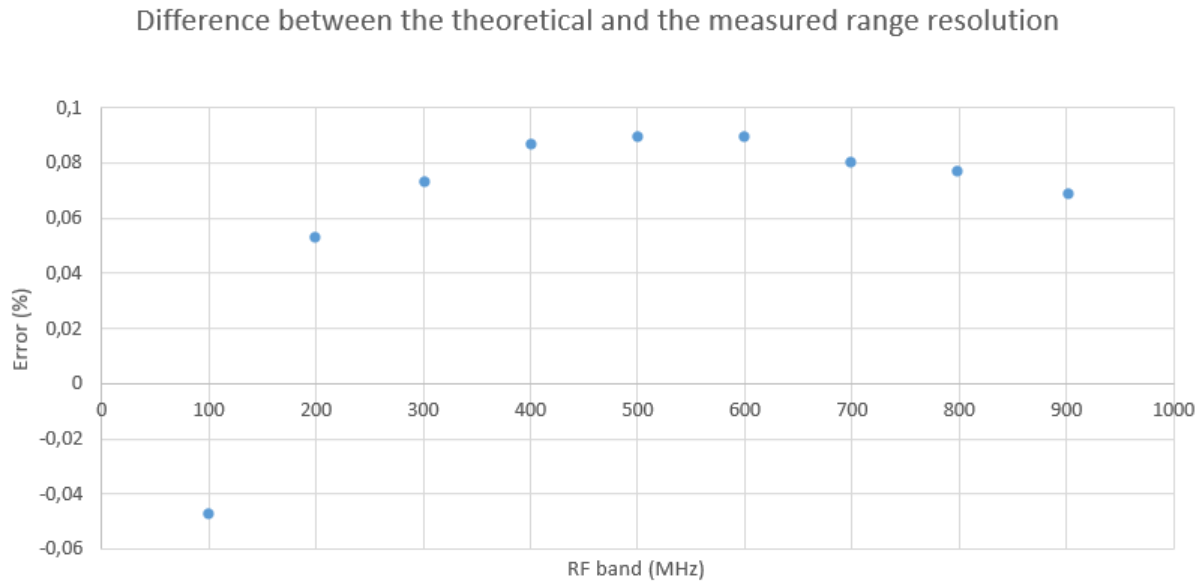

Figure 16.2: Variation of the difference between theoretical range resolution (orange) and the measured range resolution (blue) depending on the RF band (in %).

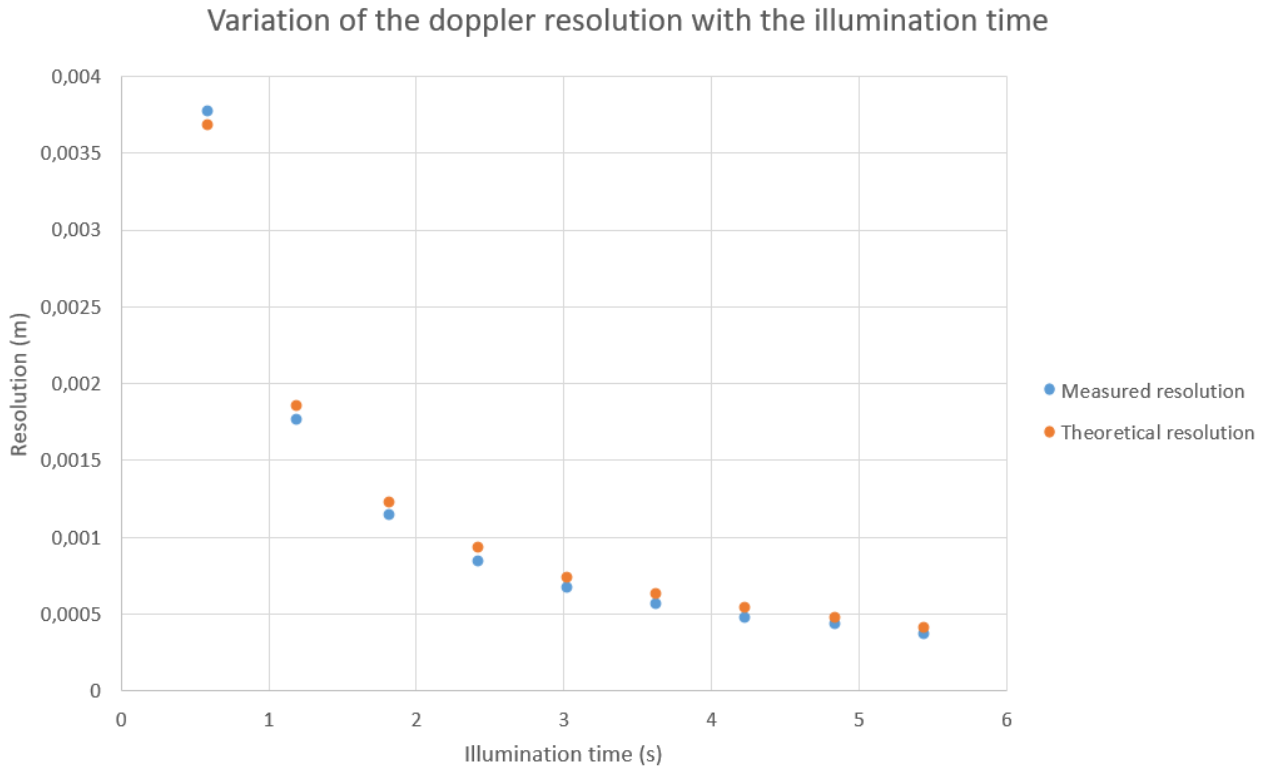

Figure 16.3: Variation of the theoretical Doppler resolution (orange) and the measured Doppler resolution (blue) depending on the illumination time.

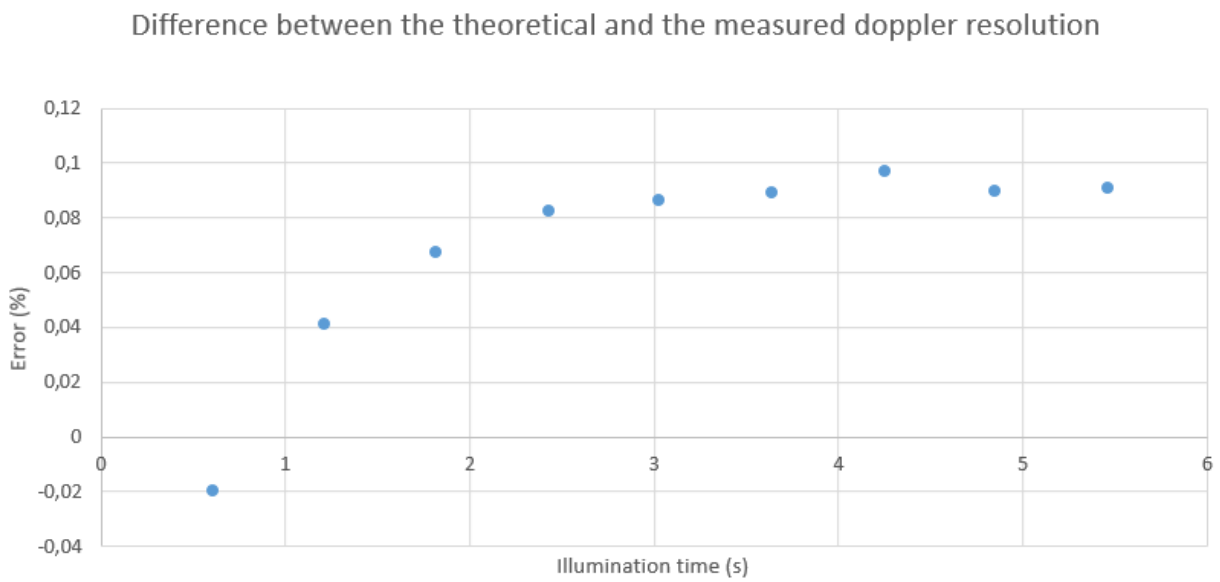

Figure 16.4: Variation of the difference between theoretical Doppler resolution (orange) and the measured Doppler resolution (blue) depending on the illumination time (in %).

16.3 Conclusion

In order to verify whether UWB scattering has an effect on the performances measured on SAR images, the resolution of different SAR images of rough surfaces were computed using the autocorrelation function of the SAR image amplitude. The SAR image measured resolution seems to follow the trend of the theoretical resolution, both in range and in Doppler, but the difference between the theoretical resolution and the measured resolution increases with the band, with a maximum resolution difference of about 10%. However, a study performed on a larger number of surfaces would be necessary to remove the effects due to the small number of averaged parameters, and validate these hypotheses.

Part VI

Conclusion and perspectives

HFR is a UWB SAR which aims at probing the first ten meters of an asteroid surface with a meter-like resolution, and at performing the 3D tomography of the asteroid's interior. Since the UWB observation of asteroids has never been performed, HFR challenges the hypotheses usually formulated for the classical Earth observation and simulations are necessary in order to estimate the performance of the instrument and its deviation from classical Earth observation SAR. As the radar performances, and thus its science return, depends on the instrument design and the geometry of observation, simulations are necessary in order to assess the instrument's capacities in a small body geometry.

The point target behaviour of HFR in the small body geometry was already evaluated in previous studies of the radar's behaviour, using the development of the SPRATS toolbox. However, no tools were available to compute the field scattered by an asteroid surface, and estimate the SAR image obtained from observing the rough surface of an asteroid. In order to overcome this limitation, a surface scattering model had to be developed. Several analytical scattering models were investigated, and their domains of validity were compared with the roughness parameters of the surface of a studied asteroid, the asteroid Itokawa.
The Kirchhoff approximation (KA) was chosen among a series of different backscattering models, since it has a wide domain of validity, and has a simple implementation. The KA, with the facet method has been used since the 2000s to successfully simulate the radar echoes backscattered by planetary surfaces and has already been implemented with the facet method. The facet method was thus associated with SPRATS and was tested on different terrain models based on Itokawa's surfaces. We showed that the KA images the surface with an acceptable precision: the rough surface position on the asteroid was correctly reproduced and the differences of the surface roughness are identified. However, a processing artifact disturbs the resulting SAR synthesis: the projection of the elevation ambiguity, the North/South ambiguity, which occurs when a planetary body is imaged with a single-pass geometry. We showed that using a multi-pass geometry of 20 passes, the mean power of the elevation ambiguity is reduced from -13 dB below the mean power of the rough patch to -18 dB, and can be further reduced by benefiting from a multi-pass geometry covering a larger elevation distance. With the reduction of the power of elevation ambiguity, the KA seems suited to image the rough surface of an asteroid.

However, the objective of HFR is to probe the subsurface of an asteroid as well as its surface. Thus, a volume backscattering model was needed to model the behaviour of an inclusion embedded below the surface. Two volume backscattering models were investigated, and the Born Approximation (BA) was selected to be applied to the subsurface of an asteroid, because of its simple implementation, and of its ability to model the field scattered by entire volumes. The BA was implemented and applied to reconstruct the position of an inclusion embedded below a surface, first in the simple Earth Observation geometry in order to validate the results, and finally in the small body geometry. The Born approximation was found to recover the point target pattern in both geometries and to correctly locate the position of the embedded target, with the measurement error induced by the fact that the SAR processor does not compensate the phase delay induced by the wave propagation in a medium which is not the void. The range resolution and the Doppler resolution are consistent with the resolution obtained from a point target in the small body geometry, and the resolution in the third dimension, the elevation resolution, was computed to be 2.2m. These results validate the BA, which will be used for now to model the field scattered by inclusions embedded below a surface.

Since HFR is supposed to probe the ten first meters of the asteroid subsurface, a resolution of 2.2 meters in the elevation direction would be too poor to perform a precise study of the asteroid shallow interior. Extending the SAR processing principle from the azimuth direction to the elevation direction, tomography algorithms (TomoSAR) can be applied to improve the resolution in the third dimension. Among several TomoSAR algorithms, the Compressive Sensing (CS) was selected thanks to its high resolution capacities, its low computational load, low complexity and its ability to compensate the delay induced by the propagation of the wave in a medium with a permittivity different than one. Using a stack of SAR images acquired from the BA, the CS was applied to recover the position of embedded target, first in the Earth observation geometry to validate the results, then in a small body

geometry to analyse the algorithm performance. The CS was found out to recover the position of the buried inclusion and improve the resolution in elevation for the small body geometry by a factor of 4, to about 50 cm. By further compensating the delay induced by the propagation of the signal in the medium, the CS was found out to have a better reconstruction of the target position. Thus, the CS can be applied to improve the resolution of HFR in the small body geometry and achieve its requirements of imaging a small body subsurface with a resolution smaller than one meter.

Finally, the deviation of performances from classical radars in UWB scattering was investigated in a preliminary analysis. Indeed, since UWB scattering challenges the hypothesis established from classical Earth observation, the performances of UWB SARs should deviate from the classical results. Two hypotheses of narrowband SAR scattering were selected, and their validity in a small body geometry were verified.
First, I studied the deviation of the UWB speckle statistics, which occurs when the SAR resolution cell is reduced and the fully developed speckle hypothesis cannot be fulfilled. By performing MCMC fits in both the Earth observation geometry and the small body geometry, I observed that speckle deviates from the expected Rayleigh behaviour when the resolution cell size decreases, to a statistics with a larger tail and a shifted maximum. This confirmed that UWB speckle does not respect the fully developed speckle hypothesis.
Then, I studied the hypothesis of bright scatterers, which is set for performing the SAR synthesis but is questioned in UWB scattering. I used time/frequency analysis to image the scatterers angular/frequency behaviour. As only the mean behaviour of the scatterers can be imaged when studying rough surfaces, while we intend to measure the mean of the behaviour of the scatterer, the deviation of the scatterers from the bright model in UWB SAR cannot be assessed with certainty.
Nevertheless, I studied the deviation of the resolution from its theoretical value in UWB scattering. By assuming that the 3dB width of the autocorrelation function is equal to the resolution, I pointed out that even if a deviation of both range and azimuth resolution can be measured when the radar RF and Doppler bands increased, the error in the resolution does not exceed 10%.

Even though the AIM mission will not be launched, a low frequency version of the radar will board the Hera mission and study the inner structure of the asteroid Didymos. Since the geometry of observation will be the same, my work on the study of the performances of HFR, as well as the results on the tomography could be used for Hera. Indeed, newer simulations adapted to the instrument could be performed using the different methods I developed, to simulate, analyse and process the radar's return when observing rough surfaces or embedded inclusions.

My Ph.D. thesis allowed to better understand the behaviour of HFR in a small body geometry, to develop tools to study the return of the instrument in a wide of different scenarios, and processing techniques to improve the instrument performances. However, further work would be needed in order to expand the range of possible scenarios and refine the results of my thesis.

First, even though the Kirchhoff approximation was chosen as our surface scattering model, its domain of validity is smaller than other scattering models' such as SSA-2 or WCA. A further study could consist in implementing the WCA, compare its result with the KA results, analyze the two methods differences occurring when performing simulations on surfaces whose roughness fall out of the domain of validity of the KA.

Further works could be performed on the BA, used to model the field scattered by an inclusion in the subsurface. Indeed, as all volume models, the BA suffers from a large computational load. This load limits the size of the simulated volume, and thus the number of inclusions since each inclusion must be separated by a distance larger than the radar's resolution cell to be identified. The large computation load of the BA also prevents us from analyzing the result of a scenario constituted of larger inclusions. Improving the computation time, by paralleling the code, and convert it so it can

be carried out by GPU computations would improve the BA computation time by a factor of 10 at least and overcome these issues. With smaller computation times, the iterative form of the Born approximation could be performed as well, assuming convergence of the results, which would overcome the hypothesis of weakly scattering targets, and apply the BA to a wider range of scenarios. Studying a scenario with wider scatterers, could as well provide results with a meaningful scattered power, as opposed to our current simulations which have scattered powers which are not representative, since they will be hidden by noise.

As the Compressive Sensing is performed from SAR images obtained from the BA, the CS weaknesses are linked to the ones of the BA. Overcoming the BA computation time would allow us to guarantee the validity of the CS by recovering the position of several inclusions, or investigate the CS results when observation inclusions that are larger than the resolution cell size. Another limitation of the current implementation of the CS since it was applied to the spectrum scattered by the inclusion only since the inclusion power is completely hidden by the power scattered by the surface. By performing simulations of larger scenes with the BA, which will be associated with higher backscattered power, the CS could be tested to recover the position of both the surface and the inclusion. Additional studies could be performed on the CS results once wider scenes are available to improve the results of the inversion, such as methods to retrieve the position of the target without knowledge of the medium permittivity and thus to retrieve an estimation of the medium permittivity, or autofocus methods to reduce the defocalization of the SAR image when the flown trajectory differs from the expected trajectory.

Finally, additional studies could also be performed on the study of UWB scattering. Even though the deviation of the scatterers has been studied from the Rayleigh behaviour, the behaviour of the UWB speckle has not been identified with a given probability density function. Further review of the state of the art of non-parametric pdf could help us find a pdf describing our speckle model. Moreover, the whiteness/isotropy study of the scatterers still require some work: the wavelet analysis study of the scatters in the small body geometry does not give satisfying results and the hyperimages of scatterers forming a rough surface gives an insight into the mean of the scatterers behaviour and not the mean behaviour of the scatterer, which makes us consider the meaning of the results. Further work would be necessary to fathom this issue.

Part VII

Appendices

Contents

Appendix A

Electromagnetic wave propagation in a medium

The following chapter describes the wave propagation in different media. We will denote by ρ and j the volume charge and current density. The propagating medium is characterized by its absolute magnetic permeability μ_a and by its absolute dielectric permittivity ϵ_a. The permeability describes the magnetic properties of the medium and the permittivity describes the electric properties of the medium.

A.1 Maxwell equations

A.1.1 Equations

The fundamental equations of the electromagnetic wave theory were written by J.C Maxwell in 1873. These equations remain widely used in several scientific disciplines and govern the behavior of an electromagnetic field in free space and media. The emitted radar signal is an electromagnetic wave considered monochromatic and planar. The behavior of this wave propagating in a medium is dictated by the Maxwell laws :

1. Faraday's induction law :
$$\nabla \times E(r,t) = -\frac{\partial B(r,t)}{\partial t} \tag{A.1}$$
2. Generalized Ampere's circuit law :
$$\nabla \times H(r,t) = J(r,t) + \frac{\partial D(r,t)}{\partial t} \tag{A.2}$$
3. Gauss law for the electric field :
$$\nabla \dot{D}(r,t) = \rho(r,t) \tag{A.3}$$
4. Gauss law for the magnetic field :
$$\nabla \dot{B}(r,t) = 0 \tag{A.4}$$

E, B, H, D, J, and ρ are functions of position and time: E being the electric field strength, in volts/m, B is the magnetic flux density, in webers/m^2, H is the magnetic field strength in amperes/m, D is the electric displacement in coulombs/m^2, J is the electric current density in amperes/m^2 and ρ is the electric charge density.

If we consider that the medium where the wave is propagating is isotropic, we can write:

$$D = \epsilon E \tag{A.5}$$

$$B = \mu H \tag{A.6}$$

Thus if the medium is isotropic, free of charge, and homogeneous, the Maxwell equations can be written:

$$\nabla \times E = -\mu \frac{\partial H}{\partial t} \tag{A.7}$$

$$\nabla \times H = \epsilon \frac{\partial E}{\partial t} \tag{A.8}$$

$$\nabla \dot{H} = 0 \tag{A.9}$$

$$\nabla \dot{E} = 0 \tag{A.10}$$

In free space, $\epsilon = \epsilon_0$ and $\mu = \mu_0$.
Using that :

$$\nabla \times (\nabla \times E) = \nabla(\nabla \cdot E) - \nabla^2 E \tag{A.11}$$

And taking the curl of A.7, substituting A.8 and A.10 we find that

$$\nabla^2 E - \mu\epsilon \frac{\partial^2 E}{\partial^2 t} = 0 \tag{A.12}$$

With the Laplacian operator ∇^2 being, in cartesian coordinates :

$$\nabla^2 = \frac{\partial^2}{\partial^2 x} + \frac{\partial^2}{\partial^2 y} + \frac{\partial^2}{\partial^2 y} \tag{A.13}$$

The simplest solution to this equation is

$$E(r,t) = E_0 \exp i(\omega t - k \cdot r) \tag{A.14}$$

Where $\omega = 2\pi f$ is the wave angular frequency, f the wave frequency, and $k = \frac{2\pi}{\lambda}$ the wave vector, which must satisfy $k^2 = \omega^2 \mu\epsilon$, r being the 3-dimensional position vector.

The magnetic field vector H is perpendicular to the electric field vector E and both are perpendicular the direction of propagation.

A.1.2 Boundary conditions

The Maxwell equations describe the behaviour of the wave but must be completed with boundary conditions to have unique solutions. We consider a wave propagating in the medium 1 and crossing a boundary to medium 2. If we assume that the boundary surface is not in motion, we can find:

$$\vec{n} \times (E_1 - E_2) = 0 \tag{A.15}$$

$$\vec{n} \times (H_1 - H_2) = J_s \tag{A.16}$$

$$\vec{n}\dot{(}B_1 - B_2) = 0 \tag{A.17}$$

$$\vec{n} \times (D_1 - D_2) = \rho_s \tag{A.18}$$

The boundary conditions state that the tangential components of E and the normal components of B are continuous across the boundary. The discontinuity of the tangential components of H is equal to the surface current density J_s and the discontinuity of the normal components of D is equal to the surface charge density ρ_s.

A.1.3 Time Harmonic fields

Electromagnetic waves of a particular frequency in a steady state form time-harmonic fields, and can be called monochromatic waves, or continuous waves (CW). The whole spectrum of electromagnetic waves can be described by CW, and their usage simplifies the Maxwell equation. For a time harmonic field, with an angular frequency ω, we note:

$$E(r,t) = \Re(E(r)e^{i\omega t}) \tag{A.19}$$

With $\Re$ being the real part of the complex quantity, and $e^{i\omega t}$ represents the time dependence. With this notation, E(r) is independent on time.
A source free, homogeneous isotropic medium is characterized by a scalar permittivity ϵ and a scalar permeability μ. With this notation we find that the Maxwell equations can be written :

$$\nabla \times E = i\omega\mu H \tag{A.20}$$

$$\nabla \times H = -i\omega\epsilon E \tag{A.21}$$

$$\nabla \dot{B} = 0 \tag{A.22}$$

$$\nabla \dot{D} = 0 \tag{A.23}$$

The boundary conditions are identical to those given in A.1.2.

The Maxwell equations dictate the behaviour of the waves in the void and different media. This behaviour is largely dependent on several medium parameters, such as the medium permittivity of the medium conductivity. The permittivity of a medium also drives one major parameter in radar measurements, which is the distance of media the wave will be penetrating before its amplitude level is comparable to the noise level.

A.2 Penetration in a lossy medium

For lossy media, which are all natural media, the permittivity ϵ is complex: $\epsilon = \epsilon_R + i\epsilon_I$. The wavenumber k=$\omega\sqrt{\mu\epsilon}$ is also complex : $k = k_R + k_I$. In a distance of $\frac{1}{k_I}$ along the direction of propagation, the wave amplitude will be attenuated by a factor of e^{-1}.
We note

$$d_p = \frac{1}{k_I} \tag{A.24}$$

the penetration depth.
If we consider a medium with a permittivity $\epsilon = \epsilon^{'} + i\epsilon^{''}$ then we can write:

$$p_d = \frac{1}{2\alpha} \tag{A.25}$$

With:

$$\alpha = \frac{2\pi}{\lambda}\Im[\epsilon^{''}] \tag{A.26}$$

Thus the higher λ and the lower frequency, the larger p_d and the deeper the wave will penetrate.

The propagation of electromagnetic waves in different media with a variety of permittivities are well known and drive the radar signal behavior. Thus, simulators can be implemented in order to model the signal scattered by a target. From this signal, the radar performances can then be computed.

SPRATS: a versatile Simulation and Processing RAdar ToolS for planetary missions

Oriane Gassot
Univ. Grenoble Alpes, CNRS, IPAG
38000 Grenoble, France
oriane.gassot@univ-grenoble-alpes.fr

Alain Hérique
Univ. Grenoble Alpes, CNRS, IPAG
38000 Grenoble, France
alain.herique@univ-grenoble-alpes.fr

Yves Rogez
Univ. Grenoble Alpes, CNRS, IPAG
38000 Grenoble,
yves.rogez@univ-grenoble-alpes.fr

Wlodek Kofman
Univ. Grenoble Alpes, CNRS, IPAG
38000 Grenoble, France
wlodek.kofman@univ-grenoble-alpes.fr

Sonia Zine
Univ. Grenoble Alpes, CNRS, IPAG
38000 Grenoble, France
sonia.zine@univ-grenoble-alpes.fr

Petit-prince Ludimbulu
Univ. Grenoble Alpes, CNRS, IPAG
38000 Grenoble, France
petitprince.ludimbulu@univ-grenoble-alpes.fr

***Abstract*—Our knowledge of the internal structure of asteroids is currently indirect and relies entirely on inferences from remote sensing observations of the surfaces. Radar observation of asteroids is the most mature technique available in order to characterize their structure, which is fundamental for understanding the small bodies' history and for planetary defense missions. However, as the small bodies' geometry is complex, simulation of the radar design and the signal is required in order to assess the instrument performance and thus the mission science return. SPRATS is a software package designed for mission and operation analysis for planetary bodies. It provides the tools to evaluate the radar concepts and mission scenarios, evaluate the processing performances, validate data processing techniques on the final data, and process real radar data when facing complex geometries different from the Earth observation geometry. The paper presents the architecture of the SPRATS toolbox along with relevant examples to illustrate its interest.**

Keywords— Radar, processing, simulation, asteroids, comets, planets, software, SPRATS, versatile

I. INTRODUCTION

Spaceborne surface penetrating radars studying planetary bodies have been embarked on past planetary missions, such as MARSIS (Mars Express-ESA) [1] or SHARAD (MRO-NASA) [2] radars that studied the Martian subsurface or CONSERT (Rosetta-ESA) [3] that studied the comet Churyumov-Gerasimenko. We can quote also upcoming radars, such as RIME (JUICE, ESA) [4] and REASON [5] (EUROPA-CLIPPER, NASA) that will study the icy shells of Galilean satellites or LFR onboard Juventas [6] (HERA, ESA) that is understudy to peer into the subsurface of the Didymos asteroid.

Even though the radars and signals design, as well as the radars performances, are acknowledged in the Earth observation geometry, the acquisition of observations on different planetary bodies requires more complex scenarios and geometries. Thus, end-to-end simulations of the measurement and processing are required in order to assess the final performances of the designed radar.

Simulation and Processing RAdar ToolS (SPRATS) is a versatile software toolbox designed for mission and operation analysis for planetary radars. It allows the definition of relevant radar parameters, the setting of realistic scenarios, simulation of the signal backscattered by point targets or extended surface, and the computation of the resulting SAR synthesis, which leads to the assessment of the radar's performances. SPRATS is also used for the preparation of space operations [7][8], the processing of real data, and the solving of the inverse problem. We present here in the first part our motivation to develop the SPRATS toolbox, and then we describe the SPRATS' architecture.

II. MOTIVATION: SIMULATION OF THE RADAR OBSERVATION OF ASTEROIDS

Asteroids are fundamental to our understanding of the formation and history of our Solar System. Their diverse population ranges from primitive building blocks, whose materials have experienced the least modification since their formation from the early solar nebula, to metallic asteroids, widely interpreted as fragments of collisionally disrupted differentiated planetesimals. The asteroid population tells us the story of planetary accretion in the early Solar System and its evolution [9] [10] [11].

However so far, the inner structure of an asteroid has never been directly measured, and our knowledge relies on inferences from surface measurements. There is some evidence that a rubble pile structure, an aggregate structure covered by regolith, is common for kilometric size bodies, but there are no direct observations [12]. If so, the size distribution of their constitutive blocks is unknown and could be fine-dust, sand, pebbles, larger blocks, or even a mixture of all of these. Direct measurements are needed to answer these questions. Furthermore, the modeling of the regolith structure and its mechanical reaction is crucial for any interaction of a spacecraft with a NEO, particularly for a mission with the objective to deflect a NEO from its trajectory. A radar operating remotely from a spacecraft is the most mature instrument capable of characterizing the internal structure and heterogeneity of small bodies from sub-meter to global scale [13]. As part of the payload of the HERA mission [14], the radar LFR will be proposed to the ESA Member States during the Ministerial Council meeting in 2019. DART (Double Asteroid Redirection Test) [15], a kinetic impactor was designed by the NASA to impact on the

978-1-7281-8942-0/20/$31.00

moon of the binary system, (65803) Didymos, while HERA, was designed in order to observe the consequence of the DART impact on the target structure and dynamic state of the moon of the Didymos system.
For future missions, an ever-increasing maturity is required for both hardware and data processing, from the proposal phase onwards. The instrument team has to demonstrate instrument end-to-end performances and compliance with science requirements, while the mission team has to propose optimized operation scenarios, realistic orbitography, and consolidated data budgets. It is especially crucial for radar, for which processing is particularly complex, and final performances are definitively dependent on the observation sequence's geometry.

III. SPRATS TOOLBOX

SPRATS is a software package that provides radar instrument designers with tools to evaluate the chosen radar concepts and mission scenarios, prepare the payload operations, evaluate and validate the processing performances, and perform data processing for the final science products.
For a given operational scenario, with a spacecraft trajectory, and with given radar instrument parameters, SPRATS computes the simulated response signal from the observed body and the resulting products of a SAR imaging. The input data and hypotheses are quite versatile to cover a various range of situations: instrument settings and system models, target body surface and sub-surface physical models, and mission scenario. SPRATS is thus an essential step in the study and verification of radar design in asteroids geometry. Indeed, the point target response is different from the point target response in the Earth geometry, and simulations are required for simple case studies and physical modeling [16], as well as for operational mission planning. In small body observation, the resolutions and sidelobe power cannot be foreseen and needs to be fully computed by SPRATS for every radar design in every geometry.

The SPRATS software package makes use of a flexible architecture in order to be easily useable by radar designers. This also confers a good evolutivity for the various situations encountered in space radar planetary science missions.

SPRATS is composed of several modules dedicated to each of the main steps for an end-to-end radar experiment simulation: radar instrument settings, orbitography, and mission scenario definition, target model and simulation, imaging and processing, and performance analysis tools. SPRATS' organization chart is presented in Fig. 1.
All data outputs from each of these modules are enriched with meta-data, which allows traceability and reproducibility of the results, and can facilitate interoperability with other ground segment equipment applications, thanks to HDF5 format.

A. Instrument module

The instrument module allows the definition of the parameters of the designed radar. This part includes the definition of the radar's number of frequency, bandwidth, PRF as well as the antenna type. A system model module is also under development to simulate the response of the overall electronics chain. Different radar concepts can be defined as a pulsed radar or a step frequency radar, for which complex radar waveform can be defined.

B. Mission scenario module

The mission scenario module provides tools to create and manipulate different study-case, realistic, or even real flown trajectories and mission scenarios (Fig. 2). All the orbitographic computations make use of the NASA/NAIF SPICE library, which offers the observation geometry information and tools about bodies and spacecraft in the solar system.

C. Target modeling module

The target-modeling module considers the modeling of the observed body in the case of data simulation. Two different sets of targets geometry can be defined:

- Point targets that are defined with their position.

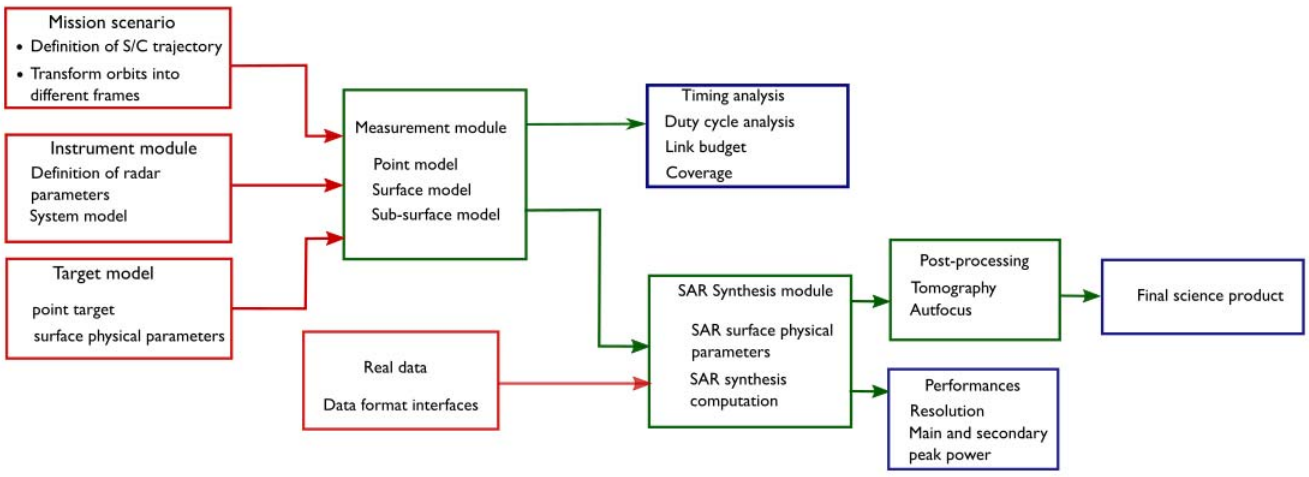

Fig. 1. SPRATS' architecture chart. Red indicates the input modules; green indicates the computation modules and blue indicates the outputs modules.

- Extended surfaces that can be either be DTM, downloaded from existing terrain models such as DTM from Mars or the Moon [17], shape models for comet nucleus or asteroids or modelled as a random rough surface. SPRATS provides different tools in order to simulate random rough surfaces, with the size, roughness and permittivity wished.

This module then provides tools to associate physical models to these geometrical definitions, such as dielectric permittivity values.

D. Simulation module

The simulation module is dedicated to the computation of the radar signal and relevant geometric parameters for the analysis of the radar performances.

1) Timing analysis

To get a first and quick approximation of the propagation path and the link budget, and analyze the characteristics of the trajectory with respect to different targets, different geometric parameters (such as the distances, the incidence angles or occultations) are computed between the trajectory positions and the defined targets. Then, starting from the orbitography definition, chronograms, instrument relative timing values such as arrival times, duty cycle ratios or transmission and reception windows durations margins can be retrieved and processed through visualization, which permits the validation of the radar design and operation scenarios, such as presented in Fig. 3.

2) Signal simulation

The simulation module also covers the function of computing the full signal received from the target defined in the target module. It can be evaluated in two different ways: considering a simple point target model or using the facet method and the Kirchhoff approximation [18], as well as other ad-hoc models.

a) Point target model

This simple model is mostly used for quick approximation for validation of the radar's performances in large parametric studies. It makes use only of geometric information from the mission scenario module, with very simple and approximate modeling of the wave propagation: amplitude and phase only are estimated from geometric parameters.

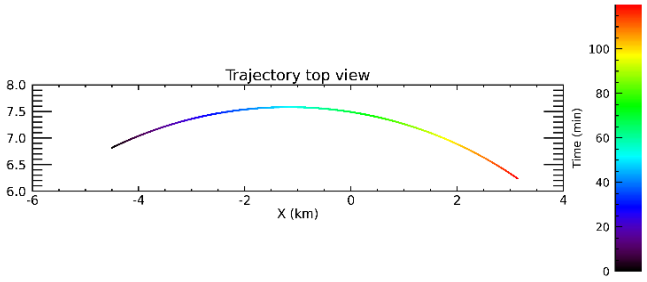

Fig. 2. Illustration of the top view of a trajectory obtained with SPRATS. The trajectory is depicted as a point in an inertial frame and is obtained by a change of frame in the fixed frame of the moon of the Didymos asteroid system.

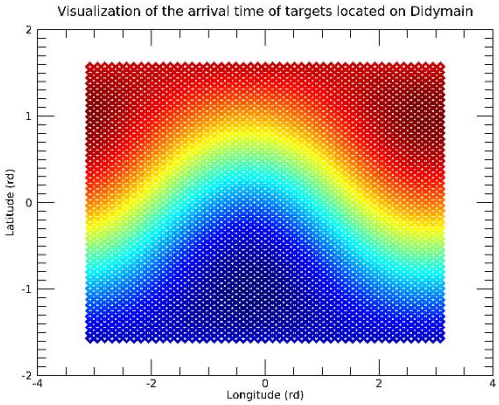

Fig. 3. Example of a plot of the mean arrival time of targets located on the Didymos asteroid, with the trajectory presented in Fig. 2 on a latitude-longitude map. Red pictures the parts of the asteroids whose mean arrival times are registered the earliest and blue pictures the parts of the asteroids where the mean arrival times are registered the latest.

a) Surface and sub-surface backscatter simulation

The backscattered spectrum from extended surfaces is computed based on the facet method with the Kirchhoff approximation [18]. It was initially developed to identify echoes coming from the Martian subsurface, by comparing SHARAD or MARSIS radargrams to physical optics simulations [19]. This simulation module is implemented so it can be run on HPC, in order to simulate large problems.
Other models are in development such as the Born approximation for sub-surface targets response simulation, and GPU based implementations are currently under work.
The spectrum radargrams can then be plotted in order to provide a first validation of the results and to analyze the resulting data, as presented in Fig. 4.

b) Ray-tracing based simulation

Other kinds of simulations are available, at a lower integrated level, as done for CONSERT instrument on Rosetta mission [8]

E. SAR Synthesis module

The SAR module allows the computation of the SAR synthesis from the output results of these simulations.
First, a SAR zone is built from a small set of geometric parameters. The SAR zone is a set of 3D points on which the SAR processing is applied, for target imaging. It can be represented as a 2D surface or a 3D volume, depending on the characteristics wished to be analyzed.
Starting from the trajectory, simulated or real measurements, and SAR zone information, the SAR processing is performed. The SAR processor is a "brute-force" SAR processor since it corrects range and Doppler together, as an inverse Fourier transform of the spectrum. Thus, we do not apply any of the classical approximation usually carried out for computing time optimization, such as what is done for Earth orbiting SAR.
To achieve reasonable processing time, the SAR synthesis is implemented on both HPC GPU and CPU nodes. An example of a 2D SAR synthesis is pictured in Fig. 5, where the range

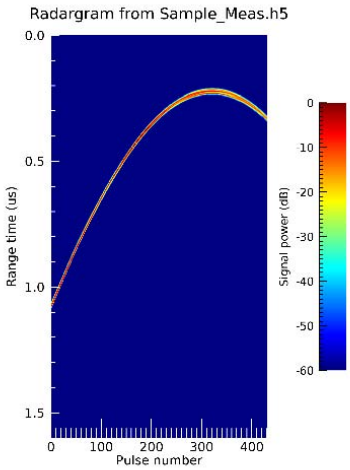

Fig. 4 Example of a radargram of a random rough surface on the Didymain asteroid, whose spectrum was computed with SPRATS.

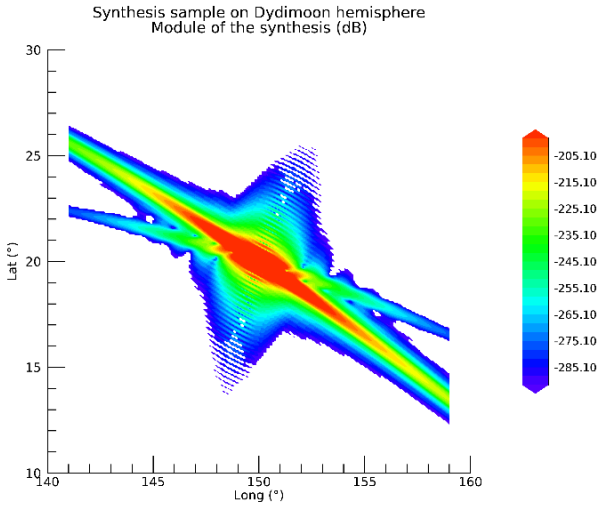

Fig. 5: Example of a SAR Synthesis of a target located at [20°, 150°] on the Didymoon asteroid, represented with an 80 dB dynamic.

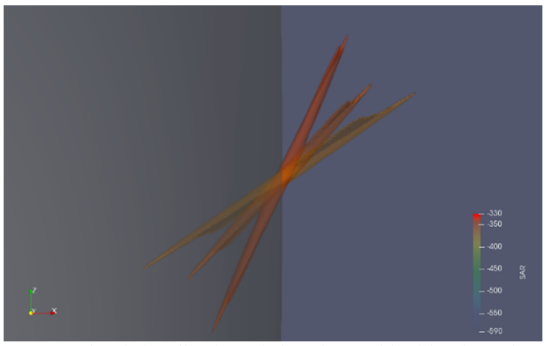

Fig. 6: Example of visualization of elevation ambiguities from three 3D SAR Synthesis of a point target with a dynamic of 60 dB, obtained with SPRATS in a multipass geometry.

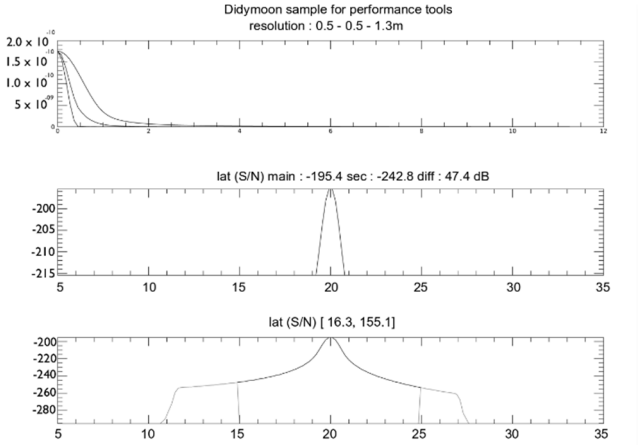

Fig. 7: Example of a SPRATS performance evaluation from the SAR synthesis presented in Fig. 5. The first graph plots the synthesis power level in the direction where the resolution is minimum, medium, and maximum, and prints the corresponding resolution. The second graph pictures the main lobe with a dynamic of 20 dB and the third graph pictures the main lobe with a dynamic of 100 dB

and doppler resolution can be computed, as well as the sidelobes power. An example of 3D SAR syntheses is pictured in Fig. 6 where the elevation resolution can be computed, as well as the elevation ambiguity pattern and direction. Output results are made compliant to the Kitware's ParaView tool.

From the SAR synthesis results of a point target, SPRATS then evaluates the radar performances by computing the size of the resolution cells in different directions, and the levels and positions of the peak sidelobes ratios, as presented in Fig. 7. Knowledge of the resolution and the sidelobes levels is fundamental to assess the mission science return and finally the validity of the flown scenario and the radar design.

F. Imaging and post-processing module

After processing the SAR synthesis, other data processing techniques can be applied to the SAR-processed data. Several methods are currently under study prior to implementation into SPRATS such as autofocus algorithms [20], or tomography algorithms implemented with the compressive sensing method [21]. These resulting data will constitute high-level science products for the radar payloads.

CONCLUSION

SPRATS is a radar software package designed for validation of instrument design and validation of radar signals within the context of mission analyses and operations in complex geometries, as well as the processing of flown radar data. SPRATS allows the definition of a radar design and orbitography, computes the spectrum backscattered by a given set of targets, and computes the resulting SAR synthesis from the spectrum. Then, it allows the processing of high-level products. The interoperable and meta-data enriched outputs, at all stages of the processing, allows them to integrate into various processing and archiving workflows. Thus, SPRATS permits the evaluation of the radar's design performances in specific scenarios and can also be used for inversion of the signal in the case of flown missions. SPRATS has already been used in a variety of studies for

different missions' phase AB, as well as in the processing of several data coming from flown missions, since it was developed for automation of MARSIS and SHARAD processing.

SPRATS is under ongoing development, with the addition of a subsurface backscattering model and super-resolving tomography algorithms, which would allow assessing the improvement capabilities of tomography with a given radar design in a given scenario, compliant with Solar System small body observation and will be used to analyze RIME and REASON data.

ACKNOWLEDGMENTS

SPRATS inherits from tools developed for CONSERT/Rosetta operations supported by CNES and from tools developed for AIM Phase A supported by the ESA's General Studies Program. RIME/Juice adaptation are developed under CNES funding. Part the computations presented in this paper were performed using the CIMENT infrastructure, which is supported by the Rhône-Alpes region and France-Grille.

REFERENCES

[1] Picardi G et al, "MARSIS: Mars Advanced Radar for Subsurface and Ionosphere Sounding" n.d.:19.

[2] Seu R et al, "SHARAD sounding radar on the Mars Reconnaissance Orbiter". Journal of Geophysical Research 2007;112.

[3] Kofman W et al, "The Comet Nucleus Sounding Experiment by Radiowave Transmission (CONSERT): A Short Description of the Instrument and of the Commissioning Stages." Space Sci Rev 2007;128:413–32.

[4] Bruzzone L et al, "RIME: Radar for Icy Moon Exploration". 2013 IEEE International Geoscience and Remote Sensing Symposium - IGARSS, Melbourne, Australia: IEEE; 2013, p. 3907–10.

[5] Blankenship D et al, "REASON for Europa. 42nd COSPAR Scientific Assembly" 2018;42:B5.3-55-18.

[6] Herique A et al, "Low Frequency Radar to Fathom Asteroids from Juventas Cubesat on HERA", EPSC Abstracts Vol. 13, EPSC-DPS2019-807-2, 2019

[7] Rogez Y et al, "The CONSERT operations planning process for the Rosetta mission." Acta Astronautica 2016;125:212–33.

[8] Kofman W et al, "Properties of the 67P/Churyumov-Gerasimenko interior revealed by CONSERT radar." Science 2015;349

[9] Chambers JE and Wetherill GW, "Making the Terrestrial Planets: N-Body Integrations of Planetary Embryos in Three Dimensions." Icarus 1998;136:304–27.

[10] Morbidelli A et al, "Source regions and timescales for the delivery of water to the Earth." Meteoritics & Planetary Science 2000;35:1309–20. h

[11] Blum J and Wurm G, "The Growth Mechanisms of Macroscopic Bodies in Protoplanetary Disks." Annu Rev Astron Astrophys 2008;46:21–56.

[12] Herique A et al, "Direct observations of asteroid interior and regolith structure: Science measurement requirements." Advances in Space Research 2018;62:2141–62.

[13] Herique A et al, "A radar package for asteroid subsurface investigations: Implications of implementing and integration into the MASCOT nanoscale landing platform from science requirements to baseline design." Acta Astronautica 2019;156:317–29.

[14] Michel P, Küppers and M, Carnelli I. "The Hera mission: European component of the ESA-NASA AIDA mission to a binary asteroid." 42nd COSPAR Scientific Assembly 2018;42:B1.1-42-18.

[15] Cheng AF et al, "Asteroid Impact and Deflection Assessment mission." Acta Astronautica 2015;115:262–9.

[16] Gassot O, Herique A ,Rogez Y and Buck. C, "Study into Ultra-Wide-Band SAR Tomography over Dry, Rocky Terrains" ESA RFP/3-14740/16/NL/FE ESA Contract No. 4000119134/16/NL/FE n.d.:65.

[17] Berquin Y, "Assessing the performances and optimizing the radar sounder design parameters for the EJSM mission (Ganymede and Europa)" Université Grenoble Alpes, 2014.

[18] Berquin Y, Herique A, Kofman W and Heggy E. "Computing low-frequency radar surface echoes for planetary radar using Huygens-Fresnel's principle: COMPUTING RADAR SURFACE ECHOES." Radio Science 2015;50:1097–109.

[19] Nouvel J-F, Herique A, Kofman W and Safaeinili, "A. Radar signal simulation: Surface modeling with the Facet Method: RADAR SIGNAL SIMULATION". Radio Science 2004;39

[20] Xi L, Guosui L and Jinlin L, "Autofocusing of ISAR Images Based on Entropy Minimization." 1999 n.d.

[21] Zhu XX and Bamler R, "Tomographic SAR Inversion by L1-Norm Regularization—The Compressive Sensing Approach." IEEE Transactions on Geoscience and Remote Sensing 2010;48:3839–46.

Appendix B

State of the art of SAR Tomography methods

B.1 Methods inherited from 2D SAR Imaging

The first experiments on tomography were inspired by classic 2D SAR imaging algorithms: they reproduced the steps of the 2D algorithms from the azimuth direction to the elevation direction. All of these models can be divided into two classes, frequency and time domain methods:

- The methods operating in the frequency domain use the Fourier transform to focus the signal along the elevation direction, despite a sampling in the elevation direction much lower than in the azimuth direction. However, these methods suffer greatly from unevenly distributed tracks and the potential weak number of passes along the elevation direction. Therefore, a step of resampling the received signals into a regular grid is performed if possible, which increases the computational load.

- The time-domain methods directly project each radar echo to all imaged ground pixels. These methods rely on the recovery of the geometric relationship between the radar and the scatterers.

One major difference between these two methods is the computational cost. The frequency-domain methods use the fast Fourier transform (FFT), whose numerical complexity is $N \cdot \log_{10}(N)$, whereas the time domain methods need to process the received signal in a 3D space, therefore the algorithm complexity goes to O(N^3), where N is the dimension of the image. Because of this complexity difference, the frequency domain methods are often privileged.

B.1.1 Frequency domain methods : the SPECAN

Description

SAR Tomography imaging algorithms construct an elevation aperture by having several observations separated in the elevation direction, and then focus the received signals backscattered from the same target. The SPECAN method (Reigber & Moreira, 2000) is an example of how to realize the signal focusing along the elevation direction with a Fourier transform. The SPECAN method includes two steps: first the deramping of the signal, which is a procedure carried out to make the signal's spatial frequency dependent on the position in elevation of the scatterer only, followed by an FFT.
A version of the algorithm in an ideal imaging geometry with sufficient and evenly distributed passes is presented. However, the actual observation number is never sufficient, and the flight distribution of the tracks is always irregular. Therefore, an additional interpolation procedure of the received signals has to be added to the original SPECAN method.
The SPECAN algorithm has two basic assumptions, retrieved in standard Earth observation. The first is that the received signal has a quadratic phase modulation, and the second is that the range migration is very small.

We will describe the SPECAN algorithm with evenly spaced tracks, and we consider the elevation direction $\vec{s}$ to have the same direction as $\vec{z}$, as presented in figure B.1. H corresponds to the total height of the volume to be imaged, d corresponds to the tracks separation in the elevation direction. The path length between the sensor at position z and a scattering element at height s_0 at a minimum range distance of r_0 can thus be expressed as:

$$r(z, s_0) = 2\sqrt{(r_0^2 + (z - s_0)^2} \approx 2r_0 + \frac{(z - s_0)^2}{r_0} \tag{B.1}$$

And the received signal s_r can be modeled as :

$$s_r(z, s_0) = \gamma(r_0, s_0) * \exp(-\frac{ik}{r_0} \cdot (z - s_0)^2) \tag{B.2}$$

Where $\gamma(r_0, s_0)$ denotes the complex reflectivity in the distance r_0, at elevation s_0 and k is the wavenumber : $\frac{2\pi}{\lambda}$. Thus the received signal consists of the complex reflectivity $\gamma(r_0, s_0)$ convolved

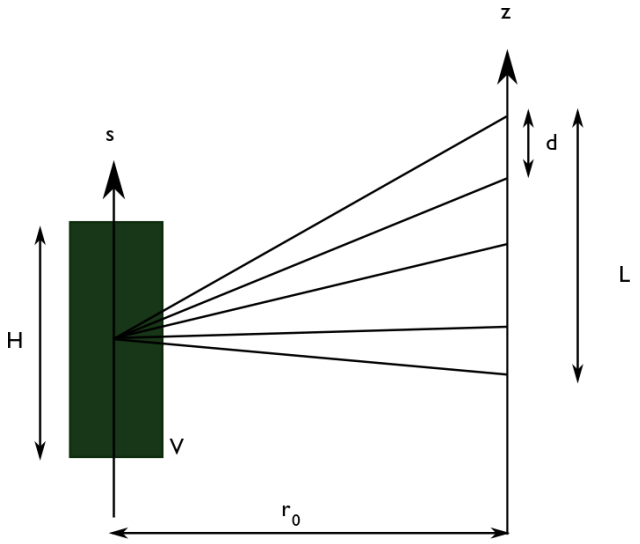

Figure B.1: Simplified tomographic imaging geometry z =s. Adapted from Reigber and Moreira (2000).

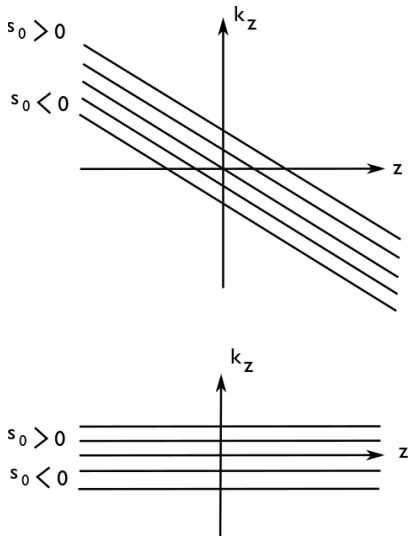

Figure B.2: Frequency dependency for tomographic signal in the k_z plane for different scatterers elevation positions before (up) and after deramping (bottom). Adapted from Adapted from Reigber and Moreira (2000).

with a quadratic phase function. This function has a zero frequency offset if $s_0 = 0$, and a positive frequency offset if the elevation of the target is positive.

The first step of the SPECAN algorithm is to compensate this phase variation by multiplying the received signal by the complex conjugate of the quadratic phase function. This operation is called the deramping and is depicted in figure B.2. It relies on the multiplication of the received signal with a deramping function u(z) :

$$u(z) = \exp \frac{ik}{r_0} \cdot z^2 \tag{B.3}$$

Thus, the demodulated signal s_d can be written :

$$s_d(z, s_0) = \gamma(r_0, s_0) * \exp(-\frac{ik}{r_0}(s_0^2 - 2 \cdot z \cdot s_0)) \tag{B.4}$$

After the operation, the spatial frequency k_z of the deramped signal s_d is no longer dependent on the position of the sensor z, but only on the elevation s_0 of scattering element

$$k_z(s_0) = \frac{\delta \arg(s_d)}{\delta z} = \frac{2ks_0}{r_0} \tag{B.5}$$

Once the deramping is performed, the SPECAN algorithm focuses the signal in the elevation direction with a fast Fourier transform (FFT). Indeed, as the k_z-domain is now equivalent to the spatial s-domain, the image result $v(s, s_0)$ is found by performing the Fourier transform of the deramped signal in the z and s -directions $S_d(k_z, s_0)$:

$$v(s, s_0) = S_d(k_z, s_0) = \gamma(r_0, s_0) \exp(\frac{ik}{r_0} s_0^2) \int_{-L/2}^{L_2} \exp(\frac{2ik}{r_0}(s_0 - s)z) dz \tag{B.6}$$

$$= \gamma(r_0, s_0) \cdot L \cdot \exp(\frac{ik}{r_0} s_0^2) \operatorname{sinc}(\frac{kL}{r_0}(s_0 - s)) \tag{B.7}$$

The final image should be independent of the position of the target. However, after the process, a phase term proportional to s_0^2 wrongs the image phase. This term should be deleted by multiplying an inverse phase term after the final image has been generated.
The SPECAN algorithm was initially developed for imaging natural surfaces such as forests and thus, it is not easily applied in a geometry with a change of permittivity. Since the areas with distinct permittivities can not be separated in the SPECAN, either the delay induced by the propagation of the wave in the medium should be taken into account in the SAR processor, or a priori knowledge of the distance by each waves in the air or in the medium should be obtained to improve the localisation of the target.

Results

To check the applicability of the SPECAN, the model was tested by Reigber and Moreira (2000) on a simulated data set :
In figure B.3 a) the simulated scatterers distribution in the azimuth/height plane is shown. 3 different scenarios are presented : they consists of a 40m volume, with three different layers with a random scatterer distribution on the left, two separated scatterers in different heights in the middle, and a single scatterer the right.
In figure B.3 b), we see the direct tomographic processing of the described scattering distribution by a sufficient amount of equally distributed tracks. The resolution is about 3m in the height direction
In figure B.3 c), the processing using a smaller amount of non-uniform and undersampled tracks shows a high ambiguity level, leading to poor image contrast and several ambiguities that are due to the signal aliasing.
In figure B.3 d), an ambiguity suppression method was applied to the results presented in figure B.3 c). The single line of scatterers is perfectly reconstructed and the sidelobes were suppressed to 15dB. We observe a clear improvement in the quality of the reconstruction for the distributed targets. However, the ambiguity remains strong on the volume distribution.

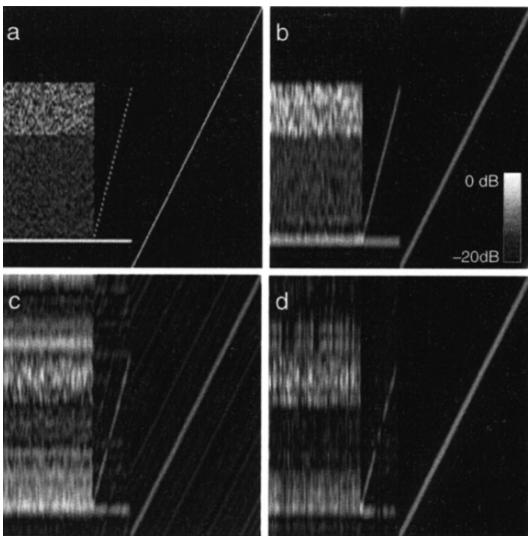

Figure B.3: SPECAN Tomographic processing of different simulated data (Reigber & Moreira, 2000).

B.1.2 Time domain methods: the TDBP

In order to overcome the limits of the frequency domain methods, which are mainly the effects resulted from the irregularly spaced tracks without any additional interpolation step, a projection method computed in the time domain was proposed by Nannini and Scheiber (2006). The time domain back projection method (TDBP), focuses every element in the volume with a reference function, which results in a target detection without any defocusing errors that would happen with irregularly spaced tracks. However, because of its large computational load it is seldom used. Additional steps were added to the TDBP to increase its efficiency. Notably, the fast-factorized back projection (FFBP) method, which was proposed by Ulander, improves the computational burden of the TDBP by subdividing the back-projection integral recursively. For a SAR image with about 10^6 pixels the FFBP is sped up as compared with TDBP by one to two orders of magnitude.

Description

With the TDBP, the data are entirely processed in the time domain. The focusing is achieved by using the geometry between the sensor and the imaged volume: every resolution cell of the 3D SAR image is focused based on the true acquisition geometry and a chosen reference function.
The TDBP starts with a stack of SAR images, already focused on the range doppler plan. For each track, the back-projected signal s_n corresponds to the n-th flight track:

$$s_n(\vec{r_i}) = \sum_{j=a_n(\vec{r_i})}^{b_n(\vec{r_i})} g_n(R_{n_{ij}}, r\vec{S}_{jn}) \cdot R_{n_{ij}} \cdot \exp(i2k_c R_{n_{ij}}) \tag{B.8}$$

With :

- $\vec{r_i}$ the position of the target
- a_n, b_n : the indexes of the first and last azimuth position of the sensor
- $r\vec{S}_{jn}$; the position vector of the sensor
- $R_{n_{ij}} = |\vec{r_i} - r\vec{S}_{jn}|$: the range distance
- $g_n(R_{n_{ij}}, r\vec{S}_{jn})$: the range compressed signal of the k-th flight track
- k_c : the center wavenumber

The back-projected signal v is then summed of all signals for all tracks and maps the volume at the position $\vec{r_i}$ and can be written:

$$v(\vec{r_i}) = \sum_{n=1}^{N} \sum_{j=a_n\vec{r_i})}^{b_n(\vec{r_i})} g_n(r_i, r_{\vec{S}_{jn}}) \cdot R_{n_{ij}} \cdot \exp(i2k_c R_{n_{ij}}) \tag{B.9}$$

With this procedure, it is possible to work directly in the real situation, with the irregularly, under sampled tracks without any resampling operation.
Since the TDBP relies simply on the knowledge of the range distance R between the spacecraft and the scatterers, it is not easily applied in a geometry with a change of permittivity. Since the areas with distinct permittivities can not be separated in the TDBP, either the delay induced by the propagation of the wave in the medium should be taken into account in the SAR processor, or a priori knowledge of the distance by each wave in the air and the medium should be obtained to improve the localization of the target.

Results

Frey et al. (2008) tested the feasibility of TDBP to observe different simulated and real point targets with a P-band SAR. The geometry of the flight tracks is pictured in figure B.4. In addition to the 11 actual flown flight tracks, their projections to the horizontal plane are pictured. An additional control track was flown with the same flight geometry as the first track. Each trajectory is separated by 56.7m, which creates a synthetic aperture of 567 m in the elevation direction. The mean range distance is about 3900m and the carrier frequency is 350MHz. This geometry provides an elevation resolution of 3m, and an unambiguous height is 30m in the elevation direction.
The results of this experiment are pictured in figure B.5. The black line represents the results of a single simulated point target, the bold blue line represents the response of a real corner reflector, and the red line indicates the echoes from two targets separated by a distance of 12m. In all cases, the points are focused with the theoretical resolution in elevation of 3 meters, at their true positions. The TDBP was thus found out to retrieve correctly the different targets positions, even though the elevation sidelobes remain high in the elevation direction for the detection of the two targets.

As both frequency-domain methods (because of their interpolation procedure) and time-domain methods have a large computational load, further work has been performed to research tomography methods that differ from the classical 2-dimensional SAR models. The Polarimetric coherence tomography, which was inspired by the improvement obtained with interferometric and polarimetric methods to 2D SAR, was implemented in order to develop a tomography with a lighter computational load.

B.2 The Polarimetric Coherence tomography

Since the number and the distribution of flight tracks have significant effects on the precise and unambiguous 3D reconstruction of a scatterer, several works have been carried out to search for a tomography method that would require a few baselines, which then reduces the risk of unevenly distributed tracks. The polarimetric interferometric SAR (POLInSAR) method was originally designed to differentiate between scattering mechanisms in forests and to derive their properties (height and biomass). With this information, it is then possible to analyze the change in the interferometric phase, along with the polarization information to extract physical parameters. Cloude (2006) first validated the method and derived the vertical scattering distribution of a forest area. In Cloude (2007) and Cloude and Papathanassiou (2008), Cloude then used a dual-baseline structure to observe a maize sample in an anechoic chamber, compared the resulting tomograms obtained with different polarization combinations and frequencies, and identified differentiated the scattering mechanisms.

Compared with the previous algorithms, the PCT (Cloude, 2006) can perform tomography imaging with a few tracks, and the polarimetric information can give a better understanding of the target's structure.

The SPECAN algorithm was initially developed for imaging natural surfaces in the air and since it relies simply on the knowledge of the range distance R between the spacecraft and the scatterers, it is not easily applied in a geometry with a change of permittivity. Either the delay induced by the propagation of the wave in the medium should be taken into account in the SAR processor, or a priori knowledge of the distance by each wave in the air or the medium should be obtained to improve the localization of the target.

B.2.1 Description

The basic geometry of radar interferometry is presented in figure B.6. The distributed scatterers on the ground at point P bring a loss of phase coherence in the interferogram, because of the phase difference between signals at either end of the baseline. The complex interferometric coherence $\hat{c}$ for two complex signals s_1 and, s_2 can be written:

$$\hat{c} = \frac{< s_1 s_1^* >}{\sqrt{< s_1 s_1^* >< s_2 s_2^* >}} \tag{B.10}$$

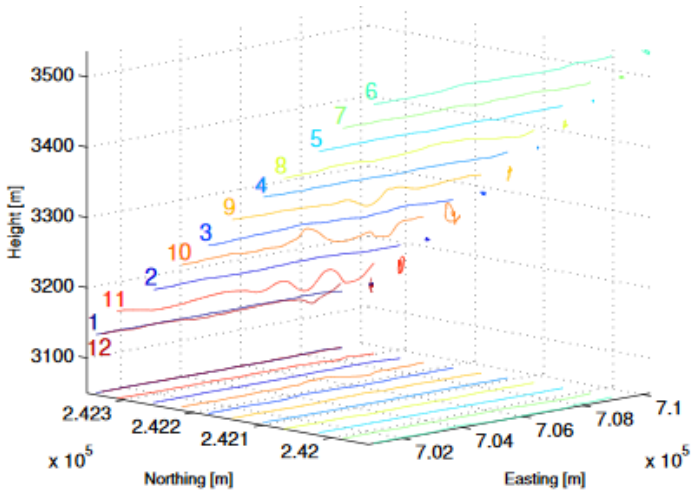

Figure B.4: TDPB P-band tomographic acquisition pattern (Frey et al., 2008).

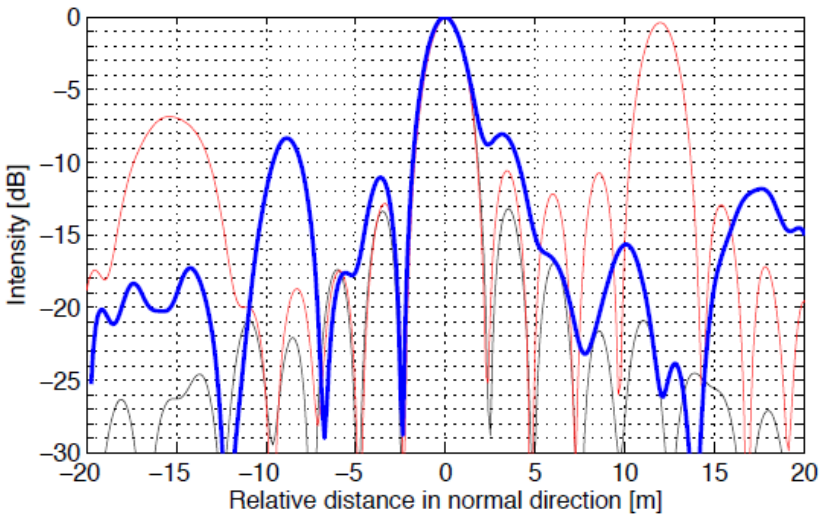

Figure B.5: Impulse responses resulting from TDBP tomographic imaging of the multibaseline P-band raw data set of: a single simulated point target (black line), two simulated point targets which are separated by a distance of 12 m in the normal direction (red line) (Frey et al., 2008).

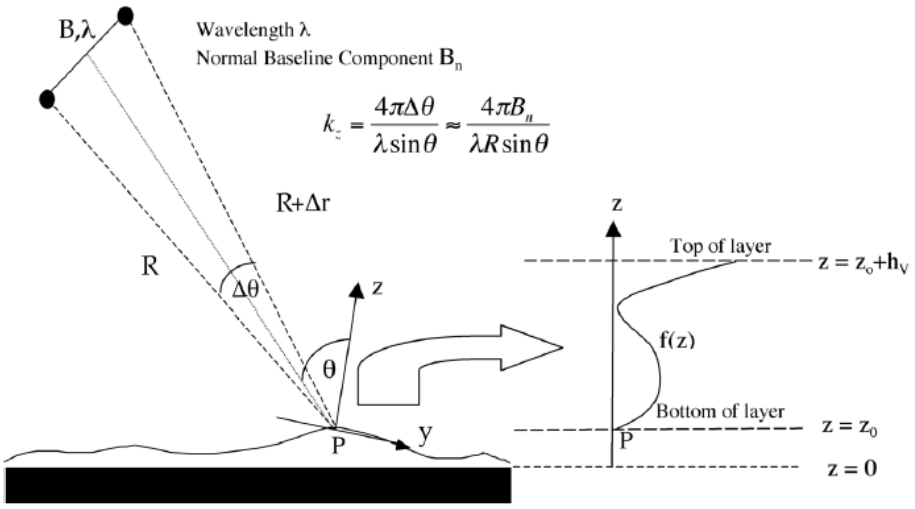

Figure B.6: Geometry of radar interferometry and definition of the vertical structure function f(z) at a point P on the surface (Cloude, 2006).

We note γ(s) the reflectivity profile in the elevation direction. The goal of the PCT is to reconstruct γ(s) from $\hat{c}$.
By noting γ(s) is bounded between s_0 and h_v, which is the elevation size of the volume to be imaged, it can be expanded in term of simpler functions, the Fourier-Legendre series, where P are the standard Legendre Polynomials :

$$\gamma(s') = \sum_n a_n P_n(s') \tag{B.11}$$

With $s' = \frac{2s}{h_v - 1}$ is called the normalized height and a_n are the Fourier Legendre coefficients.

As the coefficients a_n determine γ(s), the PCT will aim at estimating this set of coefficients from the SAR images.
We define $k_s = \frac{4\pi\Delta\Theta}{\lambda\sin(\theta)}$ the vertical wavenumber of the interferometer, which depends on the wavelength λ, the angle of incidence θ and the difference of angle $\Delta\Theta$ between the ends of the baselines. In addition, if we have a priori knowledge of the imaged volume about the vertical locations of the lowest (s_0) and highest (h_v) points of the volume imaged are known, then we can define the true topographic phase $\phi_0 = k_s \cdot s_0$ and normalized wavenumber $k_v = \frac{k_s h_v}{2}$.
With this information, the coherence can be written (Cloude, 2007):

$$\hat{c} = \exp(i\phi_0) \cdot \frac{\int_{s_0}^{h_v} \gamma(z) e^{ik_z \dot{z}} dz}{\int_{s_0}^{h_v} \gamma(z) dz} \tag{B.12}$$

and it is directly related to the unknown Legendre coefficients:

$$\hat{c} \cdot \exp(ik_v) \exp(-i\phi_0) = c_0 + a_{10}c_1 + a_{20}c_2 + ...a_{n0}c_n \tag{B.13}$$

The PCT then reduces to solving a set of linear equations. The functions c_n are weighted integrals over the Legendre polynomials.

Increasing the baseline numbers increases the numbers of c_n and thus increases the resolution. The derivation of the coefficient a_n then turns into an inversion problem with

$$a = C^{-1} g \tag{B.14}$$

Where C is a matrix that is mainly composed of c_n, a denotes the vector for a_n and g is the observation vector.
The PCT algorithm was developed by separating the propagation of the wave in the volume to be images h_v and in the air. Thus, the areas with different permittivities can be easily separated in PCT,

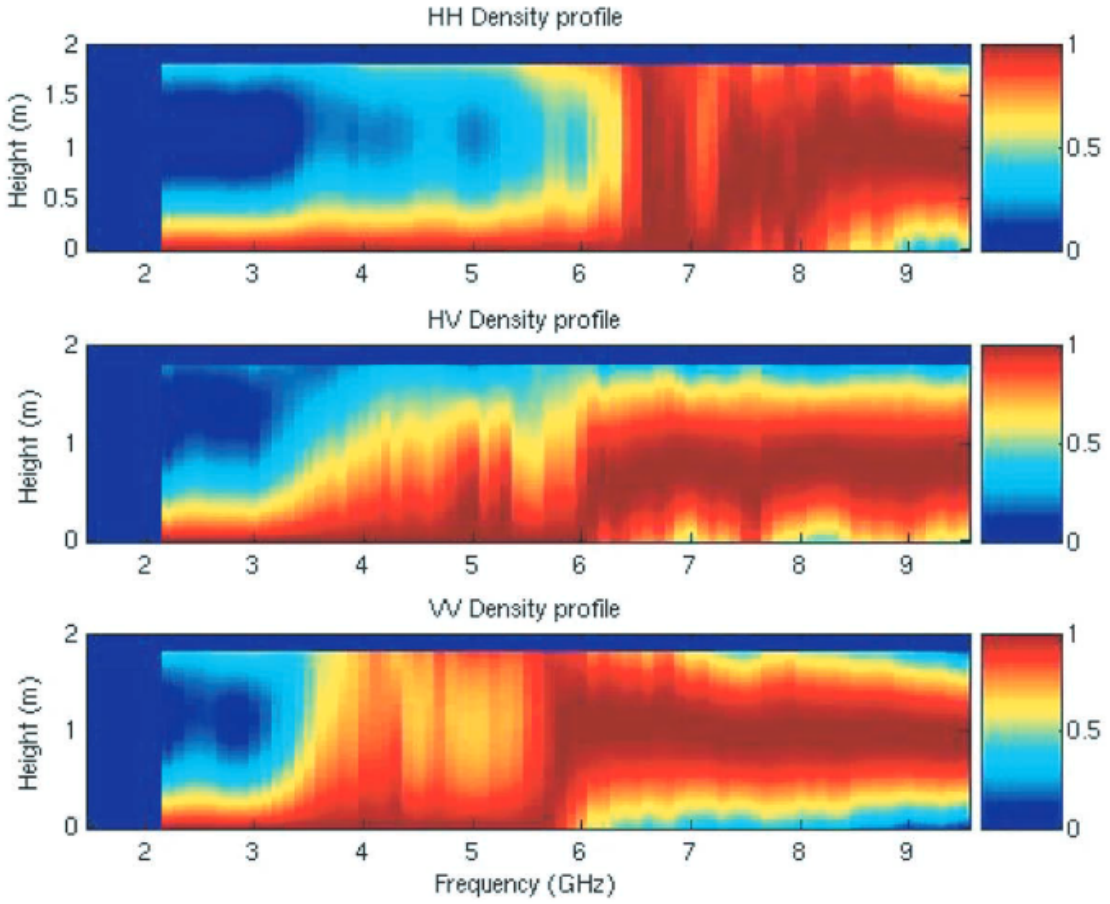

Figure B.7: Single-baseline vertical tomograms as a function of frequency and polarization (HH upper, HV center, and VV lower) (Cloude & Papathanassiou, 2008).

and the algorithm can be easily applied in a geometry with a change of permittivity, to image buried targets in the ground.

B.2.2 Results

To test the PCT, Cloud derived the 3D image of a maize sample in an anechoic chamber for a known vegetation height (1.8m). A vertical profile at each frequency could then be reconstructed. The tomograms were obtained, and show how the scattering from the vegetation changes as a function of frequency and polarization. The corresponding profiles recovered from using a dual baseline are shown in figure B.8 and using a single baseline in figure B.7.
The dual baseline results are consistent with the single-baseline retrievals but show a higher resolution, which is expected. At low frequencies (below 4 GHz), the response is dominated by surface scattering, with a relatively small amount of volume scattering. As the frequency increases, the volume-scattering contribution becomes more important, and end up dominating in VV polarization especially for frequencies greater than 6 GHz.

Although theoretically, at least one baseline can produce a tomogram using PCT, the resulting spatial resolution is low. The PCT method requires then a priori information about the volume to be imaged to ensure correct 3D reconstructions, such as the highest and lowest points of the surface. Therefore, some additional algorithm that can generate an accurate, high-resolution 3D SAR image without a priori knowledge, is still needed.

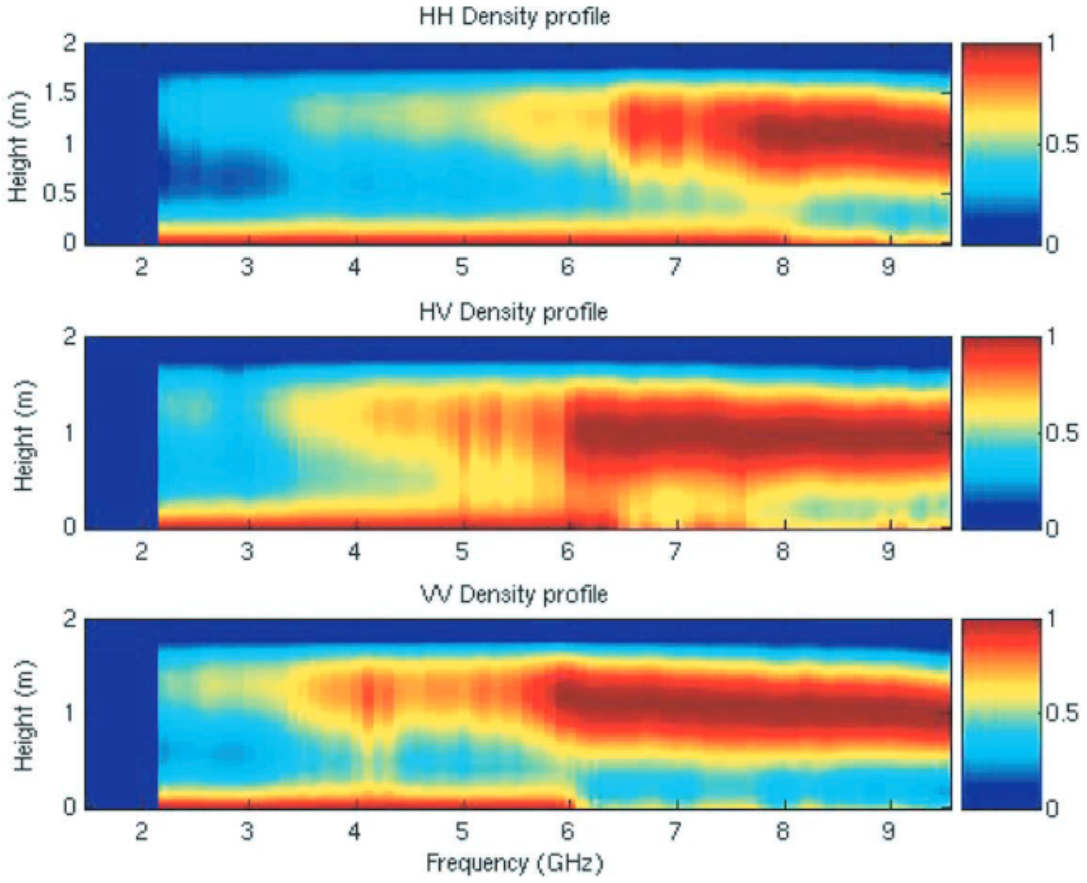

Figure B.8: Dual-baseline vertical tomograms as a function of frequency and polarization (HH upper, HV center, and VV lower) (Cloude & Papathanassiou, 2008).

B.3 Spectral Estimation

Nowadays, with the development of radars such as the German TerraSAR-X and the Italian COSMOS Skymed, both with one meter resolution, which provide very high-resolution (VHR) SAR images, it is possible to implement the tomographic mapping of surfaces that require a higher elevation resolution, such as anthropic structures, or forests. Spectral Estimation tomography methods were proposed since they have high resolution capabilities. The basic idea of these methods is to reconstruct the position, the amplitude, and phase of each scatterer by solving an inversion problem from the measurements and a matrix called the mapping matrix. The SE algorithms can be further divided into two families: the parametric and the non-parametric methods. The parametric methods need a priori knowledge on the statistical properties of the imaged area, like the number of the scatterers as opposed to the non-parametric ones, which are more flexible.

B.3.1 Parametric methods: the MUSIC algorithm

Spectral Estimation's parametric models were widely used: the M-RELAX method was first proposed by Gini et al. (2002) to solve the layover problem on SAR images and thus to provide super-resolving capability. Zhu et al. (2010) applied the NLS method to reconstruct the fine structure of a building, which shows good performances distinguishing scatterers on the roof and the ground. We will present here the implementation of the MUSIC algorithm, which was described by Nannini et al. (2011), to produce a map of the vertical structure of a forested area and estimated its height.

Description

The MUSIC algorithm (MUltiple SIgnal Classification) was originally develop to determine the parameters of multiple signals arriving at an antenna, from measurements made on these signals. Thus, the MUSIC algorithm can easily be implemented for interferometry or tomography.

The MUSIC tomography algorithm considers that in a single-pass SAR acquisition, the value of a SAR pixel g located at the position (x, r) corresponds to the integral of the reflected signal along the elevation direction :

$$g(x,r) = \int_{\Delta s} \gamma(s(x,r,s)) \exp(-\frac{4\pi}{\lambda} d_l(x,r,s))ds \tag{B.15}$$

- s is the elevation vector of size L
- γ is the reflectivity vector of size L
- d_l is the distance from the radar to each point in the elevation direction of the (x, r) pixel with l = 1...L
- λ is the wavelength.

By multiplying the number of observation with a multi-pass acquisition, the SAR image can then be obtained as :

$$g_n(x,r) = \int_{\Delta s} \gamma(s(x,r,s)) \exp(-\frac{4\pi}{\lambda} d_{l_n}(x,r,s))ds \tag{B.16}$$

With $n = 1....n$.

By discretizing this equation, we then find that

$$g = R \cdot \gamma \tag{B.17}$$

Where :

- g is the vector containing the value of the SAR image vectors
- R is a matrix composed of the coefficients $\exp(-\frac{4\pi}{\lambda} d_n(x,r,s))$, called the steering matrix
- γ is the reflectivity vector.

We note a, the steering vector, the columns of the R matrix :

$$a(s) = \exp(-\frac{4\pi}{\lambda} d_n(s)) \tag{B.18}$$

The MUSIC algorithm's basic idea is to define two subspaces: a signal and a noise subspace that are orthogonal to each other. Then, we operate on the steering matrix to create a function that represents the projection of the steering matrix on the noise subspace. If the steering vector matches a direction where a scatterer will be located, its projection on the noise subspace will be zero and thus, the position of the scatterers can be retrieved. The function of the MUSIC algorithm is defined as the inverse of the projection:

$$P_{MU}(l) = \frac{1}{a(l) E_N E_N^* a(l)} \tag{B.19}$$

With * being the complex conjugate transpose, and E_N is a $N \times M$ matrix, whose columns are the noise eigen vectors. Then the recovery of P_{MU} leads to the recovery of the elevation profiles.
The MUSIC algorithm is often applied as a first estimation of the mean phase center of the volume to be imaged. However, it relies on a priori knowledge, such as the number of phase center N_s, and thus cannot be applied to any geometry.
Since the MUSIC algorithm simply on the knowledge of the range distance R between the spacecraft and the scatterers, it is not easily applied in a geometry with a change of permittivity. Since the areas with distinct permittivities can not be separated in the SPECAN, either the delay induced by the propagation of the wave in the medium should be taken into account in the SAR processor, or a priori knowledge of the distance by each wave in the air or the medium should be obtained to improve the localization of the target.

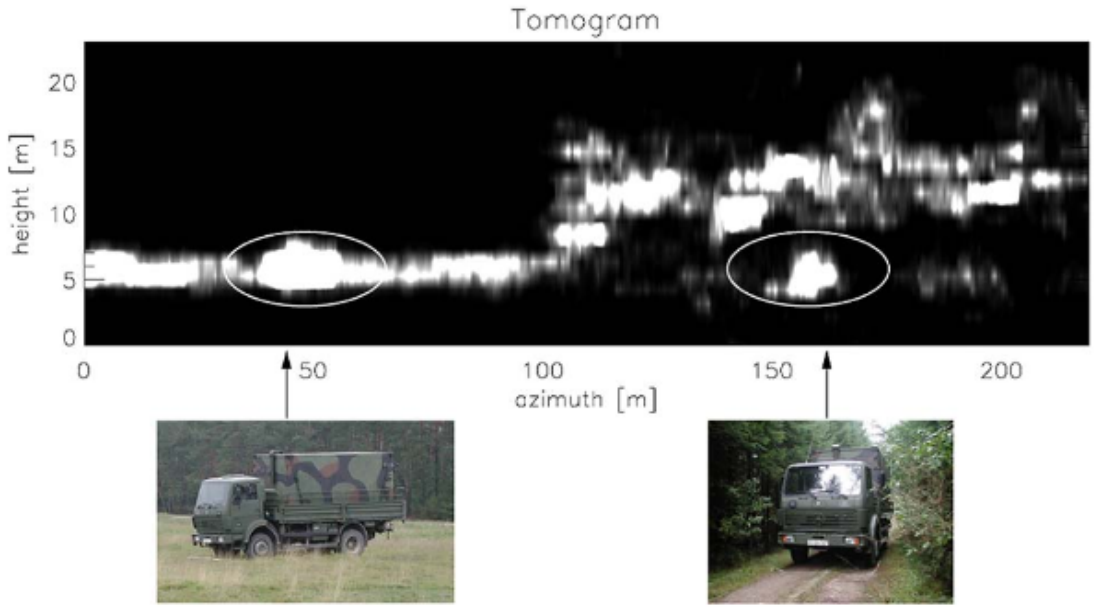

Figure B.9: Capon's tomograms located one plain truck (left) and one hidden truck (right) (Nannini et al., 2011).

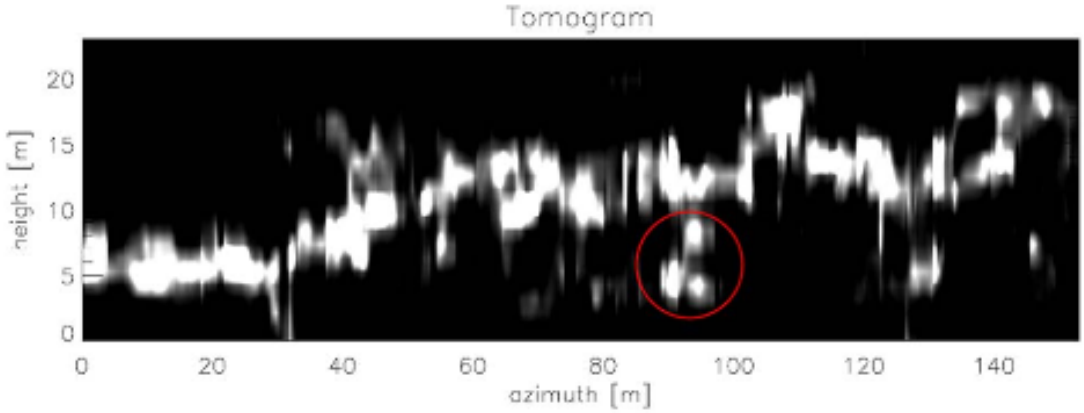

Figure B.10: MUSIC tomograms locating the hidden truck (Nannini et al., 2011).

Results

Nannini et al. (2011) imaged at L-band a forest area, with a tree height varying from 10 to 30 meters, and a hidden truck inside the forest canopy. The scene was observed with a regular horizontal grid of 21 tracks, with an average baseline of 20 meters. First, Nannini computed tomograms with the Capon method and managed to reconstruct the target position, as presented in figure B.9. However, Nannini showed that with only six acquisitions the tomograms can be obtained with MUSIC and one can reconstruct the hidden truck position, with a tomographic aperture of about 100m, as presented in figure B.10.

Thus, parametric methods are high resolution tomography algorithms that can be applied to retrieve tomograms of an observed surface, but they rely on a priori information for a correct reconstruction. Thus, non-parametric models were developed in order to compute tomography in a wider variety of geometries.

Appendix C

Earth Observation scenarios

On the Earth Observation geometry, the radar follows a straight trajectory above a flat surface: the Earth's curvature is neglecting, as well as the Earth's rotation. All simulations are carried out in an Earth-centered Inertial frame (ECI) linked to the Earth. We consider the observation of a surface centered at [0.0,0.0,0.0] in an ECI frame.

C.1 Earth Observation Single Pass observation EO-SP-1

Scenario EO-SP-1 consists of the X-band observation in the Earth observation geometry of a point target located at a surface center of the frame in [0.0,0.0,0.0]. The target spectrum is computed with SEPO.

C.1.1 Orbitography

The orbitography follows classical spaceborne radar geometry of observation: The radar follows a straight trajectory at 510 km altitude and moves along-track for 4 km at a speed of 7 km/s on the $\vec{x}$ axis. The spacecraft keeps a 24 ° slant angle with the target, located at the center of the frame at [0.0,0.0,0.0].

C.1.2 Target

The target is a point target, described by a triangular facet, whose characteristics are described in table C.1.

Table C.1: Scenario EO-SP-1: Point target characteristics in the Earth Observation geometry

Position (x,y,z) (m)	[0.0,0.0,0.0]
Size (cm)	$\lambda/100$ =0.03
Permittivity	3

C.1.3 2D SAR Synthesis area

The SAR synthesis will be carried out on a planar, rectangular two-dimensional surface, whose characteristics are described on in table C.2.

C.1.4 3D SAR Synthesis area

A 3D SAR synthesis will also be carried out on a three-dimensional cubic surface, centered on the target position, whose characteristics are described on in table C.3.

Table C.2: Scenario EO-SP-1: 10m 2D SAR synthesis characteristics.

Center (x,y,z)	[0.0,0.0,0.0]
Size (m^2)	10 × 10
Sampling (cm)	2 cm

Table C.3: Scenario EO-SP-1: Surface Echo PO 3D SAR synthesis characteristics.

Center (x,y,z)	[0.0,0.0,0.0]
Size (m^3)	10 × 10 × 10
Sampling (cm)	10 cm

C.1.5 Radar characteristics

The radar's characteristics will be based on spaceborne X-band SARs and will be working with a central frequency of 9.8 GHz, a bandwidth of 220 MHz, working with 367 frequency samples and a PRF of 2250 Hz, as depicted in table C.4.

Table C.4: Scenario EO-SP-1: Radar's characteristics.

Center Frequency	9.8 GHz
Bandwidth	220 MHz
Number of frequencies	367
PRF	2250 Hz

C.1.6 Computation means and time

The simulation of the spectrum was computed using the CPU implementation and the SAR synthesis was computed using a GPU implementation. The computation of the spectrum and the SAR synthesis with this scenario takes approximately 5 minutes.

C.2 Earth Observation Single Pass observation EO-SP-2

Scenario EO-SP-2 consists of the X-band observation of a point target with a permittivity of 1.1 located at the position [0.0,0.0,-0.25] m in the void. The target spectrum is computed with the Born approximation.

C.2.1 Orbitography

The orbitography follows classical spaceborne radar geometry of observation: The radar follows a straight trajectory at 510 km altitude and moves along-track for 10 km at a speed of 7 km/s on the $\vec{x}$ axis. The spacecraft keeps a 24 ° slant angle with the target, located at the center of the frame.

C.2.2 Target

This scenario will consider an inclusion with a permittivity ϵ_f = 1.1, as presented in figure C.1. The scenario characteristics are summarized in table C.5.

Table C.5: Scenario EO-SP-2: Interface and background volume characteristics.

	Interface	Background volume
Center (x,y,z) (m)	[0.0,0.0,0.0]	[0.0,0.0,-0.25]
Size (m^2)	0.5 × 0.5	0.5 × 0.5 × 0.5
Sampling (cm)	0.8	0.5
Permittivity ϵ_a	1.0	1.0

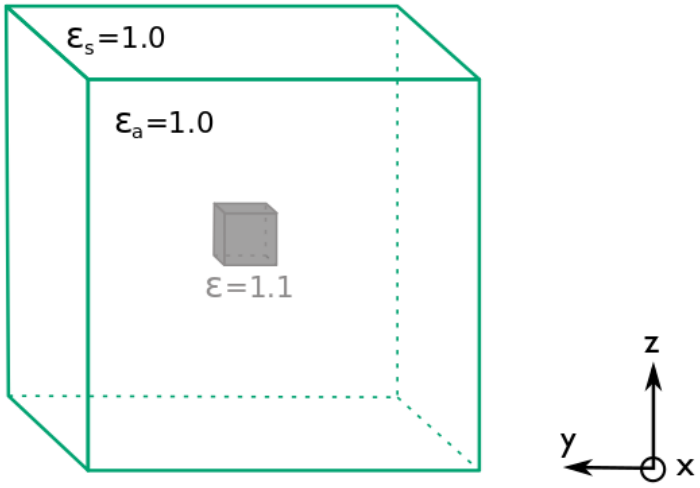

Figure C.1: Scenario EO-SP-2: Simulation scenario of a point target in the void

C.2.3 2D SAR Synthesis area

The 2D SAR synthesis will be carried out on a two-dimensional surface crossing the position of the inclusion to image the synthesis in the range-doppler plane, such as depicted in figure C.2 depicted in table C.6.

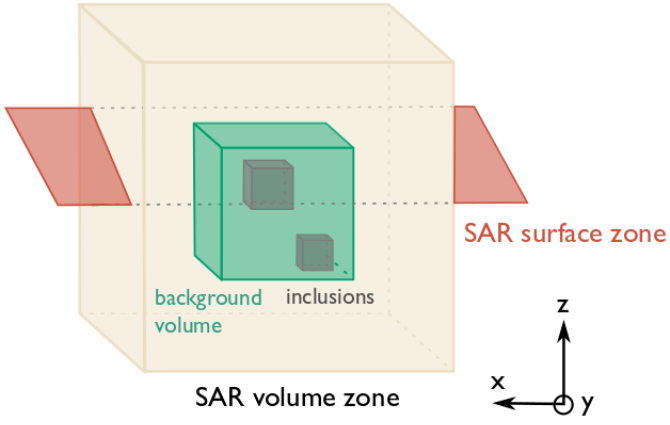

Figure C.2: Scenario EO-SP-2: SAR Synthesis geometry.

Table C.6: Scenario EO-SP-2: 2D SAR synthesis characteristics.

Center (x,y,z) (m)	[0.0,0.0,-0.25]
Size (m^2)	3 × 3
Sampling (cm)	0.6 cm

C.2.4 3D SAR Synthesis area

The 3D SAR synthesis will be carried out on a three-dimensional volume to image the SAR synthesis in the elevation plane, and observe the left-right ambiguity. The surface characteristics are depicted in table C.7.

Table C.7: Scenario EO-SP-2: 3D SAR synthesis characteristics

Center (x,y,z) (m)	[0.0,0.0,-0.25]
Size (m^3)	3 × 3 × 3
Sampling (cm)	3

C.2.5 Radar characteristics

The radar's characteristics will be based on spaceborne SARs, and will be working with a central frequency of 9.8 GHz, a bandwidth of 220 MHz, working with 25 frequency samples and a PRF of 40 Hz in order to have no aliasing in the volume under study, and to keep simulation time relatively slow. The radar characteristics are presented in table C.8.

Table C.8: Scenario EO-SP-2: Radar characteristics

Center Frequency	9.8 GHz
Bandwidth	1.0 GHz
Number of frequencies	25
PRF	40 Hz

C.2.6 Computation means and time

The SAR synthesis was computed using a GPU implementation. The computation of the spectrum and the SAR synthesis with this scenario takes approximately 15 minutes.

C.3 Earth Observation Single Pass observation EO-SP-3

Scenario EO-SP-3 consists in observing in the X-band a point target with a permittivity of 3.1 located at the position [0.0,0.0,-0.25] m, at 25 cm under the surface, in a medium with a permittivity of 3.0. The target spectrum is computed with the Born approximation.

C.3.1 Orbitography

The orbitography follows classical spaceborne radar geometry of observation: The radar follows a straight trajectory at 510 km altitude and moves along-track for 10 km at a speed of 7 km/s on the $\vec{x}$ axis. The spacecraft keeps a 24 ° slant angle with the target, located at the center of the frame.

C.3.2 Target

This scenario will consider an inclusion is embedded at 25 cm under the interface and has a permittivity ϵ_f = 3.1, as presented in figure C.3. The scenario characteristics are summarized in table C.9.

Table C.9: Scenario EO-SP-3: Interface and background volume characteristics

	Interface	Background volume
Center (x,y,z) (m)	[0.0,0.0,0.0]	[0.0,0.0,-0.25]
Size (m^2)	0.5 × 0.5	0.5 × 0.5 × 0.5
Sampling (cm)	0.8	0.5
Permittivity ϵ_a	3.0	3.0

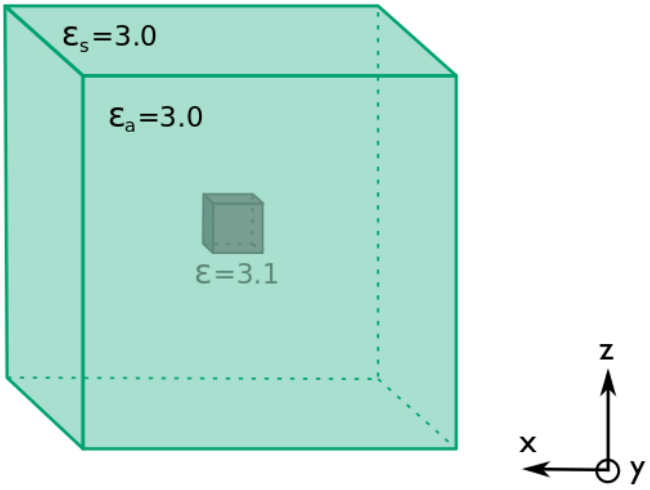

Figure C.3: Scenario EO-SP-3: Simulation scenario of a point target in a medium of permittivity 3.0

C.3.3 2D SAR Synthesis area

The 2D SAR synthesis will be carried out on a two-dimensional surface crossing the position of the inclusion to image the synthesis in the range-Doppler plane, such as depicted in figure C.4, and has the characteristics depicted in table C.10.

Table C.10: Scenario EO-SP-3: 2D SAR synthesis characteristics.

Center (x,y,z) (m)	[0.0,0.0,-0.25]
Size (m^2)	3 × 3
Sampling (cm)	0.6 cm

C.3.4 3D SAR Synthesis area

The 3D SAR synthesis will be carried out on a three-dimensional volume to image the synthesis in the elevation plane, and observe the left-right ambiguity. The surface characteristics are depicted in table C.11.

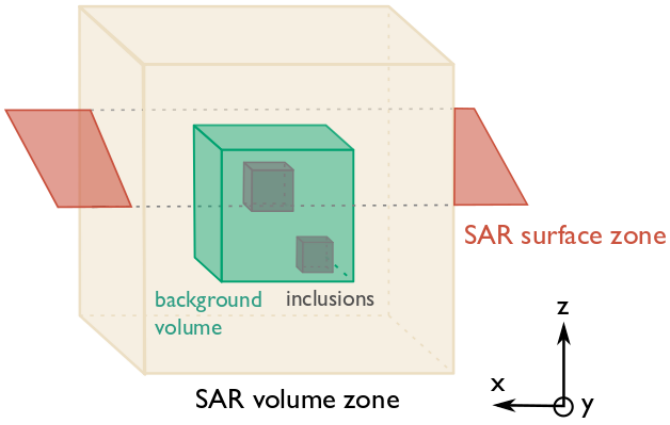

Figure C.4: Scenario EO-SP-3: SAR Synthesis geometry.

Table C.11: Scenario EO-SP-3: 3D SAR synthesis characteristics

Center (x,y,z) (m)	[0.0,0.0,-0.25]
Size (m^3)	3 × 3 × 3
Sampling (cm)	3

C.3.5 Radar characteristics

The radar's characteristics will be based on spaceborne SARs, and will be working with a central frequency of 9.8 GHz, a bandwidth of 220 MHz, working with 25 frequency samples and a PRF of 40 Hz in order to have no aliasing in the volume under study, and to keep simulation time relatively slow, as depicted in table C.12.

Table C.12: Scenario EO-SP-3: Radar characteristics

Center Frequency	9.8 GHz
Bandwidth	1.0 GHz
Number of frequencies	25
PRF	40 Hz

C.3.6 Computation means and time

The SAR synthesis was computed using a GPU implementation. The computation of the spectrum and the SAR synthesis with this scenario takes approximately 15 minutes.

C.4 Earth Observation Single Pass observation EO-SP-4

Scenario EO-SP-4 consists in observing in the X-band several random rough surface with SEPO in order to average resulting SAR synthesis parameters.

C.4.1 Orbitography

The orbitography follows classical spaceborne radar geometry of observation: The radar follows a straight trajectory at 510 km altitude, at a velocity of 7km/s. The spacecraft keeps a 24 ° slant

angle with the surface, located at the center of the frame. For each rough surface considered, 9 SAR images will be computed, with a decreasing the resolution cell size, in both range and Doppler. In order to have a squared resolution cell, the length of the radar illumination time T_{ill} is dictated by the bandwidth. By noting nband the index of the SAR image, nband =1...9, we have:

$$T_{ill} = \frac{\lambda_{max} \cdot R_0}{2.0 \cdot v \cdot \delta_a} \tag{C.1}$$

Where λ is the radar's wavelength,R_0 is the mean distance of observation, v is the spacecraft velocity, and δ_a is the azimuth resolution, set equal to the range resolution in our study, so $\delta_a = c/2B$ where c is the speed of light and B is the RF bandwidth.

C.4.2 Target

This scenario will consider 20 rough surfaces, obtained with the parameters described in table C.13

Table C.13: Scenario EO-SP-4: Rough surface roughness parameters

Center (x,y,z) (m)	[0.0,0.0,0.0]
RMS height	25 cm
Correlation Length	70 cm
DTM size	15m
Maximum Permittivity	3
Continuity assured by	Hanning Weighting

C.4.3 2D SAR Synthesis area

The 2D SAR Synthesis will be carried out on a two-dimensional plane covering the extent of the surface whose permittivity if equal to 3, as depicted in figure C.5. The characteristics of the 2D SAR Synthesis area is depicted in table C.14.

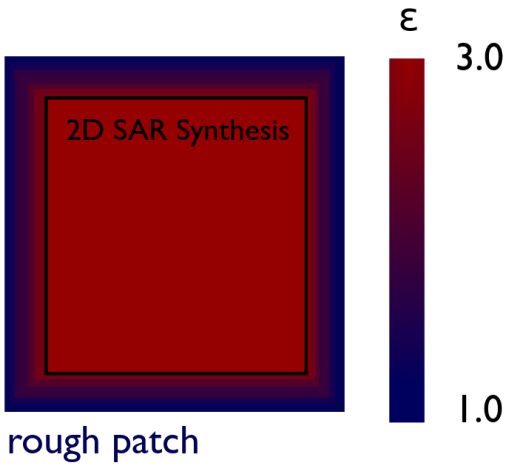

Figure C.5: Scenario EO-SP-4: SAR Synthesis geometry.

C.4.4 Radar characteristics

The radar used for our simulations will be based on X-band SAR observing the Earth, with a center frequency of 9.8 GHz. For each of the rough surfaces, 9 SAR images will be computed when the RF band varies from 100 MHz to 900 MHz. The PRF and the number of frequencies will be adjusted so

Table C.14: Scenario EO-SP-4: 2D SAR synthesis characteristics.

Center (x,y,z) (m)	[0.0,0.0,0.0]
Size (m^2)	12.5 m
Sampling (cm)	2.5 cm

that no aliasing occurs on the SAR 2D surface. By noting nband the index of the chosen band (n=1 for B=100MHz, until n=9 for B=900MHz), the characteristics of the different radars used to obtain the SAR images are described in table C.15. The resulting radar resolution cell sizes are presented in table C.16 for the 9 different RF and Doppler bands.

Table C.15: Scenario EO-SP-4: Radar characteristics

Center Frequency	9.8 GHz
Bandwidth	nband · 100 MHz
Number of frequencies	81.0 · nband
PRF	225 Hz

Table C.16: Resolution cell size depending on the RF and doppler band

nband	Resolution cell size (m^2)
1	13.58
2	3.39
3	1.51
4	0.85
5	0.54
6	0.38
7	0.28
8	0.21
9	0.17

C.4.5 Computation means and time

The simulation of the spectrum is obtained with a CPU implementation SAR synthesis was computed using a GPU implementation. For one rough surface, the simulation of the spectrum was only computed for nband = 9. The 8 other spectra were deduced from this spectrum .
The computation of the spectrum and the SAR synthesis with this scenario for one rough surface. takes approximately 30 minutes.

C.5 Earth Observation Single Pass observation EO-SP-5

Scenario EO-SP-5 consists of the X-band observation in the Earth observation geometry of a point target located at a surface center of the frame in [0.0,0.0,0.0]. The target's spectrum is computed using the point target computation tools of SPRATS.

C.5.1 Orbitography

The orbitography follows classical spaceborne radar geometry of observation: The radar follows a straight trajectory at 510 km altitude and moves along-track for 4 km at a speed of 7 km/s on the $\vec{x}$ axis. The spacecraft keeps a 24 ° slant angle with the target, located at the center of the frame at [0.0,0.0,0.0].

C.5.2 Target

The target is a point target, located in [0.0,0.0,0.0].

C.5.3 2D SAR Synthesis area

The SAR synthesis will be carried out on a planar, rectangular two-dimensional surface, whose characteristics are described on in table C.17.

Table C.17: Scenario EO-SP-5: 50m 2D SAR synthesis characteristics.

Center (x,y,z)	[0.0,0.0,0.0]
Size (m^2)	50 × 50
Sampling (cm)	20 cm

C.5.4 Radar characteristics

The radar's characteristics will be based on spaceborne X-band SARs, and will be working with a central frequency of 9.8 GHz, a bandwidth of 10 MHz, to be compliant with the narrowband specification, working with 50 frequency samples and a PRF of 70 Hz, as depicted in table C.18.

Table C.18: Scenario EO-SP-5: Radar's characteristics.

Center Frequency	9.8 GHz
Bandwidth	10 MHz
Number of frequencies	50
PRF	70 Hz

C.5.5 Computation means and time

The simulation of the spectrum was computed using the CPU implementation and the SAR synthesis was computed using a GPU implementation. The computation of the spectrum and the SAR synthesis with this scenario takes about 30 seconds.

C.6 Earth Observation Single Pass observation EO-SP-6

Scenario EO-SP-6 consists of the X-band observation in the Earth observation geometry of a extended facet located at a surface center of the frame in [0.0,0.0,0.0]. The target spectrum is computed with SEPO.

C.6.1 Orbitography

The orbitography follows classical spaceborne radar geometry of observation: The radar follows a straight trajectory at 510 km altitude and moves along-track for 4 km at a speed of 7 km/s on the

$\vec{x}$ axis. The spacecraft keeps a 24 ° slant angle with the target, located at the center of the frame at [0.0,0.0,0.0].

C.6.2 Target

The target is a 3m large facet, described by a triangular facet, whose characteristics are described in table C.19.

Table C.19: Scenario EO-SP-6: Point target characteristics in the Earth Observation geometry

Position (x,y,z) (m)	[0.0,0.0,0.0]
Size (m)	3
Permittivity	3
Normal	[0.0,0.0,1.0]

C.6.3 2D SAR Synthesis area

The SAR synthesis will be carried out on a planar, rectangular two-dimensional surface, whose characteristics are described on in table C.20.

Table C.20: Scenario EO-SP-6: 3m 2D SAR synthesis characteristics.

Center (x,y,z)	[0.0,0.0,0.0]
Size (m^2)	3×3
Sampling (cm)	1.2 cm

C.6.4 Radar characteristics

The radar's characteristics will be based on spaceborne X-band SARs, and will be working with a central frequency of 9.8 GHz, a bandwidth of 10 MHz, to comply with the narrowband requirement, working with 200 frequency samples and a PRF of 210 Hz, as depicted in table C.21.

Table C.21: Scenario EO-SP-6: Radar's characteristics.

Center Frequency	9.8 GHz
Bandwidth	10 MHz
Number of frequencies	50
PRF	70 Hz

C.6.5 Computation means and time

The simulation of the spectrum was computed using the CPU implementation and the SAR synthesis was computed using a GPU implementation. The computation of the spectrum and the SAR synthesis with this scenario takes approximately 1 minute.

C.7 Earth Observation Single Pass observation EO-SP-7

Scenario EO-SP-7 consists of the X-band observation in the Earth observation geometry of a point target located at a surface center of the frame in [0.0,0.0,0.0]. The target's spectrum is computed

using the point target computation tools of SPRATS.

C.7.1 Orbitography

The orbitography follows classical spaceborne radar geometry of observation: The radar follows a straight trajectory at 510 km altitude and moves along-track for 4 km at a speed of 7 km/s on the $\vec{x}$ axis. The spacecraft keeps a 24 ° slant angle with the target, located at the center of the frame at [0.0,0.0,0.0].

C.7.2 Target

The target is a point target, located in [0.0,0.0,0.0].

C.7.3 2D SAR Synthesis area

The SAR synthesis will be carried out on a planar, rectangular two-dimensional surface, whose characteristics are described on in table C.22

Table C.22: Scenario EO-SP-7: 50m 2D SAR synthesis characteristics.

Center (x,y,z)	[0.0,0.0,0.0]
Size (m^2)	50 × 50
Sampling (cm)	20 cm

C.7.4 Radar characteristics

The radar's characteristics will be based on spaceborne X-band SARs, and will be working with a central frequency of 9.8 GHz, a bandwidth of 1.0 GHz, to be compliant with the narrowband specification, working with 200 frequency samples and a PRF of 210 Hz, as depicted in table C.23.

Table C.23: Scenario EO-SP-7: Radar's characteristics.

Center Frequency	9.8 GHz
Bandwidth	1.0 GHz
Number of frequencies	200
PRF	210 Hz

C.7.5 Computation means and time

The simulation of the spectrum was computed using the CPU implementation and the SAR synthesis was computed using a GPU implementation. The computation of the spectrum and the SAR synthesis with this scenario takes about 30 seconds.

C.8 Earth Observation Single Pass observation EO-SP-8

Scenario EO-SP-8 consists of the X-band observation in the Earth observation geometry of a extended facet located at a surface center of the frame in [0.0,0.0,0.0]. The target spectrum is computed with SEPO.

C.8.1 Orbitography

The orbitography follows classical spaceborne radar geometry of observation: The radar follows a straight trajectory at 510 km altitude and moves along-track for 4 km at a speed of 7 km/s on the $\vec{x}$ axis. The spacecraft keeps a 24 ° slant angle with the target, located at the center of the frame at [0.0,0.0,0.0].

C.8.2 Target

The target is a 3m large facet, described by a triangular facet, whose characteristics are described in table C.24.

Table C.24: Scenario EO-SP-8: Point target characteristics in the Earth Observation geometry

Position (x,y,z) (m)	[0.0,0.0,0.0]
Size (m)	3
Permittivity	3
Normal	[0.0,0.0,1.0]

C.8.3 2D SAR Synthesis area

The SAR synthesis will be carried out on a planar, rectangular two-dimensional surface, whose characteristics are described on in table C.25.

Table C.25: Scenario EO-SP-8: 10m 2D SAR synthesis characteristics.

Center (x,y,z)	[0.0,0.0,0.0]
Size (m^2)	10 × 10
Sampling (cm)	4 cm

C.8.4 Radar characteristics

The radar's characteristics will be based on spaceborne X-band SARs, and will be working with a central frequency of 9.8 GHz, a bandwidth of 1.0 GHz, to comply with the narrowband requirement, working with 200 frequency samples and a PRF of 210 Hz, as depicted in table C.26.

Table C.26: Scenario EO-SP-8: Radar's characteristics.

Center Frequency	9.8 GHz
Bandwidth	1.0 GHz
Number of frequencies	200
PRF	210 Hz

C.8.5 Computation means and time

The simulation of the spectrum was computed using the CPU implementation and the SAR synthesis was computed using a GPU implementation. The computation of the spectrum and the SAR synthesis with this scenario takes approximately 1 minute.

C.9 Earth Observation Multipass observation EO-MP-1

C.9.1 Orbitography

The orbitography follows classical spaceborne radar geometry of observation: The radar reference trajectory follows a straight trajectory at 510 km altitude and moves along-track for 10 km at a speed of 7 km/s on the $\vec{x}$ axis. The spacecraft keeps a 24 ° slant angle with the target, located at the center of the frame. The trajectory is repeated 20 times, each separated by 4km in the vertical direction. The resulting multipass geometry is presented in figure C.6.

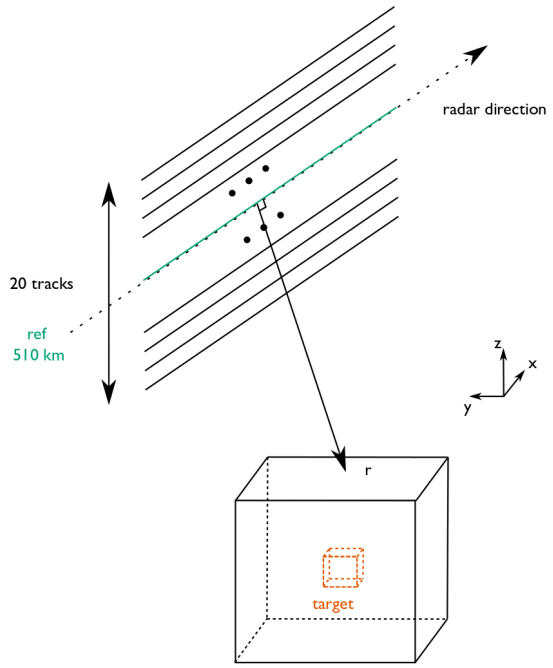

Figure C.6: Scenario EO-MP-1: Observation geometry

In order to apply the compressive sensing tomography algorithm, several orbits, with several elevation will have to be simulated. The scenario consists of imaging a volume of three meters, so according to the equations set to establish the performances of the compressive sensing method, to avoid any ambiguities, the tracks should be separated by a distance in elevation:

$$\mu \leqslant \frac{\lambda R_0}{h} = 5.7km \tag{C.2}$$

We will thus separate each trajectory by a distance of 4.5 km in elevation, which brings separation of about 4 km in the $\vec{z}$ direction, taking into account some margin.

C.9.2 Target

This scenario will consider the same target as in scenario EO-SP-3, which we will repeat here. An inclusion is embedded at 25 cm under the interface and has a permittivity ϵ_f = 3.1, as presented in figure C.7. The scenario characteristics are summarized in table C.27.

C.9.3 2D SAR synthesis

The SAR syntheses will be computed on a surface which is the interface between the void and the background volume, as presented on figure C.8. 20 syntheses, for each trajectory, were computed on these surfaces and will constitute the stack of SAR images used for the tomography. The characteristics of the SAR synthesis areas are summarized in table C.28.

Table C.27: Scenario EO-MP-1: Interface and background volume characteristics

	Interface	Background volume
Center (x,y,z) (m)	[0.0,0.0,0.0]	[0.0,0.0,-0.25]
Size (m^2)	0.5 × 0.5	0.5 × 0.5 × 0.5
Sampling (cm)	0.8	0.5
Permittivity ϵ_a	3.0	3.0

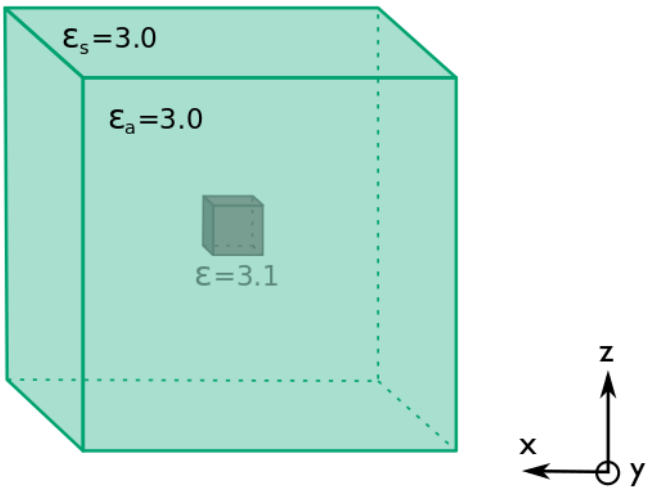

Figure C.7: Scenario EO-MP-1: Simulation scenario of a point target in a medium of permittivity 3.0

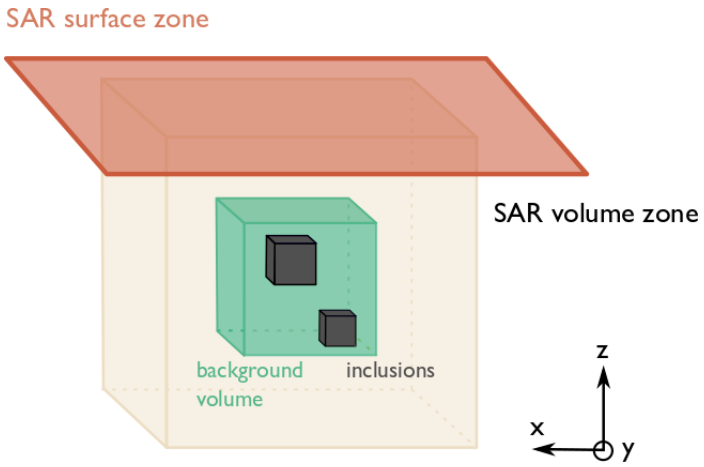

Figure C.8: Scenario EO-MP-1 : SAR Synthesis areas in the Earth Observation geometry

Table C.28: Scenario EO-MP-1: 2D SAR synthesis.

Center (x,y,z) (m)	[0.0,0.0,0.0]
Size (m^2)	5 × 5
Sampling (cm)	1 cm

C.9.4 3D SAR Synthesis area

The results of the CS tomography will be compared to the results of the 3D SAR synthesis. The 20 SAR syntheses will be computed on a $3m \times 3m \times 3m$ volume, centered at the theoretical position of the target, at [0.0,0.0,-25] cm, as presented in table C.29. After the computation, these SAR syntheses will be averaged to constitute the final SAR synthesis

Table C.29: Scenario EO-MP-1: 3D SAR synthesis characteristics

Center (x,y,z) (m)	[0.0,0.0,-0.25]
Size (m^3)	3 × 3 × 3
Sampling (cm)	3

C.9.5 Compressive sensing volume visualization of results

The tomography results will be shown in 3D volume. The elevation profile is computed along the $\vec{s}$ direction, the direction normal to the radar direction and to the range direction along 5 meters. As the profile of each scatterer is retrieved along the elevation direction, this makes the tomography results represented in a tilted way, such as in figure C.9.

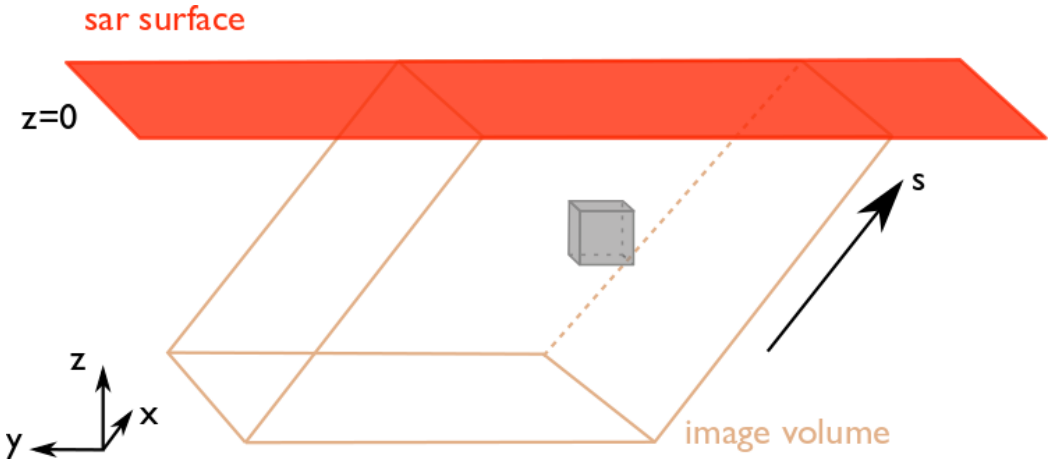

Figure C.9: Scenario EO-MP-1: Visualization of the results of the compressive sensing in the Earth Observation geometry

C.9.6 Radar characteristics

The radar's characteristics will be based on spaceborne X-band SARs, and will be working with a central frequency of 9.8 GHz, a bandwidth of 1.0 GHz, working with 25 frequency samples and a PRF of 40 Hz, as depicted in table C.30, to avoid any aliasing on the volume under study and to keep the simulation time fast.

Table C.30: Scenario EO-MP-1: Radar characteristics

Center Frequency	9.8 GHz
Bandwidth	1.0 GHz
Number of frequencies	25
PRF	40 Hz

C.9.7 Computation means and time

The SAR synthesis was computed using a GPU implementation. The computation of the spectrum and the SAR synthesis with this scenario takes approximately 5 hours, and the computation of the tomography takes approximately 5 minutes.

C.10 Earth Observation Multipass observation EO-MP-2

Scenario EO-MP-2 consists in observing with a narrowband signal a random rough surface centered in [0.0,0.0,0.0] with a permittivity of 3.0 with a multipass orbitography. The target spectrum is obtained with SEPO.

C.10.1 Orbitography

The orbitography follows classical spaceborne radar geometry of observation: The radar reference trajectory follows a straight trajectory at 510 km altitude and moves along-track for 2.2 km at a speed of 7 km/s on the $\vec{x}$ axis. The spacecraft keeps a 24 ° slant angle with the target, located at the center of the frame. The trajectory is repeated 50 times, each separated by 1.0 km in the vertical direction. The resulting multipass geometry is presented in figure C.10.

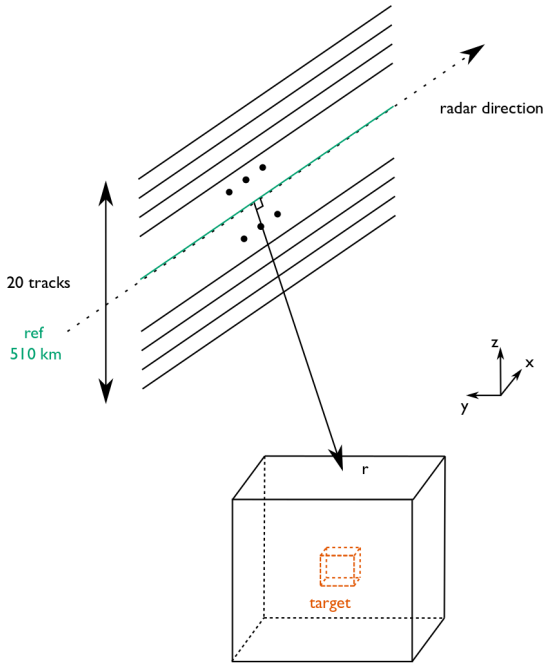

Figure C.10: Scenario EO-MP-2: Observation geometry

C.10.2 Target

The target is a 15-m large rough surface, with roughness parameters recalled and summed up in table C.31 and presented in figure C.11.

C.10.3 2D SAR synthesis

The SAR syntheses will be computed on a 12.5 large plane. 50 syntheses, for each trajectory, were computed on these surfaces and will constitute the stack of SAR images used for the tomography. The SAR synthesis areas are presented in figure C.12 and their characteristics are summarized in table C.32.

Table C.31: Scenario EO-MP-2: Rough surface roughness parameters

Center (x,y,z) (m)	[0.0,0.0,0.0]
RMS height	25 cm
Correlation Length	70 cm
DTM size	15m
Maximum Permittivity	3
Continuity assured by	Hanning Weighting

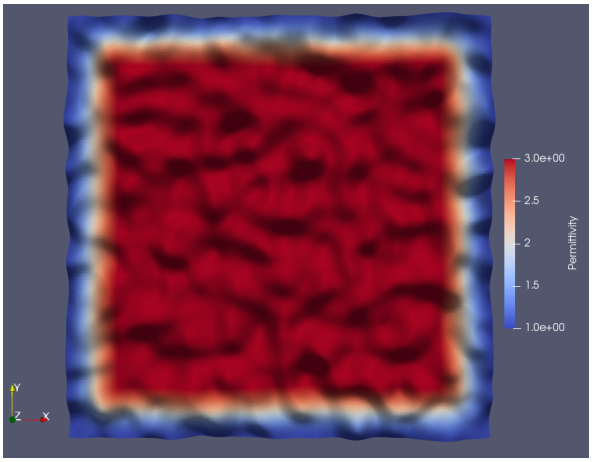

Figure C.11: Scenario EO-MP-2: Rough surface DTM

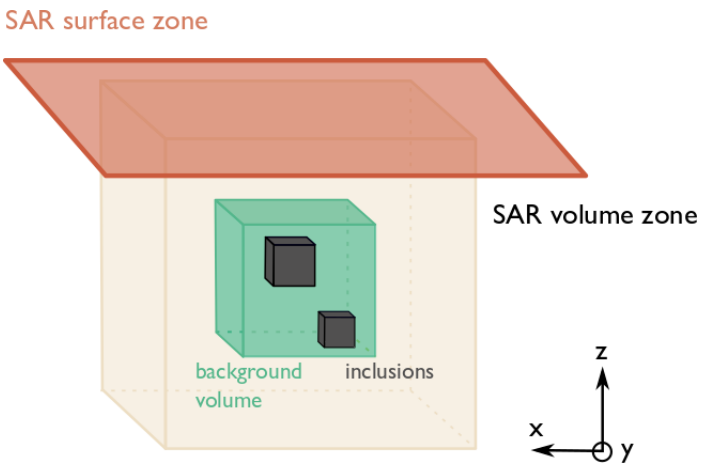

Figure C.12: Scenario EO-MP-2: SAR Synthesis areas in the Earth Observation geometry

Table C.32: Scenario EO-MP-2: 2D SAR synthesis.

Center (x,y,z) (m)	[0.0,0.0,0.0]
Size (m^2)	12.5 × 12.5
Sampling (cm)	2.5 cm

C.10.4 Radar characteristics

The radar's characteristics will be based on spaceborne X-band SARs, and will be working with a central frequency of 9.8 GHz, a bandwidth of 100 MHz, working with 81 frequency samples and a PRF of 225 Hz, as depicted in table C.33, to avoid any aliasing on the volume under study and to keep the simulation time fast.

Table C.33: Scenario EO-MP-2: Radar characteristics

Center Frequency	9.8 GHz
Bandwidth	100 MHz
Number of frequencies	81
PRF	225 Hz

C.10.5 Computation means and time

The SAR synthesis was computed using a GPU implementation. The computation of the spectrum and the SAR synthesis with this scenario takes approximately 10 minutes, and the computation of the SAR synthesis takes approximately 5 minutes.

C.11 Earth Observation Multipass observation EO-MP-3

Scenario EO-MP-3 consists in observing with a wideband signal a random rough surface centered in [0.0,0.0,0.0] with a permittivity of 3.0 with a multipass orbitography. The target spectrum is obtained with SEPO

C.11.1 Orbitography

The orbitography follows classical spaceborne radar geometry of observation: The radar reference trajectory follows a straight trajectory at 510 km altitude and moves along-track for 25 km at a speed of 7 km/s on the $\vec{x}$ axis. The spacecraft keeps a 24 ° slant angle with the target, located at the center of the frame. The trajectory is repeated 50 times, each separated by 1.0 km in the vertical direction. The resulting multipass geometry is presented in figure C.13.

C.11.2 Target

The target is a 15-m large rough surface, with roughness parameters recalled and summed up in table C.34 and presented in figure C.14.

Table C.34: Scenario EO-MP-3: Rough surface roughness parameters

Center (x,y,z) (m)	[0.0,0.0,0.0]
RMS height	25 cm
Correlation Length	70 cm
DTM size	15m
Maximum Permittivity	3
Continuity assured by	Hanning Weighting

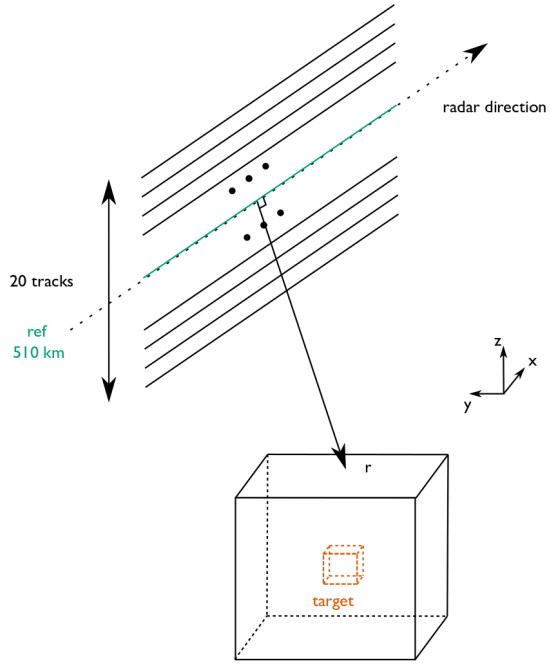

Figure C.13: Scenario EO-MP-3: Observation geometry

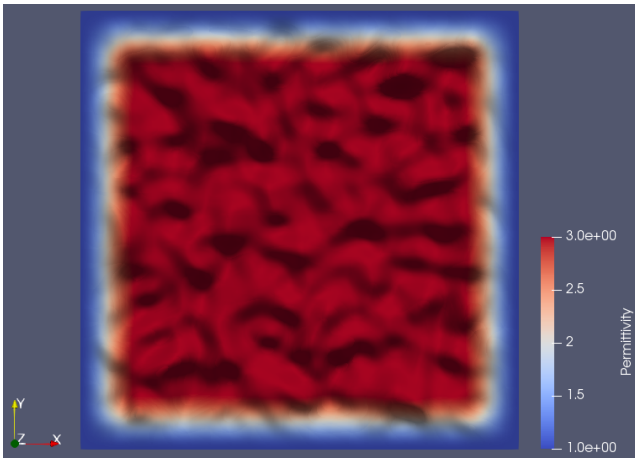

Figure C.14: Scenario EO-MP-3 : Rough surface DTM

C.11.3 2D SAR synthesis

The SAR syntheses will be computed on a 12.5 large plane. 50 syntheses, for each trajectory, were computed on these surfaces and will constitute the stack of SAR images used for the tomography. The SAR synthesis areas are presented in figure C.15 and their characteristics are summarized in table C.35.

Table C.35: Scenario EO-MP-3: 2D SAR synthesis.

Center (x,y,z) (m)	[0.0,0.0,0.0]
Size (m^2)	12.5 × 12.5
Sampling (cm)	2.5 cm

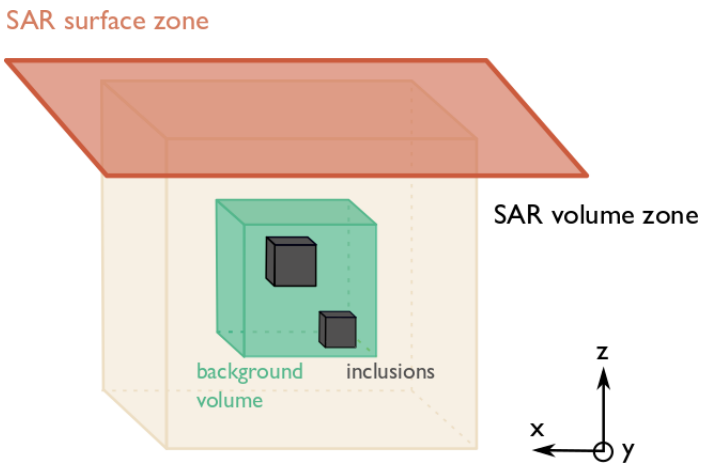

Figure C.15: Scenario EO-MP-3: SAR Synthesis areas in the Earth Observation geometry

C.11.4 Radar characteristics

The radar's characteristics will be based on spaceborne X-band SARs, and will be working with a central frequency of 9.8 GHz, a bandwidth of 500 MHz, working with 81 frequency samples and a PRF of 225 Hz, as depicted in table C.36, to avoid any aliasing on the volume under study and to keep the simulation time fast.

Table C.36: Scenario EO-MP-3: Radar characteristics

Center Frequency	9.8 GHz
Bandwidth	100 MHz
Number of frequencies	81
PRF	225 Hz

C.11.5 Computation means and time

The SAR synthesis was computed using a GPU implementation. The computation of the spectrum and the SAR synthesis with this scenario takes approximately 20 mn, and the computation of the SAR synthesis takes approximately 10 minutes.

Appendix D

Small Body scenarios

All the orbitography geometric computations in the small body geometry make use of the NASA/NAIF SPICE library *SPICE Kernel definition* (n.d.). SPICE toolkit offers data about the observation geometry as well as tools about different bodies and spacecraft in the solar system. SPICE orbitography computations are based on "kernels" which define all the characteristics of the target body.

Two different frames will be used in this study:

- First, the global J2000 reference frame is an inertial frame centered on 1999KW4.
- Then, the second frame used is the frame linked to our target body, 1999KW4 and centered on it.

All following computations and visualizations will be made in either of these frames. These kernels are provided along with the source code and may be updated with the improvement of the knowledge of the system.

D.1 Small Body Single Pass Observation SB-SP-1

Scenario EO-SB-1 consists in observing a point target located at the surface of an asteroid. The target spectrum is computed with Surface Echo PO.

D.1.1 Orbitography

For the scenario of a single pass orbitography, the radar is fixed in the J2000 frame at the position [4.44019, -10.0, 5.77], when KW4 position is fixed at the center of the frame [0.0,0.0,0.0]. This allows having incidence angles of about 30°, which are optimal for along track resolution F. T. Ulaby and Dobson (1989). The trajectory in the J2000 frame and in the frame linked to 1999KW4 is presented in figure D.1.

All visualizations are made in the frame linked to KW4: the radar trajectory is thus only due to the rotation speed of the body, which is a little more than 2.2 hours.

D.1.2 Target

The target is a point target, described by a triangular facet, located in the position [0° lat ,0° lon] on 1999 KW4. The target characteristics are summed up in table D.1.

D.1.3 2D SAR synthesis area on a 20m patch

The SAR synthesis will be observed on a 20-m patch extracted from the DTM of 1999KW4, which was downloaded from the JPL website, as represented in figure D.2. The patch characteristics are summed up in table D.2.

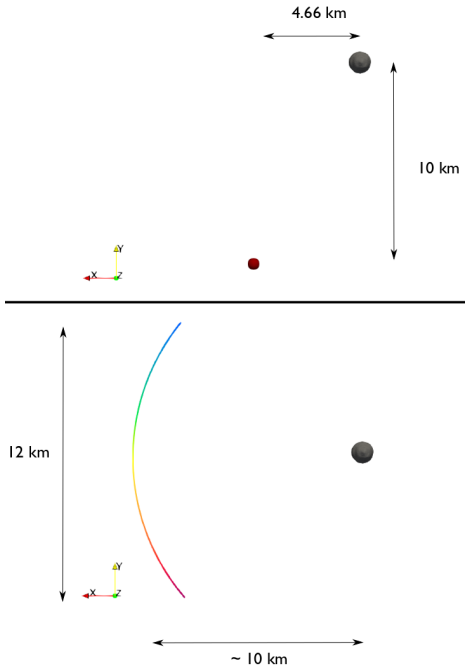

Figure D.1: Scenario SB-SP-1: Radar's trajectory in an inertial frame (top) and in the frame linked to 1999KW4 (bottom)

Table D.1: Scenario SB-SP-1: target characteristics

Position (x,y,z)	[0.592,0.000013,-0.000255]
Size (cm)	$\lambda/100 = 0.375$
Permittivity	3

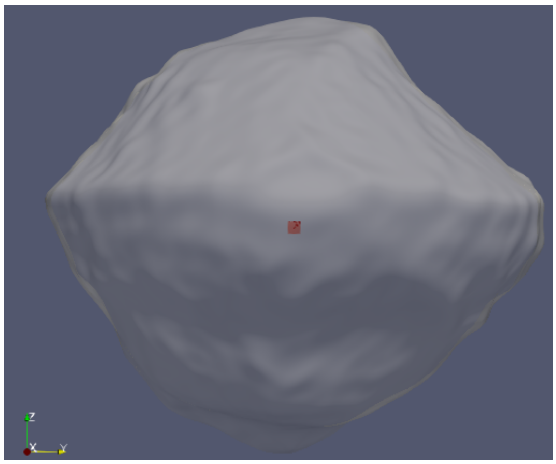

Figure D.2: Scenario SB-SP-1: The 20m patch used from the SAR synthesis and its location on 1999KW4 hemisphere

D.1.4 3D SAR synthesis area on a 10m volume

The radar simulation will be observed on a 3D 10-m patch centered on the target position. The patch characteristics are summed up in table D.3.

Table D.2: Scenario SB-SP-1: 2D SAR area characteristics

Center (x,y,z)	[0.592,0.000013,-0.000255]
Size (m^2)	10 × 10
Sampling (cm)	2 cm

Table D.3: scenario SB-SP-1: 3D SAR area characteristics

Center (x,y,z)	[0.592,0.000013,-0.000255]
Size (m^3)	10 × 10 × 10
Sampling (cm)	10 cm

D.1.5 Radar characteristics

The radar we will use for our simulations is the radar HFR (High Frequency Radar, described in Hérique et al. (2019)) developed for Ultra-Wideband study of small bodies. HFR characteristics must be chosen accordingly to our geometry of observation. Especially, the PRF and the number of frequency of the radar are chosen high enough to prevent any aliasing on our SAR surfaces. The radar characteristics are presented in table D.4.

Table D.4: Scenario SB-SP-1: Radar characteristics

Frequencies (MHz)	300-800 Hz
Number of frequencies	400
PRF(Hz)	1.0

D.1.6 Computation means and time

The computation of the spectrum was computed using a CPU implementation and the SAR synthesis was computed using a GPU implementation. The computation of the spectrum and the SAR synthesis with this scenario takes approximately 5 minutes.

D.2 Small Body Single Pass Observation SB-SP-2

Scenario SB-SP-2 consists in observing of a point target located at the surface of an asteroid, on the whole asteroid hemisphere. The target spectrum is computed with Surface Echo PO.

D.2.1 Single pass Orbitography

For the scenario of a single pass orbitography, the radar is fixed in the J2000 frame at the position [4.44019, -10.0, 5.77], when KW4 position is fixed at the center of the frame [0.0,0.0,0.0]. This allows having incidence angles of about 30°, which are optimal for along track resolution F. T. Ulaby and Dobson (1989). The trajectory in the J2000 frame and in the frame linked to 1999KW4 is presented in figure D.3.

All visualizations are made in the frame linked to KW4: the radar trajectory is thus only due to the rotation speed of the body, which is a little more than 2.2 hours.

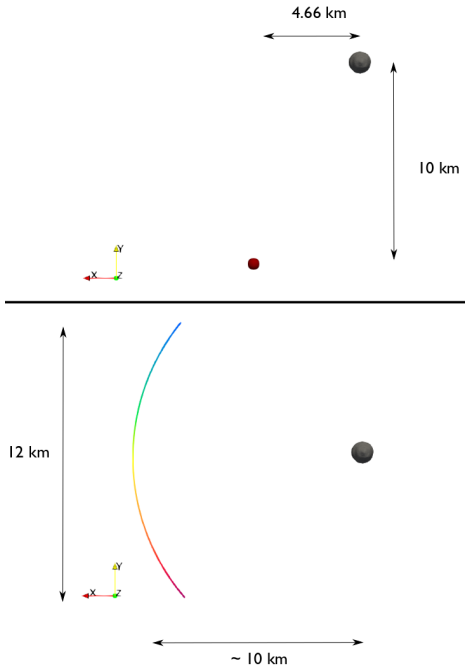

Figure D.3: Scenario SB-SP-2: Radar's trajectory in an inertial frame (top) and in the frame linked to 1999KW4 (bottom)

D.2.2 Target

The target is a point target, described by a triangular facet, located in the position [0° lat ,0° lon] on 1999 KW4. The target characteristics are summed up in table D.5.

Table D.5: Scenario SB-SP-2: target characteristics

Position (x,y,z)	[0.592,0.000013,-0.000255]
Size (cm)	0.375
Permittivity	3

D.2.3 SAR synthesis area

The radar simulation will be observed on an entire hemisphere of 1999KW4, which was downloaded from the JPL website. 1999KW4 DTM was originally with a sampling of approximately ten meters and was re-sampled to a DTM of about 0.5 meters. Our DTM is presented on figure D.4.

D.2.4 Radar characteristics

The radar we will use for our simulations is the radar HFR (High Frequency Radar, described in Hérique et al. (2019)) developed for Ultra-Wideband study of small bodies. HFR characteristics must be chosen accordingly to our geometry of observation. Especially, the PRF and the number of frequency of the radar are chosen high enough to prevent aliasing to occur on 1999KW4 half hemisphere.The radar characteristics are presented in table D.6.

D.2.5 Computation means and time

The computation of the spectrum was computed using a CPU implementation and the SAR synthesis was computed using a GPU implementation. The computation of the spectrum and the SAR synthesis

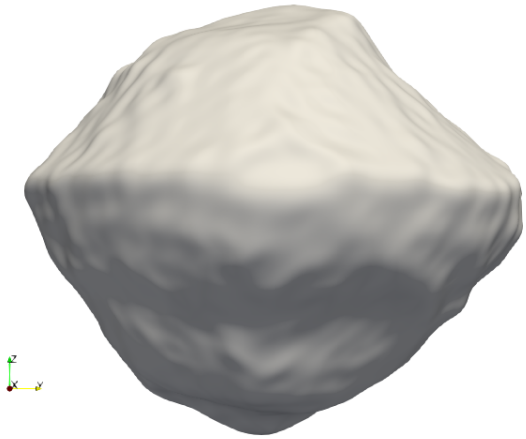

Figure D.4: Scenario SB-SP-2: SAR Surface on a whole 1999KW4 hemisphere

Table D.6: Radar characteristics for scenario SB-SP-2

Frequencies (MHz)	300-800 Hz
Number of frequencies	2200
PRF(Hz)	2.6

with this scenario takes approximately 2 hours.

D.3 Small Body Single Pass Observation SB-SP-3

Scenario EO-SB-3 consists in observing a random rough surface in a small body geometry, with roughness parameters corresponding to Itokawa's Lowlands, with a permittivity of 3.0. The target spectrum is computed with Surface Echo PO.

D.3.1 Single pass Orbitography

For the scenario of a single pass orbitography, the radar is fixed in the J2000 frame at the position [4.44019, -10.0, 5.77], when KW4 position is fixed at the center of the frame [0.0,0.0,0.0]. This allows having incidence angles of about 30°, which are optimal for along track resolution F. T. Ulaby and Dobson (1989). The trajectory in the J2000 frame and in the frame linked to 1999KW4 is presented in figure D.5.

All visualizations are made in the frame linked to KW4: the radar trajectory is thus only due to the rotation speed of the body, which is a little more than 2.2 hours.

D.3.2 Target

The target is a 20-m large rough surface, with roughness parameters taken from Itokawa's lowlands, as described in part 1. These parameters are recalled and summed up in table D.7 and presented in figure D.6

D.3.3 SAR synthesis area

The radar simulation will be observed on a 20-m patch extracted from the DTM of 1999KW4, which was downloaded from the JPL website, as represented in figure D.7. The patch characteristics are summed up in table D.8.

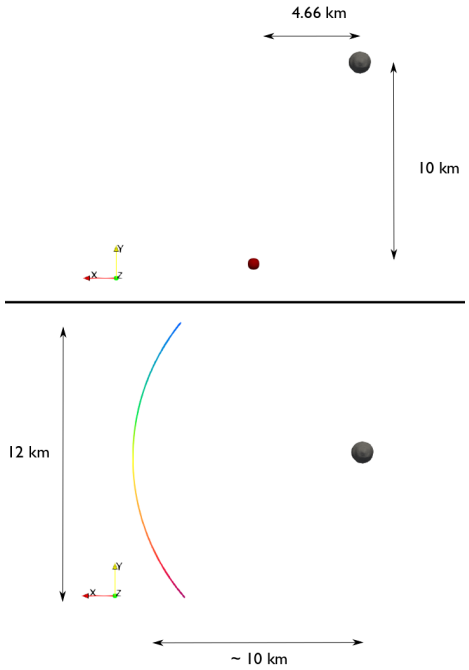

Figure D.5: Scenario SB-SP-3: Radar's trajectory in an inertial frame (top) and in the frame linked to 1999KW4 (bottom)

Table D.7: Scenario SB-SP-3: Rough surface roughness parameters

Center (x,y,z) (m)	[502.795,0.0013,-0.255]
RMS height	1.5 cm
Correlation Length	10 cm
DTM size	20m
Maximum Permittivity	3
Continuity assured by	Hanning Weighting

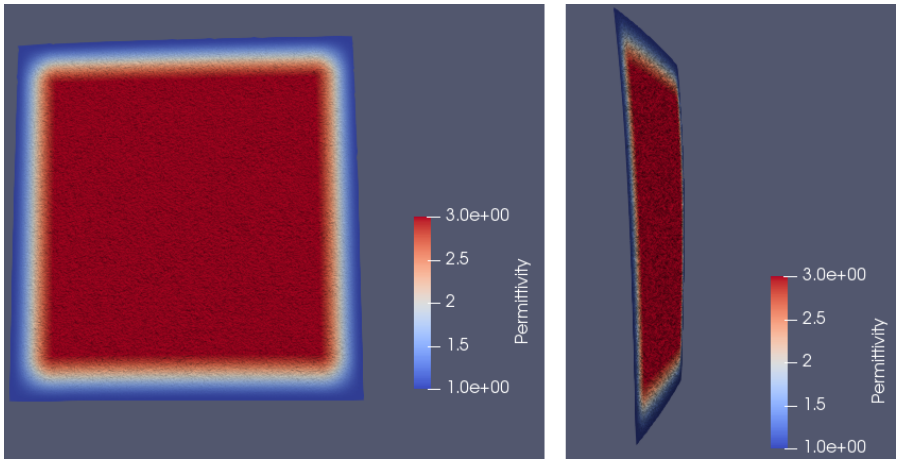

Figure D.6: Scenario SB-SP-3: Rough surface DTM

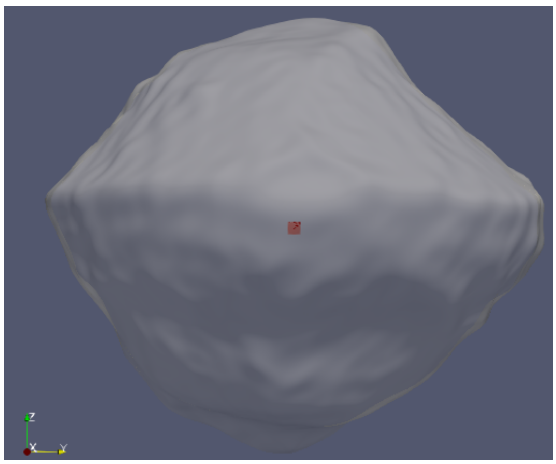

Figure D.7: Scenario SB-SP-3: The 20m patch used from the SAR synthesis and its location on 1999KW4 hemisphere

Table D.8: Scenario SB-SP-3: 2D SAR area characteristics

Center (x,y,z)	[0.592,0.000013,-0.000255]
Size (m^2)	20 × 10
Sampling (cm)	2 cm

D.3.4 Radar characteristics

The radar we will use for our simulations is the radar HFR (High Frequency Radar, described in Hérique et al. (2019))developed for Ultra-Wideband study of small bodies. HFR characteristics must be chosen accordingly to our geometry of observation. Especially, the PRF and the number of frequency of the radar are chosen high enough to prevent any aliasing on the size of the patch. The radar characteristics are presented in table D.9

Table D.9: Scenario SB-SP-3: Radar characteristics

Frequencies (MHz)	300-800 Hz
Number of frequencies	400
PRF(Hz)	1.0

D.3.5 Computation means and time

The computation of the spectrum was computed using a CPU implementation and the SAR synthesis was computed using a GPU implementation, and both were computed on the CIMENT grid of UGA to have faster computation times. The computation of the spectrum took about 1H30 hours, and the computation of the SAR synthesis with this scenario took approximately 2 hours.

D.4 Small Body Single Pass Observation SB-SP-4

Scenario EO-SB-4 consists in observing a random rough surface in a small body geometry, with roughness parameters corresponding to Itokawa's Highlands, with a permittivity of 3.0. The target spectrum is computed with Surface Echo PO.

D.4.1 Single pass Orbitography

For the scenario of a single pass orbitography, the radar is fixed in the J2000 frame at the position [4.44019, -10.0, 5.77], when KW4 position is fixed at the center of the frame [0.0,0.0,0.0]. This allows having incidence angles of about 30°, which are optimal for along track resolution F. T. Ulaby and Dobson (1989). The trajectory in the J2000 frame and in the frame linked to 1999KW4 is presented in figure D.8. All visualizations are made in the frame linked to KW4: the radar trajectory is thus only due to the rotation speed of the body, which is a little more than 2.2 hours.

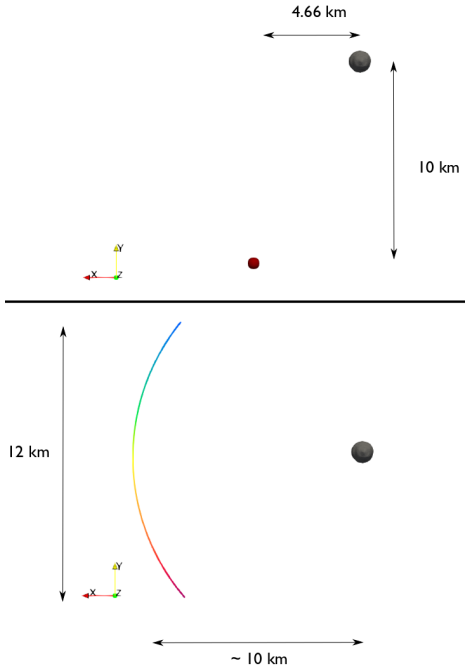

Figure D.8: Scenario SB-SP-4: Radar's trajectory in an inertial frame (top) and in the frame linked to 1999KW4 (bottom)

D.4.2 Target

The target is a 40-m large rough surface, with roughness parameters taken from Itokawa's Highlands, over which we added a smaller scale roughness, as described in part I. These parameters are summed up in table D.10 and D.11 a and presented in figure D.9.

Table D.10: Scenario SB-SP-4: Rough surface large-scale roughness parameters

RMS height	2.5 m
Correlation Length	6 m
DTM size	20m
Maximum Permittivity	3
Continuity assured by	Hanning Weighting

D.4.3 SAR synthesis area

The radar simulation will be observed on a 40-m patch extracted from the DTM of 1999KW4, which was downloaded from the JPL website, as represented in figure D.10. The patch characteristics are summed up in table D.12.

Table D.11: Scenario SB-SP-4: Rough surface smll-scale roughness parameters

Center (x,y,z) (m)	[502.795,0.0013,-0.255]
RMS height	15 cm
Correlation Length	1 m
DTM size	20m
Maximum Permittivity	3
Continuity assured by	Hanning Weighting

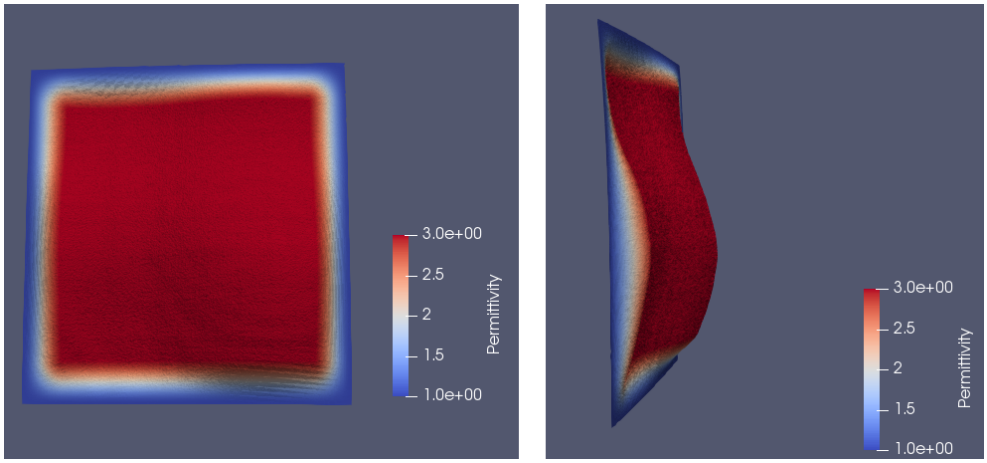

Figure D.9: Scenario SB-SP-4: Rough surface DTM

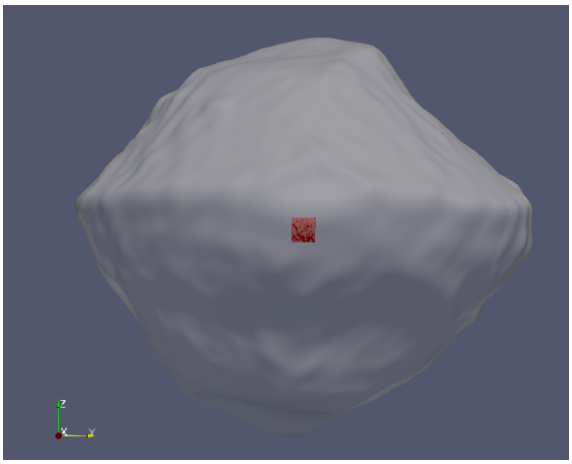

Figure D.10: Scenario SB-SP-4: The 40m patch used from the SAR synthesis and its location on 1999KW4 hemisphere

Table D.12: Scenario SB-SP-4: 2D SAR area characteristics

Center (x,y,z) (m)	[502.795,0.0013,-0.255]
Size (m^2)	40 × 40
Sampling (cm)	2 cm

D.4.4 Radar characteristics

The radar we will use for our simulations is the radar HFR (High Frequency Radar, described in Hérique et al. (2019)) developed for Ultra-Wideband study of small bodies. HFR characteristics must be chosen accordingly to our geometry of observation. Especially, the PRF and the number of frequency of the radar are chosen high enough to prevent any aliasing on our SAR surfaces. The radar characteristics are presented in table D.13.

Table D.13: Scenario SB-SP-4: Radar characteristics

Frequencies (MHz)	300-800 Hz
Number of frequencies	400
PRF(Hz)	1.0

D.4.5 Computation means and time

The computation of the spectrum was computed using a CPU implementation and the SAR synthesis was computed using a GPU implementation, and both were computed on the CIMENT grid of UGA to have faster computation times. The computation of the spectrum took about 1h30 hours, and the computation of the SAR synthesis with this scenario took approximately 2 hours.

D.5 Small Body Single Pass Observation SB-SP-5

Scenario EO-SB-5 consists in observing a random rough surface in a small body geometry, consisting of a rough part at its border and a smoother part at its center with a permittivity of 3.0. The target spectrum is computed with Surface Echo PO.

D.5.1 Orbitography

For the scenario of a single pass orbitography, the radar is fixed in the J2000 frame at the position [4.44019, -10.0, 5.77], when KW4 position is fixed at the center of the frame [0.0,0.0,0.0]. This allows having incidence angles of about 30°, which are optimal for along track resolution F. T. Ulaby and Dobson (1989). The trajectory in the J2000 frame and in the frame linked to 1999KW4 is presented in figure D.11. All visualizations are made in the frame linked to KW4: the radar trajectory is thus only due to the rotation speed of the body, which is a little more than 2.2 hours.

D.5.2 Target

The target is a 20-m large rough surface, with centered smooth area, and an external rougher area, as described in part I. The rough surface is generated with the roughness parameters described in D.14, which are reduced by 75% in the center of the patch. The corresponding patch is presented in figure D.12.

Table D.14: Scenario SB-SP-5: surface roughness parameters

Center (x,y,z) (m)	[502.795,0.0013,-0.255]
RMS height	15 cm
Correlation Length	10 cm
DTM size	20m
Maximum Permittivity	3
Continuity assured by	Hanning Weighting

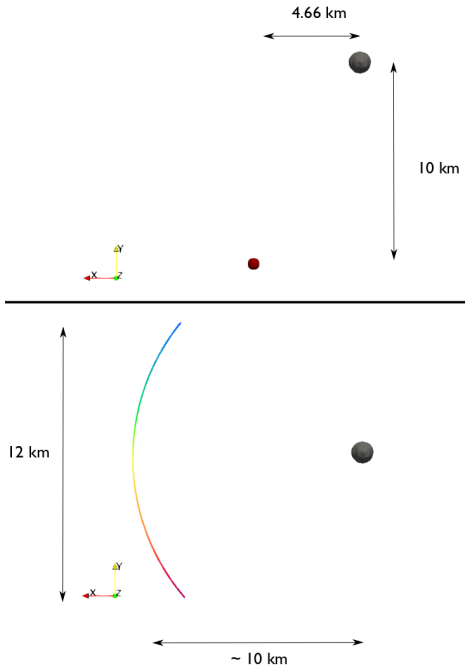

Figure D.11: Scenario SB-SP-5: Radar's trajectory in an inertial frame (top) and in the frame linked to 1999KW4 (bottom)

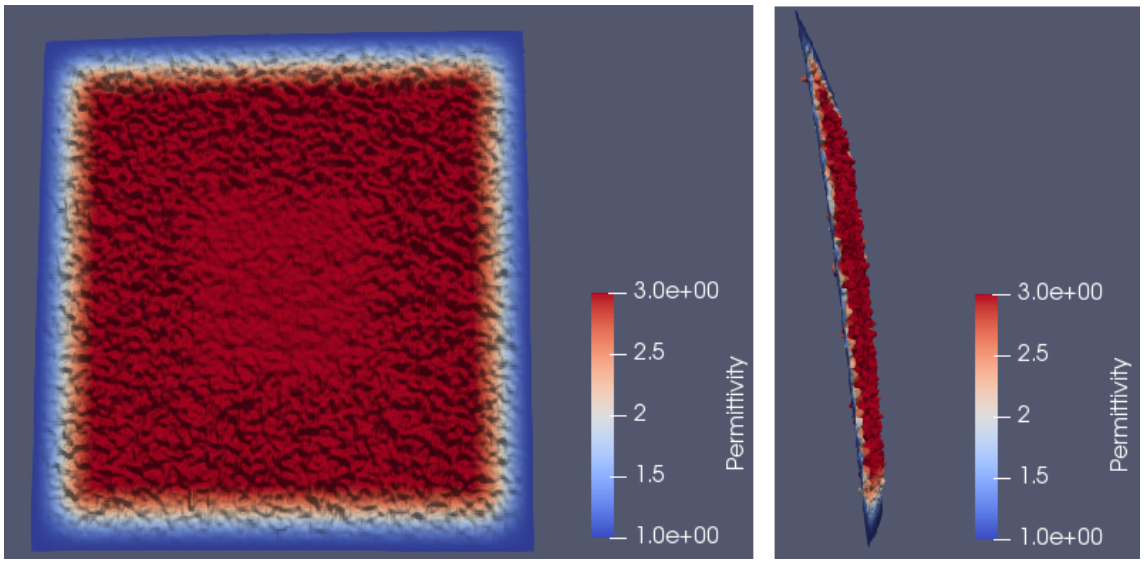

Figure D.12: Scenario SB-SP-5: Rough surface DTM

D.5.3 SAR synthesis area

The radar simulation will be observed on a 20-m patch extracted from the DTM of 1999KW4, which was downloaded from the JPL website, as represented in figure D.13. The patch characteristics are summed up in table D.15.

D.5.4 Radar characteristics

The radar we will use for our simulations is the radar HFR (High Frequency Radar, described in Hérique et al. (2019)) developed for Ultra-Wideband study of small bodies. HFR characteristics must be chosen accordingly to our geometry of observation. Especially, the PRF and the number of frequency of the radar are chosen high enough to prevent any aliasing on our SAR surfaces. The radar

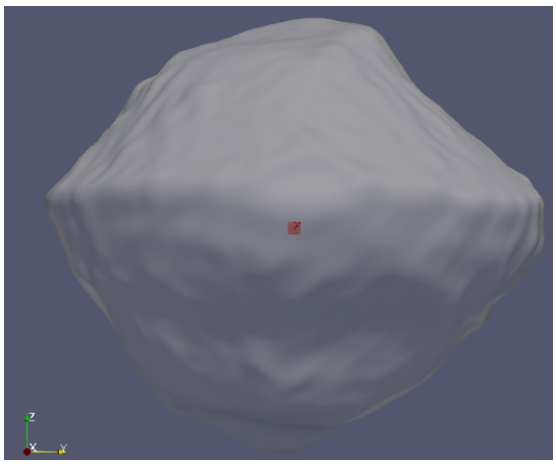

Figure D.13: Scenario SB-SP-5: The 20m patch used from the SAR synthesis and its location on 1999KW4 hemisphere

Table D.15: Scenario SB-SP-5: 2D SAR area characteristics

Center (x,y,z)	[0.592,0.000013,-0.000255]
Size (m^2)	20 × 10
Sampling (cm)	2 cm

characteristics are presented in table D.16.

Table D.16: Scenario SB-SP-5: Radar characteristics

Frequencies (MHz)	300-800 Hz
Number of frequencies	400
PRF(Hz)	1.0

D.5.5 Computation means and time

The computation of the spectrum was computed using a CPU implementation and the SAR synthesis was computed using a GPU implementation, and both were computed on the CIMENT grid of UGA to have faster computation times. The computation of the spectrum took about 1h30 hours, and the computation of the SAR synthesis with this scenario took approximately 2 hours.

D.6 Small Body Single Pass observation SB-SP-6

Scenario EO-SB-6 consists of the observation in the small body geometry of a punctual target with a permittivity of 1.1 in the void. The target spectrum is computed with the Born approximation.

D.6.1 Orbitography

For the scenario of a single pass orbitography, the radar is fixed in the J2000 frame at the position [4.44019, -10.0, 5.77], when KW4 position is fixed at the center of the frame [0.0,0.0,0.0]. This allows having incidence angles of about 30°, which are optimal for along track resolution F. T. Ulaby and Dobson (1989). The trajectory in the J2000 frame and in the frame linked to 1999KW4 is presented

in figure D.14. All visualizations are made in the frame linked to KW4: the radar trajectory is thus only due to the rotation speed of the body, which is a little more than 2.2 hours.

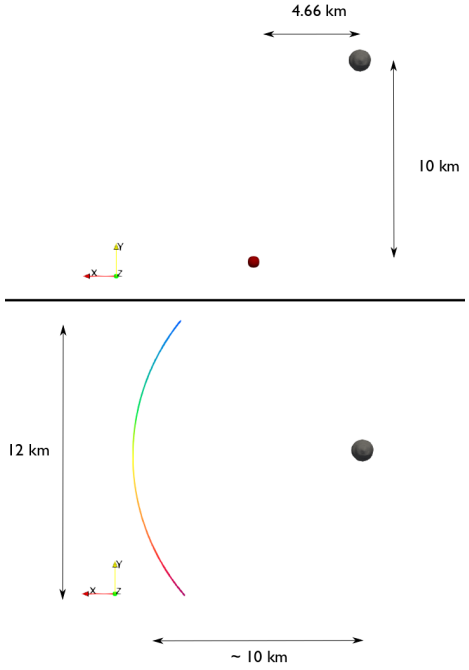

Figure D.14: Scenario SB-SP-6: Radar's trajectory in an inertial frame (top) and in the frame linked to 1999KW4 (bottom)

D.6.2 Target

This scenario will consider an inclusion is embedded at 25 cm under the interface and has a permittivity ϵ_f = 1.1, as presented in figure D.15. The scenario characteristics are summarized in table D.17.

Table D.17: Scenario SB-SP-6: Interface and background volume characteristics

	Interface	Background volume
Center (x,y,z) (m)	[390,0.0,0.0]	[389.75,0.0,0.0]
Size (m^2)	0.5 × 0.5	0.5 × 0.5 × 0.5
Sampling (cm)	2.5	0.5
Permittivity ϵ_a	1.0	1.0

D.6.3 2D SAR Synthesis area

The 2D SAR Synthesis will be carried out on a two-dimensional surface crossing the position of the inclusion to image the synthesis in the range-Doppler plane, such as depicted in figure D.16, and has the characteristics depicted in table D.18.

D.6.4 3D SAR Synthesis area

The 3D SAR Synthesis will be carried out on a three-dimensional volume to image the synthesis in the elevation plane, and observe the left-right ambiguity. The surface characteristics are depicted in table D.19

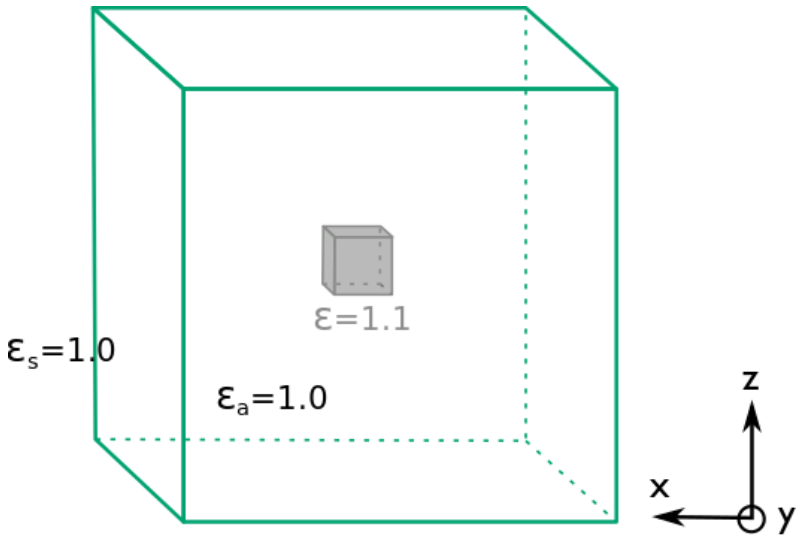

Figure D.15: Scenario SB-SP-6: Scenario of a point target in the void in the Small Body geometry

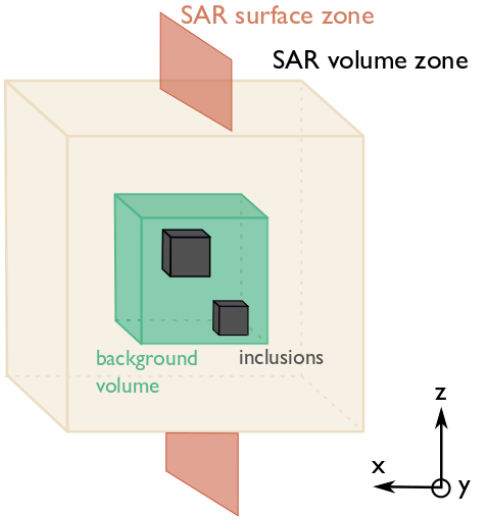

Figure D.16: Scenario SB-SP-6: SAR synthesis geometry

Table D.18: Scenario SB-SP-6: SAR surface characteristics

Center (x,y,z) (m)	[389.75,0.0,0.0]
Size (m^2)	5 × 5
Sampling (m)	0.2
Permittivity ϵ_a	1.0

Table D.19: Scenario SB-SP-6: Volume characteristics

Center (x,y,z) (m)	[0.38975,0.0,0.0]
Size (m^3)	5 × 5 × 5
Sampling (m)	0.5

D.6.5 Radar characteristics

The radar we will use for our simulations is the radar HFR (High Frequency Radar, described in Hérique et al. (2019)) developed for Ultra-Wideband study of small bodies. HFR characteristics must be chosen accordingly to our geometry of observation. Especially, the PRF and the number of frequency of the radar are chosen high enough to prevent any aliasing on our SAR surfaces. The radar characteristics are presented in table D.20

Table D.20: Scenario SB-SP-6: Radar characteristics

Frequencies (MHz)	300-800 Hz
Number of frequencies	19
PRF(Hz)	0.0265

The computation of the SAR synthesis was computed using a GPU implementation. The computation of the spectrum took about 5 minutes, and the computation of the SAR synthesis with this scenario took approximately 5 minutes.

D.7 Small Body Single Pass observation SB-SP-7

Scenario SB-SP-7 consists in observing a point target with a permittivity of 3.1, at 25 cm under the surface in a medium of a permittivity of 3.0 in a small body geometry. The target spectrum is computed with the Born approximation.

D.7.1 Orbitography

For the scenario of a single pass orbitography, the radar is fixed in the J2000 frame at the position [4.44019, -10.0, 5.77], when KW4 position is fixed at the center of the frame [0.0,0.0,0.0]. This allows having incidence angles of about 30°, which are optimal for along track resolution F. T. Ulaby and Dobson (1989). The trajectory in the J2000 frame and in the frame linked to 1999KW4 is presented in figure D.17. All visualizations are made in the frame linked to KW4: the radar trajectory is thus only due to the rotation speed of the body, which is a little more than 2.2 hours.

D.7.2 Target

This scenario will consider an inclusion is embedded at 25 cm under the interface and has a permittivity ϵ_f = 1.1, as presented in figure D.18. The scenario characteristics are summarized in table D.21.

Table D.21: Scenario SB-SP-7: Interface and background volume characteristics

	Interface	Background volume
Center (x,y,z) (m)	[390,0.0,0.0]	[389.75,0.0,0.0.0]
Size (m^2)	0.5 × 0.5	0.5 × 0.5 × 0.5
Sampling (cm)	2.5	0.5
Permittivity ϵ_a	3.0	3.0

D.7.3 2D SAR Synthesis area

The 2D SAR Synthesis will be carried out on a two-dimensional surface crossing the position of the inclusion to image the synthesis in the range-Doppler plane, such as depicted in figure D.19, and has the characteristics depicted in table D.22.

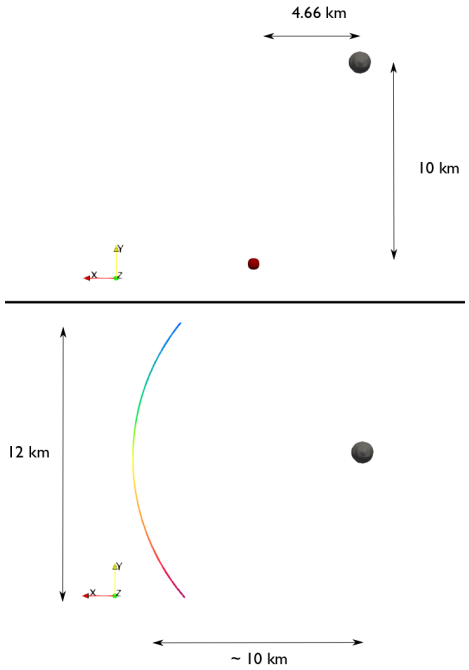

Figure D.17: Scenario SB-SP-7: Radar's trajectory in an inertial frame (top) and in the frame linked to 1999KW4 (bottom)

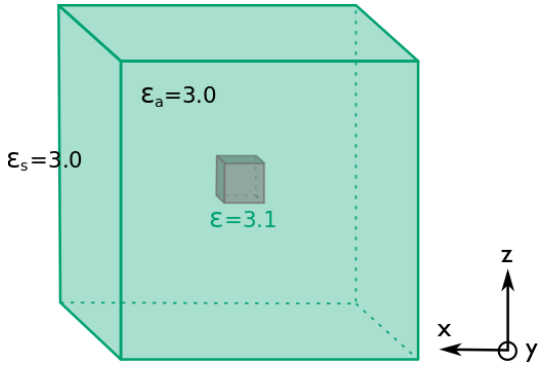

Figure D.18: Scenario SB-SP-7: Scenario of a point target in a medium of permittivity 3.0

Table D.22: Interface characteristics for scenario SB-SP-7

Center (x,y,z) (m)	[389.75,0.0,0.0]
Size (m^2)	5×5
Sampling (m)	0.2

D.7.4 3D SAR Synthesis area

The 3D SAR Synthesis will be carried out on a three-dimensional volume to image the synthesis in the elevation plane, and observe the left-right ambiguity. The surface characteristics are depicted in table D.23.

D.7.5 Radar characteristics

The radar we will use for our simulations is the radar HFR (High Frequency Radar, described in Hérique et al. (2019)) developed for Ultra-Wideband study of small bodies. HFR characteristics

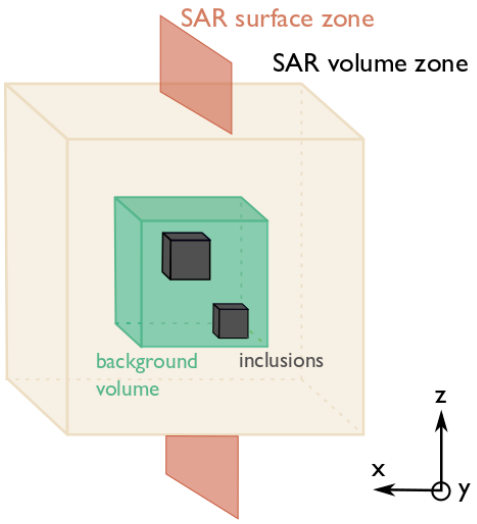

Figure D.19: Scenario SB-SP-7: SAR synthesis geometry

Table D.23: Scenario SB-SP-7: Volume characteristics

Center (x,y,z) (m)	[0.38975,0.0,0.0]
Size (m^3)	$5 \times 5 \times 5$
Sampling (m)	0.5

must be chosen accordingly to our geometry of observation. Especially, the PRF and the number of frequency of the radar are chosen high enough to prevent any aliasing on our SAR surfaces. The radar characteristics are presented in table D.24.

Table D.24: Scenario SB-SP-7: Radar characteristics

Frequencies (MHz)	300-800 Hz
Number of frequencies	19
PRF(Hz)	0.0265

D.7.6 Computation means and time

The computation of the SAR synthesis was computed using a GPU implementation. The computation of the spectrum took about 5 minutes, and the computation of the SAR synthesis with this scenario took approximately 5 minutes.

D.8 Earth Observation Single Pass observation SB-SP-8

Scenario SB-SP-8 consists in observing with 20 random rough surface, whose spectra are simulated with SEPO, in order to average resulting SAR synthesis parameters.

D.8.1 Orbitography

For the scenario of a single pass orbitography, the radar is fixed in the J2000 frame at the position [4.44019, -10.0, 5.77], when KW4 position is fixed at the center of the frame [0.0,0.0,0.0]. This allows having incidence angles of about 30°, which are optimal for along track resolution F. T. Ulaby and

Dobson (1989). The trajectory in the J2000 frame and in the frame linked to 1999KW4 is presented in figure D.20. All visualizations are made in the frame linked to KW4: the radar trajectory is thus only due to the rotation speed of the body, which is a little more than 2.2 hours.

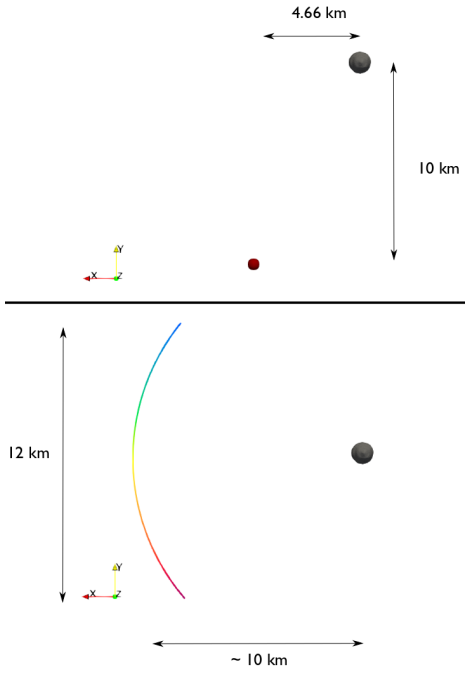

Figure D.20: Scenario SB-SP-8: Radar's trajectory in an inertial frame (top) and in the frame linked to 1999KW4 (bottom)

D.8.2 Target

This scenario will consider 20 rough surfaces, obtained with the parameters described in table D.25.

Table D.25: Scenario SB-SP-8: Rough surface roughness parameters

Center (x,y,z) (m)	[0.592,0.000013,-0.000255]
RMS height	25 cm
Correlation Length	70 cm
DTM size	15m
Maximum Permittivity	3
Continuity assured by	Hanning Weighting

D.8.3 2D SAR Synthesis area

The 2D SAR Synthesis will be carried out on a two-dimensional plane covering the extent of the surface whose permittivity if equal to 3, as depicted in figure C.5. The characteristics of the 2D SAR Synthesis area is depicted in table C.14.

D.8.4 Radar characteristics

The radar we will use for our simulations is the radar HFR (High Frequency Radar, described in Hérique et al. (2019)) developed for Ultra-Wideband study of small bodies. HFR characteristics must be chosen accordingly to our geometry of observation. Especially, the PRF and the number of

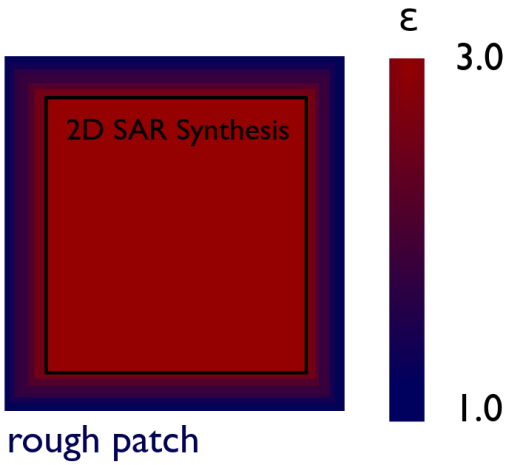

Figure D.21: Scenario SB-SP-8: SAR Synthesis geometry.

frequency of the radar are chosen high enough to prevent any aliasing on our SAR surfaces. The radar characteristics are presented in table D.26.

Table D.26: Scenario SB-SP-8: Radar characteristics

Frequencies (MHz)	300-800 Hz
Number of frequencies	19
PRF(Hz)	0.0265

D.8.5 Computation means and time

The simulation of the spectrum is obtained with a CPU implementation SAR synthesis was computed using a GPU implementation.
The computation of the spectrum and the SAR synthesis with this scenario for one rough surface takes approximately 20 minutes.

D.9 Small Body Single Pass Observation SB-SP-9

Scenario EO-SB-9 consists in observing a 3m large facet in the small body geometry with HFR.

D.9.1 Single pass Orbitography

For the scenario of a single pass orbitography, the radar is fixed in the J2000 frame at the position [4.44019, -10.0, 5.77], when KW4 position is fixed at the center of the frame [0.0,0.0,0.0]. This allows having incidence angles of about 30°, which are optimal for along track resolution F. T. Ulaby and Dobson (1989). The trajectory in the J2000 frame and in the frame linked to 1999KW4 is presented in figure D.22. All visualizations are made in the frame linked to KW4: the radar trajectory is thus only due to the rotation speed of the body, which is a little more than 2.2 hours.

D.9.2 Target

The target is a 3m-large triangular facet, with a permittivity of 3.0. The facet are summed up in table D.27

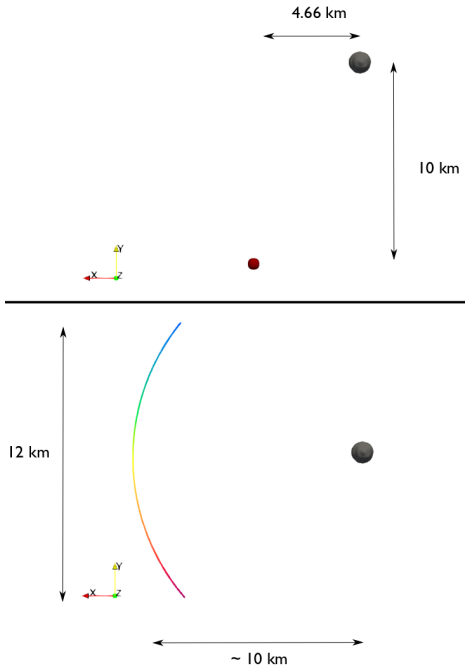

Figure D.22: Scenario SB-SP-9: Radar's trajectory in an inertial frame (top) and in the frame linked to 1999KW4 (bottom)

Table D.27: Scenario SB-SP-9: Point target characteristics in the Earth Observation geometry

Position (x,y,z) (m)	[0.592,0.000013,-0.000255]
Size (m)	3
Permittivity	3
Normal	[5.8957,-0.088993,-2.16325]

D.9.3 SAR synthesis area

The radar simulation will be observed on a 10-m spherical surface, with the characteristics described in table D.28.

Table D.28: Scenario SB-SP-9: 2D SAR area characteristics

Center (x,y,z) (m)	[502.795,0.0013,-0.255]
Size (m^2)	10 × 10
Sampling (cm)	4 cm

D.9.4 Radar characteristics

The radar we will use for our simulations is the radar HFR (High Frequency Radar, described in Hérique et al. (2019)) developed for Ultra-Wideband study of small bodies. HFR characteristics must be chosen accordingly to our geometry of observation. Especially, the PRF and the number of frequency of the radar are chosen high enough to prevent any aliasing on our SAR surfaces. The radar characteristics are presented in table D.29.

Table D.29: Scenario SB-SP-9: Radar characteristics

Frequencies (MHz)	300-800 Hz
Number of frequencies	400
PRF(Hz)	1.0

D.9.5 Computation means and time

The computation of the spectrum was computed using a CPU implementation and the SAR synthesis was computed using a GPU implementation. The computation time of the scenario takes about 1 minute.

D.10 Small Body Single Pass Observation SB-MP-1

Scenario SB-MP-1 consists in observing the response of a point target located at the surface of an asteroid, on the whole asteroid hemisphere with a multipass orbitography. The target spectrum is computed with Surface Echo PO.

D.10.1 Orbitography

To improve the performances, several orbits separated in the elevation direction are used. The incident angle can vary from 30° to 60° for an optimal along-track resolution F. T. Ulaby and Dobson (1989). We used 20 tracks *HFRAIM-HFR-TN-001 HFR Specifications - Task1(D4) 2015-06-26 V1-0.docx* (n.d.) D.23 for optimal performances, separated in the elevation direction by 100 meters each. The radar behavior will be simulated on each trajectory and the results of each trajectory will be summed.

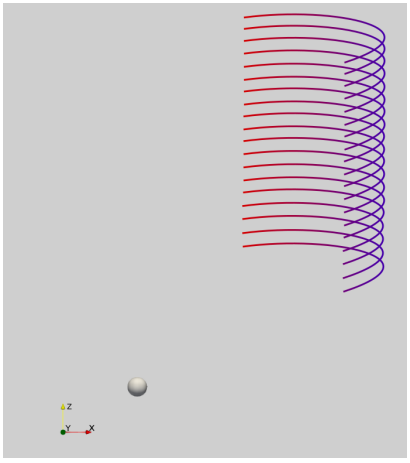

Figure D.23: Scenario SB-MP-1: Multipass orbitography in a frame linked on KW4. View from side. The colors indicate the beginning of the trajectory (red) and the end (blue)

D.10.2 Target

The target is a 20-m large rough surface, with centered smooth area, and an external rougher area, as described in part I. The rough surface is generated with the roughness parameters described in D.30, which are reduced by 75% in the center of the patch. The corresponding patch is presented in figure D.24.

Table D.30: Scenario SB-MP-1: surface roughness parameters

Center (x,y,z) (m)	[502.795,0.0013,-0.255]
RMS height	15 cm
Correlation Length	10 cm
DTM size	20m
Maximum Permittivity	3
Continuity assured by	Hanning Weighting

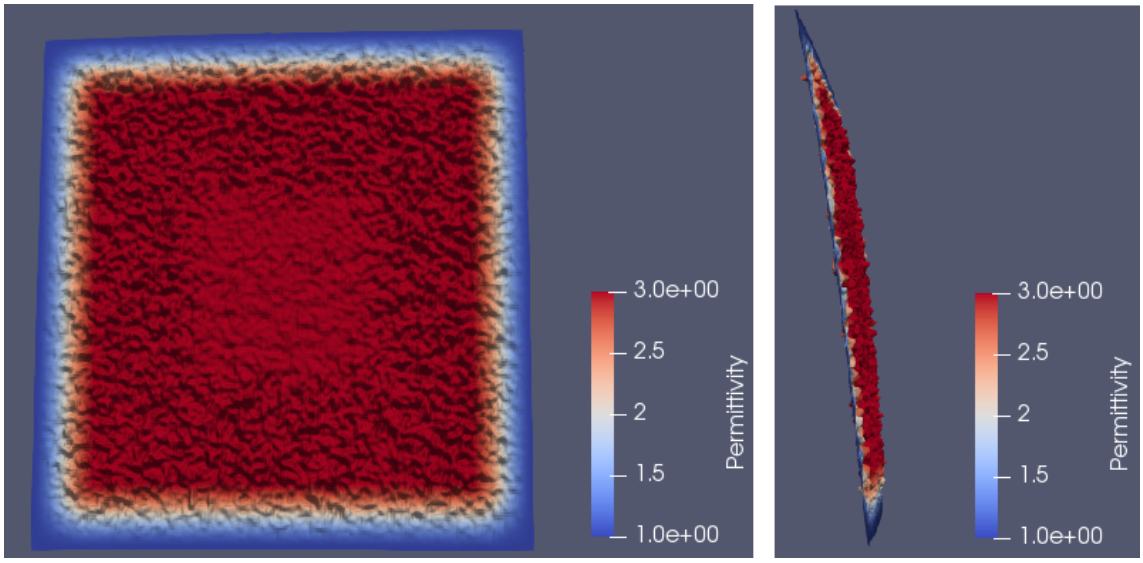

Figure D.24: Scenario SB-MP-1: Rough surface DTM

D.10.3 SAR synthesis area

The radar simulation will be observed on an entire hemisphere of 1999KW4, which was downloaded from the JPL website. 1999KW4 DTM was originally with a sampling of approximately ten meters and was resampled to a DTM of about 0.5 meters. Our DTM is presented on figure D.25.

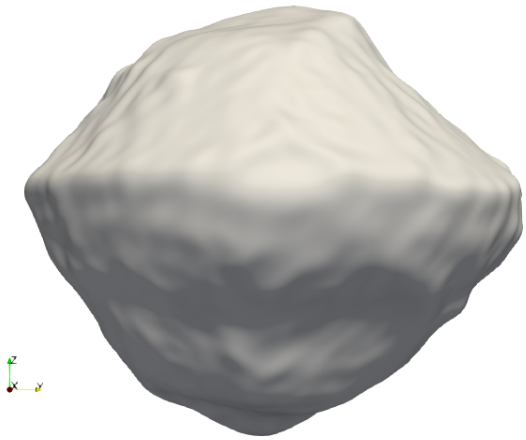

Figure D.25: Scenario SB-MP-1: SAR Surface on a whole 1999KW4 hemisphere

D.10.4 Radar characteristics

The radar we will use for our simulations is the radar HFR (High Frequency Radar, described in Hérique et al. (2019)) developed for Ultra-Wideband study of small bodies. HFR characteristics must be chosen accordingly to our geometry of observation. Especially, the PRF and the number of frequency of the radar are chosen high enough to prevent any aliasing on our SAR surfaces. The radar characteristics are presented in table D.31.

Table D.31: Scenario SB-MP-1: Radar characteristics

Frequencies (MHz)	300-800 Hz
Number of frequencies	400
PRF(Hz)	1.0

D.10.5 Computation means and time

The computation of the spectrum was computed using a CPU implementation and the SAR synthesis was computed using a GPU implementation, and both were computed on the CIMENT grid of UGA to have faster computation times. The computation of the spectrum took about 6 hours, and the computation of the SAR synthesis with this scenario took approximately 2 hours.

D.11 Small Body Multipass observation SB-MP-2

Scenario SB-MP-2 consists in observing a point target with a permittivity of 3.1 at 25 cm under the surface in a medium of a permittivity of 3.0 with a multipass, small body geometry. The target spectrum is computed with the Born approximation.

D.11.1 Orbitography

For the orbitography of the small body observation, the radar is fixed in the J2000 inertial frame at a fixed position when the targeted asteroid position is fixed at the center of the frame [0.0,0.0,0.0].

All visualizations are made in the frame linked to our asteroid. The radar trajectory is thus only due to the rotation speed of the body, which is a little more than 2.2 hours. The tomography orbitography is more limited in the small body orbitography because the incident angles can easily achieve limit values. The performances on the tomography will then be determined by the possible orbitography.

The tomography approach will be using 20 trajectories parallel to each other with a position varying in the z direction, such as depicted in figure D.26, with incident angles varying from 30° to 60°. Each of these trajectories is separated by 500 m in the $\vec{z}$ direction.

Such a scenario will bring an elevation ambiguity, with Δs the separation of the trajectories in elevation :

$$h = \frac{\lambda r_0}{2 \cdot \Delta s} = 7.1km \tag{D.1}$$

D.11.2 Target

This scenario will consider an inclusion is embedded at 25 cm under the interface and has a permittivity $\epsilon_f = 3.1$, as presented in figure D.27. The scenario characteristics are summarized in table D.32.

D.11.3 2D SAR synthesis

The SAR synthesis will be computed on the surface, on the interface between the void and our volume; as presented on figure D.28. 20 syntheses, for each trajectory, were computed on these surfaces and

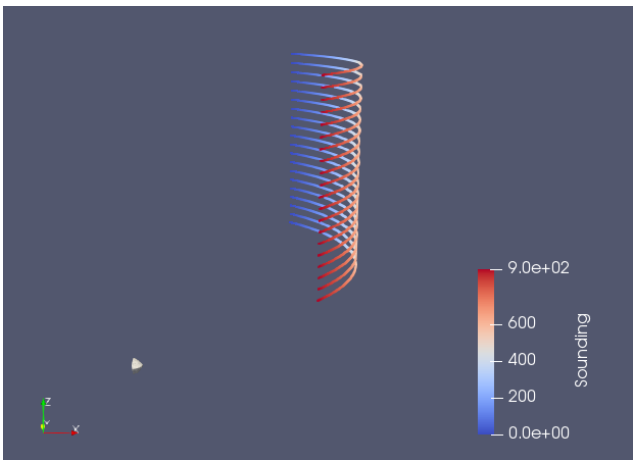

Figure D.26: Scenario SB-MP-2: The 20 trajectories used from the multipass orbitography in the small body geometry and the targeted body, 1999KW4

Table D.32: Scenario SB-MP-2: Interface and background volume characteristics

	Interface	Background volume
Center (x,y,z) (m)	[390,0.0,0.0]	[389.75,0.0,0.0.0]
Size (m^2)	0.5 × 0.5	0.5 × 0.5 × 0.5
Sampling (cm)	2.5	0.5
Permittivity ϵ_a	3.0	3.0

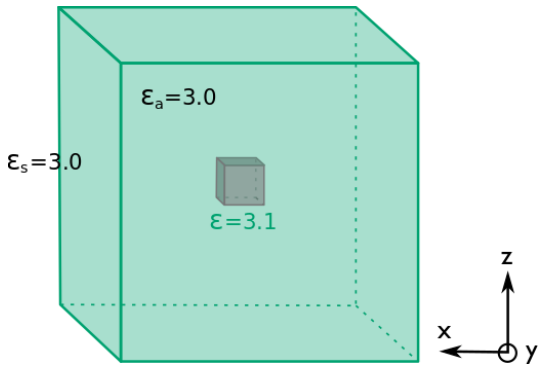

Figure D.27: Scenario SB-MP2-2: Scenario of a point target in a medium of permittivity 3.0

will constitute the stack of SAR images used for the tomography. The characteristics of the SAR synthesis areas are summarized in table D.33.

Table D.33: Scenario SB-MP-2: 2D SAR synthesis characteristics

Center (x,y,z) (m)	[390.0, 0.0, -8.0]
, Size (m^2)	2 × 2
Sampling (cm)	2 cm

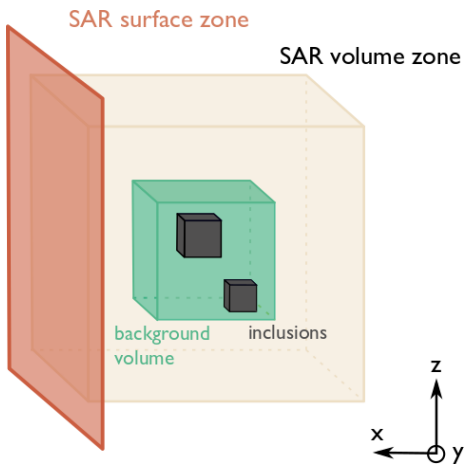

Figure D.28: Scenario SB-MP-2: SAR Synthesis areas

D.11.4 Compressive sensing volume visualization of results

The tomography results will be shown in 3D volume. The elevation profile is computed along the $\vec{s}$ direction, the direction normal to the radar direction and to the range direction, along 6 meters. As the profile of each scatterer is retrieved along the elevation direction, this makes the tomography results represented in a tilted way, such as in figure D.29.

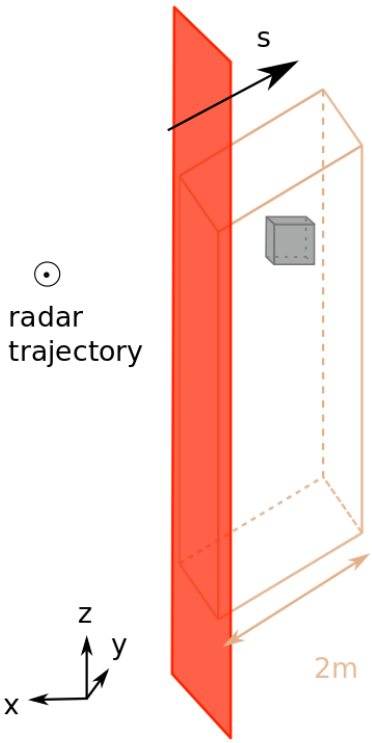

Figure D.29: Scenario SB-MP-2: Visualization of the results of the compressive sensing in the Small Body geometry

D.11.5 Radar characteristics

The radar we will use for our simulations is the radar HFR (High Frequency Radar, described in Hérique et al. (2019)) developed for Ultra-Wideband study of small bodies. HFR characteristics

must be chosen accordingly to our geometry of observation. Especially, the PRF and the number of frequency of the radar are chosen high enough to prevent any aliasing on our SAR surfaces. The radar characteristics are presented in table D.34

Table D.34: Radar characteristics for scenario SB-MP-2

Frequencies (MHz)	300-800 Hz
Number of frequencies	2200
PRF(Hz)	2.6

D.11.6 Computation means and time

The computation of the spectrum was computed using a CPU implementation and the SAR synthesis was computed using a GPU implementation, and both were computed on the CIMENT grid of UGA to have faster computation times. The computation of the spectrum took about 30 minutes, and the computation of the SAR synthesis with this scenario took approximately 5 minutes.

Appendix E

Earth Observation histograms of intensity

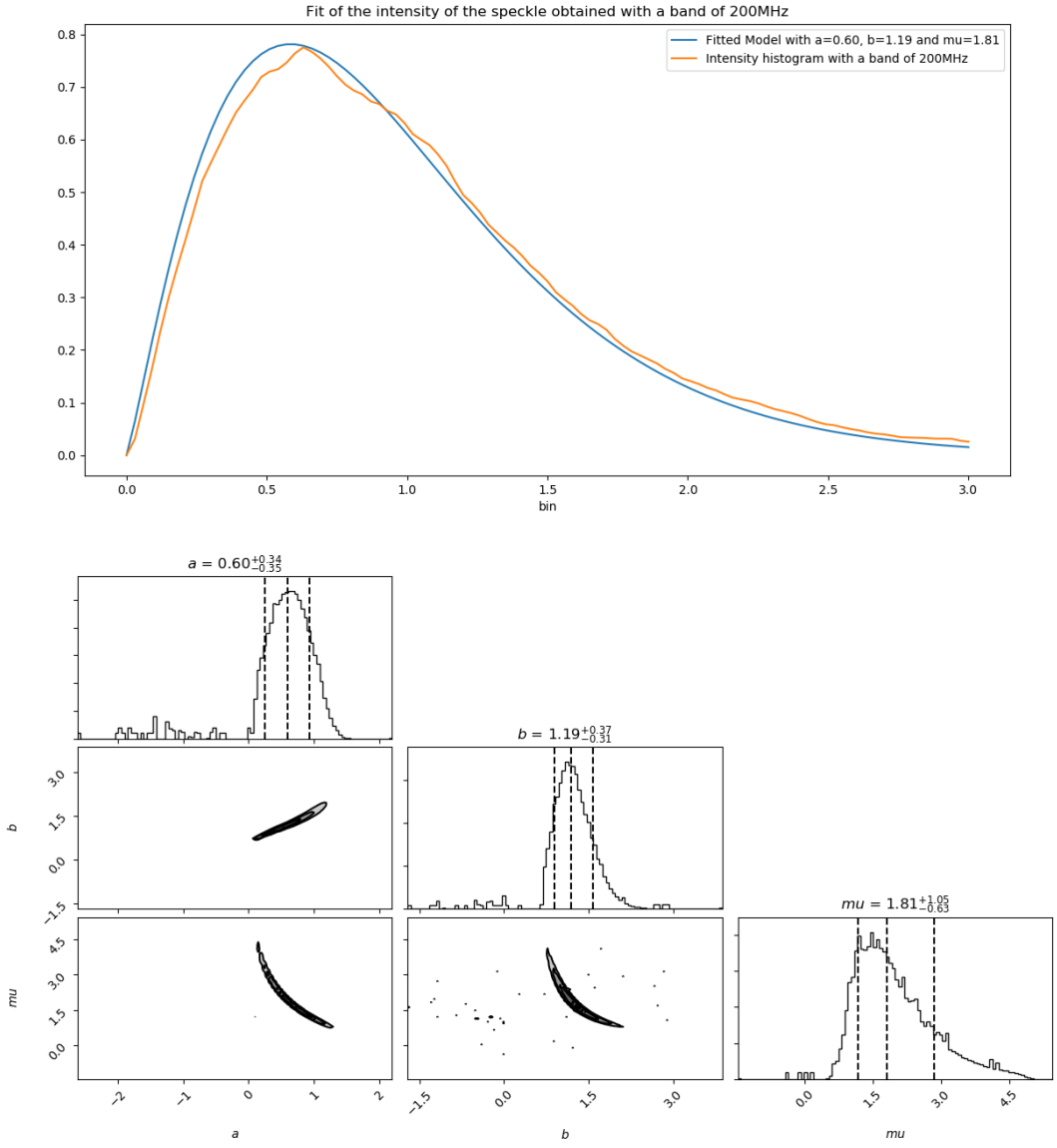

Figure E.1: Results of the fit with MCMC (top) of a speckle obtained with a band of 200MHz, Histogram of the final value of the walkers

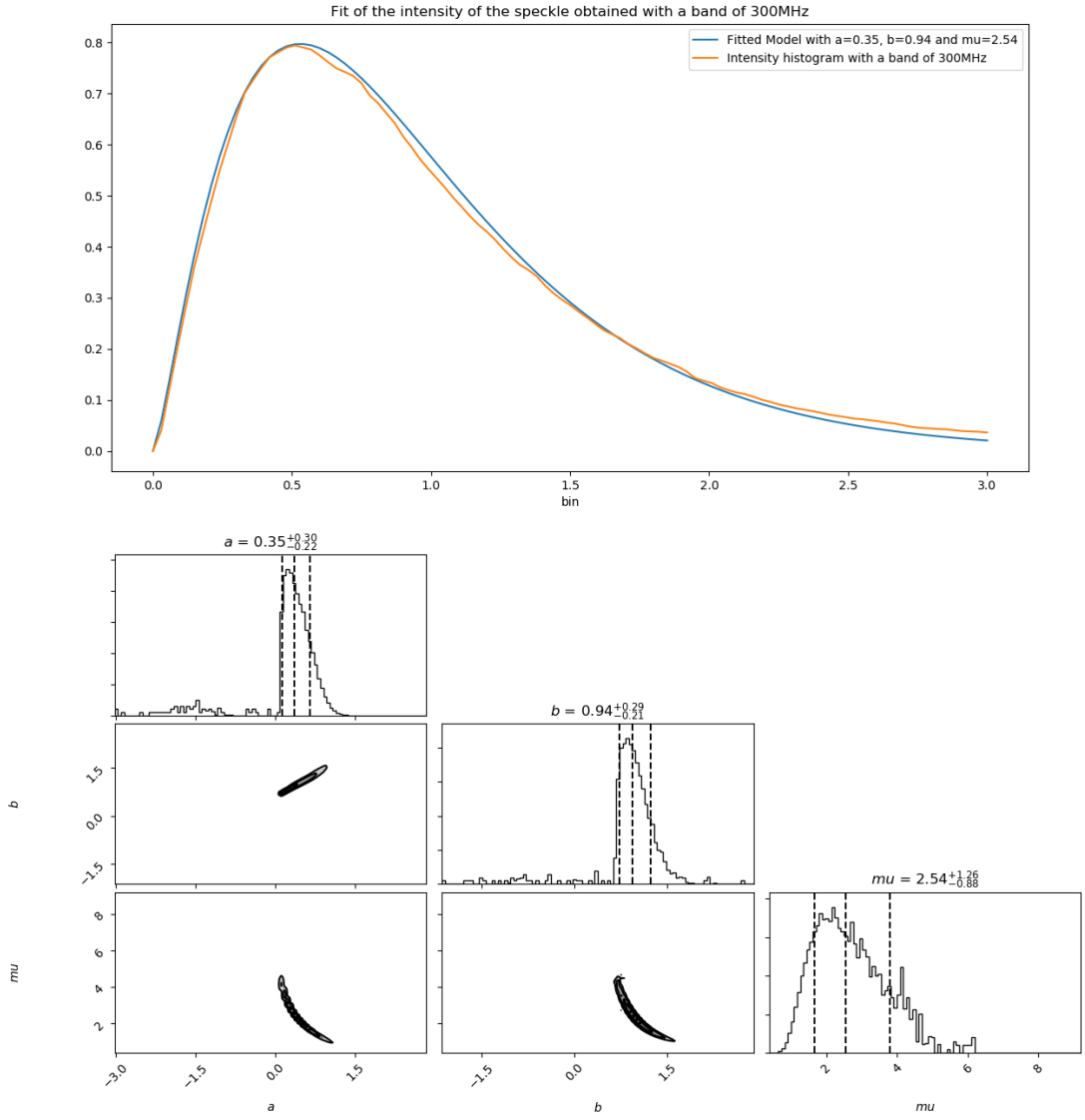

Figure E.2: Results of the fit with MCMC (top) of a speckle obtained with a band of 300MHz, Histogram of the final value of the walkers

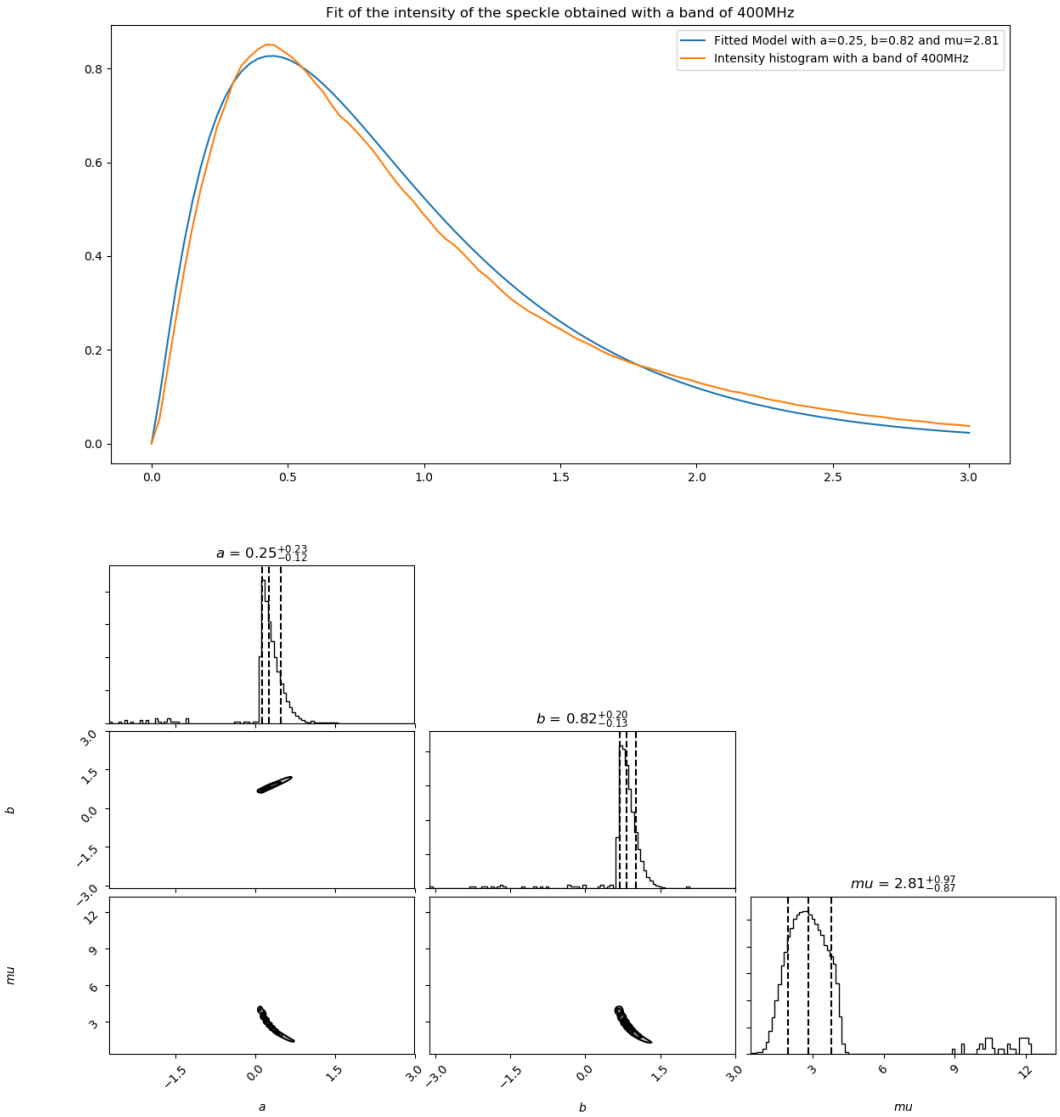

Figure E.3: Results of the fit with MCMC (top) of a speckle obtained with a band of 400MHz, Histogram of the final value of the walkers

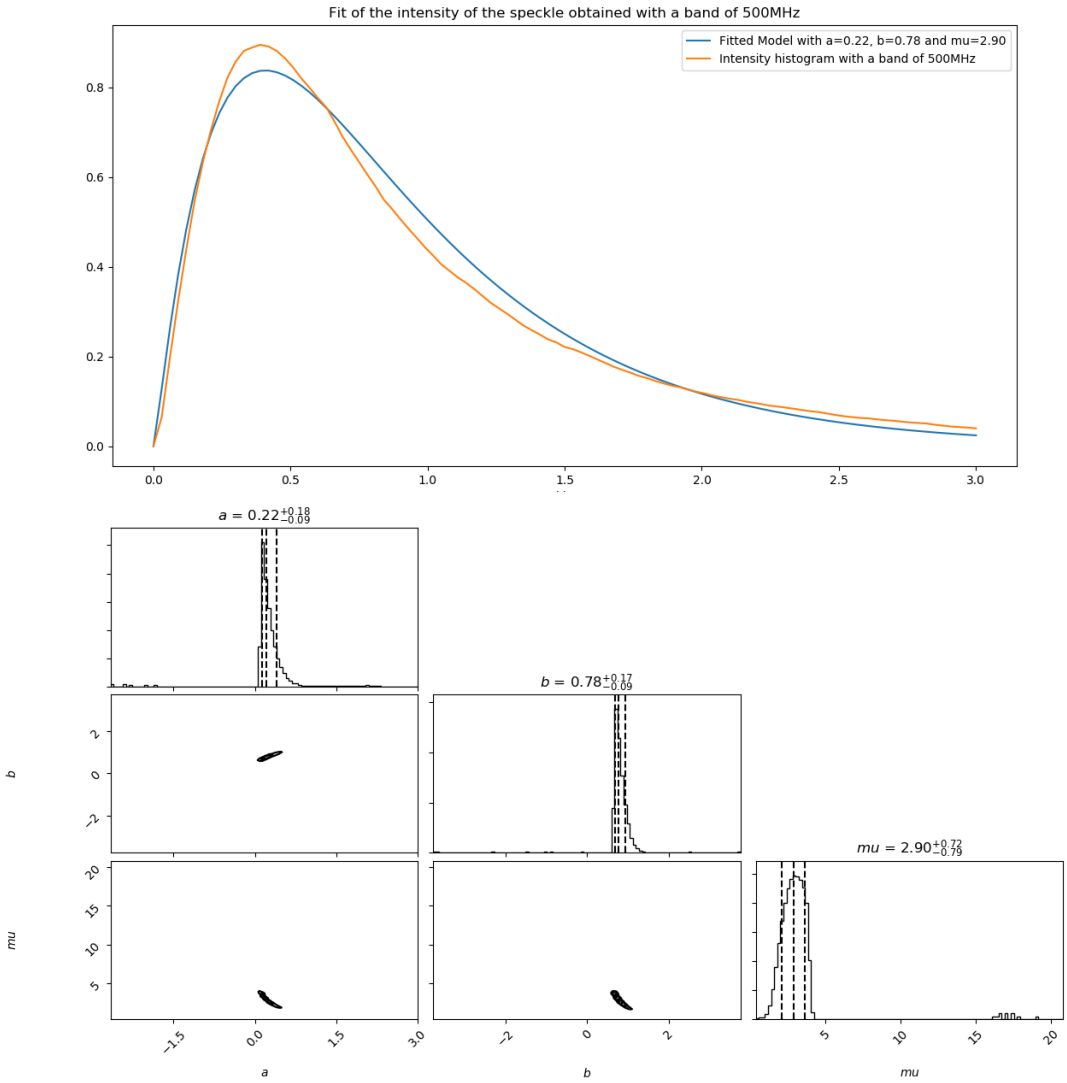

Figure E.4: Results of the fit with MCMC (top) of a speckle obtained with a band of 500MHz, Histogram of the final value of the walkers

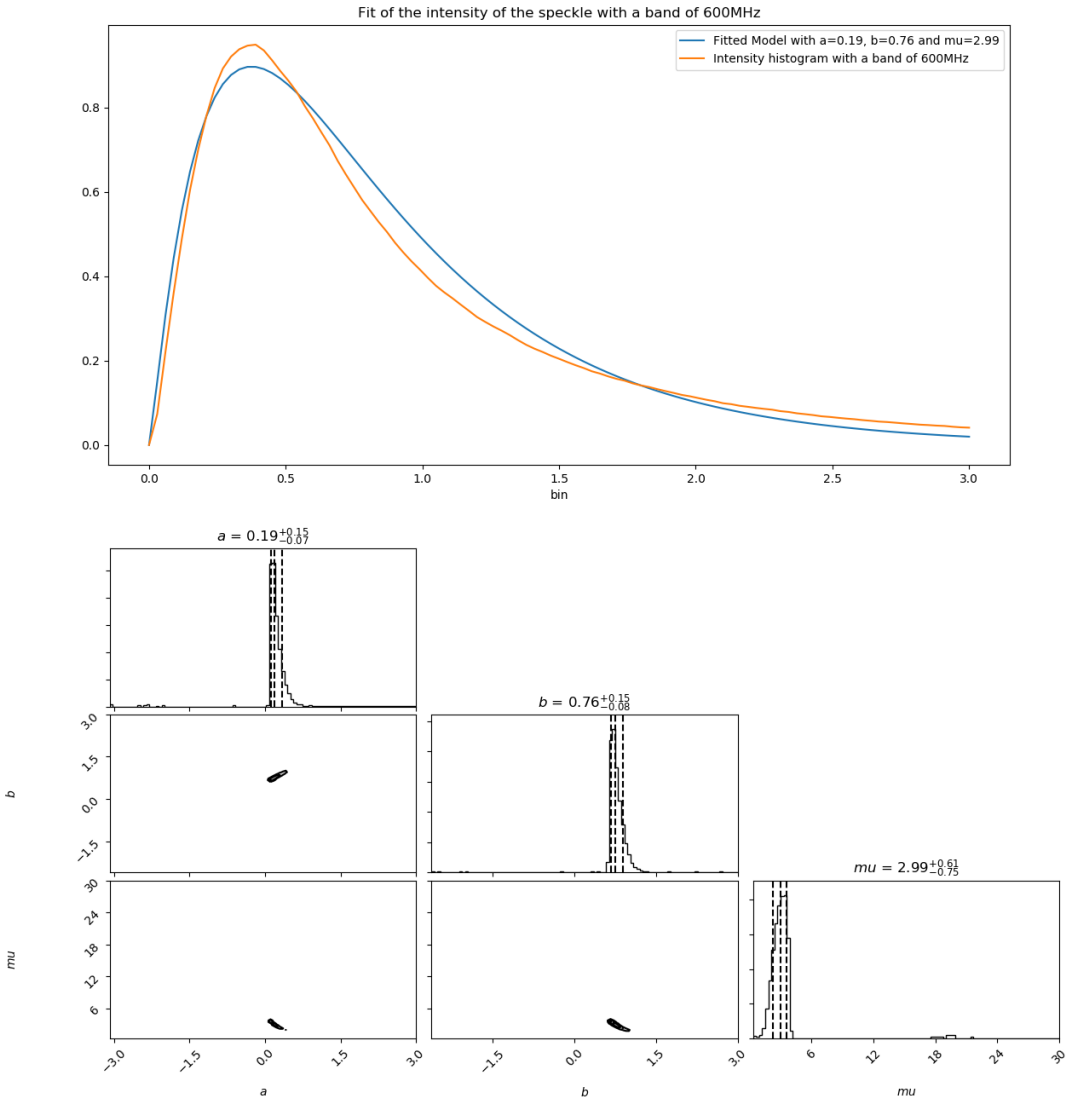

Figure E.5: Results of the fit with MCMC (top) of a speckle obtained with a band of 600MHz, Histogram of the final value of the walkers

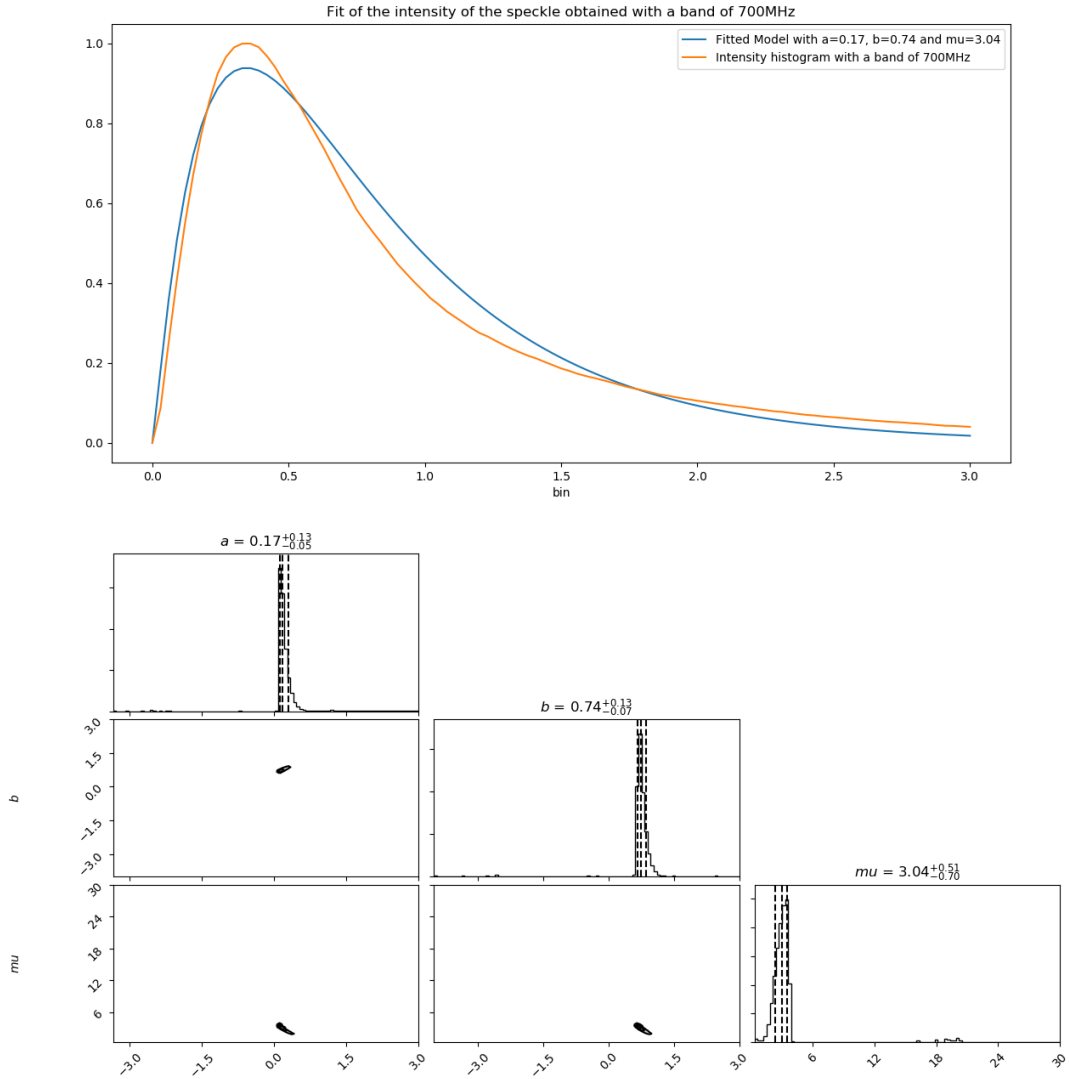

Figure E.6: Results of the fit with MCMC (top) of a speckle obtained with a band of 700MHz, Histogram of the final value of the walkers

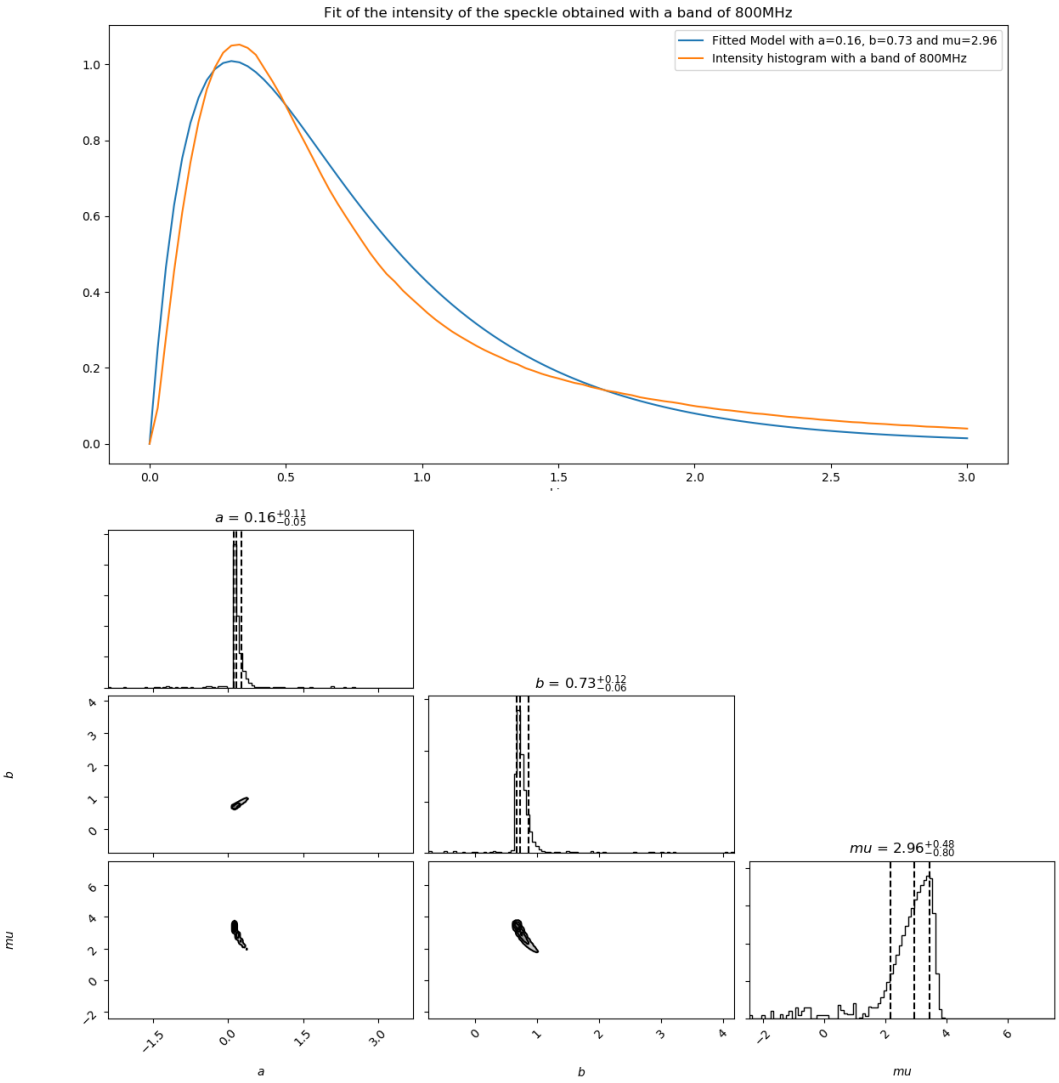

Figure E.7: Results of the fit with MCMC (top) of a speckle obtained with a band of 800MHz, Histogram of the final value of the walkers

References

Abe, S., Mukai, T., Hirata, N., Barnouin-Jha, O. S., Cheng, A. F., Demura, H., ... others (2006). Mass and local topography measurements of itokawa by hayabusa. *Science*, *312*(5778), 1344–1347.

Afifi, S., Dusséaux, R., et al. (2012). Scattering by anisotropic rough layered 2d interfaces. *IEEE Transactions on Antennas and Propagation*, *60*(11), 5315–5328.

Argenti, F., & Alparone, L. (2002). Speckle removal from sar images in the undecimated wavelet domain. *IEEE Transactions on Geoscience and Remote Sensing*, *40*(11), 2363–2374.

ASC. (2014). *Radarsat-1.* (`http://www.asc-csa.gc.ca/fra/satellites/radarsat1/default.asp`, Last accessed on 2019-01-02)

Asphaug, E. (2009). Growth and evolution of asteroids. *Annual Review of Earth and Planetary Sciences*, *37*, 413–448.

Barnouin, O., Daly, M., Palmer, E., Gaskell, R., Weirich, J., Johnson, C., ... others (2019). Shape of (101955) bennu indicative of a rubble pile with internal stiffness. *Nature geoscience*, *12*(4), 247.

Barnouin-Jha, O. S., Cheng, A. F., Mukai, T., Abe, S., Hirata, N., Nakamura, R., ... Clark, B. E. (2008). Small-scale topography of 25143 itokawa from the hayabusa laser altimeter. *Icarus*, *198*(1), 108–124.

Barrett, T. W., & Vienna, V. (2001). Technical features, history of ultra wideband communications and radar: part i, uwb communications. *Microw J*, *44*(1), 22–56.

Bass, F. G., & Fuks, I. M. (1979). *Wave scattering from statistically rough surfaces: International series in natural philosophy* (Vol. 93). Elsevier.

Beckmann, P., & Spizzichino, A. (1987). The scattering of electromagnetic waves from rough surfaces. *Norwood, MA, Artech House, Inc., 1987, 511 p.*.

Berginc, G. (2002). Small-slope approximation method: A further study of vector wave scattering from two-dimensional surfaces and comparison with experimental data. *Progress In Electromagnetics Research*, *37*, 251–287.

Berquin, Y. (2014). *Assessing the performances and optimizing the radar sounder design parameters for the ejsm mission (ganymede and europa)* (Unpublished doctoral dissertation). Universite Grenoble Alpes.

Berquin, Y., Herique, A., Kofman, W., Heggy, E., et al. (2015). Computing low-frequency radar surface echoes for planetary radar using huygens-fresnel's principle. *Radio Science*, *50*(10), 1097–1109.

Bertrand, J., & Bertrand, P. (1995). Theoretical radar imaging: from images to hyperimages. In *1995 international geoscience and remote sensing symposium, igarss'95. quantitative remote sensing for science and applications* (Vol. 1, pp. 474–476).

Billingsley, J. B., Farina, A., Gini, F., Greco, M. V., Verrazzani, L., et al. (1999). Statistical analyses of measured radar ground clutter data. *IEEE Transactions on Aerospace and electronic Systems*, *35*(2), 579–593.

Blankenship, D., Ray, T., Plaut, J., Moussessian, A., Patterson, W., Romero-Wolf, A., ... others (2018). Reason for europa. , *42*.

Blunt, L., & Jiang, X. (2003). *Advanced techniques for assessment surface topography: development of a basis for 3d surface texture standards" surfstand"*. Elsevier.

Boothe, R. R. (1969). *The weibull distribution applied to the ground clutter backscatter coefficient*

(Tech. Rep.). Army Missile Command Redstone Arsenal Research and Engineering.

Bottke Jr, W. F., Vokrouhlickỳ, D., Rubincam, D. P., Nesvornỳ, D., et al. (2006). The yarkovsky and yorp effects: Implications for asteroid dynamics. *Annu. Rev. Earth Planet. Sci.*, *34*, 157–191.

Breed, G. (2005). A summary of fcc rules for ultra wideband communications. *High Frequency Electronics*, 42-24.

Broschat, S. L., Thorsos, E. I., et al. (1997). An investigation of the small slope approximation for scattering from rough surfaces. part ii. numerical studies. *The Journal of the Acoustical Society of America*, *101*(5), 2615–2625.

Bruzzone, L., Plaut, J. J., Alberti, G., Blankenship, D. D., Bovolo, F., Campbell, B. A., ... others (2013). Rime: Radar for icy moon exploration. In *2013 ieee international geoscience and remote sensing symposium-igarss* (pp. 3907–3910).

Bucci, Crocco, Isernia, Pascazio, & OTHERS. (2001). Subsurface inverse scattering problems: quantifying, qualifying, and achieving the available information. *IEEE Transactions on Geoscience and Remote Sensing*, *39*(11), 2527-2538. doi: 10.1109/36.964991

Bus, S. J., & Binzel, R. P. (2002). Phase ii of the small main-belt asteroid spectroscopic survey: A feature-based taxonomy. *Icarus*, *158*(1), 146–177.

Candès, E. J., & Wakin, M. B. (2008). An introduction to compressive sampling. *IEEE signal processing magazine*, *25*(2), 21–30.

Cheng, A. F., Atchison, J., Kantsiper, B., Rivkin, A. S., Stickle, A., Reed, C., ... others (2015, Oct). Asteroid impact and deflection assessment mission. , *115*, 262-269. doi: 10.1016/j.actaastro.2015.05.021

Cheng, A. F., Barnouin-Jha, O., Zuber, M. T., Veverka, J., Smith, D. E., Neumann, G. A., ... others (2001). Laser altimetry of small-scale features on 433 eros from near-shoemaker. *Science*, *292*(5516), 488–491.

Cheng, A. F., et al. (2009). Fundamentally distinct outcomes of asteroid collisional evolution and catastrophic disruption. *Planetary and Space Science*, *57*(2), 165–172.

Chesley, S. R., Farnocchia, D., Nolan, M. C., Vokrouhlickỳ, D., Chodas, P. W., Milani, A., ... others (2014). Orbit and bulk density of the osiris-rex target asteroid (101955) bennu. *Icarus*, *235*, 5–22.

Chew, W. C., Wang, Y.-M., et al. (1990). Reconstruction of two-dimensional permittivity distribution using the distorted born iterative method. *IEEE transactions on medical imaging*, *9*(2), 218–225.

Cloude, S. R. (2006). Polarization coherence tomography. *Radio Science*, *41*(4).

Cloude, S. R. (2007). Dual-baseline coherence tomography. *IEEE Geoscience and Remote Sensing Letters*, *4*(1), 127–131.

Cloude, S. R., & Papathanassiou, K. P. (2008). Forest vertical structure estimation using coherence tomography. In *Igarss 2008-2008 ieee international geoscience and remote sensing symposium* (Vol. 5, pp. V–275).

Cumming, I. G., & Wong, F. H. (2005). Digital processing of synthetic aperture radar data: Algorithms and implementation [with cdrom](artech house remote sensing library). *Artech House, Boston, Massachusetts*.

Curlander, J. C., & McDonough, R. N. (1991). Synthetic aperture radar- systems and signal processing(book). *New York: John Wiley & Sons, Inc, 1991.*.

Dashen, & Wurmser. (1991). A new theory for scattering from a surface. *Journal of mathematical physics*, *32*(4), 971–985.

Dechambre, M., Biancheri-Astier, M., Ciarletti, V., Dorizon, S., Hassen-Khodja, R., Saintenoy, A., ... others (2012). Wisdom gpr measurements in a cold artificial and controlled environment. In *2012 ieee international geoscience and remote sensing symposium* (pp. 606–609).

Delbo, M., Libourel, G., Wilkerson, J., Murdoch, N., Michel, P., Ramesh, K., ... Marchi, S. (2014). Thermal fatigue as the origin of regolith on small asteroids. *Nature*, *508*(7495), 233–236.

Delbo, M., Mueller, M., Emery, J. P., Rozitis, B., & Capria, M. T. (2015). Asteroid thermophysical modeling. *Asteroids IV*, 107–128.

Dell'Elce, L., Baresi, N., Naidu, S., Benner, L., & Scheeres, D. (2017). Numerical investigation of the

dynamical environment of 65803 didymos. *Advances in Space Research*, *59*(5), 1304–1320.

DeMeo, F. E., Binzel, R. P., Slivan, S. M., & Bus, S. J. (2009). An extension of the bus asteroid taxonomy into the near-infrared. *Icarus*, *202*(1), 160–180.

Demir, M. A., Johnson, J. T., et al. (2003). Fourth-and higher-order small-perturbation solution for scattering from dielectric rough surfaces. *JOSA A*, *20*(12), 2330–2337.

Du, J., & Fa, W. (2016). *Tomography synthetic aperture radar (tomosar) technologies for the f and deflection assessment (aida) mission.*

Duquenoy, M. (2009). Analyse temps-frequence appliquee a l'imagerie sar polarimetrique. , 211.

Elachi, C., et al. (2005, May). Cassini Radar Views the Surface of Titan. *Science*, *308*(5724), 970–974. Retrieved 2019-04-04, from `http://www.sciencemag.org/cgi/doi/10.1126/science.1109919` doi: 10.1126/science.1109919

Elfouhaily, Thompson, Vandemark, Chapron, et al. (1999). A new bistatic model for electromagnetic scattering from perfectly conducting random surfaces. *Waves in Random Media*, *9*(3), 281–294.

Elfouhaily, T. M., Guérin, C.-A., et al. (2004). A critical survey of approximate scattering wave theories from random rough surfaces. *Waves in Random Media*, *14*(4), R1–R40.

ESA. (2001). *Description envisat and its mission.* (`https://earth.esa.int/c/document_library/get_file?folderId=60155&name=DLFE-848.pdf`)

ESA. (2003). *Ers 1 and 2.* (`https://www.esa.int/Our_Activities/Observing_the_Earth/ERS_1_and_2`, Last accessed on 2019-01-02)

Fabry, F. (2015). *Radar meteorology: principles and practice.* Cambridge University Press.

Ford, J., Blom, R., Crisp, J., Elachi, C., Farr, T., Saunders, R. S., ... others (1989). Spaceborne radar observations: A guide for magellan radar-image analysis. *NASA Technical Reports Server*.

Fornaro, G., Serafino, F., Soldovieri, F., et al. (2003, Mar). Three-dimensional focusing with multipass sar data. , *41*, 507-517. doi: 10.1109/TGRS.2003.809934

Fortuin, L. (1970). Survey of literature on reflection and scattering of sound waves at the sea surface. *The Journal of the Acoustical Society of America*, *47*(5B), 1209–1228.

Frey, O., Morsdorf, F., Meier, E., et al. (2008). Tomographic imaging of a forested area by airborne multi-baseline p-band sar. *Sensors*, *8*(9), 5884–5896.

Fung, A., & Eom, H. J. (1981). Note on the kirchhoff rough surface solution in backscattering. *Radio Science*, *16*(03), 299–302.

Gao, G. (2010). Statistical modeling of sar images: A survey. *Sensors*, *10*(1), 775–795.

Garcia, N., & Stoll, E. (1984). Monte carlo calculation for electromagnetic-wave scattering from random rough surfaces. *Physical review letters*, *52*(20), 1798.

Gens, R., & Van Gerenden, J. L. (1996). Review article sar interferometryâ€"issues, techniques, applications. *International Journal of Remote Sensing*, *17*(10), 1803–1835.

Gibson, W. C. (2014). *The method of moments in electromagnetics.* Chapman and Hall/CRC.

Gini, F., Lombardini, F., Montanari, M., et al. (2002). Layover solution in multibaseline sar interferometry. *IEEE Transactions on Aerospace and Electronic Systems*, *38*(4), 1344–1356.

Goodman, J. W. (1976). Some fundamental properties of speckle. *JOSA*, *66*(11), 1145–1150.

Gresham, I., Jenkins, A., Egri, R., Eswarappa, C., Kinayman, N., Jain, N., ... Lanteri, J. . (2004, Sep.). Ultra-wideband radar sensors for short-range vehicular applications. *IEEE Transactions on Microwave Theory and Techniques*, *52*(9), 2105-2122. doi: 10.1109/TMTT.2004.834185

Guerin, Soriano, Chapron, et al. (2010, August). The weighted curvature approximation in scattering from sea surfaces. *Waves in Random and Complex Media*, *20*(3), 364–384. Retrieved 2017-03-29, from `http://www.tandfonline.com/doi/abs/10.1080/17455030903563824` doi: 10.1080/17455030903563824

Guérin, Soriano, Elfouhaily, et al. (2004). Weighted curvature approximation: numerical tests for 2d dielectric surfaces. *Waves in random media*, *14*(3), 349–363.

Guérin, C.-A., & Johnson, J. T. (2015). A simplified formulation for rough surface cross-polarized backscattering under the second-order small-slope approximation. *IEEE Transactions on Geoscience and Remote Sensing*, *53*(11), 6308–6314.

Guerin, C.-A., & Sentenac, A. (2004). Second-order perturbation theory for scattering from heterogeneous rough surfaces. *JOSA A*, *21*(7), 1251–1260.

Hanson, K. M. (2000). Tutorial on markov chain monte carlo. In *Workshop for maximum entropy and bayesian methods* (pp. 9–13).

Harris, W., Woodney, L., Villanueva, G., et al. (2019). *Chimera: A mission of discovery to the first centaur.* Geneva, Switzerland.

Herique, A., Agnus, B., Asphaug, E., Barucci, A., Beck, P., Bellerose, J., ... others (2018, Oct). Direct observations of asteroid interior and regolith structure: Science measurement requirements. *Advances in Space Research.* doi: 10.1016/j.asr.2017.10.020

Hérique, A., Plettemeier, D., Lange, C., Grundmann, J. T., Ciarletti, V., Ho, T.-M., ... others (2019, Mar). A radar package for asteroid subsurface investigations: Implications of implementing and integration into the mascot nanoscale landing platform from science requirements to baseline design. *Acta Astronautica*, *156*, 317-329. doi: 10.1016/j.actaastro.2018.03.058

Hfraim-hfr-tn-001 hfr specifications - task1(d4) 2015-06-26 v1-0.docx. (n.d.).

Hill, D. (1988). Signal processing techniques for the u.s. army research laboratory stepped frequency ultra-wideband radar. *IEEE Transactions on Geoscience and Remote Sensing*, *26*(2), 195-203. doi: 10.1109/36.3021

Hyder, M., & Mahata, K. (2009). An approximate l0 norm minimization algorithm for compressed sensing. In *2009 ieee international conference on acoustics, speech and signal processing* (pp. 3365–3368).

Jacobson, S. A., & Scheeres, D. J. (2011). Dynamics of rotationally fissioned asteroids: Source of observed small asteroid systems. *Icarus*, *214*(1), 161–178.

Jakeman, E. (1980). On the statistics of k-distributed noise. *Journal of Physics A: Mathematical and General*, *13*(1), 31.

Jakeman, E., & Pusey, P. (1976). A model for non-rayleigh sea echo. *IEEE Transactions on antennas and propagation*, *24*(6), 806–814.

JAXA. (2003). *About japanese earth resources satellite "fuyo-1" (jers-1).* (`http://global.jaxa.jp/projects/sat/jers1/index.html`, Last accessed on 2019-01-02)

JAXA. (2016). *About asteroid explorer "hayabusa" (muses-c).* (`https://global.jaxa.jp/projects/sas/muses_c/`, Last accessed on 2019-28-05)

Johnson, J. T. (1999). Third-order small-perturbation method for scattering from dielectric rough surfaces. *JOSA A*, *16*(11), 2720–2736.

Johnson, W. H., J. W.and Lee, Jr., W. L. A., et al. (1979). *Seasat-a satellite scatterometer mission summary and engineering assessment report.*

Kofman, W., Hérique, A., Goutail, J.-P., Hagfors, T., Williams, I., Nielsen, E., ... others (2007). The comet nucleus sounding experiment by radiowave transmission (consert): a short description of the instrument and of the commissioning stages. *Space Science Reviews*, *128*(1-4), 413–432.

Kong, J. (2000). *J. electromagnetic wave theory.* John Wiley and sons, Inc.

Lampropoulos, G., Drosopoulos, A., Rey, N., et al. (1999). High resolution radar clutter statistics. *IEEE Transactions on Aerospace and Electronic Systems*, *35*(1), 43–60.

Lantz, C., Clark, B., Barucci, M., & Lauretta, D. (2013). Evidence for the effects of space weathering spectral signatures on low albedo asteroids. *Astronomy & Astrophysics*, *554*, A138.

Lauretta, D., Balram-Knutson, S., Beshore, E., Boynton, W. V., d'Aubigny, C. D., Della Giustina, D., ... others (2017). Osiris-rex: sample return from asteroid (101955) bennu. *Space Science Reviews*, *212*(1-2), 925–984.

Li, Liu, Song, et al. (2004). Three-dimensional reconstruction of objects buried in layered media using born and distorted born iterative methods. *IEEE Transactions on Geoscience and Remote Sensing*, *1*(2), 107-111. doi: 10.1109/LGRS.2004.826562

Liszka, E., & McCoy, J. (1982). Scattering at a rough boundaryâ€"extensions of the kirchhoff approximation. *The Journal of the Acoustical Society of America*, *71*(5), 1093–1100.

Lombardini, F. (2005). Analysis of non-gaussian speckle statistics in high-resolution sar images.

Margot, J.-L., Nolan, M., Benner, L., Ostro, S., Jurgens, R., Giorgini, J., ... others (2002). Binary asteroids in the near-earth object population. *Science*, *296*(5572), 1445–1448.

Mazrouei, S., Daly, M., Barnouin, O. S., Ernst, C., & DeSouza, I. (2014). Block distributions on itokawa. *Icarus*, *229*, 181–189.

Meecham, W. C. (1956). On the use of the kirchhoff approximation for the solution of reflection problems. *Journal of Rational Mechanics and Analysis*, *5*(2), 323–334.

Michel, P., Barnouin, O. S., Ballouz, R.-L., Walsh, K. J., Richardson, D. C., Jutzi, M., ... others (2018). Disruption and reaccumulation as the origin of the ryugu and bennu top shapes? *AGU Fall Meeting Abstracts*.

Michel, P., Cheng, A., Küppers, M., Pravec, P., Blum, J., Delbo, M., ... others (2016, Jun). Science case for the asteroid impact mission (aim): A component of the asteroid impact and deflection assessment (aida) mission. *Advances in Space Research*, *57*(12), 2529-2547. doi: 10.1016/j.asr.2016.03.031

Migliaccio, M., Gambardella, A., Tranfaglia, M., et al. (2007). Sar polarimetry to observe oil spills. *IEEE Transactions on Geoscience and Remote Sensing*, *45*(2), 506–511.

Moltenbrey, M. (2016). Dawn of small worlds. *Dawn of Small Worlds: Dwarf Planets, Asteroids, Comets, Astronomers' Universe, ISBN 978-3-319-23002-3. Springer International Publishing Switzerland, 2016*.

Moreira, A., Prats-Iraola, P., Younis, M., Krieger, G., Hajnsek, I., & Papathanassiou, K. (2013). A tutorial on synthetic aperture radar. *IEEE Geoscience and remote sensing magazine*, 1-38.

Mukai, T., Araki, H., Mizuno, T., Hatanaka, N., Nakamura, A., Kamei, A., ... Cheng, A. (2002). Detection of mass, shape and surface roughness of target asteroid of muses-c by lidar. *Advances in Space Research*, *29*(8), 1231–1235.

Murdoch, N., Sánchez, P., Schwartz, S. R., & Miyamoto, H. (2015). Asteroid surface geophysics. *arXiv preprint arXiv:1503.01931*.

Nakamura, T., Noguchi, T., Tanaka, M., Zolensky, M. E., Kimura, M., Tsuchiyama, A., ... others (2011). Itokawa dust particles: a direct link between s-type asteroids and ordinary chondrites. *Science*, *333*(6046), 1113–1116.

Nannini, M., & Scheiber, R. (2006). A time domain beamforming algorithm for sar tomography. In *Proc. eusar* (pp. 1–4).

Nannini, M., Scheiber, R., Horn, R., Moreira, A., et al. (2011). First 3-d reconstructions of targets hidden beneath foliage by means of polarimetric sar tomography. *IEEE Geoscience and Remote Sensing Letters*, *9*(1), 60–64.

Nasa neo program. (2020). `https://www.nasa.gov/planetarydefense/neoo`. (Accessed: 2020-01-28)

Nouvel, J.-F. (2003). *Sondage du sous-sol martien par un radar basse-fréquence depuis un satellite en orbite basse: analyses physiques et préparation des données* (Unpublished doctoral dissertation). Université Joseph-Fourier-Grenoble I.

Novak, L. M., Burl, M. C., et al. (1990). Optimal speckle reduction in polarimetric sar imagery. *IEEE Transactions on Aerospace and Electronic Systems*, *26*(2), 293–305.

Nozette, S., Spudis, P., Bussey, B., Jensen, R., Raney, K., Winters, H., ... others (2010). The lunar reconnaissance orbiter miniature radio frequency (mini-rf) technology demonstration. *Space Science Reviews*, *150*(1-4), 285–302.

Nyoungui, A. N., Tonye, E., Akono, A., et al. (2002). Evaluation of speckle filtering and texture analysis methods for land cover classification from sar images. *International Journal of Remote Sensing*, *23*(9), 1895–1925.

Ogilvy, J. A., & Merklinger, H. M. (1991). *Theory of wave scattering from random rough surfaces.* ASA.

Oliver, C., & Quegan, S. (2004). *Understanding synthetic aperture radar images.* SciTech Publishing, Inc.

Ono, T., Kumamoto, A., Nakagawa, H., Yamaguchi, Y., Oshigami, S., Yamaji, A., ... others (2009). Lunar radar sounder observations of subsurface layers under the nearside maria of the moon. *Science*, *323*(5916), 909–912.

Ono, T., Kumamoto, A., Yamaguchi, Y., Yamaji, A., Kobayashi, T., Kasahara, Y., & Oya, H. (2008). Instrumentation and observation target of the lunar radar sounder (lrs) experiment on-board the selene spacecraft. *Earth, Planets and Space*, *60*(4), 321–332.

Ostro, S. J., Margot, J.-L., Benner, L. A., Giorgini, J. D., Scheeres, D. J., Fahnestock, E. G., ... others

(2006). Radar imaging of binary near-earth asteroid (66391) 1999 kw4. *Science*, *314*(5803), 1276–1280.

Ovarlez, J.-P., Vignaud, L., Castelli, J.-C., Tria, M., Benidir, M., et al. (2003). Analysis of sar images by multidimensional wavelet transform. *IEE Proceedings - Radar, Sonar and Navigation*, *150*(4), 234. doi: 10.1049/ip-rsn:20030671

Panzer, B., Gomez-Garcia, D., Leuschen, C., Paden, J., Rodriguez-Morales, F., Patel, A., ... Gogineni, P. (2013). An ultra-wideband, microwave radar for measuring snow thickness on sea ice and mapping near-surface internal layers in polar firn. *Journal of Glaciology*, *59*(214), 244â€“254. doi: 10.3189/2013JoG12J128

Papa, R. J., & Lennon, J. F. (1988). Conditions for the validity of physical optics in rough surface scattering. *IEEE transactions on antennas and propagation*, *36*(5), 647–650.

Pettengill, G., Ford, P., Brown, W., Kaula, W., Keller, C., Masursky, H., ... others (1979). Pioneer venus radar mapper experiment. *Science*, *203*(4382), 806–808.

Phillips, R. J., Adams, G., Brown Jr, W., Eggleton, R., Jackson, P., Jordan, R., ... others (1973). The apollo 17 lunar sounder. In *Lunar and planetary science conference proceedings* (Vol. 4, p. 2821).

Picardi, G., Plaut, J. J., Biccari, D., Bombaci, O., Calabrese, D., Cartacci, M., ... others (2005). Radar soundings of the subsurface of mars. *science*, *310*(5756), 1925–1928.

Plettemeier, D., Hahnel, R., Hegler, S., Safaeinili, A., Plaut, J., Gaskell, B., ... others (2009). Numerical computation of radar echoes measured by marsis during phobos flybys. In *2009 ieee radar conference* (pp. 1–6).

Porcello, L. J., Massey, N. G., Innes, R. B., Marks, J. M., et al. (1976). Speckle reduction in synthetic-aperture radars. *JOSA*, *66*(11), 1305–1311.

Prockter, L., Murchie, S., Cheng, A., Krimigis, S., Farquhar, R., Santo, A., & Trombka, J. (2002). The near shoemaker mission to asteroid 433 eros. *Acta Astronautica*, *51*(1-9), 491–500.

Rayleigh, J. W. S. B. (1896). *The theory of sound* (Vol. 2). Macmillan.

Reigber, A., & Moreira, A. (2000). First demonstration of airborne sar tomography using multibaseline l-band data. *IEEE Transactions on Geoscience and Remote Sensing*, *38*(5), 2142–2152.

Rice, S. O. (1951). Reflection of electromagnetic waves from slightly rough surfaces. *Communications on pure and applied mathematics*, *4*(2-3), 351–378.

Richardson, J. (2011). Regolith generation, retention, and movement on asteroid surfaces: early modeling results. In *Lunar and planetary science conference* (Vol. 42, p. 1084).

Rubincam, D. P. (2000). Radiative spin-up and spin-down of small asteroids. *Icarus*, *148*(1), 2–11.

Sabath, Mokole, & Samaddar. (2005, june). Definition and classification of ultra-wideband signals and devices. *The Radio Science Bulletin*, *313*, 12-26.

Salucci, M., Oliveri, G., Randazzo, A., & Massa, A. (2014). Electromagnetic subsurface prospecting by a multifocusing inexact newton method within the second-order born approximation. *Journal of the Optical Society of America A*, *31*(6), 1167. doi: 10.1364/JOSAA.31.001167

Sanamzadeh, M., Tsang, L., Johnson, J. T., Burkholder, R. J., Tan, S., et al. (2017). Scattering of electromagnetic waves from 3d multilayer random rough surfaces based on the second-order small perturbation method: energy conservation, reflectivity, and emissivity. *JOSA A*, *34*(3), 395–409.

Schleher, D. (1976). Radar detection in weibull clutter. *IEEE Transactions on Aerospace and Electronic Systems*(6), 736–743.

Schmitt, M., Magnard, C., Brehm, T., & Stilla, U. (2011). Towards airborne single pass decimeter resolution sar interferometry over urban areas. In *Isprs conference on photogrammetric image analysis* (pp. 197–208).

Schneider, J. B. (2010). Understanding the finite-difference time-domain method. *School of electrical engineering and computer science Washington State University.–URL: http://www. Eecs. Wsu. Edu/˜ schneidj/ufdtd/(request data: 29.11. 2012)*.

Seu, R., Phillips, R. J., Biccari, D., Orosei, R., Masdea, A., Picardi, G., ... others (2007). Sharad sounding radar on the mars reconnaissance orbiter. *Journal of Geophysical Research: Planets*, *112*(E5).

Shannon, C. E. (1949). Communication theory of secrecy systems. *Bell system technical journal*, *28*(4), 656–715.

Shrader, W. (1973). Radar technology applied to air traffic control. *IEEE Transactions on Communications*, *21*(5), 591–605.

Soriano, & Saillard. (2001). Scattering of electromagnetic waves from two-dimensional rough surfaces with an impedance approximation. *JOSA A*, *18*(1), 124–133.

Soriano, G., Guérin, C.-A., Saillard, M., et al. (2002). Scattering by two-dimensional rough surfaces: comparison between the method of moments, kirchhoff and small-slope approximations. *Waves in random media*, *12*(1), 63–84.

Soumbatov-Gur, A. (2018). Diamonds in the sky. why?

Soumekh, M. (1999). *Synthetic aperture radar signal processing* (Vol. 7). New York: Wiley.

Spice kernel definition. (n.d.). `http://naif.jpl.nasa.gov/naif/`. (Accessed: 2019-05-08)

Spudis, P., Bussey, D., Baloga, S., Butler, B., Carl, D., Carter, L. M., ... others (2010, Mar). Initial results for the north pole of the moon from mini-sar, chandrayaan-1 mission: Mini-sar north pole results. *Geophysical Research Letters*, *37*(6). doi: 10.1029/2009GL042259

Staderini, E. (2002, 02). Uwb radar in medicine. *Aerospace and Electronic Systems Magazine, IEEE*, *17*, 13 - 18. doi: 10.1109/62.978359

Stofan, E. R., et al. (1991). Corona structures on venus: Models of origin. *Journal of Geophysical Research: Planets*, *96*(E4), 20933–20946.

Susskind, C. (1985). Who invented radar? *Endeavour*, *9*(2), 92–96.

Tabatabaeenejad, Duan, Moghaddam, et al. (2013). Coherent scattering of electromagnetic waves from two-layer rough surfaces within the kirchhoff regime. *IEEE Transactions on Geoscience and Remote Sensing*, *51*(7), 3943–3953.

Taylor, J. D. (2000). *Ultra-wideband radar technology.* CRC press.

Tebaldini, S. (2009). Algebraic synthesis of forest scenarios from multibaseline polinsar data. *IEEE Transactions on Geoscience and Remote Sensing*, *47*(12), 4132–4142.

Tholen, D. J. (1989). Asteroid taxonomic classifications. In *Asteroids ii* (pp. 1139–1150).

Thorsos, Broschat, et al. (1995). An investigation of the small slope approximation for scattering from rough surfaces. part i. theory. *The Journal of the Acoustical Society of America*, *97*(4), 2082–2093.

Thorsos, E. I. (1988). The validity of the kirchhoff approximation for rough surface scattering using a gaussian roughness spectrum. *The Journal of the Acoustical Society of America*, *83*(1), 78–92.

Tison, C., Nicolas, J.-M., Tupin, F., Maître, H., et al. (2004). A new statistical model for markovian classification of urban areas in high-resolution sar images. *IEEE transactions on geoscience and remote sensing*, *42*(10), 2046–2057.

Tria, M. (2005). Imagerie radar a synthese d'ouverture (rso) par analyse en ondelettes continues multidimensionnelles. , 317.

Trunk, G., & George, S. (1970). Detection of targets in non-gaussian sea clutter. *IEEE Transactions on Aerospace and Electronic Systems*(5), 620–628.

Ulaby, F., Kouyate, F., Brisco, B., & Williams, T. H. (1986, Mar). Textural infornation in sar images. *IEEE Transactions on Geoscience and Remote Sensing*, *GE-24*(2), 235-245. doi: 10.1109/TGRS.1986.289643

Ulaby, F. T., & Dobson, M. C. (1989). Handbook of radar scattering statistics for terrain (artech house remote sensing library). *Artech House: Norwood, MA, USA*.

Van den Berg, E., & Friedlander, M. P. (2011). Sparse optimization with least-squares constraints. *SIAM Journal on Optimization*, *21*(4), 1201-1229.

van Loon, B. (2005). Radar 101: Celebrating 101 years of development. *Proceedings of the IEEE*, *93*(4), 844–846.

Voronovich, & Zavorotny. (2012). Ocean-scattered polarized bistatic radar signals modeled with small-slope approximation. In *2012 ieee international geoscience and remote sensing symposium* (pp. 3415–3418).

Voronovich, A. (1994). Small-slope approximation for electromagnetic wave scattering at a rough interface of two dielectric half-spaces. *Waves in random media*, *4*(3), 337–368.

Voronovich, A. (1999). *Wave Scattering from Rough Surfaces* (Springer ed., Vol. 17). Berlin, Heidelberg: Springer Berlin Heidelberg. Retrieved 2017-03-21, from http://nbn-resolving.de/urn:nbn:de:1111-201109164632 (OCLC: 863752345)

Walsh, K. J., Morbidelli, A., Raymond, S. N., O'brien, D., & Mandell, A. (2012). Populating the asteroid belt from two parent source regions due to the migration of giant planets - the grand tack. *Meteoritics & Planetary Science*, *47*(12), 1941–1947.

Walsh, K. J., Richardson, D. C., Michel, P., et al. (2008). Rotational breakup as the origin of small binary asteroids. *Nature*, *454*(7201), 188.

Ward, K. (1981). Compound representation of high resolution sea clutter. *Electronics letters*, *17*(16), 561–563.

Watanabe, S.-i., Tsuda, Y., Yoshikawa, M., Tanaka, S., Saiki, T., Nakazawa, S., et al. (2017). Hayabusa2 mission overview. *Space Science Reviews*, *208*(1-4), 3–16.

Werninghaus, R. (2004). Terrasar-x mission. *Proc.SPIE*, *5236*, 5236 - 5236 - 8. Retrieved from https://doi.org/10.1117/12.511500 doi: 10.1117/12.511500

Whiteley, R. J., Tholen, D. J., Hergenrother, C. W., et al. (2002). Lightcurve analysis of four new monolithic fast-rotating asteroids. *Icarus*, *157*(1), 139–154.

Wiley, C. A. (1985). Synthetic aperture radars. *IEEE Transactions on Aerospace and Electronic Systems*, *3*, 440–443.

Wright, J. (1968). A new model for sea clutter. *IEEE Transactions on antennas and propagation*, *16*(2), 217–223.

Wu, C., & Zhang, X. (2015). Second-order perturbative solutions for 3-d electromagnetic radiation and propagation in a layered structure with multilayer rough interfaces. *IEEE Journal of Selected Topics in Applied Earth Observations and Remote Sensing*, *8*(1), 180–194.

Xi, L., Guosui, L., Ni, J., et al. (1999). Autofocusing of isar images based on entropy minimization. *IEEE Transactions on aerospace and electronic systems*.

Zhang, Chen, Yin, et al. (2011). Facet-based investigation on em scattering from electrically large sea surface with two-scale profiles: Theoretical model. *IEEE Transactions on Geoscience and Remote Sensing*, *49*(6), 1967–1975.

Zhang, H., Qian, J., et al. (2016). Validation of extended kirchhoff approximation and small slope approximation for electromagnetic scattering from ship wake surfaces. In *2016 ieee international conference on microwave and millimeter wave technology (icmmt)* (Vol. 1, pp. 36–38).

Zhu, X. X., Bamler, R., et al. (2010). Tomographic sar inversion by l1-norm regularization-the compressive sensing approach. *IEEE Transactions on Geoscience and Remote Sensing*, *48*(10), 3839–3846.